Analysis and Synthesis of Sound-Radiation with Spherical Arrays

Dissertation by

Franz Zotter

For the Degree
Doktor der Naturwissenschaften

Comittee:
Professor Robert Höldrich, Chair (IEM, KU Graz)
Professor David Wessel (CNMAT, UC Berkeley)

Institute of Electronic Music and Acoustics
University of Music and Performing Arts, Austria
September 2009

ABSTRACT

This work demonstrates a comprehensive methodology for capture, analysis, manipulation, and reproduction of spatial sound-radiation. As the challenge herein, acoustic events need to be captured and reproduced not only in one but in a preferably complete multiplicity of directions, instead. The solutions presented in this work are using the soap-bubble model, a working hypothesis about sound-radiation, and are based on fundamental mathematical descriptions of spherical acoustic holography and holophony. These descriptions enable a clear methodic approach of sound-radiation capture and reproduction. In particular, this work illustrates the implementation of surrounding spherical microphone arrays for the capture of sound-radiation, as well as the analysis of sound-radiation with a functional model. Most essential, the thesis shows how to obtain holophonic reproduction of sound-radiation. For this purpose, a physical model of compact spherical loudspeaker arrays is established alongside with its electronic control.

KURZFASSUNG

Diese Arbeit beinhaltet eine umfassende Methodik zur Aufnahme, Analyse, Manipulation und Wiedergabe von räumlicher Klangabstrahlung. Die neue Herausforderung liegt darin, akustische Ereignisse nicht nur in einer Richtung, sondern einer möglichst vollständigen Vielzahl an Richtungen zu erfassen und wiederzugeben. Die Lösungen in dieser Arbeit gehen vom Seifenblasenmodell, einer Arbeitshypothese über die Schallabstrahlung, aus und stützen sich auf mathematische Grundbeschreibungen von kugelförmiger akustischer Holografie und Holophonie. Diese Beschreibungen ermöglichen einen klaren methodischen Zugang zu Abstrahlungsaufnahme und -wiedergabe. Insbesondere wird damit die Umsetzung von umgebenden kugelförmigen Mikrofonanordnungen zur Abstrahlungsaufnahme sowie die Auswertung der Abstrahlung anhand eines funktionalen Modells gezeigt. Als wesentlichsten Beitrag zeigt die Dissertation, wie Abstrahlung holophon wiedergegeben werden kann. Dazu wird herausgearbeitet, wie kompakte kugelförmige Lautsprecheranordnungen physikalisch modelliert und elektronisch gesteuert werden.

ACKNOWLEDGEMENTS

I am very grateful for the employment I enjoyed during the research for my thesis, within the project *Virtual Gamelan Graz* (VGG) at the Institute of Electronic Music and Acoustics in Graz (IEM), on Gamelan-music. This project was an interdisciplinary research platform between the Institute of Ethno-Musicology in Graz (IME) and IEM due to an initial idea of Gerhard Nierhaus that was further developed by Professor Gerd Grupe, Alois Sontacchi, and Professor Robert Höldrich. I thank my colleagues at IEM and IME for their teamwork and the Zukunftsfonds Steiermark for their financial support (Prj. 3027). For great parts of this work, I have gratefully received support from the Austrian Research Promotion Agency (FFG), the Styrian government and the Styrian business promotion agency (SFG) under the COMET program, in the project advanced audio processing (AAP), sculptural sound.

Special thanks go to Alois Sontacchi for his project management at IEM, Johannes Zmölnig, and Thomas Musil for their PD-software and assistance. I also want to thank Josef Schalk for the construction of the icosahedral bass loudspeaker array, and the students of the Musical Acoutics Seminar 2005 for assisting the directional recordings of the Gamelan sounds. Above all, Peter Reiner and Christian Jochum for their effort in mounting the speakers, cabling, and the first acoustic and laser-vibrometry measurements, and prototype driving filters (seminar and student projects). Furthermore, thanks go to Markus Noisternig for his encouragement to explore the world, his interest and suggestions, Hannes Pomberger for his excellent work on near- and far-field beamforming with compact spherical loudspeaker arrays [Pom08]. Many thanks also go to Nino Škiljić for his work on binaural synthesis considering directional sound sources; and to Margherita Jammer and Fabian Hohl [Hoh09] for their efforts in spectral modeling of sounds and directivity (student projects). I thank Professor Helmut Fleischer (Bundeswehruniversität München) for his extensive studies on gongs and bells, and Peter Møller-Juhl (University of South Denmark, Odense) for recommending the book Fourier Acoustics.

I very deeply thank the Society for the Promotion of Electronic Music and Acoustics (GesFEMA) and the University of Music and Performing Arts for their generous support of my research visits at the Center of New Music and Audio Technology (CNMAT) in Berkeley (CA, USA). In this context, many thanks go to Professor David Wessel for the overwhelmingly warm welcome at CNMAT and

advisory, Richard Andrews for his administrative assistance, and Peter Kassakian for his interesting scientific work. Adrian Freed provided me with thousands of invaluable suggestions and critical questions and was a great inspiration in my work. Thanks to Andrew Schmeder for his improvements of the wording and proof-reading, discussions and interest in the subject, and to Rimas Avizienis for his electronic hardware prototypes.

For providing me the opportunity to talk at their institutions, I thank Ramani Duraiswami and his group PIRL, UMIACS at the Maryland University, Jens Meyer and Gary Elko (mhacoustics, Summit, NJ), Gottfried Behler (ITA, RWTH, Aachen) and Martin Pollow, as well as Sascha Spors and Jens Ahrens (Deutsche Telekom Labs, Berlin).

Special thanks to all the people at ITA Aachen, also for the important corrections to some mistakes in the electroacoustic model and for providing me with their multi-channel saxophone radiation recordings. Thanks to Zhiyun Li, Svend-Oscar Petersen, and Boaz Rafaely for their inspiring works on rigid compact spherical microphone arrays.

Professor Robert Höldrich deserves to be mentioned separately. He helped taking many steps through this thesis, spending a lot of time in fruitful discussions, encouragement, and important corrections.

Finally, above all: Thank you Ingrid and Willi for supporting so much academic education! Helmuth, thank you very much!

Contents

Chapter I

INTRODUCTION

In order to explain the purpose of analysis and synthesis of spherical sound-radiation, it is crucial to get an overview of the history and soil this particular research interest has grown on. Mainly, this work finds motivation from two research areas.

Firstly from the music or computer music perspective, the motivation for directivity pattern synthesis is associated with loudspeakers and their application as musical sound sources. According to the articles [Cur00] and [LSO06], acoustic directivity pattern synthesis mimicking the sound-radiation of musical instruments starts in the nineteen seventies, with some criticism by Pièrre Boulez about the quality of loudspeaker playback.

Secondly, room acousticians use sophisticated software packages that facilitate the acoustical design process, taking into account the directivity of sound sources. In principle, these software packages are able to simulate the basic quality measures in room acoustics but also offer realistic simulations of virtual sound scenes to make audible an acoustic room in its early design stages. Usually, the sound sources can be endowed with their own directivity to get more accurate simulation results. On the other hand it is interesting to evaluate excellent concert hall acoustics also by measurements of its directional characteristics. For this purpose, the capability of directional measurement and radiation becomes necessary.

Evidence on perceived sound-radiation. According to information provided by René Caussé (IRCAM), and the hints from Gerhard Eckel, Adrian Freed, and David Wessel, there was an experiment on the sound radiated from a violin, conducted some decades ago at IRCAM in Paris. The experiment has never been published, but had a rather important impact and serves as a motivation for the present work. René Caussé states that the experiment was presented to the audience at the conference "Artelier Ircam[1]" at IRCAM in 1989. According to his statement, it was conducted by Jean-Marie Adrien, Peter Eötvös, and Olivier Warusfel. Three versions of a violin sound were presented to the auditorium, cp. Fig. 1. The first was coming from a real violin played by a violinist. The second sound originated from a violin playback over a single loudspeaker taken

[1]Subtitle: "Maîtriser l'espace: une étude sur le rayonnement des sources sonores"

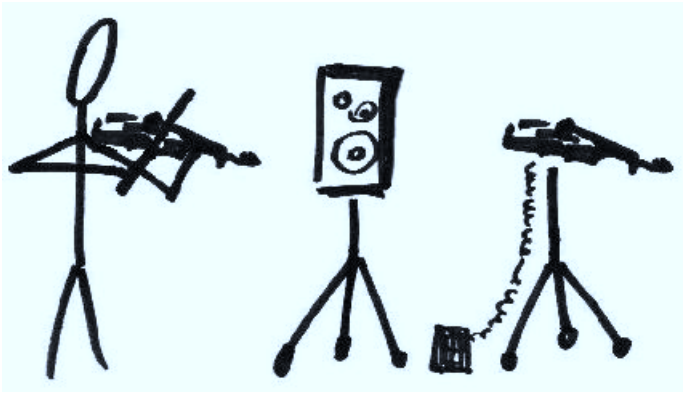

Figure 1: Violin radiation demonstration at IRCAM.

from a recording with a single microphone. The third version was produced by the vibration of the violin bridge reconstructed at the bridge of a stand-mounted violin[2].

In contrast to the loudspeaker playback, the sound radiated by the artificially excited violin has been described as lively and present, exhibiting much bigger similarity to the violin played by the violinist. This demonstration is regarded being a strong evidence for the perceptual influence of sound-radiation; even if it is unknown to what extent sound-coloration has been isolated as a possible cue by equalization.

Systematic directivity capture and reproduction? It might be a good idea regard sound-radiation of sources separately from its diffusion into rooms. In order to systematically develop tools for directivity analysis and synthesis, two questions should be posed:

- How do we determine the overall directivity patterns of sound sources?
- How can we make room acoustics measurements with directivity adjustable to particular kinds of natural sound sources?

1.1 A Soap-Bubble Model of Sound-Radiation

Before getting into the details in the subsequent sections, I offer an illustrative image of how to interpret sound radiation, capture, and synthesis of sound sources.

[2]Original announement: "La prise de son sur le violon est réalisée par deux céramiques piezoélectriques placées au bas des pieds de chevalet. Les deux cristaux sont sensibles à la force dynamique qui leur est appliqué, et sont suffisemment durs et légers pour supporter la pression statique exercée par les cordes, et ne pas modifier le fonctionnement du chevalet. L'ensemble est monté sur un violon de qualité."

Let us assume a free sound field (no sources or obstacles) and an ideal[3] soap bubble that is large enough to enclose a musician and an instrument. As the instrumentalist produces sounds, the soap-bubble surface vibrates strictly according to the motion of the air molecules. The wave-form of the vibration represents the sound radiated to the respective point of observation on the sphere. Generally, the quality of the sound may vary between different points of observation. Specifically, the loudness and timbre of the radiated sound is dependent on the position of the observer with respect to the instrument.

Figure 2: Soap-bubble model of acoustic radiation.

Capturing the radiated sound. According to literature on acoustics (e.g. Williams [Wil99]), it is sufficient to completely identify the motion of this continuous surface in order to describe the acoustic sound-radiation of enclosed sound sources entirely. This type of setting is called *exterior problem*. A continuous capture of this motion may seem out of reach, but spatial sampling of the spherical surface with microphones, i.e. a *surrounding spherical microphone array*, is feasible, see Fig. 3.

Reproducing the radiated sound. Given a suitable arrangement of loudspeakers (ideally a spherical membrane that can be driven in every mode of vibration at every frequency) the acoustic radiation from a sound source can be reproduced entirely. The goal is to produce the same patterns of motion on a *soap bubble* around this technical device as those, the capture of which has been described above. A feasible way of achieving this is again to sample the spherical

[3]The surface of the bubble must not have mass, stiffness, or friction.

Figure 3: Capturing the sound-radiation of the *bonang barung* with 26 microphones in a hemispherical arrangement in an acoustically damped chamber at IEM (in the picture: Rainer Schütz (Institute of Ethnomusicology, Graz) playing it).

surface with individually driven loudspeakers, i.e. a *compact spherical loudspeaker array*.

What has been neglected implicitly? To capture the sound appropriately, the microphones and the surrounding room must not be an obstacle in the sound field, i.e. they must not cause reflections of the radiated sound. Otherwise the problem becomes a *mixed interior and exterior problem*, cf. [Wil99].

In free-field conditions, or an anechoic measurement chamber, a playback device can be matched as to produce the same directivity pattern as measured from an instrument. However, when operating in ordinary rooms, i.e. a different acoustic load, sound sources with the same free-field sound-radiation might produce different sound-radiation. This is due to the different shape, different inner impedance, and different reflection or diffraction characteristics. As a rigorous assumption, the influence of these aspects will be neglected in the following considerations. In fact, this assumption might hold as many instruments have a much higher mechanical impedance than the sound field (*maladjustment of impedances*).

1.2 Musical Instrument Model

Whoever has played a musical instrument has experienced that the production of musical sounds depends on many parameters. For most instruments, a huge variation of the sound can be achieved by slightly changing parameters or configurations of the instrument. Essentially, several parameters have an impact on the timbre, the pitch, or other properties of the sound, see Fig. 4.

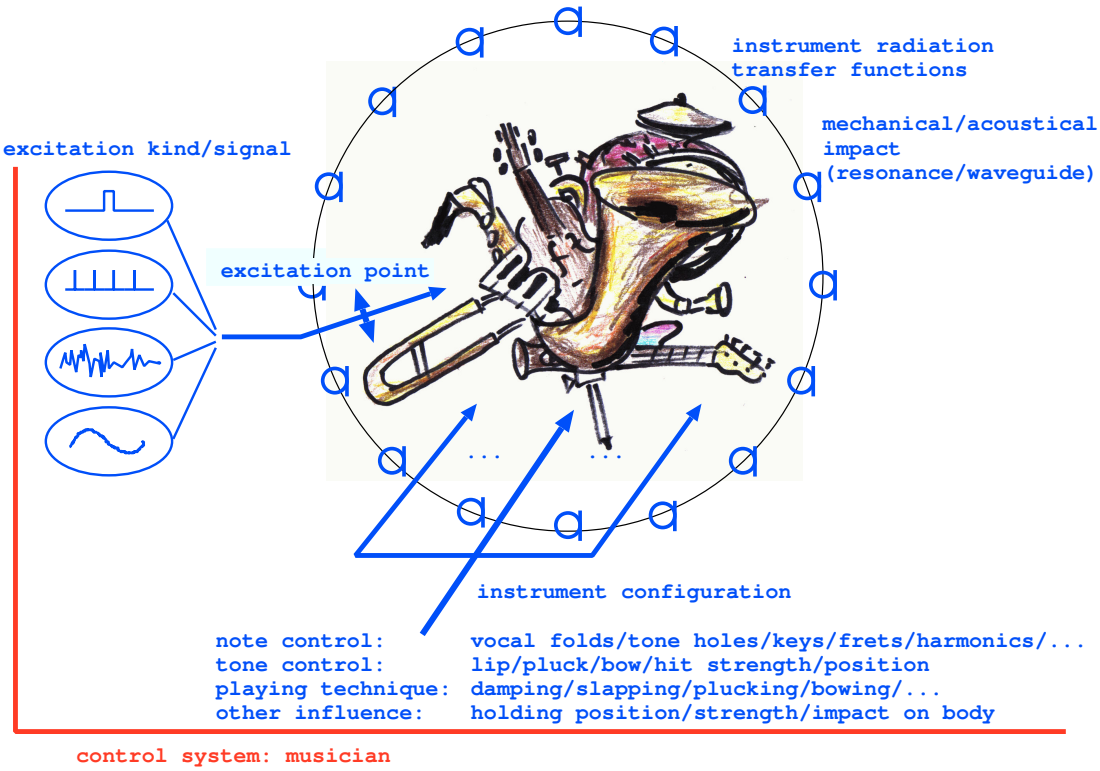

Figure 4: A generic musical instrument model illustrates that many parameters may be involved in the process of sound production with musical instruments.

In order to get reproducible and clean measurements of the musical acoustics of instruments, there are usually two classical strategies:

- "playing" musical instruments artificially, i.e. with robotic devices
- "playing" artificial musical instruments, i.e. physical models

From a musical point of view, one could easily argue against both approaches: well-trained musicians might be better in playing musical instruments than scientists playing the instrument artificially, or playing artificial musical instruments for the purpose of a measurement[4].

[4]The corollary that musicians are better in either playing musical instruments artificially, or playing artificial musical instruments than scientists playing natural musical instruments might be incorrect and fail :-).

Instrumental sound plus radiation analysis and synthesis developed within in this thesis can be summarized as to follow an alternative hypothesis:

Hypothesis

- Natural conditions for production of musical sounds with instruments depend on many control quantities (playing techniques, time-variant instruments, ...) thus technical mounting and excitation seems inappropriate, and it is hard to provide all synthesis parameters properly.
- Synchronous recordings of multi-channel microphone array sound samples with musicians can be considered being the most realistic mode of analyzing sound and radiation.

1.3 Organization of Contents

In the second chapter of this thesis, acoustics in spherical coordinates, i.e. the solutions of the Helmholtz equation (wave equation in the frequency domain), is revisited as a mathematical/physical basis of all the following chapters. Advanced readers may skip this section. However, some practical aspects about boundary value problems and the description of sources are given.

The third chapter describes how the base solutions of the acoustics in spherical coordinates can be manipulated in various ways. Above all, it shows how canonic forms of coordinate transforms affect the spherical base-solutions, and their implementation for the real-valued spherical harmonics is described as well. Furthermore, hints on other manipulations like correlation, multiplication, truncation and its relevance, as well as important relations between circular and spherical convolution are given.

As being essential for all kinds of discrete-space spherical boundaries, the fourth chapter describes how to discretize the spherical surface using microphones or loudspeakers for holographic analysis or holophonic synthesis. It provides a comprehensive overview of the literature about sampling and transform strategies on spherical surfaces, which is the key to the decomposition of measured and reconstructed fields into spherical base-solutions.

The fifth chapter elaborates on the practical capture and analysis of radiating sound with *spherical microphone arrays surrounding* the source. Based on an overview of existing works, a generic principle of acoustic sound-radiation and the problem with the retrieval of the primal signal is given. As a holistic solution, additive analysis and synthesis of partials, in sound and radiation, is given, based on the total-power spectrogram gathered from all microphones. The chapter shows

the analyses of some musical instrument sounds and their graphical representation, including two special cases exploiting spherical symmetries. It concludes with an outlook on adaptive blind channel identification, and an outlook on parametric sound-radiation models.

The sixth chapter presents the second practical contribution in this context: The application of *compact spherical loudspeaker arrays* for sound-radiation synthesis based on practical measurement data. Measurements with microphones and laser-vibrometry are considered as suitable means within this chapter. Furthermore, a model consisting of a solid sphere with individually vibrating discrete spherical caps and a continuous spherical membrane are introduced and studied. The first model concludes with a complete electroacoustic system analysis, illustrating the capacities of compact spherical loudspeaker arrays and directivity control thereof. The latter model illustrates that, inside compact spherical loudspeaker arrays, a common interior volume is beneficial. Moreover, efficient control and radial beamforming are briefly discussed.

The seventh and last chapter gives a general conclusion and offers an outlook on future work.

Chapter II

ACOUSTICS IN SPHERICAL COORDINATES

This extended review of theoretical basics intends to provide a thorough understanding of the relations required to solve the *soap-bubble problem*. Hereby, this chapter introduces fundamental mathematical descriptions, not only capable of solving the sound-radiation capture and playback problem but also various other problems that share a simple description in the spherical coordinate system. The chapter aims to work as a detailed reference, the content of which is collected from many sources in literature, in order to give a comprehensive overview of underlying principles and problems. Specifically, it shows the standard solution of the wave-equation (in particular the Helmholtz equation) in spherical coordinates, representations of point and plane-wave sources, as well as spherical boundary value problems.

The wave-equation. The linear lossless wave equation for the time-domain sound pressure $p(\boldsymbol{r},t)$ and the Euler equation for the particle velocity $\boldsymbol{v}(\boldsymbol{r},t)$ can be written as (see Franck Giron [Gir96], Earl G. Williams [Wil99], and Nail A. Gumerov and Ramani Duraiswami [GD04]):

$$\Delta p(\boldsymbol{r},t) = \frac{1}{c^2}\,\ddot{p}(\boldsymbol{r},t)\,, \tag{1}$$

$$\rho_0\,\dot{\boldsymbol{v}}(\boldsymbol{r},t) = -\boldsymbol{\nabla}\,p(\boldsymbol{r},t)\,, \tag{2}$$

where $\boldsymbol{r}$ is the position vector in space $\mathbb{R}^3$, t the time variable, c the speed of sound, $\boldsymbol{\nabla} = \partial/\partial\boldsymbol{r}$ is the gradient, $\Delta = \boldsymbol{\nabla}^{\mathrm{T}}\boldsymbol{\nabla}$ the Laplacian, $\dot{()} = \partial/\partial t$ the first and $\ddot{()} = \partial^2/\partial t^2$ the second derivative with respect to time, and ρ_0 the air density. Within the Fourier expansion integral $p(\boldsymbol{r},t) = \int_{-\infty}^{\infty} p(\boldsymbol{r},\omega)\ \mathrm{e}^{\mathrm{i}\omega t}\ d\omega$, the wave equation simplifies to the Helmholtz equation. With $\frac{1}{c^2}\,\ddot{p}(\boldsymbol{r},\omega) = \frac{(\mathrm{i}\omega)^2}{c^2}\ p(\boldsymbol{r},\omega)$ and $\rho_0\ \dot{\boldsymbol{v}}(\boldsymbol{r},\omega) = (\mathrm{i}\omega)\,\rho_0\ \boldsymbol{v}(\boldsymbol{r},\omega)$, as well as the wave-number $k = \omega/c$, Eqs. (1) and (2) become:

$$\left(\Delta + k^2\right) p(\boldsymbol{r},\omega) = 0, \tag{3}$$

$$\frac{\rho_0 c}{\mathrm{i}}\ k\ \boldsymbol{v}(\boldsymbol{r},\omega) = -\boldsymbol{\nabla} p(\boldsymbol{r},\omega)\,. \tag{4}$$

The Helmholtz equation can be solved according to the definition of the gradient and the Laplacian in the respective coordinate system. In Cartesian coordinates $\boldsymbol{\nabla} = (\partial/\partial x, \partial/\partial y, \partial/\partial z)^{\mathrm{T}}$, and $\Delta = \partial^2/\partial x^2 + \partial^2/\partial y^2 + \partial^2/\partial z^2$.

In the remainder of this thesis, Fourier coefficients are used to describe the sound pressure $p(\boldsymbol{r}) = p(\boldsymbol{r}, \omega)$, and velocity $\boldsymbol{v}(\boldsymbol{r}) = \boldsymbol{v}(\boldsymbol{r}, \omega)$. We omit the frequency variable ω for better readability.

2.1 Solving the Helmholtz-Equation in Spherical Coordinates

In order to determine the expression for the gradient $\boldsymbol{\nabla}$ and the Laplacian Δ in spherical coordinates, the relations between Cartesian and spherical coordinates have to be considered

$$\boldsymbol{r} = \begin{pmatrix} x \\ y \\ z \end{pmatrix} = r \begin{pmatrix} \cos(\varphi)\sin(\vartheta) \\ \sin(\varphi)\sin(\vartheta) \\ \cos(\vartheta) \end{pmatrix}, \quad \mathring{\boldsymbol{r}} = \begin{pmatrix} r \\ \varphi \\ \vartheta \end{pmatrix} = \begin{pmatrix} \sqrt{x^2+y^2+z^2} \\ \arctan\left(\frac{y}{x}\right) \\ \arctan\left(\frac{\sqrt{x^2+y^2}}{z}\right) \end{pmatrix}. \tag{5}$$

The spherical coordinates r, φ, and ϑ are called radius, azimuth and zenith angle, respectively. The Laplacian for the spherical coordinate system is computed from the chain of the partial derivatives $\boldsymbol{\nabla}_{\boldsymbol{r}} = \boldsymbol{\nabla}_{\boldsymbol{r}}\, \mathring{\boldsymbol{r}}^{\mathrm{T}}\, \boldsymbol{\nabla}_{\mathring{\boldsymbol{r}}}$, see Eq. (122), hence $\Delta = \boldsymbol{\nabla}_{\mathring{\boldsymbol{r}}}^{\mathrm{T}} \left(\boldsymbol{\nabla}_{\boldsymbol{r}}\, \mathring{\boldsymbol{r}}^{\mathrm{T}}\right)^{\mathrm{T}} \left(\boldsymbol{\nabla}_{\boldsymbol{r}}\, \mathring{\boldsymbol{r}}^{\mathrm{T}}\right) \boldsymbol{\nabla}_{\mathring{\boldsymbol{r}}}$. Its definition yields [BSMM01]:

$$\begin{aligned} \Delta p(\boldsymbol{r}) &= \Delta_r\, p(\boldsymbol{r}) + \Delta_\varphi\, p(\boldsymbol{r}) + \Delta_\vartheta\, p(\boldsymbol{r}) \\ &= \frac{1}{r^2}\frac{\partial^2 r^2 p(\boldsymbol{r})}{\partial r^2} + \frac{1}{r^2\sin^2(\vartheta)}\frac{\partial^2 p(\boldsymbol{r})}{\partial \varphi^2} + \frac{1}{r^2\sin(\vartheta)}\frac{\partial}{\partial \vartheta}\left(\sin(\vartheta)\frac{\partial p(\boldsymbol{r})}{\partial \vartheta}\right). \end{aligned} \tag{6}$$

A homogeneous solution of the Helmholtz equation $\Delta\, p(\boldsymbol{r}) + k^2\, p(\boldsymbol{r}) = 0$ is found with the product ansatz and separation of variables [Wei08]:

$$p(\boldsymbol{r}) = R(kr)\Phi(\varphi)\Theta(\vartheta), \tag{7}$$

$$\frac{1}{p(\boldsymbol{r})} \cdot | \qquad \Delta\, p(\boldsymbol{r}) + k^2\, p(\boldsymbol{r}) = 0 \tag{8}$$

$$\frac{1}{R(kr)}\Delta_r\, R(kr) + k^2 + \frac{1}{\Phi(\varphi)}\Delta_\varphi\, \Phi(\varphi) + \frac{1}{\Theta(\vartheta)}\Delta_\vartheta\, \Theta(\vartheta) = 0 \tag{9}$$

To separate the above into three differential equations in r, ϑ, and φ, the terms dependent on the respective other two quantities are replaced by constants:

$$\begin{pmatrix} \frac{1}{R(kr)} \cdot \frac{1}{r^2}\frac{\partial^2}{\partial r^2} r^2 R(kr) + k^2 \\ \frac{1}{\Phi(\varphi)} \cdot \frac{1}{r^2\sin^2(\vartheta)}\frac{\partial^2}{\partial \varphi^2}\Phi(\varphi) \\ \frac{1}{\Theta(\vartheta)} \cdot \frac{1}{r^2\sin(\vartheta)}\frac{\partial}{\partial \vartheta}\left(\sin(\vartheta)\frac{\partial}{\partial \vartheta}\Theta(\vartheta)\right) \end{pmatrix} = \begin{pmatrix} \frac{n(n+1)}{r^2} \\ -\frac{m^2}{r^2\sin^2(\vartheta)} \\ -\frac{n(n+1)}{r^2} + \frac{m^2}{r^2\sin^2(\vartheta)} \end{pmatrix}. \tag{10}$$

With the numbers $n(n+1)$ and m^2 involved in the separation constants on the right hand side of Eq. (10), the Helmholtz equation is split up into three differential equations known from literature. Using positive integer indices $n, m \in \mathbb{N}^0$: $m \leq n$

provides complete harmonic sets of orthogonal solutions on the intervals $0 < r \leq \infty$, $0 \leq \vartheta \leq \pi$ and the periodic interval $0 \leq \varphi \leq 2\pi$ [Zio95]. In particular, these are a spherical Bessel differential equation for $R(kr)$, a linear differential equation for $\Phi(\varphi)$, and an associated Legendre differential equation for $\tilde{\Theta}(\cos(\vartheta)) = \Theta(\vartheta)$, and $\mu = \cos(\vartheta)$ cf. [Wei08, BSMM01]:

$$\begin{pmatrix} \frac{\partial^2}{\partial(kr)^2}(kr)^2 R(kr) + \left[(kr)^2 - n\,(n+1)\right] R(kr) \\ \frac{\partial^2}{\partial\varphi^2}\Phi(\varphi) + m^2\Phi(\varphi) \\ \frac{\partial}{\partial\mu}\left[\frac{1}{1-\mu^2}\frac{\partial}{\partial\mu}\tilde{\Theta}(\mu)\right] + \left[n\,(n+1) - \frac{m^2}{1-\mu^2}\right]\tilde{\Theta}(\mu) \end{pmatrix} = \begin{pmatrix} 0 \\ 0 \\ 0 \end{pmatrix}. \tag{11}$$

The spherical Bessel and Neumann functions or the Hankel functions of the first and second kind solve the spherical Bessel differential equation. The linear differential equation is solved by sines and cosines, or complex exponentials, and the Legendre differential equation is solved by Legendre functions of the first and second kind. Symbolically, the complete set of solutions for the ansatz functions in $p(\boldsymbol{r}) = R(kr)\Phi(\varphi)\Theta(\vartheta)$ is written as

$$R(kr) = R_n(kr) = \left\{ j_n(kr),\ y_n(kr) \mid h_n^{(1)}(kr),\ h_n^{(2)}(kr) \right\}, \tag{12}$$

$$\Phi(\varphi) = \Phi_m(\varphi) = \left\{ \sin(m\varphi),\ \cos(m\varphi) \mid \mathrm{e}^{\pm \mathrm{i}m\varphi} \right\}, \tag{13}$$

$$\Theta(\vartheta) = \Theta_n^m(\vartheta) = \left\{ P_n^m(\mu),\ Q_n^m(\mu) \right\}. \tag{14}$$

2.1.1 Selection of Physical Solutions

In acoustics, the above solutions of the Helmholtz equation are used to describe source-free sound fields. These source-free fields are separated from source-domains by a spherical boundary, on which the sound pressure or particle velocity can be described by convergent, non-singular angular solutions. Using both angular and radial solutions, the whole source-free part is mathematically fully described due to the known values on its boundary. The source-free field must not contain singularities, and is often referred to as the region of convergence.

Feasible angular solutions. For the dependency on μ, typically the Legendre functions of the second kind (slashed-through below) are omitted due to their singularities at $\mu = \pm 1$, which render them useless for the description of spherical boundary value problems[1]

$$\Theta_n^m(\vartheta) = \left\{ P_n^m(\mu),\ \cancel{Q_n^m(\mu)} \right\}. \tag{15}$$

[1]Note that a slight variation of the radius towards the source-free part of the field must make singularities vanish from the spherical boundary. This is impossible if already the angular functions are singular. However, Legendre functions of the second kind have to be considered when dealing with prolate/oblate spheroidal coordinates, cf. [Wik08a].

In azimuth φ, the selection of either the complex exponential or the real valued sine and cosine harmonics does not affect the applicability of the angular solutions. Alternatively, the real-valued version can be written in terms of Chebyshev polynomials of the first $T_m(\cos(\varphi)) = \cos(m\varphi)$ and the second kind $\sqrt{1-\cos^2(\varphi)}\,U_{m-1}(\cos(\varphi)) = \sin(m\varphi)$. A selection has to be made arbitrarily. There are two options of excluding the functions with slash-through

$$\Phi_m(\varphi) = \{\sin(m\varphi),\ \cos(m\varphi) \,|\, \cancel{\mathrm{e}^{\pm \mathrm{i}m\varphi}}\}\,, \text{ or} \tag{16}$$

$$\hat{\Phi}_m(\varphi) = \left\{\cancel{\sin(m\varphi),\ \cos(m\varphi)} \,|\, \mathrm{e}^{\pm \mathrm{i}m\varphi}\right\}. \tag{17}$$

For convenience, the combination of both angular solutions is usually denoted by a single symbol Y_n^m, the spherical harmonic. Its dependency on both angles can be expressed by a unit vector

$$\boldsymbol{\theta} = \begin{pmatrix} \cos(\varphi)\sin(\vartheta) \\ \sin(\varphi)\sin(\vartheta) \\ \cos(\vartheta) \end{pmatrix}. \tag{18}$$

Usually the range for m is redefined as $m \in \mathbb{Z} : -n \leq m \leq n$, which facilitates the selection between the different azimuth harmonics, see Sec. 2.2. With a scalar orthonormalization constant $N_n^{|m|}$, the real-valued spherical harmonics are written as

$$Y_n^m(\boldsymbol{\theta}) := N_n^{|m|}\ \Phi_m(\varphi)\ \Theta_n^{|m|}(\vartheta). \tag{19}$$

Feasible radial solutions. The selection of admissible radial functions is also done by regarding the singularities of the functions involved. For interior boundary value problems, the functions must not be singular inside a bounded domain $kr < kr_0 \to \infty$, which may reach infinite size. The only feasible solution is the spherical Bessel function $j_n(kr)$ because it is regular for every $kr \geq 0$.

Conversely, for exterior boundary value problems the functions may be singular at $kr < kr_0$ and must be non-singular at $kr > kr_0 > 0$. This requirement is met by all radial solutions. Using the radial impedance $z_r(kr) = \frac{p(kr)}{v_r(kr)}$ of the free sound field, the acoustic power can be written as depending on the sound pressure only $w(kr) = p(kr)\,v_r^*(kr) = |p(kr)|^2/z_r(kr)$. According to Sommerfeld's radiation condition, radiating functions must provide a positive and real-valued power dissipation $w(kr)$ in the far-field. This requires a purely resistive impedance $\lim_{kr\to\infty} z(kr) \in \mathbb{R}^+$. In fact, the impedance approaches the impedance of the one-dimensional plane-wave in the far-field $\lim_{kr\to\infty} z_r(kr) = \rho_0 c$. With the Euler equation $\mathrm{i}\rho_0 c\, v_r(kr) = -\frac{\partial}{\partial(kr)}\, p(kr)$, this identity directly yields the Sommerfeld

radiation condition[2] [Wik08b]

$$\lim_{r\to\infty}\left(\quad -\frac{\mathrm{i}\rho_0 c\, p(kr)}{\frac{\partial}{\partial(kr)}\, p(kr)} \stackrel{!}{=} \rho_0 c \quad \right) \tag{20}$$

$$\lim_{r\to\infty}\left(\frac{\partial}{\partial(kr)} p\,(kr) + \mathrm{i}\, p\,(kr)\right) = 0, \tag{21}$$

With the above definitions, only the spherical Hankel function of the second kind $h_n^{(2)}(kr)$ fulfills the Sommerfeld radiation condition, see Appendix A. The set of solutions for the interior boundary value problem (regular) and the exterior boundary value problem (singular) is consequently reduced to the functions:

$$R_n(kr) = \left\{ j_n(kr),\ \cancel{y_n(kr) + h_n^{(1)}(kr)},\ h_n^{(2)}(kr) \right\}. \tag{22}$$

The spherical Bessel functions are real-valued and therefore represent harmonic standing waves. Conversely, spherical Hankel functions of the second kind are waves travelling towards $kr \to \infty$ with increasing time $t \to \infty$. As all $h_n^{(2)}(kr)$ share the expressions $\mathrm{e}^{-\mathrm{i}kr}$, the expansion in $\mathrm{e}^{\mathrm{i}\omega t}$ and observation of a point of constant phase on the wave $-\mathrm{i}kr + \mathrm{i}\omega t \stackrel{!}{=} const.$ demonstrates this behavior.

As the two radial functions have a Wronskian cf. [AW04, Wil99, BSMM01] that is unequal to zero, they form a set of independent solutions:

$$W(kr) = \begin{vmatrix} j_n(kr) & h_n^{(2)}(kr) \\ j_n'(kr) & h_n'^{(2)}(kr) \end{vmatrix} = j_n(kr)\ h_n'^{(2)}(kr) - j_n'(kr)\ h_n^{(2)}(kr) = \frac{1}{\mathrm{i}\,(kr)^2}. \tag{23}$$

2.2 Spherical Base-Solutions

The total solution is given as a sum of feasible solutions Eqs. (19) (22) of the Helmholtz equation, cf. [Gir96, Wil99, GD04]:

$$\begin{aligned} p\,(kr, \boldsymbol{\theta}) &= \sum_{n=0}^{\infty} \sum_{m=-n}^{n} \left[b_{nm} j_n\,(kr) + c_{nm} h_n^{(2)}\,(kr) \right] Y_n^m\,(\boldsymbol{\theta}), \\ &= \sum_{n=0}^{\infty} \sum_{m=-n}^{n} \left[b_{nm} R_n^m\,(kr, \boldsymbol{\theta}) + c_{nm} S_n^m\,(kr, \boldsymbol{\theta}) \right], \end{aligned} \tag{24}$$

with $Y_n^m(\boldsymbol{\theta})$ are the normalized spherical harmonics depending on the unit vector $\boldsymbol{\theta}$. $j_n(kr)$ are the spherical Bessel functions, and $h_n^{(2)}(kr)$ are the spherical Hankel functions of the second kind depending on the product of wave-number and radius kr. Equivalently, $R_n^m\,(kr, \boldsymbol{\theta}) = j_n\,(kr)\, Y_n^m\,(\boldsymbol{\theta})$ is the regular incident field solution, and $S_n^m\,(kr, \boldsymbol{\theta}) = h_n^{(2)}\,(kr)\, Y_n^m\,(\boldsymbol{\theta})$ is the singular radiating field solution, cf. [GD04]. b_{nm} and c_{nm} can be called the *wave spectrum* of the incident and radiating field, respectively.

[2] Note that the Sommerfeld radiation condition will look different if $\mathrm{e}^{-\mathrm{i}\omega t}$ is used for harmonic expansions with respect to frequency.

Spherical harmonics. The spherical harmonics are base functions for a harmonic decomposition of distributions on the two-dimensional sphere $\mathbb{S}^2$ (depicted in Fig. 5). For example, in this sense the spherical harmonics can be applied to describe the vibrational modes of a spherical surface. In contrast to the Fourier kernel on the plane $\mathbb{R}^2$, which equals $\mathrm{e}^{\mathrm{i}k_x x}\mathrm{e}^{\mathrm{i}k_y y}$, the complex-valued spherical harmonics are defined as:

$$\hat{Y}_n^m(\boldsymbol{\theta}) = \hat{N}_n^{|m|}\ \hat{\Phi}_m(\varphi)\ \Theta_n^m(\vartheta). \tag{25}$$

The associated Legendre functions $P_n^{|m|}(\mu)$ determine the transform kernel in $\mu = \cos(\vartheta)$ with the zenith angle ϑ, whereas in azimuth (=latitude) direction, we obtain the Fourier-kernel $\mathrm{e}^{\mathrm{i}m\varphi}$; the spatial frequency indices are $n \in \mathbb{N}_0$ and $m \in \mathbb{Z} : -n \leq m \leq n$. $\hat{N}_n^{|m|}$ is a scalar normalization constant. Usually, the index n is referred to as *order* and the index m as *degree*[3]. In many cases it is sufficient to use the real-valued spherical harmonics:

$$Y_n^m(\boldsymbol{\theta}) = N_n^{|m|}\ P_n^{|m|}(\cos(\vartheta)) \cdot \begin{cases} \sin(m\varphi) & \text{, for } m < 0, \\ \cos(m\varphi) & \text{, for } m \geq 0. \end{cases} \tag{26}$$

With the normalization constant $N_n^{|m|}$ the spherical harmonics describe an orthonormal set of base functions. Orthonormality holds as the integral (inner product) of two spherical harmonics over the sphere vanishes for different indices

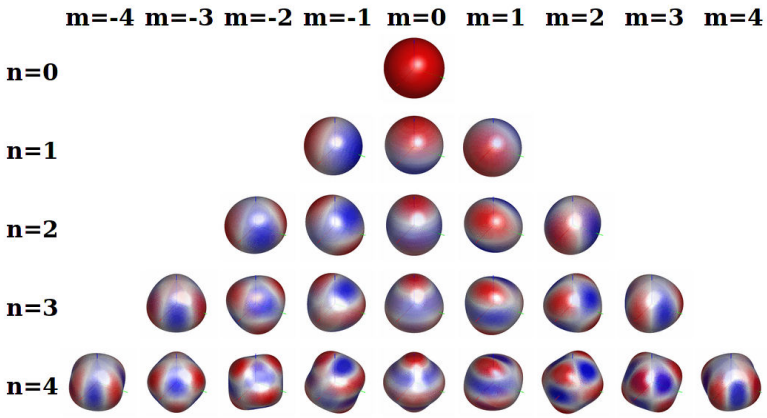

Figure 5: The real-valued spherical harmonics for $n = 0 \ldots 4$ as modes of vibration on a spherical surface. The index n (*order*) counts the nodal circles, and $|m|$ (*degree*) counts those running through the north and south pole.

[3]In many mathematics and physics textbooks the nomenclature is just the opposite. Most literature on spatial audio and spherical harmonics, however, uses these labels. Thanks to Nail A. Gumerov for clarification.

and equals unity otherwise. Accordingly, the property is written using a product of Kronecker deltas:

$$\int_{\mathbb{S}^2} Y_n^m(\boldsymbol{\theta})\; Y_{n'}^{m'}(\boldsymbol{\theta})\; d\boldsymbol{\theta} = \delta_{nn'}\,\delta_{mm'}. \tag{27}$$

Using the orthonormality, a spherical harmonics transform integral of $g(\boldsymbol{\theta})$ can be given:

$$g(\boldsymbol{\theta}) = \sum_{n'=0}^{\infty}\sum_{m'=-n'}^{n'} \gamma_{n'm'}\; Y_{n'}^{m'}(\boldsymbol{\theta}) \qquad \mid Y_n^m(\boldsymbol{\theta}), \int_{\mathbb{S}^2} d\boldsymbol{\theta}$$

$$\int_{\mathbb{S}^2} g(\boldsymbol{\theta})\; Y_n^m(\boldsymbol{\theta})\; d\boldsymbol{\theta} = \sum_{n'=0}^{\infty}\sum_{m'=-n'}^{n'} \gamma_{n'm'} \int_{\mathbb{S}^2} Y_{n'}^{m'}(\boldsymbol{\theta})\; Y_n^m(\boldsymbol{\theta})\; d\boldsymbol{\theta}$$

$$\int_{\mathbb{S}^2} g(\boldsymbol{\theta})\; Y_n^m(\boldsymbol{\theta})\; d\boldsymbol{\theta} = \sum_{n'=0}^{\infty}\sum_{m'=-n'}^{n'} \gamma_{n'm'}\; \delta_{nn'}\delta_{mm'}$$

$$\Rightarrow \int_{\mathbb{S}^2} g(\boldsymbol{\theta})\; Y_n^m(\boldsymbol{\theta})\; d\boldsymbol{\theta} =: \gamma_{nm} \tag{28}$$

$$\mathcal{SHT}\left\{g(\boldsymbol{\theta})\right\} =: \gamma_{nm}.$$

Without truncation, the expansion of γ_{nm} in spherical harmonics is complete

$$\sum_{n=0}^{\infty}\sum_{m=-n}^{n} \gamma_{nm}\; Y_n^m(\boldsymbol{\theta}) = g(\boldsymbol{\theta}), \tag{29}$$

and fulfills the Parseval theorem

$$\int_{\mathbb{S}^2} |g(\boldsymbol{\theta})|^2\; d\boldsymbol{\theta} = \sum_{n=0}^{\infty}\sum_{m=-n}^{n} |\gamma_{nm}|^2. \tag{30}$$

Normalization constant. The normalization constant N_n^m is defined as:

$$N_n^m = (-1)^m \sqrt{\frac{(2n+1)\,(2-\delta_m)}{4\pi}\frac{(n-m)!}{(n+m)!}}, \tag{31}$$

wherein ()! is the factorial. In Appendix B a recurrent computation of N_n^m is given for efficient numerical implementation.

Legendre functions. The associated Legendre functions can be determined by the following recurrence relations for $m \geq 0$, cf. [Wil99, GD04, Wei08]:

$$P_0^0(\mu) = 1 \tag{32}$$

$$P_n^n(\mu) = -(2n-1)\,P_{n-1}^{n-1}(\mu)\,\sqrt{1-\mu^2} \qquad \forall n \in \mathbb{Z} : n > 0 \tag{33}$$

$$P_n^{n-1}(\mu) = (2n-1)\,\mu P_{n-1}^{n-1}(\mu) \qquad \forall n \in \mathbb{Z} : n > 0 \tag{34}$$

$$(n-m)\,P_n^m(\mu) = (2n-1)\,\mu P_{n-1}^m(\mu) - (n+m-1)\,P_{n-2}^m(\mu) \tag{35}$$

$$\forall n, m \in \mathbb{Z} : n \geq 3;\; 0 \leq m \leq n-2$$

For negative m, the following relation holds [Wei08]:

$$P_n^{-m}(\mu) = (-1)^m \frac{(n-m)!}{(n+m)!} P_n^m(\mu). \tag{36}$$

Usually, it is efficient and stable to use the recurrence relations on the numerical values directly. For other, mathematical purposes, it might also be advantageous to store the polynomial coefficients. Appendix B gives a structure to store these coefficients, which can also be calculated using the recurrence relations.

Spherical Hankel-, Bessel-, and Neumann-functions. The spherical Bessel function can be derived from the $\mathrm{sinc}(kr)$-function $\sin(kr)/(kr)$, [Wei08]:

$$j_n(kr) = (-1)^n (kr)^n \left(\frac{d}{kr\, d(kr)}\right)^n \frac{\sin(kr)}{kr}. \tag{37}$$

Similarly, the spherical Neumann function is derived from $-\cos(kr)/(kr)$

$$y_n(kr) = (-1)^{n+1} (kr)^n \left(\frac{d}{kr\, d(kr)}\right)^n \frac{\cos(kr)}{kr}. \tag{38}$$

The spherical Hankel function $h_n^{(1)}(kr)$ is a complex-valued composite of both $j_n(kr)$ and $y_n(kr)$; $h_n^{(2)}(kr)$ is its complex conjugate:

$$h_n^{(1)}(kr) = j_n(kr) + \mathrm{i}\, y_n(kr), \qquad h_n^{(2)} = h_n^{(1)*} \tag{39}$$

All radial functions allow for a computation with the same recurrence relation. We use the generic term $f_n(kr)$ that can be replaced for each distinct radial solution $f_n(kr) = \{j_n(kr), y_n(kr), h_n^{(1)}(kr), h_n^{(2)}(kr)\}$, cf. Williams [Wil99]:

$$f_n(kr) = \frac{2n-1}{kr} f_{n-1}(kr) - f_{n-2}(kr). \tag{40}$$

The derivatives that are necessary to obtain the radial velocity $v_r(\boldsymbol{r})$ out of Eqs. (2) and (24), are defined as, cf. [Wil99, GD04, Wei08]:

$$f_n'(kr) = f_{n-1}(kr) - \frac{n+1}{kr} f_n(kr). \tag{41}$$

The spherical Bessel and Neumann functions and their derivatives are depicted in Fig. 6. In practice, it is rather important to understand the asymptotic behavior of the magnitudes of the spherical Hankel functions. Their so-called near- and far-field regions, see Fig. 7, explain the properties of sound-radiation of higher-order sources. In particular, higher-order components decay rapidly with increasing radius within the near-field of a source. In the far-field of a source, however, all orders share the same rate of radial decay. For instance at $kr = 1$, a fourth order source has to be 40dB louder than a monopole to achieve the same sound pressure at $kr \geq 8$.

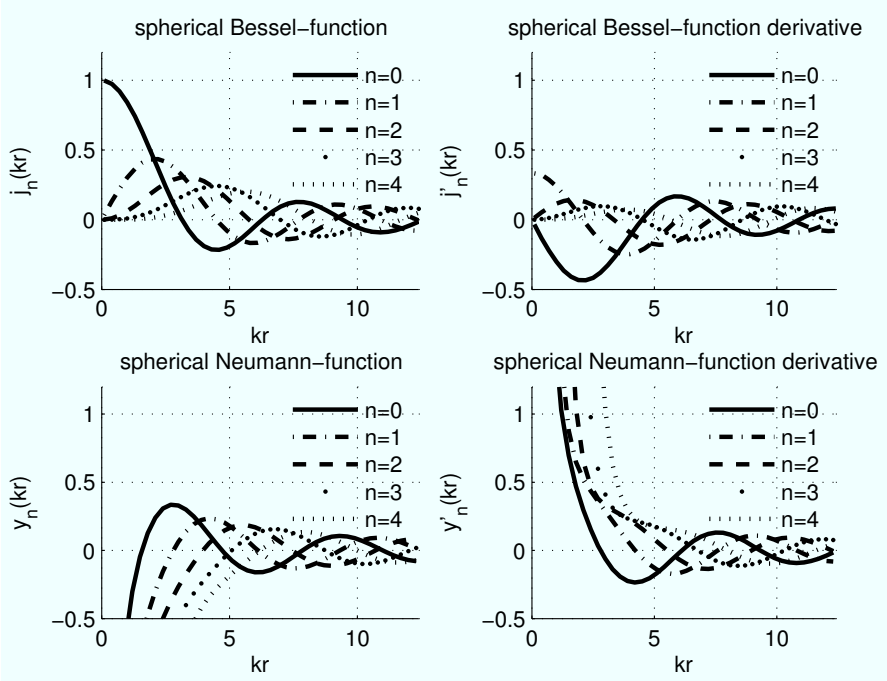

Figure 6: Spherical Bessel- and Neumann functions and their derivatives are the radial solution of the Helmholtz equation in the spherical coordinate system.

The asymptotic behavior of the near-field region of the Bessel function is also helpful to describe source-free incident fields. Note that in Appendix C, it is shown how to circumvent numerical errors in the proximity of $kr = 0$ for high orders. For both functions we obtain (cf. [AW04])

$$\left|h_n^{(1,2)}(kr)\right| \propto \begin{cases} (2n+1)!!/\,(kr)^{n+1}\,, & \text{in the near-field } kr \ll 2 \\ 1/\,(kr)\,, & \text{far-field } \frac{n(n+1)}{2} \ll kr \end{cases} \tag{42}$$

$$j_n(kr) \propto (kr)^n/(2n+1)!!, \quad \text{in the near-field } kr \ll \sqrt{2(2n+3)}. \tag{43}$$

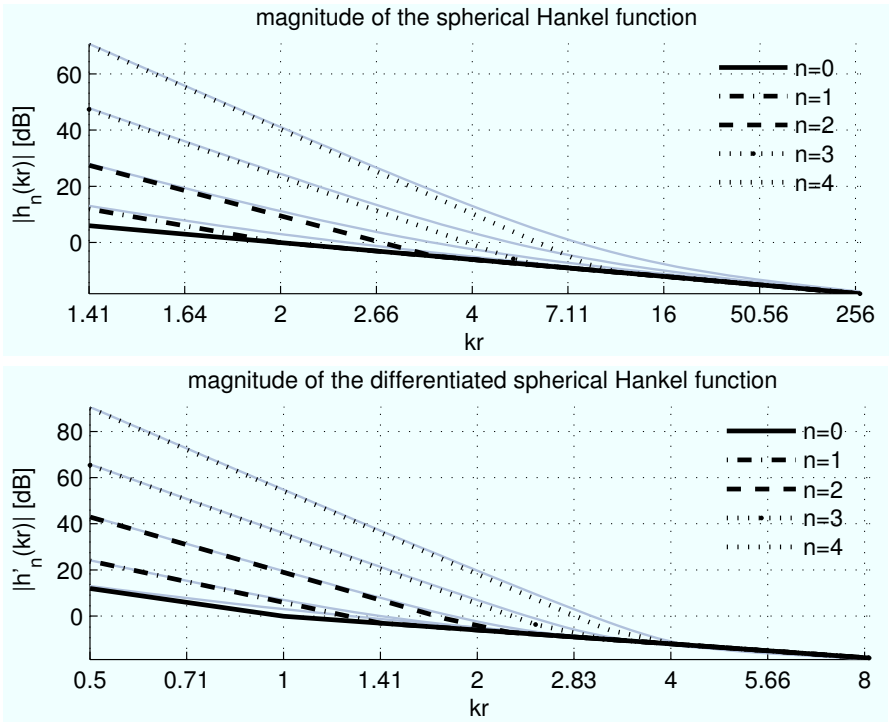

Figure 7: The magnitudes of the spherical Hankel functions and their derivatives clearly indicate the near- and far-field ranges of the functions.

2.3 Spherical Boundary Value Problems

Boundary value problems are used to describe the convergent, source-free part of a sound field, given its boundary values. Spherical boundary value problems can be split up into three main types of problems, enumerated below. In all cases, assume the boundary values of the source-free field are known on one or two spheres, concentric to the origin.

1. Interior Problem: The spherical sound pressure distribution $p\left(kr_0, \boldsymbol{\theta}\right)$ (Dirichlet problem) or particle velocity distribution $v_r\left(kr_0, \boldsymbol{\theta}\right)$ (Neumann problem) due to sources outside r_0 is given/known from measurements. The interior free-field for $r \leq r_0$ is fully described mathematically and can be evaluated at every point[4].

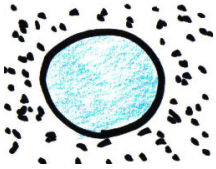

2. Exterior Problem: A Dirichlet boundary value condition $p\left(kr_0, \boldsymbol{\theta}\right)$ or a Neumann boundary value condition $v_r\left(kr_0, \boldsymbol{\theta}\right)$ due to sources inside r_0 is given/known from measurements. The exterior free-field for $r \geq r_0$ is fully determined.

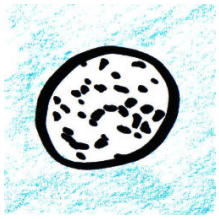

3. „Mixed“ Problems

   (a) I: Two Dirichlet boundary conditions $p\left(kr_1, \boldsymbol{\theta}\right)$ and $p\left(kr_2, \boldsymbol{\theta}\right)$, or two Neumann boundary conditions $v_r\left(kr_1, \boldsymbol{\theta}\right)$ and $v_r\left(kr_2, \boldsymbol{\theta}\right)$ due to sources both inside r_2 and outside r_1 are given/known from measurements at two concentric spheres $0 < r_1 < r_2$. The free-field enclosed between the spheres is fully determined[4].

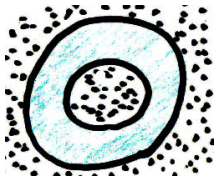

   (b) II: Two Dirichlet boundary conditions $p\left(kr_2, \boldsymbol{\theta}\right)$ and $p\left(kr_1, \boldsymbol{\theta}\right)$, or two Neumann boundary conditions $v_r\left(kr_2, \boldsymbol{\theta}\right)$ and $v_r\left(kr_1, \boldsymbol{\theta}\right)$ due to sources between r_1 and r_2 are given/known from measurements at two concentric spheres $0 < r_1 < r_2$. The two free-fields, one enclosed by the smaller sphere, the other one outside the larger sphere, are fully determined[4].

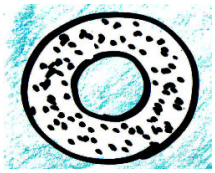

[4] As demonstrated in the example later, interior problems, or problems with irradiating fields, exhibit some exceptions. These are due to the zeros of the spherical Bessel functions $j_n(kr)$, or its derivative $j_n'(kr)$ at specific frequencies. At those frequencies, the sound pressure or the sound particle velocity, respectively, cannot produce n^{th} order components of a field, alone.

(c) III: A Dirichlet or Neumann boundary value is given at a spherical surface with radius r_0, which can be due to an incident or radiating field. Assume scattering of the field by a medium having another impedance z and lying inside, outside, or at the radius r_0, respectively. This impedance can be either defined in the spherical harmonics or space domain, depending on its modal or angular characteristics.

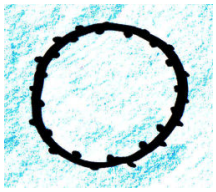

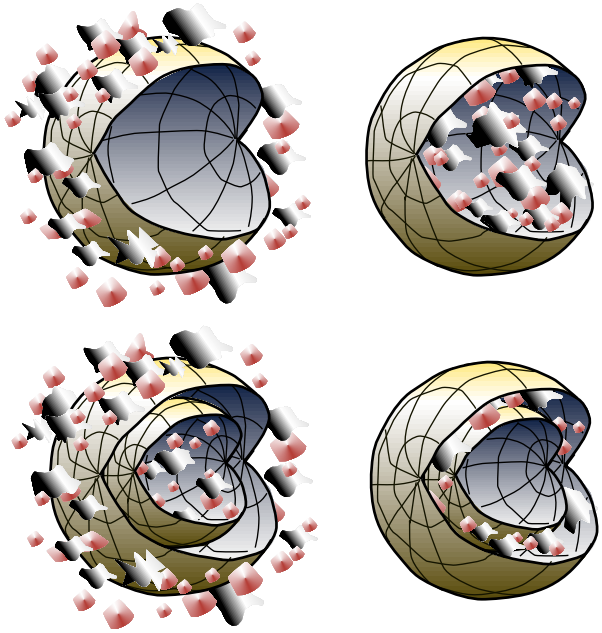

Figure 8: Schematic sketch of four spherical boundary value problems. Red dots represent sources of radiation and the grey particles obstacles to the sound field. The (virtual) spherical surfaces are enclosing/excluding homogeneous acoustic fields.

Note that the spherical boundary conditions above are prototypes for obtaining simple analytic solutions in terms of the spherical base-solutions. Arbitrary boundary conditions can generally be more complicated, possibly involving multiple scattering, angle dependent impedances, non-concentric spheres, and non-spherical geometries.

2.3.1 Spherical Wave Spectrum

For spherical boundary value problems, in which r is constant, it is useful to stay within the domain of spherical harmonics, i.e., not to perform the expansion into the angular variable $\boldsymbol{\theta}$. According to Williams [Wil99], this domain is called the

spherical wave spectrum

$$\psi_n^m\left(kr\right) = \mathcal{SHT}\left\{p\left(kr, \boldsymbol{\theta}\right)\right\}. \tag{44}$$

The radial component $\nu_n^m\left(kr\right)$ of the sound particle velocity in the *spherical wave spectrum* is related to the pressure by the Euler equation Eqs. (2), (4)

$$\begin{aligned} \nu_n^m\left(kr\right) &= \mathcal{SHT}\left\{v_r\left(kr, \boldsymbol{\theta}\right)\right\}, \\ i\rho_0 c\, k\, \nu_n^m\left(kr\right) &= -\frac{\partial}{\partial r}\psi_n^m\left(kr\right) = -k\frac{\partial}{\partial\left(kr\right)}\psi_n^m\left(kr\right). \end{aligned} \tag{45}$$

The expansion of *spherical wave spectra* is straightforward, using:

$$p\left(kr, \boldsymbol{\theta}\right) = \sum_{n,m} \psi_n^m\left(kr\right) Y_n^m\left(\boldsymbol{\theta}\right). \tag{46}$$

Particularly, pressure and particle velocity spectra are obtained from Eqs. (24), (44), and (45)

$$\psi_n^m\left(kr\right) = \qquad b_{nm} j_n\left(kr\right) + c_{nm} h_n^{(2)}\left(kr\right), \tag{47}$$

$$\nu_n^m\left(kr\right) = \frac{\mathrm{i}}{\rho_0 c}\left[b_{nm} j_n'\left(kr\right) + c_{nm} h_n'^{(2)}\left(kr\right)\right]. \tag{48}$$

In practice, *spherical wave spectra* are determined by a finite set of spatially discrete probes from acoustic measurements of $p(kr_0, \boldsymbol{\theta}_l)$ or $v_r(kr_0, \boldsymbol{\theta}_l)$ with a set of microphones. To convert the measurement data into *spherical wave spectra*, discrete spherical harmonic transforms (DSHT) have to be approximated under the assumption of angularly band-limited distributions (see Sec. 4.2).

Considering the regular and singular solutions $j_n(kr)$ and $h_n^{(2)}(kr)$ in Sec. 2.1.1, one family of coefficients b_{nm} and c_{nm} must vanish for pure interior or exterior problems:

1. Exterior problems: $b_{nm} \equiv 0$.

2. Interior problems: $c_{nm} \equiv 0$,

2.3.2 Spherical Boundary Value/Condition Examples

Example 1: Exterior problem, radiation into free-field. Assuming a purely radiating field, the coefficients c_{nm} of the exterior problem (singular solution) are determined by the *spherical wave spectrum* of the sound pressure or particle velocity at a given radius r_0. For radiation capture, the microphone-measurement surface must enclose a well-centered source that fulfills the requirement of an angular band-limitation. For playback, a set of loudspeakers provides

the required sound field by inverse DSHT of the *spherical wave spectrum*. Given $\psi_n^m(kr_0)$ in the frequency domain and setting $b_{nm} \equiv 0$ in Eq. (47), we equate:

$$\begin{aligned} \psi_n^m(kr_0) &= c_{nm} h_n^{(2)}(kr_0), \\ c_{nm} &= \frac{\psi_n^m(kr_0)}{h_n^{(2)}(kr_0)}. \end{aligned} \tag{49}$$

The coefficients c_{nm} allow for the evaluation of the sound field at every $kr \geq kr_0$.

Example 2: Interior problem, free incident field. Assuming a purely incident field without scattering, the coefficients b_{nm} of the interior problem (regular solution) can be determined by the *spherical wave spectrum* at a given surface kr_0. Once again the requirement of an angular band-limitation must be fulfilled. Given or provided $\psi_n^m(kr_0)$, we obtain the complex-valued frequency domain distribution by setting $c_{nm} \equiv 0$ in Eq. (47):

$$\begin{aligned} \psi_n^m(kr_0) &= b_{nm} j_n(kr_0), \\ b_{nm} &= \frac{\psi_n^m(kr_0)}{j_n(kr_0)}. \end{aligned} \tag{50}$$

An application of this type of problem is higher-order Ambisonics (HOA) capture. For incident field capture, compact open-sphere configurations of microphone arrays identify the spectrum $\psi_n^m(kr_0)$ by DSHT. In practice however, divisions by the zeros of $j_n(kr)$ must be avoided. For HOA-playback, the spectrum $\psi_n^m(kr_0)$ is provided computing a discretized version of a spherical source distribution Sec. 2.4 with surrounding spherical loudspeaker arrays and inverse DSHT ("HOA-*Decoder*"), which does not suffer from a division by zero problem.

Alternatively, if both *spherical wave spectra* $\psi_n^m(kr_0)$ as well as $\nu_n^m(kr_0)$ are known, the coefficients b_{nm} can be found more robustly from a linear combination, using arbitrary scalars α and β:

$$\begin{aligned} \alpha\psi_n^m(kr_0) + \beta\nu_n^m(kr_0) &= b_{nm}\left[\alpha\, j_n(kr_0) + \frac{\mathrm{i}\beta}{\rho_0 c}\, j_n'(kr_0)\right], \\ b_{nm} &= \frac{\alpha\psi_n^m(kr_0) + \beta\nu_n^m(kr_0)}{\alpha\, j_n(kr_0) + \frac{\mathrm{i}\beta}{\rho_0 c}\, j_n'(kr_0)}. \end{aligned} \tag{51}$$

Something similar is achieved, for instance, when applying cardioid microphones in compact open-sphere microphone arrays, which can circumvent divisions by zero. In this case, as given in the work [BR07] of Balmages and Rafaely, the coefficients in the above equations are $\alpha = 1$, and $\beta = -\rho_0 c$.

Another way to prevent divisions by zero uses spheres of different radii kr_l and a modified DSHT, which considers the frequency dependence of the radial functions, see [Raf08].

Example 3a: Mixed problem I, separation of radiated from incident field, given two *spherical wave spectra*. This approach has been shown in Weinreich and Arnold's work [WA80], by using measurements with a microphone array arranged in concentric spheres. The *spherical wave spectra* of the sound pressure $\psi_n^m(kr_1)$ and $\psi_n^m(kr_2)$ are given by DSHT based on discrete measurements. From that, the coefficients b_{nm} and c_{nm} are found by elimination in Eq. (47):

$$\begin{aligned}\psi_n^m(kr_1) &= b_{nm} j_n(kr_1) + c_{nm} h_n^{(2)}(kr_1),\\ \psi_n^m(kr_2) &= b_{nm} j_n(kr_2) + c_{nm} h_n^{(2)}(kr_2),\end{aligned}$$

resulting in:

$$b_{nm} = \frac{\psi_n^m(kr_1)\, h_n^{(2)}(kr_2) - \psi_n^m(kr_2)\, h_n^{(2)}(kr_1)}{j_n(kr_1)\, h_n^{(2)}(kr_2) - j_n(kr_2)\, h_n^{(2)}(kr_1)}, \tag{52}$$

$$c_{nm} = -\frac{\psi_n^m(kr_1)\, j_n(kr_2) - \psi_n^m(kr_2)\, j_n(kr_1)}{j_n(kr_1)\, h_n^{(2)}(kr_2) - j_n(kr_2)\, h_n^{(2)}(kr_1)}. \tag{53}$$

Note that this approach will not work in the case of two zeros of the spherical Bessel functions at both kr_1 and kr_2.

In that case, it would be better to measure the *spherical wave spectrum* of the pressure and the radial particle velocity $\psi_n^m(kr_0)$ and $\nu_n^m(kr_0)$ at the same radius $r_0 = r_1 = r_2$. The coefficients b_{nm} and c_{nm} are similarly determined as above:

$$\begin{aligned}\psi_n^m(kr_0) &= b_{nm} j_n(kr_0) + c_{nm} h_n^{(2)}(kr_0),\\ \nu_n^m(kr_0) &= \frac{\mathrm{i}}{\rho_0 c}\left[b_{nm} j_n'(kr_0) + c_{nm} h_n'^{(2)}(kr_0)\right],\end{aligned}$$

yielding:

$$b_{nm} = \frac{\psi_n^m(kr_0)\, h_n'^{(2)}(kr_0) - \frac{\rho_0 c}{\mathrm{i}}\, \nu_n^m(kr_0)\, h_n^{(2)}(kr_0)}{j_n(kr_0)\, h_n'^{(2)}(kr_0) - j_n'(kr_0)\, h_n^{(2)}(kr_0)}, \tag{54}$$

$$c_{nm} = -\frac{\psi_n^m(kr_0)\, j_n'(kr_0) - \frac{\rho_0 c}{\mathrm{i}}\, \nu_n^m(kr_0)\, j_n(kr_0)}{j_n(kr_0)\, h_n'^{(2)}(kr_0) - j_n'(kr_0)\, h_n^{(2)}(kr_0)}. \tag{55}$$

Using the Wronskian Eq. (23) the equations simplify to

$$b_{nm} = (kr_0)^2\left[\mathrm{i}\psi_n^m(kr_0)\, h_n'^{(2)}(kr_0) - \rho_0 c\, \nu_n^m(kr_0)\, h_n^{(2)}(kr_0)\right], \tag{56}$$

$$c_{nm} = -(kr_0)^2\left[\mathrm{i}\psi_n^m(kr_0)\, j_n'(kr_0) - \rho_0 c\, \nu_n^m(kr_0)\, j_n(kr_0)\right]. \tag{57}$$

Example 3b: Mixed problem III, computation of radiated and incident field, given a *spherical wave spectrum* and the radial impedance at the same radius. In principle, there are different kinds of impedances related to boundary conditions on spherical surfaces. In particular, we consider an acoustic impedance and a mechanical admittance

1. The modal/acoustic impedance of the free sound field is defined by

$$z_n^{m,\mathrm{ac}}\left(kr_0\right) = \frac{\psi_n^{m,\mathrm{ac}}(kr_0)}{\nu_n^m(kr_0)} = \begin{cases} \frac{\rho_0 c}{\mathrm{i}} \frac{j_n(kr_0)}{j_n'(kr_0)}, & \text{interior problem} \\ \frac{\rho_0 c}{\mathrm{i}} \frac{h_n^{(2)}(kr_0)}{h_n'^{(2)}(kr_0)}, & \text{exterior problem} \\ z_n^{m,\mathrm{ac}}(kr_0), & \text{other.} \end{cases} \tag{58}$$

   Note that this kind of impedance is not dependent on the angles but on the indices n, m. The relation is convolutive: given a velocity distribution on kr_0, the pressure tends to be spatially smoothed. Modal vibrations of spherical membranes may also show this kind of impedance.

2. The radial mechanical impedance distribution exhibits an angular dependency

$$z^{\mathrm{me}}\left(\boldsymbol{\theta}\right) = \left.\frac{p^{\mathrm{me}}\left(\boldsymbol{\theta}\right)}{v_r\left(\boldsymbol{\theta}\right)}\right|_{r=r_0}. \tag{59}$$

   This relation is not convolutive but directly dependent on the angles.

In many cases it is necessary to have both impedances combined, e.g. for a vibrating mechanical structure coupled with the sound field. Conversion of the mechanical impedance into spherical harmonics yields:

$$p^{\mathrm{me}}(\boldsymbol{\theta}) = z^{\mathrm{me}}(\boldsymbol{\theta})\, v_r(\boldsymbol{\theta}), \tag{60}$$

$$\int_{\mathbb{S}^2} d\boldsymbol{\theta}\, Y_n^m(\boldsymbol{\theta}) \Bigg| \quad \sum_{n,m} \psi_n^{m,\mathrm{me}}\, Y_n^m(\boldsymbol{\theta}) = \sum_{n',m'} \nu_{n'}^{m'}\, z^{\mathrm{me}}(\boldsymbol{\theta})\, Y_{n'}^{m'}(\boldsymbol{\theta}), \tag{61}$$

$$\psi_n^{m,\mathrm{me}} = \sum_{n',m'} \nu_{n'}^{m'} \underbrace{\int_{\mathrm{S}^2} z^{\mathrm{me}}(\boldsymbol{\theta})\, Y_n^m(\boldsymbol{\theta})\, Y_{n'}^{m'}(\boldsymbol{\theta})\, d\boldsymbol{\theta}}_{z_{n'n}^{m'm,\mathrm{me}}}. \tag{62}$$

In principle, both types of impedances interconnect via the velocity. Superposition of the pressures due to the sound field $\psi_n^{m,\mathrm{ac}}(kr_0)$ and due to the mechanical structure $\psi_n^{m,\mathrm{me}}$ yields the total pressure on the boundary:

$$\begin{aligned} \psi_n^{m,\mathrm{tot}} &= \psi_n^{m,\mathrm{ac}}(kr_0) + \psi_n^{m,\mathrm{me}} \\ &= \sum_{n'=0}^{\infty} \sum_{m'=-n'}^{n'} \left(z_{n'}^{m',\mathrm{ac}}(kr_0) \delta_{n'n} \delta_{m'm} + z_{n'n}^{m'm,\mathrm{me}} \right) \nu_{n'}^{m'} = \sum_{n'=0}^{\infty} \sum_{m'=-n'}^{n'} z_{n'n}^{m'm}\, \nu_{n'}^{m'}. \end{aligned} \tag{63}$$

From this, we can derive two useful equations that yield a sound pressure $\psi_n^{m,\mathrm{ac}}(kr)$ due to a structural pressure distribution $\psi_n^{m,\mathrm{tot}}$. The second equation considers the tensor-inverse of the impedance $z_{n'n}^{m'n}$, i.e. the admittance $\gamma_{n'n}^{m'm}$:

$$\psi_n^{m,\mathrm{tot}} = \sum_{n'=0}^{\infty} \sum_{m'=-n'}^{n'} z_{n'n}^{m'm}\, \frac{\psi_{n'}^{m',\mathrm{ac}}(kr_0)}{z_{n'}^{m'}(kr_0)}, \tag{64}$$

$$\psi_n^{m,\mathrm{ac}}(kr) = z_n^{m,\mathrm{ac}}(kr) \sum_{n'=0}^{\infty} \sum_{m'=-n'}^{n'} \gamma_{n'n}^{m'm}\, \psi_n^{m,\mathrm{tot}}. \tag{65}$$

With mechanical impedances that are spherically uniform, $z^{\mathrm{me}}(\boldsymbol{\theta}) = const$, the total impedance is $z_{n'n}^{mm'} = z_n^m \delta_{n'n} \delta_{mm'}$ and can be expressed by adding a constant to Eq. (58). For zero velocity boundaries (sound-hard) the impedance equals ∞, in case of a "pressure-release" sphere it becomes 0. The concept of the impedance facilitates the computation of sound fields scattered by a spherical surface with given impedance.

Given the impedance $z_n^m(kr_0)$ and the *spherical wave spectrum* of the pressure, the velocity can be computed with $\nu_n^m(kr_0) = \psi_n^m(kr_0)/z_n^m(kr_0)$. Therefore, using Eqs. (56), (57), the desired coefficients equal

$$b_{nm} = (kr_0)^2 \left[\mathrm{i} h_n'^{(2)}(kr_0) - \frac{\rho_0 c}{z_n^m(kr_0)} h_n^{(2)}(kr_0) \right] \psi_n^m(kr_0), \tag{66}$$

$$c_{nm} = -(kr_0)^2 \left[\mathrm{i} j_n'(kr_0) - \frac{\rho_0 c}{z_n^m(kr_0)} j_n(kr_0) \right] \psi_n^m(kr_0). \tag{67}$$

This type of solution is useful, for instance, when given a rigid sphere $z_n^m(kr_0) = \infty$, on which the sound pressure distribution has been identified (compact rigid spherical microphone array). It is possible to compute the incident field, compensating for the reflection on the surface. Possible multiple back-scattering between the spherical surface and distant sources or obstacles is usually neglected.

2.4 Spherical Source Distributions

In some cases involving irradiating fields, spherical boundary value problems suffer from division by zero Eq. (50), see also Footnote[4]. In holophonic problems, a spherical source distribution can be employed to obtain a stable solution. In contrast to spherical boundary value problems, a continuous distribution of sources always excites the interior field without zeros as shown in this section.

Consider a continuous source strength distribution $f(\boldsymbol{\theta})$ that excites the inhomogeneous Helmholtz equation at the radius r_0:

$$\left(\Delta + k^2\right) p = -\frac{\delta(r - r_0)}{r^2} f(\boldsymbol{\theta}). \tag{68}$$

This inhomogeneous differential equation is solved by a product ansatz, cf. [MF53]

$$p(kr, \boldsymbol{\theta}) = R(kr)\, \Phi(\boldsymbol{\theta}). \tag{69}$$

The angular part $\Phi(\boldsymbol{\theta})$ is easily described by the spherical harmonics transform pair of $f(\boldsymbol{\theta})$, cf. Eq. (28), and yields the *modal source-strength* [ZPF09]

$$\phi_{nm} = \iint_{\mathrm{S}^2} f(\boldsymbol{\theta})\, Y_n^m(\boldsymbol{\theta})\, d\boldsymbol{\theta}, \tag{70}$$

$$f(\boldsymbol{\theta}) = \sum_{n=0}^{\infty} \sum_{m=-n}^{n} \phi_{nm}\, Y_n^m(\boldsymbol{\theta}), \tag{71}$$

hence the radial solution $g_{\mathrm{R}}(kr)$ of the Green's function for one harmonic becomes

$$p(kr, \boldsymbol{\theta}) = g_{\mathrm{R}}(kr)\ \phi_{nm}\, Y_n^m(\boldsymbol{\theta}). \tag{72}$$

With the Laplace operator split into its radial and angular parts $\Delta = \Delta_r + \Delta_{\boldsymbol{\theta}}$ and the eigenvalue eigenfunction pair of the angular part $\Delta_{\boldsymbol{\theta}} Y_n^m(\boldsymbol{\theta}) = -\frac{n(n+1)}{r^2}\ Y_n^m(\boldsymbol{\theta})$, the insertion of the ansatz results in an inhomogeneous, one-dimensional spherical Bessel differential equation

$$\left[\Delta_r + k^2 - \frac{n(n+1)}{r^2}\right]\ g_{\mathrm{R}}(kr) = -\frac{\delta(r - r_l)}{r^2} \tag{73}$$

Since we use two independent homogeneous functions $j_n(kr)$ and $h_n^{(2)}(kr)$ as its solution, the inhomogeneous radial part $g_{\mathrm{R}}(kr)$ can be solved by *variation of parameters*, cf. [Kre99, MF53]

$$g_{\mathrm{R}}(kr) = -j_n(kr) \int_r^\infty \frac{h_n^{(2)}(kr)}{W(kr)} \frac{\delta(r - r_l)}{r^2} \frac{dkr}{k} - h_n^{(2)}(kr) \int_0^r \frac{j_n(kr)}{W(kr)} \frac{\delta(r - r_l)}{r^2} \frac{dkr}{k}, \tag{74}$$

wherein $W(kr)$ is the Wronski-determinant Eq. (23) of the two functions. Eventually, the complete solution of the inhomogeneous problem, the spherical source distribution, can be given as

$$p(kr, \boldsymbol{\theta} | \phi_{nm}) = -\mathrm{i}k \sum_{n=0}^{\infty} \sum_{m=-n}^{n} \phi_{nm}\ Y_n^m(\boldsymbol{\theta}) \begin{cases} h_n^{(2)}(kr_l)\ j_n(kr), & \text{for } r \leq r_l, \\ j_n(kr_l)\ h_n^{(2)}(kr), & \text{for } r \geq r_l. \end{cases} \tag{75}$$

This approach is particularly useful when describing point sources, Sec. 2.4.2, or spherical arrangements thereof, as in higher-order Ambisonics, or other open spherical loudspeaker arrays. Such arrangements are well-defined using the above equation after sampling the surface function $f(\boldsymbol{\theta})$. The advantage of this formulation is that the sound pressure and particle velocity are explicitly not restricted by boundary conditions (Dirichlet/Neumann) between the sampling points as the Helmholtz equation stays homogeneous there, cf. [ZPF09].

2.4.1 Spherical Source Distribution Problem

Assume a controllable spherical source distribution with the source strength distribution $f(\boldsymbol{\theta})$. The *spherical wave spectrum* of the upper branch of Eq. (75) is related to the *modal source-strength* ϕ_{nm} and yields the modal coefficients

$$\psi_n^m(kr) = -\mathrm{i}k\ j_n(kr)\ h_n^{(2)}(kr_l)\ \phi_{nm}, \tag{76}$$

$$\Rightarrow b_{nm} = -\mathrm{i}k\ h_n^{(2)}(kr_l)\ \phi_{nm}. \tag{77}$$

It is easy to see that if the latter was replaced by

$$\phi_{nm} = \frac{h_n^{(2)}(k\hat{r}_l)}{h_n^{(2)}(kr_l)}\ \hat{\phi}_{nm}, \tag{78}$$

the interior field due to sources at any radius $r < \hat{r}_l$ can be simulated by the sources at r_l:

$$\psi_n^m(kr) = -\mathrm{i}k\, j_n(kr)\ \cancel{h_n^{(2)}(kr_l)}\ \frac{h_n^{(2)}(k\hat{r}_l)}{\cancel{h_n^{(2)}(kr_l)}}\ \hat{\phi}_{nm}, \tag{79}$$

which solves the holophonic higher-order Ambisonics (HOA) reproduction problem, cf. [ZPF09].

Furthermore, if b_{nm} can be measured, e.g. using Eq. (51) or Eq. (66), the determination of a matching source distribution at $\phi_{nm}|_{r_l}$ can be calculated assuming r_l:

$$\phi_{nm}|_{r_l} = \frac{\mathrm{i}}{k\ h_n^{(2)}(kr_l)}\, b_{nm}. \tag{80}$$

This solves the holographic problem, in which sources at a given radius shall be identified by measuring b_{nm}.

2.4.2 Expansion of a Point-Source

The Green's function of the Helmholtz equation in three dimensions is defined as the inhomogeneous differential equation

$$\left(\Delta + k^2\right) G\left(\boldsymbol{r}, \boldsymbol{r}_0\right) = -\delta\left(\boldsymbol{r} - \boldsymbol{r}_0\right). \tag{81}$$

Its well-known solution is a point source in Cartesian coordinates [MF53]

$$G\left(\boldsymbol{r}, \boldsymbol{r}_0\right) = \frac{\mathrm{e}^{-\mathrm{i}k\|\boldsymbol{r}-\boldsymbol{r}_0\|}}{4\pi\left\|\boldsymbol{r} - \boldsymbol{r}_0\right\|} \tag{82}$$

that fulfills the radiation condition; the arguments $\boldsymbol{r}, \boldsymbol{r}_0$ are commutable. Either way, one argument specifies the point of observation and the other one the location of the source, respectively. The Green's function in terms of spherical base-solutions is defined by [MF53, Wei08]

$$\left(\Delta + k^2\right) G\left(\boldsymbol{r}, \boldsymbol{r}_0\right) = -\frac{\delta\left(r - r_0\right)}{r^2}\ \delta\left(1 - \boldsymbol{\theta}_0^{\mathrm{T}}\ \boldsymbol{\theta}\right), \tag{83}$$

The angular term on the right hand side follows from the transform Eq. (28)

$$\delta\left(1 - \boldsymbol{\theta}_0^{\mathrm{T}}\boldsymbol{\theta}\right) = \sum_{n=0}^{\infty}\ \sum_{m=-n}^{n}\ Y_n^m\left(\boldsymbol{\theta}\right)\ Y_n^m\left(\boldsymbol{\theta}_0\right). \tag{84}$$

Due to Eq. (75), the *spherical wave spectrum* of the point source equals

$$\mathcal{SHT}_{nm}\left\{G\left(\boldsymbol{r},\boldsymbol{r}_0\right)\right\} = -\mathrm{i}k\, Y_n^m\left(\boldsymbol{\theta}_0\right) \begin{cases} j_n\left(kr\right)\; h_n^{(2)}\left(kr_0\right), & \text{for } r \le r_0, \\ h_n^{(2)}\left(kr\right)\; j_n\left(kr_0\right), & \text{for } r \ge r_0, \end{cases} \tag{85}$$

$$G\left(\boldsymbol{r},\boldsymbol{r}_0\right) = \sum_{n=0}^{\infty}\sum_{m=-n}^{n} \mathcal{SHT}_{nm}\left\{G\left(\boldsymbol{r},\boldsymbol{r}_0\right)\right\}\; Y_n^m\left(\boldsymbol{\theta}\right).$$

This representation is not only useful when describing the field of point sources, but also represents an initial value for the computation of higher-order translation operators.

Regular omnidirectional field. The imaginary part of the Green's function describes an omnidirectional standing wave that is regular at $\boldsymbol{r} = \boldsymbol{r}_0$:

$$G_R\left(\boldsymbol{r},\boldsymbol{r}_0\right) = -\frac{\sin\left(k\left\|\boldsymbol{r}-\boldsymbol{r}_0\right\|\right)}{4\pi\left\|\boldsymbol{r}-\boldsymbol{r}_0\right\|} = \Im\left\{G\left(\boldsymbol{r},\boldsymbol{r}_0\right)\right\} \tag{86}$$

Using Eq. (85), the shifted omnidirectional standing wave corresponds to:

$$\begin{aligned} \mathcal{SHT}\left\{G_R\left(\boldsymbol{r},\boldsymbol{r}_0\right)\right\} &= \Im\left\{-\mathrm{i}k j_n\left(kr\right) h_n^{(2)}\left(kr_0\right) Y_n^m\left(\boldsymbol{\theta}_0\right)\right\} \\ &= -k j_n\left(kr\right) j_n\left(kr_0\right) Y_n^m\left(\boldsymbol{\theta}_0\right). \end{aligned} \tag{87}$$

This describes a shifted regular field. It also represents a set of initial values for the computation of higher-order translation operators.

2.4.3 Expansion of a Plane-Wave

An incident plane wave from the direction φ_0, ϑ_0 is described by

$$p\left(\boldsymbol{r},\boldsymbol{k}_0\right) = \mathrm{e}^{\mathrm{i}\boldsymbol{k}_0^{\mathrm{T}}\boldsymbol{r}}, \qquad \boldsymbol{k}_0 = k\boldsymbol{\theta}_0 = k\begin{pmatrix}\cos\left(\varphi_0\right)\sin\left(\vartheta_0\right)\\ \sin\left(\varphi_0\right)\sin\left(\vartheta_0\right)\\ \cos\left(\vartheta_0\right)\end{pmatrix}. \tag{88}$$

The *spherical wave spectrum* expansion of the incident plane wave $\mathrm{e}^{\mathrm{i}\boldsymbol{k}_0^{\mathrm{T}}\boldsymbol{r}}$ can be obtained by using the Green's function Eq. (85), letting $r_0 \gg r$, see Arfken [AW04], Fitzpatrick [Fit02], since

$$\begin{aligned} \lim_{r_0\gg r}\left\|\boldsymbol{r}-\boldsymbol{r}_0\right\| &= \lim_{r_0\gg r}\sqrt{r_0^2 + r^2 - 2\boldsymbol{r}_0^{\mathrm{T}}\boldsymbol{r}} \qquad (89)\\ &= \lim_{r_0\gg r}\left[r_0 + \frac{1}{1!\;2\;r_0}\left(r^2 - 2\boldsymbol{r}_0^{\mathrm{T}}\boldsymbol{r}\right) - \ldots\right] = r_0 - \boldsymbol{\theta}_0^{\mathrm{T}}\boldsymbol{r} \approx r_0, \end{aligned}$$

$$\Rightarrow \lim_{r_0\gg r}\frac{\mathrm{e}^{-\mathrm{i}k\left\|\boldsymbol{r}-\boldsymbol{r}_0\right\|}}{\left\|\boldsymbol{r}-\boldsymbol{r}_0\right\|} = \frac{\mathrm{e}^{-\mathrm{i}kr_0}}{4\pi r_0}. \tag{90}$$

So with Eq. (85) and the far-field approximation of the spherical Hankel functions Eq. (350) $\lim_{r_0\to\infty} h_n^{(2)}(kr_0) = \frac{\mathrm{i}^{n+1}\mathrm{e}^{-\mathrm{i}kr_0}}{kr_0}$, the plane-wave yields

$$p(\boldsymbol{r},\boldsymbol{k}_0) = \frac{4\pi r_0}{\mathrm{e}^{-\mathrm{i}kr_0}}\,\frac{k}{\mathrm{i}}\sum_{n=0}^{\infty}\sum_{m=-n}^{n} j_n(kr)\,Y_n^m(\boldsymbol{\theta})\;\frac{\mathrm{i}^{n+1}\mathrm{e}^{-\mathrm{i}kr_0}}{kr_0}\,Y_n^m(\boldsymbol{\theta}_0)\,.$$

Consequently, its *spherical wave spectrum* becomes

$$\mathcal{SHT}_{nm}\{p(\boldsymbol{r},\boldsymbol{k}_0)\} = 4\pi\,\mathrm{i}^n\,j_n(kr)\;Y_n^m(\boldsymbol{\theta}_0)\,, \tag{91}$$

$$p(\boldsymbol{r},\boldsymbol{k}_0) = \sum_{n=0}^{\infty}\sum_{m=-n}^{n}\mathcal{SHT}_{nm}\{p(\boldsymbol{r},\boldsymbol{k}_0)\}\;Y_n^m(\boldsymbol{\theta})\,.$$

2.4.4 Expansion of a Line-Source

According to Morse and Feshbach [MF53], the following relation between the solution in the two-dimensional circular cylindrical coordinates and the spherical base-solutions holds:

$$\mathcal{SHT}_{nm}\left\{J_m(kr\sin\vartheta)\begin{pmatrix}\cos(m\varphi)\\ \sin(m\varphi)\end{pmatrix}\right\} = \sum_{n=m}^{\infty}\frac{4\pi}{\mathrm{i}^{n-m}}Y_n^m(\varphi,\pi/2)\;j_n(kr)\,, \tag{92}$$

$$\mathcal{SHT}_{nm}\left\{H_m^{(2)}(kr\sin\vartheta)\begin{pmatrix}\cos(m\varphi)\\ \sin(m\varphi)\end{pmatrix}\right\} = \sum_{n=m}^{\infty}\frac{4\pi}{\mathrm{i}^{n-m}}Y_n^m(\varphi,\pi/2)\;h_n^{(2)}(kr)\,. \tag{93}$$

Therefore it is possible to turn a two dimensional problem (e.g. Ambisonics) into a three dimensional spherical problem. For example a line-source in circular cylindrical coordinates with $\rho = r\sin(\vartheta)$

$$G_L(\boldsymbol{r},\rho_0,\varphi_0) = \frac{\pi}{\mathrm{i}}\cos\left[m(\varphi-\varphi_0)\right]\begin{cases}J_m(k\rho)\;H_m^{(2)}(k\rho_0)\,, & \rho\le\rho_0,\\ H_m^{(2)}(k\rho)\;J_m(k\rho_0) & \rho\ge\rho_0,\end{cases} \tag{94}$$

is equivalent to, using Eqs. (92)(93)(94),

$$\mathcal{SHT}_{nm}\{G_L(\boldsymbol{r},\rho_0,\varphi_0)\} = \frac{4\pi^2}{\mathrm{i}^{n-m+1}}\begin{cases}j_n(kr)\;H_m^{(2)}(k\rho_0)\;Y_n^m(\varphi_0,\pi/2)\,, & r\le\rho_0,\\ h_n^{(2)}(kr)\;J_m(k\rho_0)\;Y_n^m(\varphi_0,\pi/2)\,, & r\gg\rho_0,\end{cases} \tag{95}$$

however with poor convergence for $r\ge\rho_0$.

2.5 Acoustic Holography and Holophony with Spherical Arrays

This section gives a brief naming convention to some important problems that are solved by spherical boundary value problems or using spherical source distributions. Essentially, radiation (exterior problem) or irradiation (interior problem) of sound can be captured by microphones and predicted at other locations. Or just as well, both radiation and irradiation can be reproduced by loudspeakers.

Spherical acoustic holography means the measurement of an acoustic field along a spherical surface for the purpose of evaluation at other radii. This can be achieved by suitable arrangements of microphones. If properly done, the measured part of the field will be used to compute either the *spherical wave spectrum* of the exterior problem Eq. (49), or the *modal source strength* of a surrounding spherical source distribution Eq. (80). Insertion into the spherical base-solutions allows for calculation of the field at other radii. There are two types of dedicated arrangements for capture

- *surrounding spherical microphone arrays* for the identification of radiation (exterior problems)
- *compact spherical microphone arrays* for the identification of irradiation (HOA recording)

Spherical acoustic holophony means the synthesis or playback of an acoustic field matching outside or within the spherical reproduction facility. Suitable arrangements of loudspeakers can be used to achieve this. If properly done, the *spherical wave spectrum* of an exterior problem or the *modal source strength* of a surrounding spherical source distribution will be generated. There are two main types of dedicated playback arrangements

- *compact spherical loudspeaker arrays* for reproduction of radiation (exterior problem)
- *surrounding spherical loudspeaker arrays* for reproduction of irradiation (HOA playback)

Chap. 4 is the key to practical implementations with discrete spherical arrays. Partly, this concept is summarized in [Zot09].

Chapter III

MANIPULATION OF SPHERICAL BASE SOLUTIONS

The base solutions of the Helmholtz equation, as introduced in the previous chapter Chap. 2, are capable of describing entire homogeneous incident and radiating sound fields even if only spherical wave spectra are known on one or more surfaces. What has not been told so far is how to transform these spherical base-solutions to other, new coordinate origins. While this is fairly easy in Cartesian coordinates, a transform of coordinates requires special attention using spherical base-solutions.

This chapter presents a derivation of the transform methods using the literature on the *addition theorem for the scalar wave-equation*. The novel contribution in this derivation is the usage of real-valued matrices to represent the spherical harmonics. For practical reasons, full transforms (translation and rotation) are decomposed into simple transform steps. The derivation yields the computation of each of these simple transform steps for base-solutions using either real- or complex-valued spherical harmonics. Finally, approaches and literature about other manipulation techniques such as correlation, multiplication, and spherical convolution are provided. Another novel contribution for spherical convolution is the recurrent relation between spherical and cylindrical convolution. This allows to directly transform circular harmonics windows known from discrete-time windowing-techniques to spherical convolution kernels.

3.1 Coordinate Transforms of Spherical Base Solutions (Addition Theorem for the Scalar Wave Equation)

In the following section, rotation and translation of the reference coordinate system $\boldsymbol{r}$ to a new one by a 3×3 rotation matrix $\boldsymbol{Q}$ and an offset $\boldsymbol{d}$ is given by

$$\boldsymbol{r}' = \boldsymbol{Q}\,\boldsymbol{r} + \boldsymbol{d}. \tag{96}$$

Interrelations between spherical base-solutions defined on the two distinct coordinate systems can be established and shall be explored here. The principle behind this technique is the so called *addition theorem for the scalar wave equation* described in Chew [Che92], Gumerov and Duraiswami [GD01, GD03, GD04]. The

derivations here follow strictly the outlined steps given in the references. As a novel contribution, recurrence relations for real-valued spherical harmonics are directly obtained, here.

Rotation of the Cartesian coordinates. A rotation $\boldsymbol{Q}$ of the Cartesian coordinates can be written as 3×3 matrix, which is determined by the three rotational degrees of freedom. $\boldsymbol{Q}$ is often decomposed into a rotation $\boldsymbol{Q}_z(\gamma)$ around the z-axis, followed by a rotation around the y-axis $\boldsymbol{Q}_y(\beta)$, and a third rotation around the z-axis $\boldsymbol{Q}_z(\alpha)$, cf. Fig. 9 and e.g. [GD01, GD03, GD04]. This zyz-rotation is for Cartesian coordinates:

$$\boldsymbol{r}' = \boldsymbol{Q}(\alpha, \beta, \gamma)\, \boldsymbol{r}, \tag{97}$$

$$\boldsymbol{Q}(\alpha, \beta, \gamma) = \boldsymbol{Q}_z(\alpha)\, \boldsymbol{Q}_y(\beta)\, \boldsymbol{Q}_z(\gamma), \tag{98}$$

$$\boldsymbol{Q}_z(\alpha) = \begin{pmatrix} \cos(\alpha) & -\sin(\alpha) & 0 \\ \sin(\alpha) & \cos(\alpha) & 0 \\ 0 & 0 & 1 \end{pmatrix}, \quad \boldsymbol{Q}_y(\beta) = \begin{pmatrix} \cos(\beta) & 0 & \sin(\beta) \\ 0 & 1 & 0 \\ -\sin(\beta) & 0 & \cos(\beta) \end{pmatrix}.$$

The inverse rotation is obtained by exchanging the order and signs of the angles $\boldsymbol{Q}^{-1}(\alpha, \beta, \gamma) = \boldsymbol{Q}(-\gamma, -\beta, -\alpha)$.

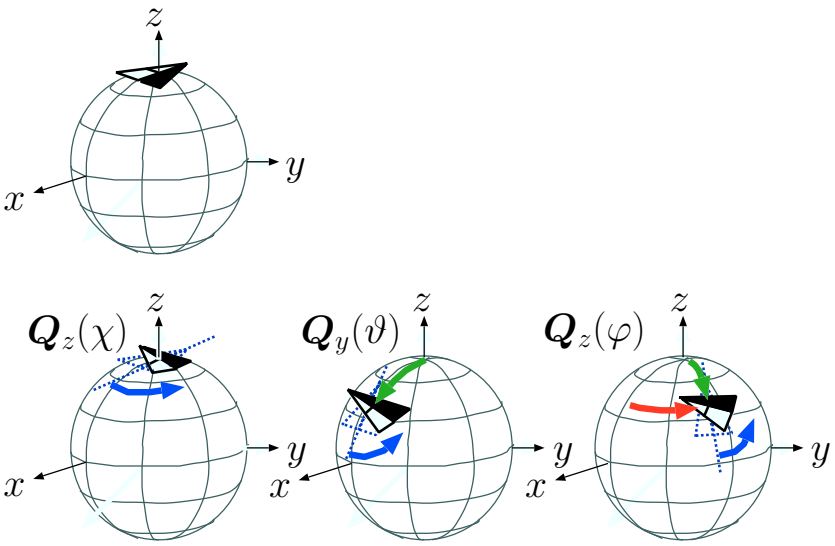

Figure 9: zyz rotation.

Translation of the Cartesian coordinates. Shifting the Cartesian coordinates by an offset vector $\boldsymbol{d}$ is easily described as an addition of the 3×1 components. In terms of the spherical base-solutions, translation is more complicated as a shift of the origin affects both angular and radial coordinates. Therefore, it may theoretically require all spherical base-solutions up to infinite order to represent a single shifted base-solution.

Coordinate transforms and spherical base-solutions. Basically, the spherical base-solutions for either regular incident fields $\hat{\boldsymbol{R}}_n^m(\boldsymbol{r})$ or singular radiating fields $\hat{\boldsymbol{S}}_n^m(\boldsymbol{r})$ can be given as

$$\hat{\boldsymbol{R}}_n^m(\boldsymbol{r}) = j_n\left(kr\right)\, \hat{\boldsymbol{Y}}_n^m(\boldsymbol{\theta}), \tag{99}$$

$$\hat{\boldsymbol{S}}_n^m(\boldsymbol{r}) = h_n^{(2)}\left(kr\right)\, \hat{\boldsymbol{Y}}_n^m(\boldsymbol{\theta}), \tag{100}$$

The formulations here express the complex-valued spherical harmonics in terms of a 2×2 real-valued matrix $\hat{\boldsymbol{Y}}_n^m\left(\boldsymbol{\theta}\right)$. The underlying intention is to make the relation to the real-valued spherical harmonics Eq. (183) more obvious while still keeping the benefits of complex-valued calculations using the matrix notation. In doing so, the complex-valued nature of the angular solutions will be kept strictly separate from the complex values of the radial solutions

$$\hat{\boldsymbol{\Phi}}_m\left(\varphi\right) = \begin{pmatrix} \cos\left(m\varphi\right) & -\sin\left(m\varphi\right) \\ \sin\left(m\varphi\right) & \cos\left(m\varphi\right) \end{pmatrix} = \left(\hat{\boldsymbol{\Phi}}_1(\varphi)\right)^m, \tag{101}$$

$$\hat{\boldsymbol{Y}}_n^m(\boldsymbol{\theta}) = \hat{N}_n^m\, P_n^m(\mu)\, \hat{\boldsymbol{\Phi}}_m(\varphi). \tag{102}$$

The indices are defined for the range $n, m \in \mathbb{N}_0 : m \leq n$. Free sound fields (complex-valued) of either type (incident/radiating) can be entirely described as infinite sum over the base solutions weighted with the coefficients $\boldsymbol{b}_{nm}$ and $\boldsymbol{c}_{nm}$:

$$\boldsymbol{b}_{nm} = \begin{pmatrix} b_{nm}^{(real)} & -b_{nm}^{(imag)} \\ b_{nm}^{(imag)} & b_{nm}^{(real)} \end{pmatrix}, \qquad \boldsymbol{c}_{nm} = \begin{pmatrix} c_{nm}^{(real)} & -c_{nm}^{(imag)} \\ c_{nm}^{(imag)} & c_{nm}^{(real)} \end{pmatrix}, \tag{103}$$

$$\boldsymbol{p}_R = \begin{pmatrix} p_R^{(real)} & -p_R^{(imag)} \\ p_R^{(imag)} & p_R^{(real)} \end{pmatrix}, \qquad \boldsymbol{p}_S = \begin{pmatrix} p_S^{(real)} & -p_S^{(imag)} \\ p_S^{(imag)} & p_S^{(real)} \end{pmatrix} e^{\mathrm{i}\angle h_n^{(2)}(kr)}, \tag{104}$$

$$\boldsymbol{p}_R(\boldsymbol{r}) = \sum_n^\infty \sum_{m=0}^n \boldsymbol{b}_{nm}\, \hat{\boldsymbol{R}}_n^m(\boldsymbol{r}), \tag{105}$$

$$\boldsymbol{p}_S(\boldsymbol{r}) = \sum_n^\infty \sum_{m=0}^n \boldsymbol{c}_{nm}\, \hat{\boldsymbol{S}}_n^m(\boldsymbol{r}). \tag{106}$$

For the coordinate transform problem, the distinct spherical base-solutions shall be denoted more generically as $\hat{\boldsymbol{F}}_n^m(\boldsymbol{r}) = \left\{\hat{\boldsymbol{R}}_n^m(\boldsymbol{r}) | \hat{\boldsymbol{S}}_n^m(\boldsymbol{r})\right\}$ and $\hat{\boldsymbol{E}}_n^m(\boldsymbol{r}') = \left\{\hat{\boldsymbol{R}}_n^m(\boldsymbol{r}') | \hat{\boldsymbol{S}}_n^m(\boldsymbol{r}')\right\}$, as given in [GD01, GD03, GD04]. This allows for freely selecting the appropriate type of solution according to the situation prevailing in the respective coordinate system. Consequently, the sound pressure in the two different coordinate systems $\boldsymbol{r}$ and $\boldsymbol{r}'$ equals

$$\boldsymbol{p}_F(\boldsymbol{r}) = \sum_n^\infty \sum_{m=0}^n \boldsymbol{f}_{nm}\, \hat{\boldsymbol{F}}_n^m(\boldsymbol{r}), \tag{107}$$

$$\boldsymbol{p}_E(\boldsymbol{r}') = \sum_n^\infty \sum_{m=0}^n \boldsymbol{e}_{nm}\, \hat{\boldsymbol{E}}_n^m(\boldsymbol{r}'). \tag{108}$$

The transform between both coordinate systems can be written as

$$\boldsymbol{p}_F(\boldsymbol{r}) = \int_{\mathbb{R}^3} \boldsymbol{T}(\boldsymbol{r}', \boldsymbol{r})\ \boldsymbol{p}_E(\boldsymbol{r}')\ d\boldsymbol{r}'. \tag{109}$$

The transform operator can be easily transformed into the spherical harmonics with respect to the two different coordinate systems $\boldsymbol{r}$ and $\boldsymbol{r}'$. Due to the orthogonality of the base solutions in the respective coordinate systems using $\int \hat{\boldsymbol{E}}_{n_x}^{m_x}(\boldsymbol{r}')\hat{\boldsymbol{Y}}_n^m(\boldsymbol{\theta}')d\boldsymbol{\theta}' = \delta_{n_x n}\delta_{m_x m}\hat{\boldsymbol{E}}_{n_x}^{m_x}(\boldsymbol{r}')$, the above equation reduces to

$$\hat{\boldsymbol{F}}_n^m(\boldsymbol{r}) = \sum_{n'=0}^{\infty}\sum_{m'=0}^{n'} \hat{\boldsymbol{T}}_{n'n}^{m'm}(\boldsymbol{Q}, \boldsymbol{d})\ \hat{\boldsymbol{E}}_{n'}^{m'}(\boldsymbol{r}'). \tag{110}$$

The operator $\hat{\boldsymbol{T}}_{n'n}^{m'm}(\boldsymbol{Q}, \boldsymbol{d})$ transforms the solution $\hat{\boldsymbol{E}}_{n'}^{m'}(\boldsymbol{r}')$ into a solution $\hat{\boldsymbol{F}}_n^m(\boldsymbol{r})$. In other words, the base solution $\hat{\boldsymbol{F}}_n^m(\boldsymbol{r})$ in the coordinate system $\boldsymbol{r}$ can always be expressed as linear combination of base solutions $\hat{\boldsymbol{E}}_{n'}^{m'}(\boldsymbol{r}')$ in the coordinate system $\boldsymbol{r}' = \boldsymbol{Q}\,\boldsymbol{r} + \boldsymbol{d}$ using the weights $\hat{\boldsymbol{T}}_{n'n}^{m'm}(\boldsymbol{Q}, \boldsymbol{d})$. Eq. (110) is therefore called addition theorem for the scalar wave equation. The following sections show how the coefficients $\hat{\boldsymbol{T}}_{n'n}^{m'm}(\boldsymbol{Q}, \boldsymbol{d})$ can be determined.

3.1.1 Gradient and its Commutativity with Transforms

The ∇-operator (gradient) is defined as:

$$\nabla = \begin{pmatrix} \frac{\partial}{\partial x} \\ \frac{\partial}{\partial y} \\ \frac{\partial}{\partial z} \end{pmatrix}. \tag{111}$$

Applying the chain rule to obtain the gradient in transformed coordinates yields

$$\nabla_{\boldsymbol{r}} = \left(\nabla_{\boldsymbol{r}}\ \boldsymbol{r}'^{\mathrm{T}}\right)\ \nabla_{\boldsymbol{r}'} = \nabla_{\boldsymbol{r}}\left(\boldsymbol{r}^{\mathrm{T}}\boldsymbol{Q}^{\mathrm{T}} + \boldsymbol{d}^{\mathrm{T}}\right)\nabla_{\boldsymbol{r}'} = \boldsymbol{Q}^{\mathrm{T}}\,\nabla_{\boldsymbol{r}'} \tag{112}$$

in Cartesian coordinates. It must be invariant to a change of the coordinate system $\boldsymbol{T}(\boldsymbol{r}, \boldsymbol{r}')$

$$\boldsymbol{\nabla}_{\boldsymbol{r}}\boldsymbol{p}(\boldsymbol{r}) = \int_{\mathbb{R}^3} \boldsymbol{T}(\boldsymbol{r}', \boldsymbol{r})\ \boldsymbol{Q}^{\mathrm{T}}\,\boldsymbol{\nabla}_{\boldsymbol{r}'}\boldsymbol{p}(\boldsymbol{r}')\ d\boldsymbol{r}'. \tag{113}$$

Since we define the spherical base-solutions having the dimensions 2×2, the gradient must be re-written to 6×2; we use *bdiag* to denote a block diagonal

matrix:

$$\boldsymbol{\nabla}_{\boldsymbol{r}} = \begin{pmatrix} \boldsymbol{I}\,\partial/\partial x \\ \boldsymbol{I}\,\partial/\partial y \\ \boldsymbol{I}\,\partial/\partial z \end{pmatrix} \tag{114}$$

$$\boldsymbol{\nabla}_{\boldsymbol{r}} \hat{\boldsymbol{F}}_n^m\left(\boldsymbol{r}\right) = \sum_{n'=0}^{\infty} \sum_{m'=0}^{n'} \begin{pmatrix} \hat{\boldsymbol{T}}_{n'n}^{m'm}(\boldsymbol{Q},\boldsymbol{d}) & \boldsymbol{0} & \boldsymbol{0} \\ \boldsymbol{0} & \hat{\boldsymbol{T}}_{n'n}^{m'm}(\boldsymbol{Q},\boldsymbol{d}) & \boldsymbol{0} \\ \boldsymbol{0} & \boldsymbol{0} & \hat{\boldsymbol{T}}_{n'n}^{m'm}(\boldsymbol{Q},\boldsymbol{d}) \end{pmatrix} \boldsymbol{Q}_{6\times 6}^{\mathrm{T}}\, \boldsymbol{\nabla}_{\boldsymbol{r}'} \hat{\boldsymbol{E}}_{n'}^{m'}\left(\boldsymbol{r}'\right),$$

$$\boldsymbol{\nabla}_{\boldsymbol{r}} \hat{\boldsymbol{F}}_n^m\left(\boldsymbol{r}\right) = \sum_{n'=0}^{\infty} \sum_{m'=0}^{n'} \mathrm{bdiag}\left\{\hat{\boldsymbol{T}}_{n'n}^{m'm}(\boldsymbol{Q},\boldsymbol{d})\right\}\, \boldsymbol{Q}_{6\times 6}^{\mathrm{T}}\, \boldsymbol{\nabla}_{\boldsymbol{r}'}\, \hat{\boldsymbol{E}}_{n'}^{m'}\left(\boldsymbol{r}'\right). \tag{115}$$

As shown later in Eq. (149), the gradient of the spherical base-solutions equals a linear combination of two or more spherical base-solutions in the same coordinate system. The introduction of alternative orthonormal coordinates $\hat{\boldsymbol{r}}$ Eq. (124) instead of $\boldsymbol{r}$ simplifies the expressions to yield

$$\boldsymbol{\nabla}_{\hat{\boldsymbol{r}}} \hat{\boldsymbol{F}}_n^m(\hat{\boldsymbol{r}}) = \sum_{n'=0}^{\infty} \sum_{m'=-n'}^{\infty} \hat{\boldsymbol{G}}_{n'n}^{m'm}\, \hat{\boldsymbol{F}}_{n'}^{m'}(\hat{\boldsymbol{r}}), \tag{116}$$

$$\hat{\boldsymbol{G}}_{n'n}^{m'm} = \begin{pmatrix} \hat{g}_{n'n}^{(\hat{x}),m'm}\boldsymbol{I} \\ \hat{g}_{n'n}^{(\hat{y}),m'm}\boldsymbol{I} \\ \hat{g}_{n'n}^{(\hat{z}),m'm}\boldsymbol{I} \end{pmatrix}. \tag{117}$$

Coordinate transform and gradient must be commutative. A spherical base-function in one coordinate system is equivalent to a linear combination of the spherical base-functions in another coordinate system, using the coefficients $\hat{\boldsymbol{T}}_{n'n}^{m'n}(\boldsymbol{Q},\boldsymbol{d})$. Not all the coefficients are easy to compute, however some are analytically known. As will be shown below, the gradient also equals a linear combination of base solutions with coefficients $\hat{\boldsymbol{G}}_{n'n}^{m'm}$ that are well-defined. In general, the gradient in a shifted coordinate system must lead to the same result as the gradient in the original coordinate system, evaluated at the shifted points. Therefore both operations must be commutative. The commutative law between the two matrix-type operations is used to obtain interrelations between elements of the transform operator $\hat{\boldsymbol{T}}_{n'n}^{m'm}(\boldsymbol{Q},\boldsymbol{d})$, cf. [Che92, GD01, GD03, GD04].

Generally, there must be equivalence between the gradient in different coordinate systems. Starting from the addition theorem Eq. (110) and inserting the

gradient Eq. (116) on both sides as well as the addition theorem on the left yields:

$$\boldsymbol{\nabla}_{\hat{\boldsymbol{r}}}\, \hat{\boldsymbol{F}}_n^m(\hat{\boldsymbol{r}}) = \sum_{n_1,m_1} \mathrm{bdiag}\left\{\hat{\boldsymbol{T}}_{n_1 n}^{m_1 m}\right\} \boldsymbol{Q}_{6\times 6}^{\mathrm{T}}\, \boldsymbol{\nabla}_{\hat{\boldsymbol{r}}'}\, \hat{\boldsymbol{E}}_{n_1}^{m_1}(\hat{\boldsymbol{r}}') \quad (118)$$

$$\sum_{n_3,m_3} \hat{\boldsymbol{G}}_{n_3 n}^{m_3 m}\, \hat{\boldsymbol{F}}_{n_3}^{m_3}(\hat{\boldsymbol{r}}) = \sum_{n_1,m_1}\sum_{n_2,m_2} \mathrm{bdiag}\left\{\hat{\boldsymbol{T}}_{n_1 n}^{m_1 n}\right\} \boldsymbol{Q}_{6\times 6}^{\mathrm{T}}\, \hat{\boldsymbol{G}}_{n_2 n_1}^{m_2 m_1}\, \hat{\boldsymbol{E}}_{n_2}^{m_2}(\hat{\boldsymbol{r}}')$$

$$\sum_{n_3,m_3}\sum_{n_4,m_4} \hat{\boldsymbol{G}}_{n_3 n}^{m_3 m}\, \hat{\boldsymbol{T}}_{n_4 n_3}^{m_4 m_3}\, \hat{\boldsymbol{E}}_{n_4}^{m_4}(\hat{\boldsymbol{r}}') = \sum_{n_1,m_1}\sum_{n_2,m_2} \mathrm{bdiag}\left\{\hat{\boldsymbol{T}}_{n_1 n}^{m_1 n}\right\} \boldsymbol{Q}_{6\times 6}^{\mathrm{T}}\, \hat{\boldsymbol{G}}_{n_2 n_1}^{m_2 m_1}\, \hat{\boldsymbol{E}}_{n_2}^{m_2}(\hat{\boldsymbol{r}}').$$

Exploiting the orthonormality of the spherical base-functions $\hat{\boldsymbol{E}}_{n'}^{m'}(\hat{\boldsymbol{r}}')$ within the same reference frame $\hat{\boldsymbol{r}}'$ using $\int \hat{\boldsymbol{E}}_{n'}^{m'}(\hat{\boldsymbol{r}}')\hat{\boldsymbol{Y}}_n^m(\hat{\boldsymbol{\theta}}')d\hat{\boldsymbol{\theta}}' = \delta_{nn'}\delta_{mm'}\hat{\boldsymbol{E}}_n^m(\hat{\boldsymbol{r}}')$ yields:

$$\sum_{n_3,m_3} \hat{\boldsymbol{G}}_{n_3 n}^{n_3 m}\, \hat{\boldsymbol{T}}_{n' n_3}^{m' m_3}\, \hat{\boldsymbol{E}}_{n'}^{m'}(\hat{\boldsymbol{r}}') = \sum_{n_1,m_1} \mathrm{bdiag}\left\{\hat{\boldsymbol{T}}_{n_1 n}^{m_1 m}\right\} \boldsymbol{Q}_{6\times 6}^{\mathrm{T}}\, \hat{\boldsymbol{G}}_{n' m_1}^{m' m_1}\, \hat{\boldsymbol{E}}_{n'}^{m'}(\hat{\boldsymbol{r}}'), \quad (119)$$

$$\sum_{n_2,m_2} \hat{\boldsymbol{G}}_{n_2 n}^{n_2 m}\, \hat{\boldsymbol{T}}_{n' n_2}^{m' m_2} = \sum_{n_1,m_1} \mathrm{bdiag}\left\{\hat{\boldsymbol{T}}_{n_1 n}^{m_1 m}\right\} \boldsymbol{Q}_{6\times 6}^{\mathrm{T}}\, \hat{\boldsymbol{G}}_{n' m_1}^{m' m_1}. \quad (120)$$

Since $\hat{\boldsymbol{G}}_{n' n}^{m' n}$ is very sparse, the last equation yields simple recurrence relations between the entries in the transform matrix $\hat{\boldsymbol{T}}_{n' n}^{m' m}(\boldsymbol{Q}, \boldsymbol{d})$. These recurrence relations provide computational means to derive higher-order transform relations from the known ones (spherical harmonics addition theorem, Green's functions).

3.1.2 Deriving the Gradient on Spherical Base-Solutions

Expressing the gradient as combination of base functions. The conversion between Cartesian and spherical coordinates is important for the derivation of the gradient ($\mu = \cos(\vartheta)$):

$$\mathring{\boldsymbol{r}} = \begin{pmatrix} kr \\ \varphi \\ \mu \end{pmatrix} = \begin{pmatrix} k\sqrt{x^2+y^2+z^2} \\ \arctan\left(y/x\right) \\ z/r \end{pmatrix}. \quad (121)$$

In preparation to define the gradient with respect to the spherical coordinates $\mathring{\boldsymbol{r}}$, the partial derivatives for the chain rule using Eq. (121) equal

$$\begin{aligned}
\frac{1}{k}\nabla_{\boldsymbol{r}} &= \nabla_{\boldsymbol{r}}\,\mathring{\boldsymbol{r}}^{\mathrm{T}}\,\nabla_{\mathring{\boldsymbol{r}}} \\
&= \begin{pmatrix} \partial kr/\partial x & \partial\varphi/\partial x & \partial\mu/\partial x \\ \partial kr/\partial y & \partial\varphi/\partial y & \partial\mu/\partial y \\ \partial kr/\partial z & \partial\varphi/\partial z & \partial\mu/\partial z \end{pmatrix} \begin{pmatrix} \partial/\partial kr \\ \partial/\partial\varphi \\ \partial/\partial\mu \end{pmatrix} \qquad (122) \\
&= \begin{pmatrix} \cos(\varphi)\sqrt{1-\mu^2} & -\frac{\sin(\varphi)}{kr\sqrt{1-\mu^2}} & -\frac{\mu}{kr}\cos(\varphi)\sqrt{1-\mu^2} \\ \sin(\varphi)\sqrt{1-\mu^2} & \frac{\cos(\varphi)}{kr\sqrt{1-\mu^2}} & -\frac{\mu}{kr}\sin(\varphi)\sqrt{1-\mu^2} \\ \mu & 0 & \frac{1-\mu^2}{kr} \end{pmatrix} \begin{pmatrix} \partial/\partial kr \\ \partial/\partial\varphi \\ \partial/\partial\mu \end{pmatrix} \\
&= \begin{pmatrix} \hat{\boldsymbol{\Phi}}_1(\varphi) & \begin{matrix} 0 \\ 0 \end{matrix} \\ \begin{matrix} 0 & 0 \end{matrix} & 1 \end{pmatrix} \begin{pmatrix} \sqrt{1-\mu^2} & 0 & -\frac{\mu}{kr}\sqrt{1-\mu^2} \\ 0 & \frac{1}{kr\sqrt{1-\mu^2}} & 0 \\ \mu & 0 & \frac{1-\mu^2}{kr} \end{pmatrix} \begin{pmatrix} \frac{\partial}{\partial kr} \\ \frac{\partial}{\partial\varphi} \\ \frac{\partial}{\partial\mu} \end{pmatrix}.
\end{aligned}$$

We observe that a rotation matrix $\hat{\boldsymbol{\Phi}}_1(\varphi)$, i.e. the first degree azimuth solution, is part of the partial derivatives. Since the rotation structurally relates the derivatives with respect to x and y it cannot usefully yield an application of the *addition theorem*, cf. Eq. (101). In the next paragraph, the usual modification of the coordinate system [Che92, GD01, GD03, GD04] is introduced that allows us to employ this theorem.

A new coordinate system incorporating the trigonometric addition theorem. In terms of the azimuthal solutions, the following redefinition of the coordinates is beneficial (note that the matrix $\boldsymbol{L}$ represents the imaginary constant $\mathrm{i} = \sqrt{-1}$ in real-valued matrix notation, and the factor $1/\sqrt{2}$ provides normalization $\hat{\boldsymbol{r}}^{\mathrm{T}}\hat{\boldsymbol{r}} = r^2\,\boldsymbol{I}$):

$$\boldsymbol{I} = \begin{pmatrix} 1 & 0 \\ 0 & 1 \end{pmatrix}, \qquad \boldsymbol{L} = \begin{pmatrix} 0 & -1 \\ 1 & 0 \end{pmatrix}, \qquad \boldsymbol{L}\,\boldsymbol{L} = -\boldsymbol{I} \qquad (123)$$

$$\hat{\boldsymbol{r}} = \begin{pmatrix} \hat{\boldsymbol{x}} \\ \hat{\boldsymbol{y}} \\ \hat{\boldsymbol{z}} \end{pmatrix} = \frac{1}{\sqrt{2}} \begin{pmatrix} x\boldsymbol{I} + y\boldsymbol{L} \\ x\boldsymbol{I} - y\boldsymbol{L} \\ z\boldsymbol{I}\,\sqrt{2} \end{pmatrix}, \qquad \hat{\boldsymbol{x}} = \hat{\boldsymbol{y}}^{\mathrm{T}}. \qquad (124)$$

For a coordinate transform $\boldsymbol{r}' = \boldsymbol{Q}\,\boldsymbol{r} + \boldsymbol{d}$ with $\boldsymbol{Q} = \begin{pmatrix} q_{xx'} & q_{yx'} & q_{zx'} \\ q_{xy'} & q_{yy'} & q_{zy'} \\ q_{xz'} & q_{yz'} & q_{zz'} \end{pmatrix}$, $\boldsymbol{d} = \begin{pmatrix} d_x \\ q_y \\ q_z \end{pmatrix}$,

the following redefinitions are necessary:

$$\hat{\boldsymbol{r}}' = \hat{\boldsymbol{Q}}\,\hat{\boldsymbol{r}} + \hat{\boldsymbol{d}}, \quad \hat{\boldsymbol{d}} = \frac{1}{\sqrt{2}} \begin{pmatrix} d_x \boldsymbol{I} + d_y \boldsymbol{L} \\ d_x \boldsymbol{I} - d_y \boldsymbol{L} \\ d_z \boldsymbol{I}\,\sqrt{2} \end{pmatrix}, \quad \hat{\boldsymbol{Q}} = \begin{pmatrix} \boldsymbol{Q}_{\hat{\boldsymbol{x}}\hat{\boldsymbol{x}}'} & \boldsymbol{Q}_{\hat{\boldsymbol{y}}\hat{\boldsymbol{x}}'} & \boldsymbol{Q}_{\hat{\boldsymbol{z}}\hat{\boldsymbol{x}}'} \\ \boldsymbol{Q}_{\hat{\boldsymbol{x}}\hat{\boldsymbol{y}}'} & \boldsymbol{Q}_{\hat{\boldsymbol{y}}\hat{\boldsymbol{y}}'} & \boldsymbol{Q}_{\hat{\boldsymbol{z}}\hat{\boldsymbol{y}}'} \\ \boldsymbol{Q}_{\hat{\boldsymbol{x}}\hat{\boldsymbol{z}}'} & \boldsymbol{Q}_{\hat{\boldsymbol{y}}\hat{\boldsymbol{z}}'} & \boldsymbol{Q}_{\hat{\boldsymbol{z}}\hat{\boldsymbol{z}}'} \end{pmatrix}, \tag{125}$$

$$\hat{\boldsymbol{Q}} = \frac{1}{2} \begin{pmatrix} (q_{xx'} + q_{yy'})\boldsymbol{I} - (q_{yx'} - q_{xy'})\boldsymbol{L} & (q_{xx'} - q_{yy'})\boldsymbol{I} + (q_{yx'} + q_{xy'})\boldsymbol{L} & \sqrt{2}\,(q_{zx'}\boldsymbol{I} + q_{zy'}\boldsymbol{L}) \\ (q_{xx'} - q_{yy'})\boldsymbol{I} - (q_{yx'} + q_{xy'})\boldsymbol{L} & (q_{xx'} + q_{yy'})\boldsymbol{I} + (q_{yx'} - q_{xy'})\boldsymbol{L} & \sqrt{2}\,(q_{zx'}\boldsymbol{I} - q_{zy'}\boldsymbol{L}) \\ \sqrt{2}\,(q_{xz'}\boldsymbol{I} - q_{yz'}\boldsymbol{L}) & \sqrt{2}\,(q_{xz'}\boldsymbol{I} + q_{yz'}\boldsymbol{L}) & 2q_{zz'}\boldsymbol{I} \end{pmatrix}.$$

Gradient in the new coordinate system. The redefined gradient and the chain rule yield

$$\boldsymbol{\nabla}_{\hat{\boldsymbol{r}}} = \begin{bmatrix} (\boldsymbol{I}\partial/\partial x + \boldsymbol{L}\partial/\partial y)/\sqrt{2} \\ (\boldsymbol{I}\partial/\partial x - \boldsymbol{L}\partial/\partial y)/\sqrt{2} \\ \boldsymbol{I}\partial/\partial z \end{bmatrix} = \begin{bmatrix} \boldsymbol{\nabla}_{\hat{\boldsymbol{x}}} \\ \boldsymbol{\nabla}_{\hat{\boldsymbol{y}}} \\ \boldsymbol{\nabla}_{\hat{\boldsymbol{z}}} \end{bmatrix}, \qquad \boldsymbol{\nabla}_{\hat{\boldsymbol{r}}}\,\hat{\boldsymbol{r}}^{\mathrm{T}} = \boldsymbol{I}_{6\times 6}. \tag{126}$$

$$\boldsymbol{\nabla}_{\hat{\boldsymbol{r}}} = \boldsymbol{\nabla}_{\hat{\boldsymbol{r}}}\,\hat{\boldsymbol{r}}'^{\,\mathrm{T}}\,\boldsymbol{\nabla}_{\hat{\boldsymbol{r}}'} = \hat{\boldsymbol{Q}}^{\mathrm{T}}\,\boldsymbol{\nabla}_{\hat{\boldsymbol{r}}'}. \tag{127}$$

It becomes clear in the next equations that, within the new coordinate system, the rotation matrix $\hat{\boldsymbol{\Phi}}_m(\varphi)$ in Eq. (122) increments/decrements the degrees of the azimuth harmonics. In addition, another useful property will be taken into account by expanding $\boldsymbol{I}\partial/\partial\varphi = -\boldsymbol{L}\,\boldsymbol{L}\,\partial/\partial\varphi$:

$$m\hat{\boldsymbol{\Phi}}_m(\varphi) = -\boldsymbol{L}\,\frac{\partial}{\partial\varphi}\hat{\boldsymbol{\Phi}}_m(\varphi). \tag{128}$$

With the partial derivatives in Eq. (122), the operators $\frac{1}{k}\boldsymbol{\nabla}_{\hat{\boldsymbol{x}}}$, $\frac{1}{k}\boldsymbol{\nabla}_{\hat{\boldsymbol{y}}}$, and $\frac{1}{k}\boldsymbol{\nabla}_{\hat{\boldsymbol{z}}}$ yield

$$\begin{aligned} \frac{1}{k}\boldsymbol{\nabla}_{\hat{\boldsymbol{x}}} &= \frac{1}{k}\begin{pmatrix} \boldsymbol{\nabla}_{\hat{\boldsymbol{x}}}\,kr, & \boldsymbol{L}\,\boldsymbol{\nabla}_{\hat{\boldsymbol{x}}}\,\varphi, & \boldsymbol{\nabla}_{\hat{\boldsymbol{x}}}\,\mu \end{pmatrix} \begin{pmatrix} \boldsymbol{I}\partial/\partial kr \\ -\boldsymbol{L}\partial/\partial\varphi \\ \boldsymbol{I}\partial/\partial\mu \end{pmatrix}, \\ &= \frac{1}{kr\sqrt{1-\mu^2}\,\sqrt{2}}\,\hat{\boldsymbol{\Phi}}_1(\varphi)\,\left[(1-\mu^2)\boldsymbol{I}\left(kr\frac{\partial}{\partial kr} - \mu\frac{\partial}{\partial\mu}\right) + \boldsymbol{L}\frac{\partial}{\partial\varphi}\right], \end{aligned} \tag{129}$$

$$\frac{1}{k}\boldsymbol{\nabla}_{\hat{\boldsymbol{y}}} = \frac{1}{k}\boldsymbol{\nabla}_{\hat{\boldsymbol{x}}}^{\mathrm{T}} = \frac{1}{kr\sqrt{1-\mu^2}\,\sqrt{2}}\left[(1-\mu^2)\boldsymbol{I}\left(kr\frac{\partial}{\partial kr} - \mu\frac{\partial}{\partial\mu}\right) - \boldsymbol{L}\frac{\partial}{\partial\varphi}\right]\,\hat{\boldsymbol{\Phi}}_1^{\mathrm{T}}(\varphi), \tag{130}$$

$$\frac{1}{k}\boldsymbol{\nabla}_{\hat{\boldsymbol{z}}} = \boldsymbol{I}\left(\mu\frac{\partial}{\partial kr} + \frac{1-\mu^2}{kr}\frac{\partial}{\partial\mu}\right). \tag{131}$$

As given in [GD01, GD03], the above operators are simplified by using recurrence relations of the spherical base-solutions involving the derivatives.

Inserting $f_n(kr)\, P_n^m(\mu)$ for the gradient in $\hat{\boldsymbol{z}}$

$$\frac{1}{k}\frac{\partial}{\partial z} f_n(kr) P_n^m(\mu) = \left[\mu P_n^m(\mu) \frac{\partial}{\partial kr} f_n(kr) + \frac{f_n(kr)}{kr}(1-\mu^2)\frac{\partial}{\partial \mu} P_n^m(\mu) \right],$$

the following recurrence relations are used

$$\mu P_n^m(\mu) = \frac{n+m}{2n+1} P_{n-1}^m(\mu) + \frac{(n-m+1)}{2n+1} P_{n+1}^m(\mu) \tag{132}$$

$$(1-\mu^2)\frac{\partial}{\partial \mu} P_n^m(\mu) = \frac{(n+1)(n+m)}{2n+1} P_{n-1}^m(\mu) - \frac{n(n-m+1)}{2n+1} P_{n+1}^m(\mu) \tag{133}$$

$$\frac{(n+1) f_n(kr)}{kr} = f_{n-1}(kr) - \frac{\partial}{\partial kr} f_n(kr) \tag{134}$$

$$\frac{n f_n(kr)}{kr} = f_{n+1}(kr) + \frac{\partial}{\partial kr} f_n(kr), \tag{135}$$

and it remains

$$\frac{1}{k}\frac{\partial}{\partial z} f_n(kr) P_{n-1}^m(\mu) = \left[\frac{n+m}{2n+1} f_{n-1}(kr) P_{n-1}^m(\mu) - \frac{n-m+1}{2n+1} f_{n+1}(kr) P_{n+1}^m(\mu) \right],$$

$$\frac{1}{k}\boldsymbol{\nabla}_{\hat{\boldsymbol{z}}} \boldsymbol{F}_n^m(\hat{\boldsymbol{r}}) = \frac{\hat{N}_n^m (n+m)}{N_{n-1}^m (2n+1)} \boldsymbol{F}_{n-1}^m(\hat{\boldsymbol{r}}) - \frac{\hat{N}_n^m (n-m+1)}{N_{n+1}^m (2n+1)} \boldsymbol{F}_{n+1}^m(\hat{\boldsymbol{r}}). \tag{136}$$

Note that for $n = 0$ the expression $\boldsymbol{F}_{n-1}^m(\hat{\boldsymbol{r}})$ vanishes.

Additionally, the operators $\frac{1}{k}\boldsymbol{\nabla}_{\hat{\boldsymbol{x}}}$ and $\frac{1}{k}\boldsymbol{\nabla}_{\hat{\boldsymbol{y}}} = \frac{1}{k}\boldsymbol{\nabla}_{\hat{\boldsymbol{x}}}^{\mathrm{T}}$ are simplified by recurrence relations given in [GD01, GD03]

$$\frac{\sqrt{2}}{\hat{N}_n^m k}\boldsymbol{\nabla}_{\hat{\boldsymbol{x}}} \hat{\boldsymbol{F}}_n^m(\hat{\boldsymbol{r}}) = \hat{\boldsymbol{\Phi}}_1(\varphi) \cdot \left[\sqrt{1-\mu^2}\boldsymbol{I}\frac{\partial}{\partial kr} - \frac{1}{kr}\left(\mu\sqrt{1-\mu^2}\boldsymbol{I}\frac{\partial}{\partial \mu} + \frac{1}{\sqrt{1-\mu^2}}\boldsymbol{L}\frac{\partial}{\partial \varphi} \right) \right] \cdot \hat{\boldsymbol{\Phi}}_m(\varphi) P_n^m(\mu) f_n(kr),$$

$$\frac{\sqrt{2}}{\hat{N}_n^m k}\boldsymbol{\nabla}_{\hat{\boldsymbol{y}}} \hat{\boldsymbol{F}}_n^m(\hat{\boldsymbol{r}}) = \hat{\boldsymbol{\Phi}}_1^{\mathrm{T}}(\varphi) \cdot \left[\sqrt{1-\mu^2}\boldsymbol{I}\frac{\partial}{\partial kr} - \frac{1}{kr}\left(\mu\sqrt{1-\mu^2}\boldsymbol{I}\frac{\partial}{\partial \mu} - \frac{1}{\sqrt{1-\mu^2}}\boldsymbol{L}\frac{\partial}{\partial \varphi} \right) \right] \cdot \hat{\boldsymbol{\Phi}}_m(\varphi) P_n^m(\mu) f_n(kr).$$

Utilizing the addition theorem of sine and cosine, as well as the recurrence relations

of the Legendre polynomials [GD01, GD03] and the radial functions (134),(135)

$$\hat{\mathbf{\Phi}}_{m+1}(\varphi) = \hat{\mathbf{\Phi}}_1(\varphi)\,\hat{\mathbf{\Phi}}_m(\varphi), \tag{137}$$

$$\hat{\mathbf{\Phi}}_{m-1}(\varphi) = \hat{\mathbf{\Phi}}_1^{\mathrm{T}}(\varphi)\,\hat{\mathbf{\Phi}}_m(\varphi), \tag{138}$$

$$\sqrt{1-\mu^2}P_n^m(\mu) = \frac{1}{2n+1}P_{n-1}^{m+1}(\mu) - \frac{1}{2n+1}P_{n+1}^{m+1}(\mu), \tag{139}$$

$$\sqrt{1-\mu^2}P_n^m(\mu) = \frac{(n-m+1)(n-m+2)}{2n+1}P_{n-1}^{m-1}(\mu) + \frac{(n+m-1)(n+m)}{2n+1}P_{n+1}^{m-1}(\mu), \tag{140}$$

$$-\mu\sqrt{1-\mu^2}\frac{\partial}{\partial\mu}P_n^m(\mu) - \frac{m}{\sqrt{1-\mu^2}}P_n^m(\mu) = -\frac{(n+m-1)(n+m)}{2n+1}P_{n-1}^{m-1}(\mu) + \frac{(n-m+1)(n-m+2)}{2n+1}P_{n+1}^{m+1}(\mu), \tag{141}$$

$$-\mu\sqrt{1-\mu^2}\frac{\partial}{\partial\mu}P_n^m(\mu) + \frac{m}{\sqrt{1-\mu^2}}P_n^m(\mu) = -\frac{(n+1)(n+m-1)(n+m)}{2n+1}P_{n-1}^{m-1}(\mu) - \frac{n(n-m+1)(n-m+2)}{2n+1}P_{n+1}^{m-1}(\mu), \tag{142}$$

the equations remain

$$\frac{\sqrt{2}}{\hat{N}_n^m k}\boldsymbol{\nabla}_{\hat{\boldsymbol{x}}}\hat{\boldsymbol{F}}_n^m(\hat{\boldsymbol{r}}) = \hat{\mathbf{\Phi}}_{m+1}(\varphi)\cdot \left[\frac{1}{2n+1}P_{n-1}^{m+1}(\mu)f_{n-1}(kr) + \frac{1}{2n+1}P_{n+1}^{m+1}(\mu)f_{n+1}(kr)\right],$$

$$\frac{\sqrt{2}}{\hat{N}_n^m k}\boldsymbol{\nabla}_{\hat{\boldsymbol{y}}}\hat{\boldsymbol{F}}_n^m(\hat{\boldsymbol{r}}) = \hat{\mathbf{\Phi}}_{m-1}(\varphi)\cdot\left[-\frac{(n+m-1)(n+m)}{2n+1}P_{n-1}^{m-1}(\mu)f_{n-1}(kr) - \frac{(n-m+1)(n-m+2)}{2n+1}P_{n+1}^{m-1}(\mu)f_{n+1}(kr)\right].$$

These are for fully normalized base solutions:

$$\frac{\sqrt{2}}{k}\boldsymbol{\nabla}_{\hat{\boldsymbol{x}}}\hat{\boldsymbol{F}}_n^m(\hat{\boldsymbol{r}}) = \frac{\hat{N}_n^m}{N_{n-1}^{m+1}(2n+1)}\hat{\boldsymbol{F}}_{n-1}^{m+1}(\hat{\boldsymbol{r}}) + \frac{\hat{N}_n^m}{N_{n+1}^{m+1}(2n+1)}\hat{\boldsymbol{F}}_{n+1}^{m+1}(\hat{\boldsymbol{r}}), \tag{143}$$

$$\frac{\sqrt{2}}{k}\boldsymbol{\nabla}_{\hat{\boldsymbol{y}}}\hat{\boldsymbol{F}}_n^m(\hat{\boldsymbol{r}}) = -\frac{\hat{N}_n^m(n+m-1)(n+m)}{N_{n-1}^{m-1}(2n+1)}\hat{\boldsymbol{F}}_{n-1}^{m-1}(\hat{\boldsymbol{r}}) - \frac{\hat{N}_n^m(n-m+1)(n-m+2)}{N_{n+1}^{m-1}(2n+1)}\hat{\boldsymbol{F}}_{n+1}^{m-1}(\hat{\boldsymbol{r}}). \tag{144}$$

The constants involved can be gathered into new expressions, such as given in [GD01,

GD03, GD04]

$$a_n^m = \begin{cases} \sqrt{\frac{(n-|m|+1)(n+|m|+1)}{(2n+1)(2n+3)}}, & \text{for } n \geq 0 \text{ and } -n \leq m \leq n \\ 0, & \text{else.} \end{cases} \tag{145}$$

$$b_n^m = \begin{cases} \sqrt{\frac{(n-m-1)(n-m)}{(2n-1)(2n+1)}}, & \text{for } n \geq 0 \text{ and } 0 \leq m \leq n \\ -\sqrt{\frac{(n-m-1)(n-m)}{(2n-1)(2n+1)}}, & \text{for } n \geq 0 \text{ and } -n \leq m < 0 \\ 0, & \text{else.} \end{cases} \tag{146}$$

In order to simplify, we use the constants and Kronecker deltas to re-write the theorems representing the gradient with its components:

$$\frac{1}{k}\boldsymbol{\nabla}\hat{\boldsymbol{F}}_n^m(\hat{\boldsymbol{r}}) = \sum_{n'=0}^{\infty}\sum_{m'=-n'}^{n'} \hat{\boldsymbol{G}}_{n'n}^{m'm}\hat{\boldsymbol{F}}_{n'}^{m'}(\hat{\boldsymbol{r}}), \tag{147}$$

$$\hat{\boldsymbol{G}}_{n'n}^{m'm} = \begin{pmatrix} \frac{1}{\sqrt{2}}\boldsymbol{I}\left[-b_n^m\,\delta_{n',n-1}^{m',m+1} + b_{n+1}^{-m-1}\,\delta_{n',n+1}^{m',m+1}\right] \\ \frac{1}{\sqrt{2}}\boldsymbol{I}\left[-b_n^{-m}\,\delta_{n',n-1}^{m',m-1} + b_{n+1}^{m-1}\,\delta_{n',n+1}^{m',m-1}\right] \\ \boldsymbol{I}\left[a_{n-1}^m\,\delta_{n',n-1}^{m',m} - a_n^m\,\delta_{n',n+1}^{m',m}\right] \end{pmatrix} \tag{148}$$

$$= \begin{pmatrix} \frac{1}{\sqrt{2}}\boldsymbol{I}\left[-b_{n'+1}^{m'-1}\,\delta_{n'+1,n}^{m'-1,m} + b_{n'}^{-m'}\,\delta_{n'-1,n}^{m'-1,m}\right] \\ \frac{1}{\sqrt{2}}\boldsymbol{I}\left[-b_{n'+1}^{-m'-1}\,\delta_{n'+1,n}^{m'+1,m} + b_{n'}^{m'}\,\delta_{n'-1,n}^{m'+1,m}\right] \\ \boldsymbol{I}\left[a_{n'}^{m'}\,\delta_{n'+1,n}^{m',m} - a_{n'-1}^{m'}\,\delta_{n'-1,n}^{m',m}\right] \end{pmatrix}. \tag{149}$$

Eq. (149) can be described in two ways, depending on which pair of indices (either n, m, or n', m') is used as summation variable, see right hand side of Eq. (151). A complete recurrence scheme is given in the following section.

3.1.3 General Recurrence Relations for Coordinate Transforms

The approach to obtain interrelations between the transform coefficients in $\hat{\boldsymbol{T}}^{m'm}_{n'n}(\hat{\boldsymbol{Q}},\hat{\boldsymbol{d}})$ was plotted in Eq. (120). With the modified $\boldsymbol{\nabla}_{\hat{\boldsymbol{r}}}$-operator, this becomes

$$\sum_{n_2,m_2} \hat{\boldsymbol{G}}^{n_2,m}_{n_2 n}\, \hat{\boldsymbol{T}}^{m'm_2}_{n'n_2}(\hat{\boldsymbol{Q}},\hat{\boldsymbol{d}}) = \sum_{n_1 m_1} \operatorname{diag}\left\{\hat{\boldsymbol{T}}^{m_1 m}_{n_1 n}(\hat{\boldsymbol{Q}},\hat{\boldsymbol{d}})\right\}\, \hat{\boldsymbol{Q}}^{\mathrm{T}}\; \hat{\boldsymbol{G}}^{m'm_1}_{n'm_1}, \tag{150}$$

according to the definitions of the rotation matrix $\hat{\boldsymbol{Q}}$ from Eq. (125), and $\hat{\boldsymbol{G}}^{m'm}_{n'n}$ from Eq. (149). In particular, the complete relation yields

$$\begin{pmatrix} -b^{m}_{n}\hat{\boldsymbol{T}}^{m',m+1}_{n',n-1} + b^{-m-1}_{n+1}\,\hat{\boldsymbol{T}}^{m',m+1}_{n',n+1} \\ -b^{-m}_{n}\hat{\boldsymbol{T}}^{m',m-1}_{n',n-1} + b^{m-1}_{n+1}\,\hat{\boldsymbol{T}}^{m',m-1}_{n',n+1} \\ \frac{1}{\sqrt{2}}(a^{m}_{n-1}\hat{\boldsymbol{T}}^{m',m}_{n',n-1} - a^{m}_{n}\,\hat{\boldsymbol{T}}^{m',m}_{n',n+1}) \end{pmatrix} =$$

$$\begin{pmatrix} \left[-b^{m'-1}_{n'+1}\,\hat{\boldsymbol{T}}^{m'-1,m}_{n'+1,n} + b^{-m'}_{n'}\,\hat{\boldsymbol{T}}^{m'-1,m}_{n'-1,n}\right]\hat{\boldsymbol{Q}}^{\mathrm{T}}_{\hat{\boldsymbol{x}}\hat{\boldsymbol{x}}'} + \left[-b^{-m'-1}_{n'+1}\,\hat{\boldsymbol{T}}^{m'+1,m}_{n'+1,n} + b^{m'}_{n'}\,\hat{\boldsymbol{T}}^{m'+1,m}_{n'-1,n}\right]\hat{\boldsymbol{Q}}^{\mathrm{T}}_{\hat{\boldsymbol{x}}\hat{\boldsymbol{y}}'} + \\ \left[-b^{m'-1}_{n'+1}\,\hat{\boldsymbol{T}}^{m'-1,m}_{n'+1,n} + b^{-m'}_{n'}\,\hat{\boldsymbol{T}}^{m'-1,m}_{n'-1,n}\right]\hat{\boldsymbol{Q}}^{\mathrm{T}}_{\hat{\boldsymbol{y}}\hat{\boldsymbol{x}}'} + \left[-b^{-m'-1}_{n'+1}\,\hat{\boldsymbol{T}}^{m'+1,m}_{n'+1,n} + b^{m'}_{n'}\,\hat{\boldsymbol{T}}^{m'+1,m}_{n'-1,n}\right]\hat{\boldsymbol{Q}}^{\mathrm{T}}_{\hat{\boldsymbol{y}}\hat{\boldsymbol{y}}'} + \\ \left[-b^{m'-1}_{n'+1}\,\hat{\boldsymbol{T}}^{m'-1,m}_{n'+1,n} + b^{-m'}_{n'}\,\hat{\boldsymbol{T}}^{m'-1,m}_{n'-1,n}\right]\hat{\boldsymbol{Q}}^{\mathrm{T}}_{\hat{\boldsymbol{z}}\hat{\boldsymbol{x}}'} + \left[-b^{-m'-1}_{n'+1}\,\hat{\boldsymbol{T}}^{m'+1,m}_{n'+1,n} + b^{m'}_{n'}\,\hat{\boldsymbol{T}}^{m'+1,m}_{n'-1,n}\right]\hat{\boldsymbol{Q}}^{\mathrm{T}}_{\hat{\boldsymbol{z}}\hat{\boldsymbol{y}}'} + \end{pmatrix}$$

$$\begin{pmatrix} +\sqrt{2}\left[a^{m'}_{n'}\,\hat{\boldsymbol{T}}^{m',m}_{n'+1,n} - a^{m'}_{n'-1}\,\hat{\boldsymbol{T}}^{m',m}_{n'-1,n}\right]\hat{\boldsymbol{Q}}^{\mathrm{T}}_{\hat{\boldsymbol{x}}\hat{\boldsymbol{z}}'} \\ +\sqrt{2}\left[a^{m'}_{n'}\,\hat{\boldsymbol{T}}^{m',m}_{n'+1,n} - a^{m'}_{n'-1}\,\hat{\boldsymbol{T}}^{m',m}_{n'-1,n}\right]\hat{\boldsymbol{Q}}^{\mathrm{T}}_{\hat{\boldsymbol{y}}\hat{\boldsymbol{z}}'} \\ +\frac{1}{\sqrt{2}}\left[a^{m'}_{n'}\,\hat{\boldsymbol{T}}^{m',m}_{n'+1,n} - a^{m'}_{n'-1}\,\hat{\boldsymbol{T}}^{m',m}_{n'-1,n}\right]\hat{\boldsymbol{Q}}^{\mathrm{T}}_{\hat{\boldsymbol{z}}\hat{\boldsymbol{z}}'} \end{pmatrix} \tag{151}$$

This equation describes recurrence relations[1] for $\hat{\boldsymbol{T}}^{m'm}_{n'n}(\hat{\boldsymbol{Q}},\hat{\boldsymbol{d}})$ that only depend on the modified rotation matrix $\hat{\boldsymbol{Q}}$. From the above equation, the full set of coefficients for the translation operator can be computed by knowing some initial values for $\hat{\boldsymbol{T}}^{m'm}_{n'n}(\hat{\boldsymbol{Q}},\hat{\boldsymbol{d}})$. Note, however, that these recurrence relations have to be customized in order to deliver applicable expressions for calculation. Furthermore, it is an important task to provide sufficient coefficients for initialization. It is most appropriate to reduce the complexity of the above equations by decomposition of the transforms into simple components.

3.1.4 Decomposition of General Transforms into Simpler Steps

Without loss of generality, full coordinate transforms with a matrix $\boldsymbol{Q}$ and a vector $\boldsymbol{d}$ can be decomposed into smaller steps. It is easy to think about $\hat{\boldsymbol{T}}^{m'm}_{n'n}(\boldsymbol{Q},\boldsymbol{d})$ as being separately a rotation and a translation, i.e. $\hat{\boldsymbol{T}}^{m'm}_{n'n}(\boldsymbol{Q},\boldsymbol{0})$ and $\hat{\boldsymbol{T}}^{m'm}_{n'n}(\boldsymbol{I},\boldsymbol{d})$, respectively. The pure rotation operation is also known as the *Wigner*-D function [KR03, KR08].

[1] The recurrence relations given in Gumerov and Duraiswami [GD01, GD03, GD04] have a different sign on the right hand side, the reason of which was not found, and its influence is unclear. However recurrence relations based on Eq. (177) were successfully tested.

However, it even makes sense to further split these parts up into simpler sub-transforms.

Decomposition of rotation into z-$y\frac{\pi}{2}$-z-$y\frac{\pi}{2}$-z. In terms of arbitrary rotation, it is useful to exploit the properties of the rotations around the z-axis since this operation is very efficient. Therefore it is useful to split up the three rotations into a zyz-rotation. Even further, it makes sense to perform the more complicated part, the y-rotation, at a fixed angle $\pi/2$ only and represent the variable part in terms of a z-rotation cf. Fig. 10, see also [PH07b]. Hereby, rotation is efficiently split up into a z-$y\frac{\pi}{2}$-z-$y\frac{\pi}{2}$-z-rotation

$$\begin{aligned} \boldsymbol{r}' &= \boldsymbol{Q}(\alpha,\beta,\gamma)\,\boldsymbol{r} \\ &= \boldsymbol{Q}_z(\alpha)\,\boldsymbol{Q}_y(\beta)\,\boldsymbol{Q}_z(\gamma)\,\boldsymbol{r} \\ &= \underbrace{\boldsymbol{Q}_z(\alpha+\pi/2)\,\boldsymbol{Q}_{y\frac{\pi}{2}}\,\boldsymbol{Q}_z(\beta+\pi)\,\boldsymbol{Q}_{y\frac{\pi}{2}}\,\boldsymbol{Q}_z(\gamma+\pi/2)}_{\boldsymbol{Q}_{z\text{-}y\frac{\pi}{2}\text{-}z\text{-}y\frac{\pi}{2}\text{-}z}(\alpha,\beta,\gamma)}\,\boldsymbol{r}. \end{aligned} \tag{152}$$

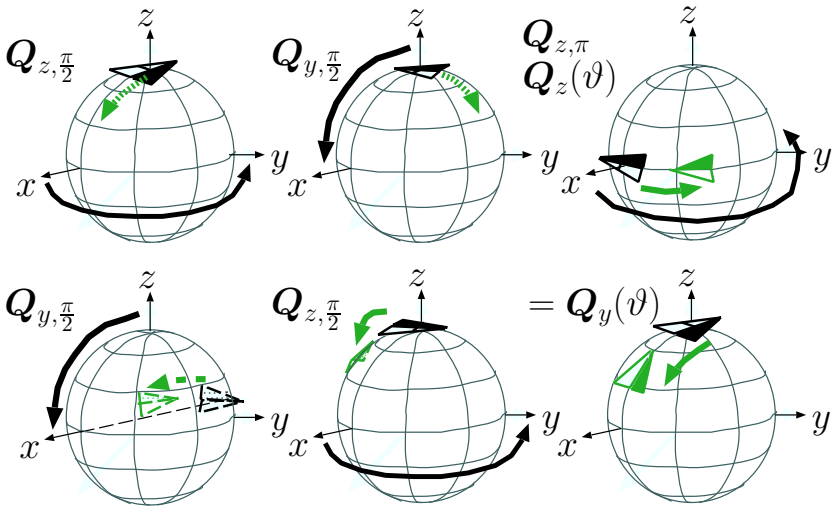

Figure 10: y-rotation represented in terms of a z-$y\frac{\pi}{2}$-z-$y\frac{\pi}{2}$-z rotation containing only constant rotations around y.

Decomposition of translations into z-displacement and rotations. Translation is also efficient when regarding only one direction of translation, in particular the translation towards the positive z-axis, cf. [GD01, GD03, GD04]. Rotational transform of the coordinate system into a suitable coordinate system helps to obtain any arbitrary $\boldsymbol{d}$ by using translation towards z $\boldsymbol{d}_z$

$$\boldsymbol{d} = \boldsymbol{Q}(\varphi_d,\vartheta_d,0)\,\boldsymbol{d}_z = \boldsymbol{Q}(\varphi_d,\vartheta_d,0)\begin{pmatrix}0\\0\\1\end{pmatrix}\|\boldsymbol{d}\|. \tag{153}$$

With the inverse rotation $\boldsymbol{Q}(\varphi_d, \vartheta_d, 0)^{-1} = \boldsymbol{Q}(0, -\vartheta_d, -\varphi_d)$, this representation reads as

$$\begin{aligned} \boldsymbol{r}' &= \boldsymbol{r} + \boldsymbol{d} \\ &= \boldsymbol{Q}(0, -\vartheta_d, -\varphi_d) \left[\boldsymbol{Q}(\varphi_d, \vartheta_d, 0)\, \boldsymbol{r} + \boldsymbol{d}_z \right]. \end{aligned} \tag{154}$$

Fully decomposed transform. A full transform with $\boldsymbol{d}$ and $\boldsymbol{Q}$ in terms of the more efficiently evaluated parts $\boldsymbol{Q}_{y\frac{\pi}{2}}$, $\boldsymbol{Q}_z(\cdot)$, and $\boldsymbol{d}_z$ could be symbolically described as

$$\begin{aligned} &\boldsymbol{r}' = \boldsymbol{Q}\, \boldsymbol{r} + \boldsymbol{d} \\ &= \boldsymbol{Q}_{z\text{-}y\frac{\pi}{2}\text{-}z\text{-}y\frac{\pi}{2}\text{-}z}(0, -\varphi_d, -\vartheta_d) \left[\underbrace{\boldsymbol{Q}_{z\text{-}y\frac{\pi}{2}\text{-}z\text{-}y\frac{\pi}{2}\text{-}z}(\varphi_d, \vartheta_d, 0)\, \boldsymbol{Q}_{z\text{-}y\frac{\pi}{2}\text{-}z\text{-}y\frac{\pi}{2}\text{-}z}(\alpha, \beta, \gamma)}_{\boldsymbol{Q}_{z\text{-}y\frac{\pi}{2}\text{-}z\text{-}y\frac{\pi}{2}\text{-}z}(\alpha', \beta', \gamma')}\, \boldsymbol{r} + \boldsymbol{d}_z \right]. \end{aligned} \tag{155}$$

If the two rotations in the brackets are represented as a single rotation, this transform can be reduced to 2 rotations with 5 variable and 1 fixed angles around z, 4 fixed angles around y, plus the translation along z.

Known simple transform relations. Mirror symmetry with respect to y

$$\begin{aligned} \boldsymbol{Q}_{my} &= \begin{pmatrix} 1 & 0 & 0 \\ 0 & -1 & 0 \\ 0 & 0 & 1 \end{pmatrix}, \qquad \hat{\boldsymbol{Y}}_n^m(\boldsymbol{\theta}) = \hat{\boldsymbol{Y}}_n^{-m}(\boldsymbol{Q}_{my}\, \boldsymbol{\theta}), \\ \Rightarrow T_{n'n}^{m'm}(\boldsymbol{Q}_{my}) &= \delta_{n'n}^{m',-m}. \end{aligned} \tag{156}$$

Rotation around z by 90°

$$\begin{aligned} \boldsymbol{Q}_{z\frac{\pi}{2}} &= \begin{pmatrix} 0 & 1 & 0 \\ -1 & 0 & 0 \\ 0 & 0 & 1 \end{pmatrix}, \qquad \hat{\boldsymbol{Y}}_n^m(\boldsymbol{\theta}) = \begin{pmatrix} 0 & -1 \\ 1 & 0 \end{pmatrix}^m \hat{\boldsymbol{Y}}_n^m(\boldsymbol{Q}_{z\frac{\pi}{2}}\, \boldsymbol{\theta}), \\ \Rightarrow T_{n'n}^{m'm}\left(\boldsymbol{Q}_{z\frac{\pi}{2}}\right) &= \begin{pmatrix} 0 & -1 \\ 1 & 0 \end{pmatrix}^m \delta_{n'n}^{m'm}. \end{aligned} \tag{157}$$

Mirror symmetry with respect to x

$$\boldsymbol{Q}_{mx} = \boldsymbol{Q}_{z\frac{\pi}{2}}^{-1}\, \boldsymbol{Q}_{my}\, \boldsymbol{Q}_{z\frac{\pi}{2}} = \begin{pmatrix} -1 & 0 & 0 \\ 0 & 1 & 0 \\ 0 & 0 & 1 \end{pmatrix}, \quad \hat{\boldsymbol{Y}}_n^m(\boldsymbol{\theta}) = (-1)^m \hat{\boldsymbol{Y}}_n^{-m}(\boldsymbol{Q}_{mx}\, \boldsymbol{\theta}),$$

$$\Rightarrow T_{n'n}^{m'm}(\boldsymbol{Q}_{mx}) = (-1)^m\, \delta_{n'n}^{m',-m}. \tag{158}$$

Mirror symmetry with respect to z

$$\boldsymbol{Q}_{mz} = \begin{pmatrix} 1 & 0 & 0 \\ 0 & 1 & 0 \\ 0 & 0 & -1 \end{pmatrix}, \qquad \hat{\boldsymbol{Y}}_n^m(\boldsymbol{\theta}) = (-1)^{n+m}\hat{\boldsymbol{Y}}_n^m(\boldsymbol{Q}_{mz}\,\boldsymbol{\theta}),$$

$$\Rightarrow T_{n'n}^{m'm}(\boldsymbol{Q}_{mz}) = (-1)^{n+m}\delta_{n'n}^{m',m}. \tag{159}$$

3.1.5 Recurrence Relations for Translation in z Direction

For translation towards z, all entries in the rotation matrix except for $\hat{\boldsymbol{Q}}_{\hat{\boldsymbol{x}}\hat{\boldsymbol{x}}'} = \hat{\boldsymbol{Q}}_{\hat{\boldsymbol{y}}\hat{\boldsymbol{y}}'} = \hat{\boldsymbol{Q}}_{\hat{\boldsymbol{z}}\hat{\boldsymbol{z}}'} = \boldsymbol{I}$ are zero. Therefore, this translation can be written as the complex scalar $\hat{T}_{n'n}^{m'm}(\boldsymbol{d}_z)$.

A translation into z-direction only, i.e., a shift along the rotation axis, must preserve orthogonality in azimuth. Therefore the base solutions in azimuth remain orthogonal, and there is no way for a solution of index m' to be made dependent to m in the shifted reference frame other than $m' = m$. Consequently, the operator reduces to a *diagonal form* wrt. m and m'

$$\hat{T}_{n'n}^{m'm}(\boldsymbol{d}_z) = \delta_{mm'}\,\hat{T}_{n'n}^{m'm}(\boldsymbol{d}_z) \tag{160}$$

$$\hat{\boldsymbol{F}}_n^m(\hat{\boldsymbol{r}}) = \sum_{n'=0}^{\infty} \hat{T}_{n'n}^{mm}(\boldsymbol{d}_z)\hat{\boldsymbol{E}}_{n'}^m(\hat{\boldsymbol{r}}').$$

Since mirroring the y-axis before and after the transform does not affect the translation along z, we also get

$$\hat{T}_{n'n}^{mm}(\boldsymbol{d}_z) = \delta_{n2n}^{m2,-m}\,\hat{T}_{n_1n_2}^{m_1,m_2}(\boldsymbol{d}_z)\,\delta_{n'n_1}^{m',-m_1} = \hat{T}_{n'n}^{-m',-m}(\boldsymbol{d}_z). \tag{161}$$

Furthermore, mirroring the z-axis before and after translation yields the inverse operation. Exploiting the symmetry and orthogonality of the unitary transform operation reveals

$$\hat{T}_{nn'}^{mm}(-\boldsymbol{d}_z) = (-1)^{n'-m}\,\hat{T}_{nn'}^{mm}(\boldsymbol{d}_z)(-1)^{n-m},$$

$$\sum_{n'} \hat{T}_{n'n''}^{mm}(-\boldsymbol{d}_z)\,\hat{T}_{nn'}^{mm}(\boldsymbol{d}_z) = \delta_{n''n} \quad \Longrightarrow \hat{T}_{nn'}^{mm}(\boldsymbol{d}_z) = (-1)^{n+n'}\hat{T}_{n'n}^{mm}(\boldsymbol{d}_z). \tag{162}$$

Hence, evaluation of $\hat{T}_{nn'}^{mm}(\boldsymbol{d}_z)$ by recurrence relations is only required for $0 \le m$ and $0 \le n' \le n$ while other values are defined by Eqs. (161) (162).

The recurrence relations in the first and third line of Eq. (151) for $m' = m+1$ and $m' = m$ remain :

$$\begin{pmatrix} \hat{T}_{n',n+1}^{m+1,m+1}(\boldsymbol{d}_z) \\ \hat{T}_{n',n+1}^{mm}(\boldsymbol{d}_z) \end{pmatrix} = \begin{pmatrix} \frac{1}{b_{n+1}^{-m-1}}\left[-b_{n'+1}^m\hat{T}_{n'+1,n}^{mm}(\boldsymbol{d}_z) + b_{n'}^{-m-1}\hat{T}_{n'-1,n}^{mm}(\boldsymbol{d}_z) + b_n^m\hat{T}_{n',n-1}^{m+1,m+1}(\boldsymbol{d}_z)\right] \\ \frac{1}{a_n^m}\left[-a_{n'}^m\hat{T}_{n'+1,n}^{mm}(\boldsymbol{d}_z) + a_{n'-1}^m\hat{T}_{n'-1,n}^{mm}(\boldsymbol{d}_z) + a_{n-1}^m\hat{T}_{n',n-1}^{mm}(\boldsymbol{d}_z)\right] \end{pmatrix}. \tag{163}$$

Note that the start values for $T^{mm}_{n'0}(\boldsymbol{d}_z)$ are known. It is important to know that both recurrence relations must be evaluated at $n' = 0$ for $n \geq 1$ at the start of the recurrence, at which the expression $T^{mm}_{n'-1,n}(\boldsymbol{d}_z)$ vanishes. The second relation allows progression in n, and the first relation progresses in m.

Initial values for z-displacement. The Green's function located at the origin $\boldsymbol{r} = \boldsymbol{0}$ correspond to zero-order base functions

$$G(\boldsymbol{r}) = \frac{-ik}{\sqrt{4\pi}} \sqrt{\frac{1}{4\pi}} \frac{\mathrm{e}^{-\mathrm{i}kr}}{-kr} = \frac{-ik}{\sqrt{4\pi}}\, S_0^0(\boldsymbol{r}), \tag{164}$$

$$G_R(\boldsymbol{r}) = \frac{k}{\sqrt{4\pi}} \sqrt{\frac{1}{4\pi}} \frac{-\sin(kr')}{-kr} = \frac{-k}{\sqrt{4\pi}}\, R_0^0(\boldsymbol{r}). \tag{165}$$

The coordinate transform for translation is expressed by $\boldsymbol{r}' = \boldsymbol{r} + \boldsymbol{d}$ without rotation $\boldsymbol{Q} = \boldsymbol{I}$. Referring to Eqs. (85)(87) in Sec. 2.4.2, the representation of the Green's functions at the coordinates $\boldsymbol{d}$ expresses a basic form of translation and yield a scalar value:

$$G(\boldsymbol{r})\, \boldsymbol{I} = \sum_{n'=0}^{\infty} \sum_{m'=-n'}^{n'} \begin{cases} -ik\, \hat{\boldsymbol{S}}^{-m'}_{n'}(\boldsymbol{d})\, \hat{\boldsymbol{R}}^{m'}_{n'}(\boldsymbol{r}'), & \text{for } r' < d, \\ -ik\, \hat{\boldsymbol{R}}^{-m'}_{n'}(\boldsymbol{d})\, \hat{\boldsymbol{S}}^{m'}_{n'}(\boldsymbol{r}'), & \text{for } r' > d, \end{cases}$$

$$G_R(\boldsymbol{r})\, \boldsymbol{I} = \sum_{n'=0}^{\infty} \sum_{m'=-n'}^{n'} -k\, \hat{\boldsymbol{R}}^{-m'}_{n'}(\boldsymbol{d})\, \hat{\boldsymbol{R}}^{m'}_{n'}(\boldsymbol{r}').$$

Note that for $m = 0$, only the cosine component is non-zero, i.e. stays scalar-valued. As a consequence of

$$S_0^0(\boldsymbol{r}) = \frac{\sqrt{4\pi}}{-ik} G(\boldsymbol{r}), \text{ and } R_0^0(\boldsymbol{r}) = \frac{\sqrt{4\pi}}{-k} G_R(\boldsymbol{r}),$$

the coefficients $\hat{T}^{mm}_{n'n}(\boldsymbol{d}_z)$ for displacements in z can be directly read from the above equations using $n = m = 0$:

$$\hat{T}^{00}_{n'0}(\boldsymbol{d}_z)\, \boldsymbol{I} = \sqrt{2n'+1} \begin{cases} h^{(2)}_n(k\, d_z), & \text{for } \hat{\boldsymbol{S}}^0_0(\boldsymbol{r}) \leftarrow \hat{\boldsymbol{R}}^0_{n'}(\boldsymbol{r}'), \\ & \\ j_n(k\, d_z), & \text{for } \begin{array}{r} \hat{\boldsymbol{S}}^0_0(\boldsymbol{r}) \leftarrow \hat{\boldsymbol{S}}^0_{n'}(\boldsymbol{r}'), \\ \hat{\boldsymbol{R}}^0_0(\boldsymbol{r}) \leftarrow \hat{\boldsymbol{R}}^0_{n'}(\boldsymbol{r}'). \end{array} \end{cases} . \tag{166}$$

3.1.6 Rotation Around z-Axis

In general, a rotation is always defined for a common $n = n'$. This can easily be seen by considering the orthogonality of the radial propagation terms regarding the complete base solutions. The radial propagation terms depend on the order n only, hence

$$\hat{\boldsymbol{T}}^{m'm}_{n'n}(\boldsymbol{Q}) = \hat{\boldsymbol{T}}^{m'm}_{n'n}(\boldsymbol{Q})\, \delta_{n'n}. \tag{167}$$

The (azimuthal) rotation around the z-axis is easily described using the properties of the azimuthal solutions directly. In particular, these are the *addition theorems* of the sine and cosine:

$$\hat{\boldsymbol{\Phi}}_m(\varphi' - \varphi_1) = \hat{\boldsymbol{\Phi}}_{-m}(\varphi_1)\ \hat{\boldsymbol{\Phi}}_m(\varphi'). \tag{168}$$

Defining $\varphi = \varphi' - \varphi_1$ and considering φ_1 as rotation angle, this is a transform $\boldsymbol{\Phi}_m(\varphi) = \hat{\boldsymbol{\Phi}}_{-m}(\varphi_1)\hat{\boldsymbol{\Phi}}_m(\varphi')$. The corresponding Cartesian coordinate transform equals

$$\boldsymbol{r}' = \boldsymbol{Q}_z(\varphi_1)\ \boldsymbol{r}, \tag{169}$$

$$\boldsymbol{Q}_z(\varphi_1) = \begin{pmatrix} \cos(\varphi_1) & -\sin(\varphi_1) & 0 \\ \sin(\varphi_1) & \cos(\varphi_1) & 0 \\ 0 & 0 & 1 \end{pmatrix}. \tag{170}$$

It is obvious that the transform rule $\boldsymbol{T}_{n'n}^{m'm}(\boldsymbol{Q}_z(\varphi_1))$ is described as

$$\hat{\boldsymbol{T}}_{n'n}^{m'm}\left(\boldsymbol{Q}_z(\varphi_1)\right) = \hat{\boldsymbol{\Phi}}_m(\varphi_1)\delta_{n'n}\delta_{m'm}. \tag{171}$$

Using the *addition theorem* for $\hat{\boldsymbol{\Phi}}_m(\varphi_1) = \left(\hat{\boldsymbol{\Phi}}_1(\varphi_1)\right)^m$ allows efficient computation. The transform relation yields

$$\hat{\boldsymbol{F}}_n^m(\hat{\boldsymbol{r}}) = \hat{\boldsymbol{\Phi}}_m\left(\varphi_1\right)\ \hat{\boldsymbol{F}}_n^m(\hat{\boldsymbol{r}}'). \tag{172}$$

3.1.7 Recurrence Relation for $\pi/2$-Rotation Around y

A rotation around y by $\pi/2$ is defined as

$$\boldsymbol{Q} = \begin{pmatrix} 0 & 0 & -1 \\ 0 & 1 & 0 \\ 1 & 0 & 0 \end{pmatrix} \qquad \Rightarrow \hat{\boldsymbol{Q}} = \frac{1}{2}\begin{pmatrix} \boldsymbol{I} & -\boldsymbol{I} & -\sqrt{2}\boldsymbol{I} \\ -\boldsymbol{I} & \boldsymbol{I} & -\sqrt{2}\boldsymbol{I} \\ \sqrt{2}\boldsymbol{I} & \sqrt{2}\boldsymbol{I} & \boldsymbol{0} \end{pmatrix}. \tag{173}$$

It can be seen from the recurrence relation and its initialization (see later) that this operator yields a real-valued scalar (i.e. the *Wigner-d* functions evaluated at $\pi/2$, cf. [KR03, KR08]), hence the thin letter $T_{nn}^{mm}(\boldsymbol{Q}_{y\frac{\pi}{2}})$ is sufficient for its description. It also has the following properties together with its inverse, which rotates by $-\pi/2$:

$$\hat{T}_{nn}^{m'm}(\boldsymbol{Q}_{y\frac{\pi}{2}}) = (-1)^{m+m'}\hat{T}_{nn}^{m'm}(\boldsymbol{Q}_{y\frac{\pi}{2}}^{-1}) \tag{174}$$

$$\sum_{n'} \hat{T}_{nn}^{m''m'}(\boldsymbol{Q}_{y\frac{\pi}{2}}^{-1})\ \hat{T}_{nn}^{mm'}(\boldsymbol{Q}_{y\frac{\pi}{2}}) = \delta_{m''m} \quad \Longrightarrow \hat{T}_{nn}^{mm'}(\boldsymbol{Q}_{y\frac{\pi}{2}}) = (-1)^{m+m'}\hat{T}_{nn}^{m'm}(\boldsymbol{Q}_{y\frac{\pi}{2}}). \tag{175}$$

Furthermore, the following interesting symmetry holds, which facilitates conversion to real-valued notation later

$$\begin{aligned}\hat{\boldsymbol{Y}}_n^m(\boldsymbol{Q}_{y\frac{\pi}{2}}\,\boldsymbol{\theta}) &= \hat{\boldsymbol{Y}}_n^m(\boldsymbol{Q}_{mx}\boldsymbol{Q}_{y\frac{\pi}{2}}\boldsymbol{Q}_{mz}\,\boldsymbol{\theta}),\\ T_{nn}^{m'm}(\boldsymbol{Q}_{y\frac{\pi}{2}}) &= \sum_{m_1,m_2}(-1)^m\delta_{nn}^{m_2,-m}\,T_{nn}^{m_1m_2}(\boldsymbol{Q}_{y\frac{\pi}{2}})(-1)^{n+m_1}\delta_{nn}^{m'm_1}\\ &= (-1)^{n+m+m'}\,T_{nn}^{-m',m}(\boldsymbol{Q}_{y\frac{\pi}{2}}).\end{aligned} \tag{176}$$

Therefore, only $0 \le m' \le m$ needs to be evaluated while the other values are found due to symmetry. As there may only be coefficients combining the harmonics at the same order $\hat{T}_{n'n}^{m'm}\delta_{n'n}$, for $n = n'+1$, the recurrence relation in the first line of Eq. (151) reduces to

$$\hat{T}_{n-1,n-1}^{m',m+1}(\boldsymbol{Q}_{y\frac{\pi}{2}}) = \frac{1}{2\,b_n^m}\left[b_n^{m'-1}\,\hat{T}_{nn}^{m'-1,m}(\boldsymbol{Q}_{y\frac{\pi}{2}}) - b_n^{-m'-1}\,\hat{T}_{nn}^{m'+1,m}(\boldsymbol{Q}_{y\frac{\pi}{2}}) + 2a_{n-1}^{m'}\,\hat{T}_{nn}^{m',m}(\boldsymbol{Q}_{y\frac{\pi}{2}}).\right] \tag{177}$$

Initial values of $\pi/2$-rotation around y. Axially symmetric spherical harmonics distributions are most easily expressed when the rotation axis coincides with the z-axis. Such distributions have non-zero coefficients for $m = 0$ only. If the axial symmetry of a distribution is given rotated to any arbitrary axis, the addition theorem can be utilized to describe the equivalence to a distribution aligned with the z-axis:

$$P_n(\boldsymbol{\theta}_1^{\mathrm{T}}\boldsymbol{\theta}')\,\boldsymbol{I} = \sum_{m'=-n}^{n}\hat{\boldsymbol{Y}}_n^{-m'}(\boldsymbol{\theta}_1)\,\hat{\boldsymbol{Y}}_n^{m'}(\boldsymbol{\theta}'). \tag{178}$$

This corresponds to

$$\hat{\boldsymbol{Y}}_n^0(\chi, \arccos(\boldsymbol{\theta}_1^{\mathrm{T}}\boldsymbol{\theta}')) = \sqrt{\frac{4\pi}{2n+1}}\sum_{m'=-n}^{n}\hat{\boldsymbol{Y}}_n^{-m'}(\boldsymbol{\theta}_1)\,\hat{\boldsymbol{Y}}_n^{m'}(\boldsymbol{\theta}'), \tag{179}$$

Note that the equation contains several angular differences

$$\arccos(\boldsymbol{\theta}_1^{\mathrm{T}}\boldsymbol{\theta}') = \vartheta_1 - \vartheta', \qquad \text{and } \hat{\boldsymbol{\Phi}}_{m'}^{\mathrm{T}}(\varphi_1)\,\hat{\boldsymbol{\Phi}}_{m'}(\varphi') = \cos(m(\varphi'-\varphi_1)), \tag{180}$$

and there is no dependency on χ since $m = 0$. We may regard the angles φ_1 and ϑ_1 as the orientation of the z'-axis, i.e. $\boldsymbol{\theta}_1$. Re-defining (χ, ϑ) to $\boldsymbol{\theta}$, this is simply $\hat{\boldsymbol{Y}}_n^0(\boldsymbol{\theta}) = \sqrt{\frac{4\pi}{2n+1}}\sum_{m'=-n}^{n}\hat{\boldsymbol{Y}}_n^{-m'}(\boldsymbol{\theta}_1)\,\hat{\boldsymbol{Y}}_n^{m'}(\boldsymbol{\theta}')$. Consequently, the initial values of the rotation operator $\hat{T}_{nn}^{m'm}(\boldsymbol{Q}_{y\frac{\pi}{2}})$ are

$$\hat{T}_{nn}^{m'0}(\boldsymbol{Q}_{y\frac{\pi}{2}})\,\boldsymbol{I} = \sqrt{\frac{4\pi}{2n+1}}\hat{\boldsymbol{Y}}_n^{-m'}(0,\pi/2) = \sqrt{\frac{4\pi}{2n+1}}\hat{N}_n^{|m'|}\,P_n^{|m'|}(0)\,\boldsymbol{I}. \tag{181}$$

3.1.8 Transform Relations for Spherical Base Solutions with Real-Valued Spherical Harmonics

Using the Euler identity and again $\boldsymbol{L}$ representing the imaginary constant i $= \sqrt{-1}$, the normalized real-valued base solutions

$$\boldsymbol{F}_n^m(\hat{\boldsymbol{r}}) = \begin{pmatrix} F_{n,c}^m(\hat{\boldsymbol{r}}) \\ F_{n,s}^m(\hat{\boldsymbol{r}}) \end{pmatrix} \tag{182}$$

can be easily related to their complex-valued counterpart $\hat{\boldsymbol{F}}_n^m(\hat{\boldsymbol{r}})$

$$\begin{aligned} \hat{\boldsymbol{F}}_n^m(\hat{\boldsymbol{r}}) &= \frac{1}{\sqrt{2-\delta_m}} \left[\boldsymbol{I}\ F_{n,c}^m(\hat{\boldsymbol{r}}) + \boldsymbol{L}\ F_{n,s}^m(\hat{\boldsymbol{r}}) \right] \\ \boldsymbol{F}_n^m(\hat{\boldsymbol{r}}) &= \sqrt{2-\delta_m}\, \hat{\boldsymbol{F}}_n^m(\hat{\boldsymbol{r}}) \begin{pmatrix} 1 \\ 0 \end{pmatrix}. \end{aligned} \tag{183}$$

The evaluation of the transform expressions for z-translation, z-rotation, and $y\frac{\pi}{2}$ rotation are well-described by the recurrence relations for the complex-valued case. Real-valued expressions directly follow from these relations.

Real-valued transform for z-translation. The z-translation transform preserves the orthogonality between azimuth solutions $\delta_{mm'}$ and the same re-normalization of real-valued solutions is required on both sides. So this transform is equal to the complex-valued case:

$$\boldsymbol{F}_n^m(\hat{\boldsymbol{r}}) = \sum_{n'=0}^{\infty} T_{n'n}^{mm}(\boldsymbol{d}_z)\, \boldsymbol{E}_{n'}^m(\hat{\boldsymbol{r}}'), \tag{184}$$

$$T_{n'n}^{mm}(\boldsymbol{d}_z) = \hat{T}_{n'n}^{mm}(\boldsymbol{d}_z). \tag{185}$$

Therefore, the initialization and recurrence relations for real-valued z-translation remain unchanged

$$T_{n'0}^{00}(\boldsymbol{d}_z)\ \boldsymbol{I} = \sqrt{2n'+1} \begin{cases} h_n^{(2)}(k\, d_z), & \text{for } \boldsymbol{S}_0^0(\boldsymbol{r}) \leftarrow \boldsymbol{R}_{n'}^0(\boldsymbol{r}'), \\ & \boldsymbol{S}_0^0(\boldsymbol{r}) \leftarrow \boldsymbol{S}_{n'}^0(\boldsymbol{r}'), \ , \\ j_n(k\, d_z), & \text{for } \boldsymbol{R}_0^0(\boldsymbol{r}) \leftarrow \boldsymbol{R}_{n'}^0(\boldsymbol{r}'). \end{cases}$$

$$\begin{pmatrix} T_{n',n+1}^{m+1,m+1}(\boldsymbol{d}_z) \\ T_{n',n+1}^{mm}(\boldsymbol{d}_z) \end{pmatrix} = \begin{pmatrix} \frac{1}{b_{n+1}^{-m-1}} \left[-b_{n'+1}^m T_{n'+1,n}^{mm}(\boldsymbol{d}_z) + b_{n'}^{-m-1} T_{n'-1,n}^{mm}(\boldsymbol{d}_z) + b_n^m T_{n',n-1}^{m+1,m+1}(\boldsymbol{d}_z) \right] \\ \frac{1}{a_n^m} \left[-a_{n'}^m T_{n'+1,n}^{mm}(\boldsymbol{d}_z) + a_{n'-1}^m T_{n'-1,n}^{mm}(\boldsymbol{d}_z) + a_{n-1}^m T_{n',n-1}^{mm}(\boldsymbol{d}_z) \right] \end{pmatrix},$$

$$T_{nn'}^{mm}(\boldsymbol{d}_z) = (-1)^{n+n'} T_{n'n}^{mm}(\boldsymbol{d}_z).$$

Note, again, that for $n = 0$ the $n-1$ terms on the right hand side vanish, and that the initialization has to be carried out for n up to $n = 2\mathrm{N}$ first.

Real-valued transform for z-rotation. Conveniently, the rotation around the z-axis works exactly the same way for real-valued spherical harmonics as it does for complex-valued spherical harmonics in real-valued matrix notation

$$\boldsymbol{Y}_n^m(\boldsymbol{\theta}) = \hat{\boldsymbol{\Phi}}_m(\varphi_1)\ \boldsymbol{Y}_n^m(\boldsymbol{\theta}').$$

Real-valued transform for $y\frac{\pi}{2}$ rotation. For a rotation by 90° around y, the transform differs from the complex-valued case in real-valued matrix representation. The following holds, cf. Eqs. (183)(176)

$$\begin{aligned}
\hat{\boldsymbol{Y}}_n^m(\boldsymbol{\theta}) &= \frac{1}{\sqrt{2-\delta_m}}\left[\boldsymbol{I}\ Y_{n,c}^m(\boldsymbol{\theta}) + \boldsymbol{L}\ Y_{n,s}^m(\boldsymbol{\theta})\right] = \sum_{m'=-n}^{n'} \hat{T}_{nn}^{m'm}(\boldsymbol{Q}_{y\frac{\pi}{2}})\ \hat{\boldsymbol{Y}}_n^{m'}(\boldsymbol{\theta}') \qquad (186)\\
&= \sum_{m'=0}^{n} \frac{2-\delta_{m'}}{2}\left[\hat{T}_{nn}^{m'm}(\boldsymbol{Q}_{y\frac{\pi}{2}})\ \hat{\boldsymbol{Y}}_n^{m'}(\boldsymbol{\theta}') + \hat{T}_{nn}^{-m',m}(\boldsymbol{Q}_{y\frac{\pi}{2}})\ \hat{\boldsymbol{Y}}_n^{-m'}(\boldsymbol{\theta}')\right]\\
&= \sum_{m'=0}^{n} \frac{\sqrt{2-\delta_{m'}}}{2}\Bigg[\boldsymbol{I}\left(1+(-1)^{n+m+m'}\right)\hat{T}_{nn}^{m'm}(\boldsymbol{Q}_{y\frac{\pi}{2}})Y_{n,c}^{m'}(\boldsymbol{\theta}') +\\
&\qquad\qquad \boldsymbol{L}\left(1-(-1)^{n+m+m'}\right)\hat{T}_{nn}^{m'm}(\boldsymbol{Q}_{y\frac{\pi}{2}})Y_{n,s}^{m'}(\boldsymbol{\theta}')\Bigg].
\end{aligned}$$

Consequently, the equation for the real-valued solutions reads as

$$\boldsymbol{Y}_n^m(\boldsymbol{\theta}) = \sum_{m'=0}^{n} \operatorname{diag}\left\{\begin{matrix}\delta_{(n+m+m' \mod 2)}\\ \delta_{(n+m+m'+1 \mod 2)}\end{matrix}\right\} T_{nn}^{m'm}(\boldsymbol{Q}_{y\frac{\pi}{2}})\boldsymbol{Y}_n^{m'}(\boldsymbol{\theta}'), \qquad (187)$$

$$T_{nn}^{m'm}(\boldsymbol{Q}_{y\frac{\pi}{2}}) = \sqrt{2-\delta_{m'}}\sqrt{2-\delta_m}\ \hat{T}_{nn}^{m'm}(\boldsymbol{Q}_{y\frac{\pi}{2}}). \qquad (188)$$

Re-written into real-valued notation, initialization of $T_{nn}^{m'm}\left(\boldsymbol{Q}_{y\frac{\pi}{2}}\right)$ needs to be done for $0 \le m' \le 2\mathrm{N}$ using Eq. (189), the recurrence relation for $\mathrm{N} \ge n \ge 2$, $0 \le m \le \min\{n-2, 2\mathrm{N}-n\}$, and $m+1 \le m' \le n$ using Eq. (190), and the symmetry Eq. (191) yields coefficients for $m'+1 \le m \le n$:

$$T_{nn}^{m'0}(\boldsymbol{Q}_{y\frac{\pi}{2}}) = \sqrt{\frac{4\pi}{2n+1}}N_n^{|m'|}\,P_n^{|m'|}(0), \qquad (189)$$

$$\begin{aligned}
T_{n-1,n-1}^{m',m+1}(\boldsymbol{Q}_{y\frac{\pi}{2}}) = \frac{\sqrt{2-\delta_{m+1}}}{2\ b_n^m\sqrt{2-\delta_m}}\Bigg\{\sqrt{2-\delta_{m'}}\Bigg[\frac{b_n^{m'-1}}{\sqrt{2-\delta_{m'-1}}}\,T_{nn}^{m'-1,m}(\boldsymbol{Q}_{y\frac{\pi}{2}}) \qquad (190)\\
- \frac{b_n^{-m'-1}}{\sqrt{2-\delta_{m'+1}}}\,T_{nn}^{m'+1,m}(\boldsymbol{Q}_{y\frac{\pi}{2}})\Bigg] + 2a_{n-1}^{m'}\,T_{nn}^{m',m}(\boldsymbol{Q}_{y\frac{\pi}{2}})\Bigg\},
\end{aligned}$$

$$T_{nn}^{mm'}(\boldsymbol{Q}_{y\frac{\pi}{2}}) = (-1)^{m+m'}T_{nn}^{m'm}(\boldsymbol{Q}_{y\frac{\pi}{2}}). \qquad (191)$$

3.2 Coordinate Transform Recipes

With the given recurrence schemes, a full transform of coordinates $\boldsymbol{r} = \boldsymbol{Q}\,\boldsymbol{r}' + \boldsymbol{d}$ is decomposed into the following steps, symbolically

$$\boldsymbol{E}(\boldsymbol{r}) = \boldsymbol{T}(\boldsymbol{Q}_2)\,\boldsymbol{T}(d_z)\,\boldsymbol{T}(\boldsymbol{Q}_1)\;\boldsymbol{F}(\boldsymbol{r}'), \tag{192}$$

with d_z representing translation into the z-axis and $\boldsymbol{Q}$ rotations of the coordinate system. Rotation itself is further decomposed into fixed rotations around y and variable rotations around z

$$\boldsymbol{T}(\boldsymbol{Q}) = \boldsymbol{T}(\boldsymbol{Q}_z)\,\boldsymbol{T}_{\boldsymbol{Q}_{y\frac{\pi}{2}}}\,\boldsymbol{T}(\boldsymbol{Q}_z)\,\boldsymbol{T}_{\boldsymbol{Q}_{y\frac{\pi}{2}}}\,\boldsymbol{T}(\boldsymbol{Q}_z). \tag{193}$$

The calculation of the $\boldsymbol{T}(d_z)$ matrices is depicted in Fig. 11 and makes use of Eqs. (166), (163), (162).

Rotation around z is described in Eq. (172).

Fig. 12 shows the scheme to compute coefficients $\boldsymbol{T}_{\boldsymbol{Q}_{y\frac{\pi}{2}}}$ using Eqs. (189), (190), (191), and how they apply to sine- and cosine-dependent spherical harmonics, cf. Eq. (187).

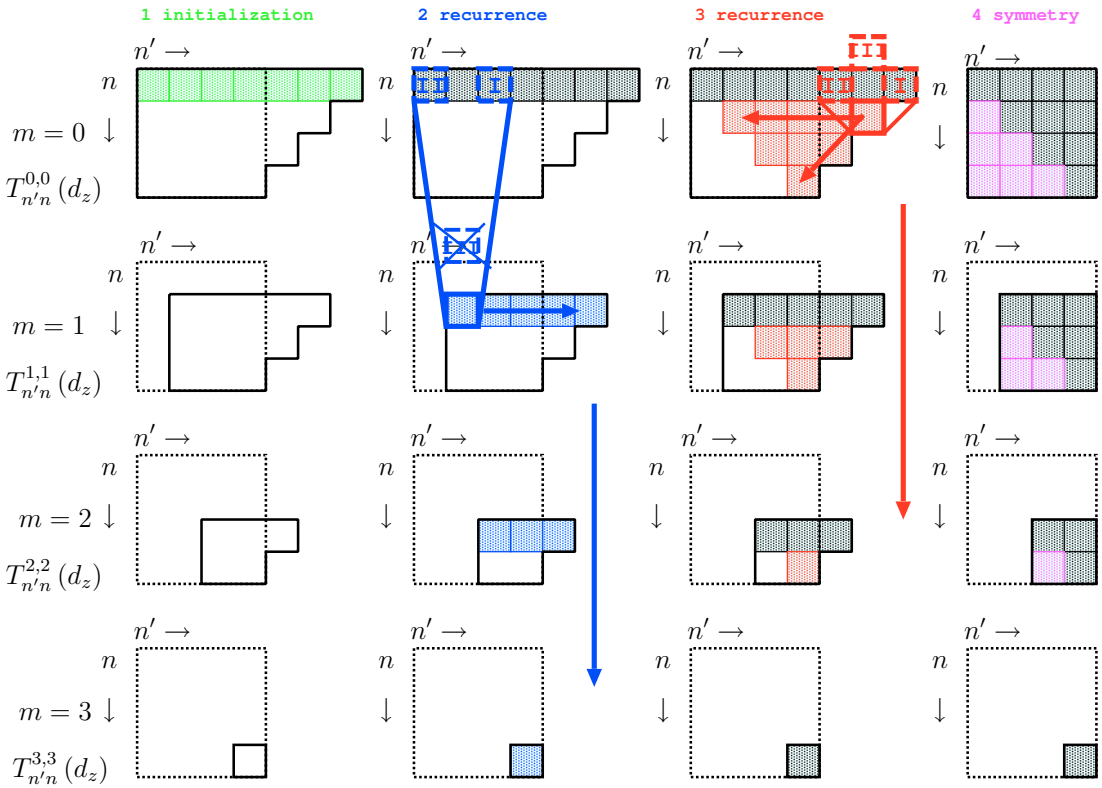

Figure 11: Scheme for computation of the $T^{mm}_{n'n}(d_z)$ transform coefficients for N = 3 using the initialization Eq. (166), recurrence Eq. (163), and symmetry Eq. (162)

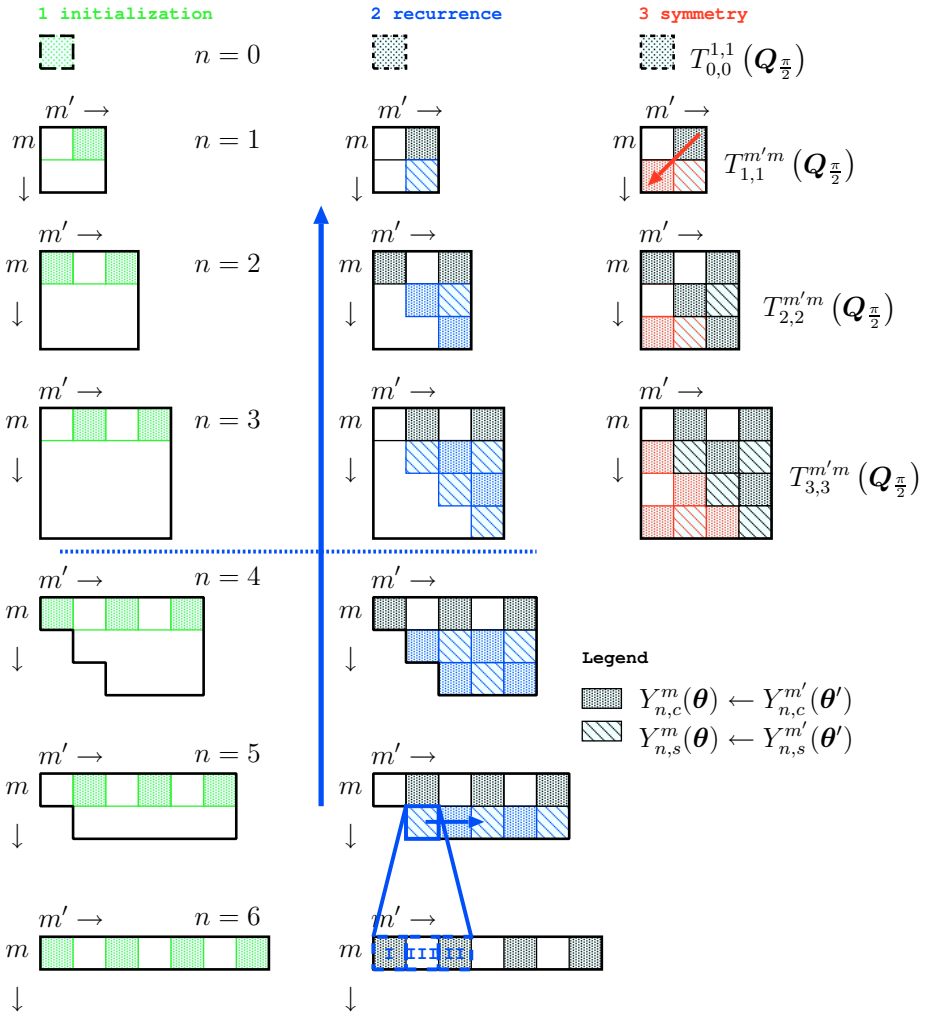

Figure 12: Scheme for computation of the $T^{m'm}_{nn}(\boldsymbol{Q}_{y\frac{\pi}{2}})$ transform coefficients for N = 3 using the initialization Eq. (189), recurrence Eq. (190), symmetry Eq. (191), and exclusive application to sine or cosine Eq. (187).

3.3 Other Manipulations of Spherical Base Solutions

Aside from coordinate transforms, many other ways of manipulating the spherical base-solutions are interesting in terms of sound-radiation. Above all, rotational matching and the manipulation of angular data is interesting for sound-radiation analysis and synthesis.

3.3.1 Spherical Correlation

Rotational matching of angular data is the key to similarity detection of radiation data on the sphere. However, the result of spherical correlation is not defined on the sphere S^2 anymore, but on SO(3), a hyperspherical space with 3 angles, i.e. the 3 rotational degrees of freedom. Spherical correlation $c(\alpha, \beta, \gamma)$ takes one of both input functions $g(\boldsymbol{\theta})$, $a(\boldsymbol{\theta})$, rotates it by the 3 variable rotation angles, and integrates it over the other function, see [DH94] and [KR08]

$$
\begin{aligned}
c(\alpha,\beta,\gamma) &= \int_{\mathbb{S}^2} g(\boldsymbol{\theta})\; a(\boldsymbol{Q}^{-1}(\alpha,\beta,\gamma)\;\boldsymbol{\theta})\; d\boldsymbol{\theta}, \qquad (194)\\
&= \sum_{n,m}\sum_{n',m'} g_{nm}\; a_{n'm'} \sum_{m''=-n'}^{n'} T_{n'}^{m''m'}(-\gamma,-\beta,-\alpha) \underbrace{\int_{\mathbb{S}^2} Y_n^m(\boldsymbol{\theta})\, Y_{n'}^{m''}(\boldsymbol{\theta})\; d\boldsymbol{\theta}}_{=\delta_{mm''}\delta_{nn''}},\\
&= \sum_{n=0}^{\infty}\sum_{m=-n}^{n}\sum_{m'=-n}^{n} g_{nm}\; a_{nm'}\; T_n^{mm'}(-\gamma,-\beta,-\alpha).
\end{aligned}
$$

Rotational matching can be done by finding three rotation angles (α, β, γ) that maximize $c(\alpha, \beta, \gamma)$.

3.3.2 Spherical Convolution (and its Relation to Circular Convolution)

Filtering operations of angular data on the sphere are performed using spherical convolution. The output must yield a result that is defined on the S^2-sphere in order to work. One of the input functions of this operation, $a(\boldsymbol{\theta})$, serves as a convolution kernel. The convolution operation integrates the inversely rotated function $a(\boldsymbol{\theta})$ over the input function $g(\boldsymbol{\theta})$ evaluated at the rotated z-axis unit vector, with both rotations using all 3 rotation angles of the integration variable. Due to its definition, the spherical harmonics coefficients of the kernel with $m \neq 0$ are omitted as they yield zero after integration around α. According Driscoll and

Healy [DH94], the definition of spherical convolution is

$$
\begin{aligned}
c(\boldsymbol{\theta}) &= \int_{SO(3)} g(\boldsymbol{Q}(\alpha,\beta,\gamma)\begin{pmatrix}0\\0\\1\end{pmatrix})\; a(\boldsymbol{Q}^{-1}(\alpha,\beta,\gamma)\;\boldsymbol{\theta})\; d\alpha\, d\beta\, d\gamma. \qquad (195)\\
&= \sum_{n,m}\sum_{n',m'} g_{nm}\, a_{n'm'} \underbrace{\int_{SO(3)} Y_n^m(\alpha,\beta) Y_{n'}^{m'}(\boldsymbol{Q}^{-1}(\alpha,\beta,\gamma)\;\boldsymbol{\theta}) d\alpha d\beta d\gamma}_{=\delta_{m'0}\delta_{nn'} Y_n^m(\boldsymbol{\theta})}\\
&= \sum_{n=0}^{\infty}\sum_{m=-n}^{n} g_{nm}\; a_{n,0}\; Y_n^m(\boldsymbol{\theta}).
\end{aligned}
$$

Note that also the truncation of the spherical harmonics to a maximum order $n \leq$ N can also be understood in terms of convolution. Such a truncation corresponds to an angular band limitation, i.e., a limitation of the resolution by convolution.

In order to characterize the properties of a given convolution integral, it is sufficient to regard the spectral convolution kernel a_n that can be expanded to the angular space by a series of Legendre-polynomials $P_n(\cos(\vartheta))$. To observe and modify the shape of a_n in the angular space, the equivalence between Legendre and Chebyshev polynomials is practical. In particular, Chebyshev polynomials (of the first kind) are the even-symmetric circular harmonics, i.e. cosine harmonics. As convolution in circular harmonics is better understood by most engineers, it is convenient to find the equivalent expression of the kernel in this domain.

Relation between Legendre and Chebyshev polynomials. The Legendre polynomials $P_n(\mu)$ and the Chebyshev polynomials $T_m(\mu)$ of the first kind follow the recurrence relations:

$$
\begin{aligned}
P_0(\mu) &= 1 && (196)\\
P_1(\mu) &= \mu && (197)\\
P_n(\mu) &= \frac{2n-1}{n}\mu P_{n-1}(\mu) - \frac{n-1}{n} P_{n-2}(\mu) \qquad \forall n \in \mathbb{N}_0 : n \geq 3, && (198)\\
T_0(\mu) &= 1 && (199)\\
T_1(\mu) &= \mu && (200)\\
T_m(\mu) &= 2\,\mu\, T_{m-1}(\mu) - T_{m-2}(\mu) \qquad \forall m \in \mathbb{N}_0 : m \geq 3. && (201)
\end{aligned}
$$

The Chebyshev polynomials are even-symmetric circular harmonics:

$$
T_m(\cos(\alpha)) \;=\; \cos(m\,\alpha). \qquad (202)
$$

Therefore using $\mu = \cos(\alpha)$, the expansion into Chebyshev polynomials is a cosine transform, i.e. the Chebyshev transform. Both the Legendre and Chebyshev polynomials are orthogonal polynomials in the range $-1 \leq \mu \leq 1$. As all polynomials

only contain powers μ^k up to $k \leq n$ or $k \leq m$, the two representations must be equivalent. This equivalence can be easily expressed in matrix notation with the polynomial coefficients $t_{m,k}$ and $p_{n,k}$ weighted by the powers μ^k and the expansion coefficients $c_t[m]$ and $c_p[n]$. We equate both representations

$$\begin{pmatrix} \mu^0, & \mu^1, & \mu^3, & \dots \end{pmatrix} \boldsymbol{P}\, \boldsymbol{c}_p \stackrel{!}{=} \begin{pmatrix} \mu^0, & \mu^1, & \mu^3, & \dots \end{pmatrix} \boldsymbol{T}\, \boldsymbol{c}_t \tag{203}$$

$$\boldsymbol{P} = \begin{pmatrix} p_{0,0}, & 0, & p_{2,0}, & 0, & p_{4,0} & \dots \\ 0, & p_{1,1}, & 0, & p_{3,1}, & 0, & \dots \\ \vdots, & 0, & p_{2,2}, & 0, & p_{4,2} & \dots \\ \vdots, & \vdots, & 0, & p_{3,3}, & 0, & \dots \\ \vdots, & \vdots, & \vdots, & 0, & p_{4,4}, & \dots \\ \vdots, & \vdots, & \vdots, & \vdots, & \ddots, & \ddots \end{pmatrix}, \boldsymbol{T} = \begin{pmatrix} t_{0,0}, & 0, & t_{2,0}, & 0, & t_{4,0} & \dots \\ 0, & t_{1,1}, & 0, & t_{3,1}, & 0, & \dots \\ \vdots, & 0, & t_{2,2}, & 0, & t_{4,2} & \dots \\ \vdots, & \vdots, & 0, & t_{3,3}, & 0, & \dots \\ \vdots, & \vdots, & \vdots, & 0, & t_{4,4}, & \dots \\ \vdots, & \vdots, & \vdots, & \vdots, & \ddots, & \ddots \end{pmatrix} \tag{204}$$

The conversion follows by inversion after omitting the powers of μ in Eq. (203)

$$\boldsymbol{T}\, \boldsymbol{c}_t = \boldsymbol{P}\, \underbrace{\boldsymbol{P}^{-1}\boldsymbol{T}}_{:=\boldsymbol{W}}\, \boldsymbol{c}_t, \tag{205}$$

$$\boldsymbol{c}_p = \boldsymbol{W}\, \boldsymbol{c}_t. \tag{206}$$

Instead of computing the polynomial coefficients and matrix inversion, the conversion can be defined in terms of the recurrence relations:

$$(1-\mu^2)\frac{\partial}{\partial \mu} P_n(\mu) = \frac{n(n+1)}{2n+1}\, \left[P_{n-1}(\mu) - P_{n+1}(\mu)\right], \tag{207}$$

$$(1-\mu^2)\frac{\partial}{\partial \mu} T_m(\mu) = \frac{m}{2}\, \left[T_{m-1}(\mu) - T_{m+1}(\mu)\right]. \tag{208}$$

The transform relation W_{nm} must also hold after taking the derivative:

$$\sum_{n=0}^{n} W_{nm} P_n\left(\mu\right) = T_m\left(\mu\right), \tag{209}$$

$$\sum_{n=0}^{n} W_{nm} \frac{\partial}{\partial \mu} P_n\left(\mu\right) = \frac{\partial}{\partial \mu} T_m\left(\mu\right). \tag{210}$$

Insertion of the recurrence relations divided by $(1-\mu^2)$ yields:

$$\sum_{n'} W_{n'm} \frac{n'(n'+1)}{2n'+1} \left[P_{n'-1}(\mu) - P_{n'+1}(\mu)\right] = \frac{m}{2} \left[T_{m-1}(\mu) - T_{m+1}(\mu)\right], \tag{211}$$

The remaining Chebyshev polynomials are expanded into Legendre polynomials:

$$\sum_{n'} W_{n'm} \frac{n'(n'+1)}{2n'+1} \left[P_{n'-1}(\mu) - P_{n'+1}(\mu)\right] = \frac{m}{2} \sum_{n''} \left[W_{n'',m-1} P_{n''}(\mu) - W_{n'',m+1} P_{n''}(\mu)\right]. \tag{212}$$

Exploiting the orthogonality relation $\int_{-1}^{1} P_{n'}(\mu)P_n(\mu)d\mu = \alpha\delta_{n'n}$, this results after division by the scale factor α:

$$\frac{(n+1)(n+2)}{2n+3}W_{n+1,m} - \frac{n(n-1)}{2n-1}W_{n-1,m} = \frac{m}{2}\left[W_{n,m-1} - W_{n,m+1}\right]. \qquad (213)$$

We know the start values $W_{00} = W_{11} = 1$ and $W_{10} = W_{01} = 0$. In order to apply the recurrence, it is useful to set $m = n + 2l - 1$ with $l \in \mathbb{N}_0$:

$$W_{n,n+2l} = \tfrac{2}{n+2l-1}\left[-\tfrac{(n+1)(n+2)}{2n+3}W_{n+1,n+2l-1} + \tfrac{n(n-1)}{2n-1}W_{n-1,n+2l-1}\right] + W_{n,n+2l-2} \qquad (214)$$

as expressions in this relation vanish at given indices, i.e. $W_{nm} = 0$ for $n > m$, $m < 0$, $n < 0$, or $\mod(n,2) \neq \mod(m,2)$.

The derivation of the inverse transform $\tilde{W}_{mn}$ yields equivalent solutions, using $\tilde{W}_{00} = \tilde{W}_{11} = 1$, $\tilde{W}_{10} = \tilde{W}_{01} = 0$, $m = n + 2l - 1$, and $W_{mn} = 0$ for $m > n$, $n < 0$, $m < 0$, or $\mod(m,2) \neq \mod(n,2)$:

$$\tilde{W}_{m,m+2l} = \tfrac{2(m+2l)-1}{2(m+2l-1)(m+2l)}\left[(m-1)\tilde{W}_{m-1,m+2l-1} - (m+1)\tilde{W}_{m+1,m+2l-1}\right] + \tilde{W}_{m,m+2l-2}. \qquad (215)$$

Conversion between Legendre / Chebyshev coefficients. The above relations are especially useful since the properties of the symmetric *window functions* well-known from signal processing [OSB99] can be directly exploited to describe the spatial characteristics of *spherical filters* and vice versa:

$$c_n^{(p)} = \sum_{m=0}^{\mathrm{M}} W_{nm}\, c_m^{(t)}, \qquad\qquad c_m^{(t)} = \sum_{n=0}^{\mathrm{N}} \tilde{W}_{mn}\, c_n^{(p)}, \qquad (216)$$

using the recurrences Eq. (214) and Eq. (215) that are illustrated in Fig. 13. For spherical filters see also [Dan01, p. 184, 186][Boy00, p. 421].

Fig. 14 shows known window functions in their Legendre-representation. Fig. 15 illustrates what happens when directly using the *window functions* as *spherical filters* without conversion. Note that the orthonormalization has to be taken care of separately; it is excluded from the above equations.

Angular resolution of N-truncated spherical harmonics (and circular harmonics). The maximum resolution of the spherical harmonics can be expressed in terms of a rotationally symmetric, band-limited beam. This is quite similar to the description in Rafaely [Raf04] and Poletti [Pol05], but explicit approximations for different definitions of the resolution are given here for the orders of truncation $2 \leq \mathrm{N} \leq 15$. Its transform coefficients γ_n can be found by transforming $g(\mu) = \delta(1-\mu)$, a beam pointing towards $\mu = \cos(\vartheta) \stackrel{!}{=} 1$, into spherical

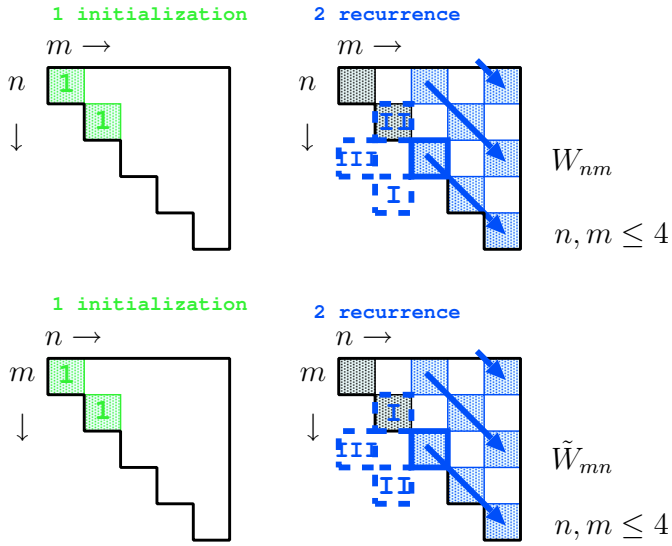

Figure 13: Recurrences for conversion between Legendre and Chebyshev coefficients, according to Eq. (214), and Eq. (215).

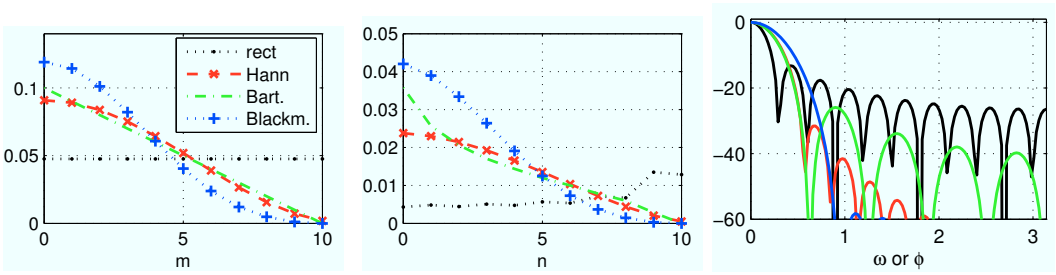

(a) Nrmlzd. Chebyshev coeffs. (b) Nrmlzd. Legendre coeffs. (c) Beam characteristics.

Figure 14: For the manipulation of spherical beam characteristics (main/side lobes), conversion of known window functions from the domain of Chebyshev polynomials into the Legendre polynomial domain is helpful. a) shows the series of normalized Chebyshev coefficients, b) the normalized Legendre coefficients, and c) the resulting beam characteristics.

harmonics. Its expansion truncated to $n \leq \mathrm{N}$ and normalized to 1 corresponds to

$$\gamma_n = 2\pi \int_{-1}^{1} N_n P_n(\mu)\delta(1-\mu)\,d\mu = 2\sqrt{(2n+1)\pi}, \tag{217}$$

$$g_{\mathrm{sph}}(\cos(\vartheta)) = \frac{1}{(\mathrm{N}+1)^2}\sum_{n=0}^{\mathrm{N}} \gamma_n N_n P_n(\cos(\vartheta)) = \sum_{n=0}^{\mathrm{N}} \frac{2n+1}{(\mathrm{N}+1)^2} P_n(\cos(\vartheta)). \tag{218}$$

The main lobe width can be referred to as the -3dB, -6dB or $-\infty$dB width of this function. Fig. 16 and Table 1 shows the spherical beam width compared with an even symmetric circular beam width (or DTFT main lobe):

$$g_{\mathrm{circ}}(\cos(\varphi)) = \frac{1}{2\mathrm{N}+1}\sum_{m=0}^{\mathrm{N}} (2-\delta_m)\cos(m\varphi) = \frac{\sin\left[(\mathrm{N}+0.5)\,\varphi\right]}{(2\mathrm{N}+1)\sin(\varphi/2)}. \tag{219}$$

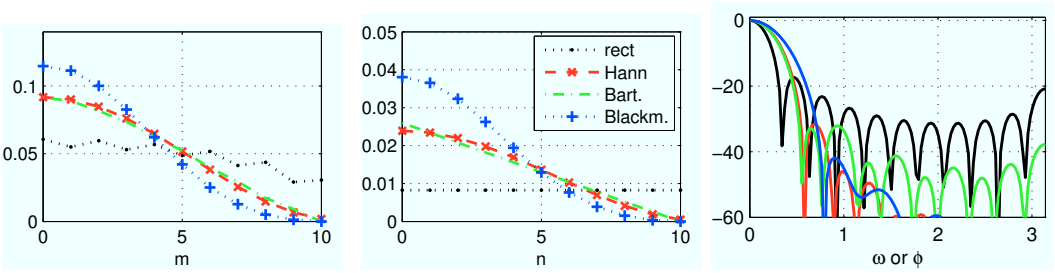

(a) Nrmlzd. Chebyshev coeffs. (b) Nrmlzd. Legendre coeffs. (c) Beam characteristics.

Figure 15: It is informative to utilize the window sequences in the Legendre domain. Choosing rectangular, Hann, Bartlett and Blackman windows for the normalized Legendre coefficients b), the expansion yields c). Equal results are obtained using the normalized Chebyshev coefficients in a). c) differs from Fig. 14 c).

	spherical beam			circular beam		
	-3dB	-6dB	-∞dB	-3dB	-6dB	-∞dB
$\angle$	$\approx \frac{187}{N+1}^\circ$	$\approx \frac{256}{N+1}^\circ$	$\approx \frac{439}{N+1}^\circ$	$\approx \frac{160}{N+0.5}^\circ$	$\approx \frac{218}{N+0.5}^\circ$	$= \frac{360}{N+0.5}^\circ$
ϵ	N = 2					
	-2.59°	-3.05°	$+0.06^\circ$	-0.92°	-1.05°	0°
	N = 5					
	-0.05°	-0.06°	$+0.00^\circ$	-0.01°	-0.01°	0°
	N = 15					
	$+0.11^\circ$	$+0.13^\circ$	$+0.00^\circ$	$+0.03^\circ$	$+0.03^\circ$	0°

Table 1: Approximation $\angle$ and approximation errors ϵ for main lobe widths of truncated spherical and circular harmonics.

Radial region of convergence for N-truncated shifted point-source. Fig. 17 illustrates the bounded radial region of convergence that is inherent to truncated-order decompositions into spherical base-solutions. As a rule-of-thumb, a diameter ϕ can be given in wave-lengths as to bound this region

$$\frac{\phi}{\lambda} \leq \frac{N}{\pi} \approx \frac{N}{3}. \tag{220}$$

Roughly speaking, this relation is responsible for the *sweet-spot* in Ambisonics and characterizes the maximum alias-free diameter of compact spherical loudspeaker arrays, cf. [WA01, ZPF09, ZSH07]. In terms of musical instrument recording, this diameter roughly limits the diameter, within which the instrument should be carefully centered, i.e. the *centering problem* cf. 5.1.5.

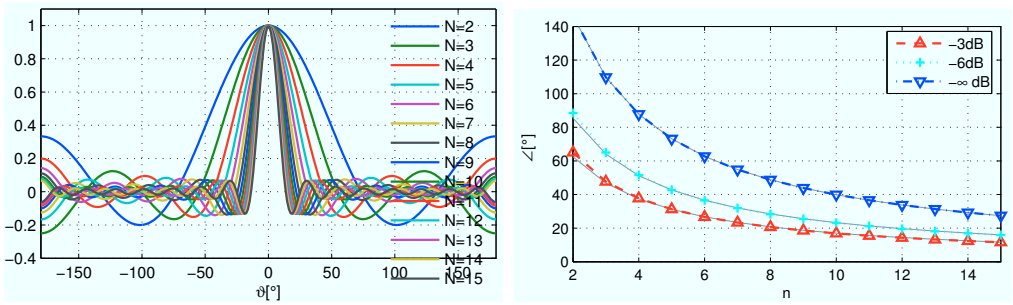

(a) Characteristics of band-limited spherical beams and their main lobe width.

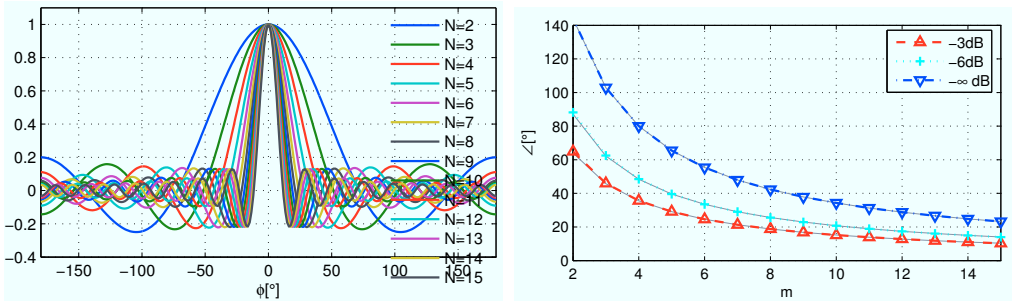

(b) Characteristics of band-limited circular beams (or DTFT) and their main lobe width.

Figure 16: Illustration of band-limited spherical and circular beam-widths.

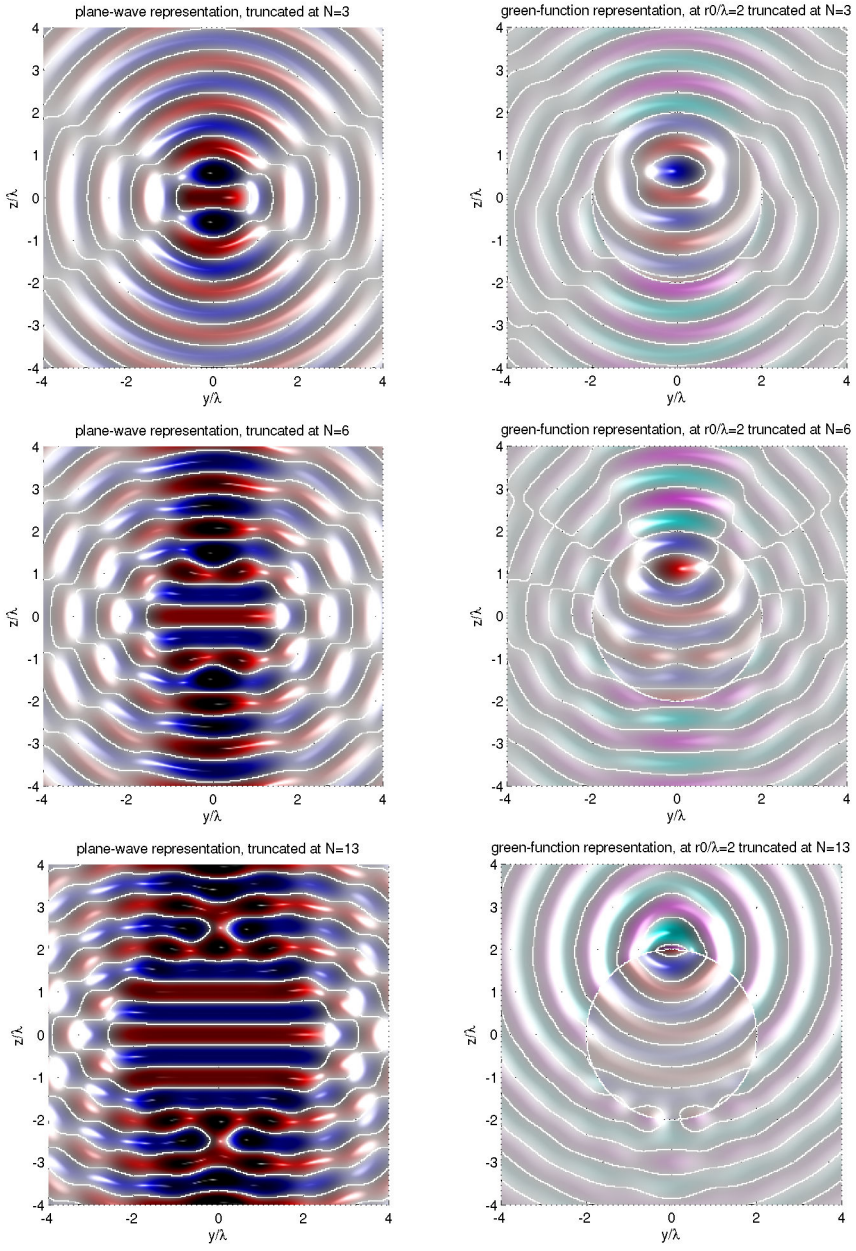

Figure 17: Plane-wave and Green's function (at $\theta_0 = 0$, $r_0/\lambda = 2$) representation using truncated-order spherical base-solutions for different truncation numbers N. The radial region of convergence $r/\lambda \leq \mathrm{N}/6$ becomes obvious.

3.3.3 Spherical Multiplication

The operation of multiplying two functions $g(\boldsymbol{\theta})$ and $a(\boldsymbol{\theta})$ on the sphere can also be performed in their spherical harmonics decomposition. The resulting coefficients c_{nm} are linear combinations of the products $g_{n_1,m_1}\, a_{n_2,m_2}$. The linear factors describing these linear combinations are called Gaunt coefficients $C^{m_1,m_2,m}_{n_1,n_2,n}$, cf. [DH94]

$$c(\boldsymbol{\theta}) = g(\boldsymbol{\theta})\, a(\boldsymbol{\theta}), \tag{221}$$

$$\xrightarrow{\mathcal{SHT}} \quad c_{nm} = \sum_{n_1,m_1,n_2,m_2} C^{m_1,m_2,m}_{n_1,n_2,n}\; g_{n_1,m_1}\, a_{n_2,m_2}. \tag{222}$$

The computational effort to evaluate the Gaunt coefficient is unfortunately high. There are some resources dealing with a faster evaluation that use tensor calculus. Usually, Gaunt coefficients are given for complex-valued spherical harmonics. For more information regarding efficient evaluation of the Gaunt coefficients, the interested reader is referred to [Xu96, Séb98, PH07a].

Spherical multiplication is especially interesting to describe degeneracy of the orthogonality relation for incompletely sampled spheres, on which a sampling density function a_{nm} is available [PPS01], i.e. $D^{m_1,m}_{n_1,n} = \sum_{n_2,m_2} C^{m_1,m_2,m}_{n_1,n_2,n}\, a_{n_2,m_2}$.

Moreover, the angular impedance problem given above can only be solved using Gaunt coefficients. Furthermore, it can be interesting to apply *angular windows* to given angular functions, in order to emphasize or attenuate particular angular domains. However, this might mainly yield high-order decompositions. Alternatively, the approach in [PZ09] could be employed for spherical windowing using limited orders.

An unresolved question closely related to the Gaunt coefficients is: *Is there a (unique) minimum phase on the sphere?*. This minimum phase should be defined such that the coefficient used to create an angular magnitude pattern can be resolved at lowest orders $n \to 0$. As any pattern can be decomposed of a magnitude multiplied by a complex-valued phase (or real-valued sign), one way to solve the question could utilize the Gaunt-coefficients.

Chapter IV

DISCRETE SPHERICAL HARMONICS TRANSFORM

Many scientific disciplines use the discrete Fourier-transform (DFT) for the analysis or interpolation of discrete samples of data in time, space, or frequency. In this chapter, the DFT on the sphere, the discrete spherical harmonics transform (DSHT), is of particular interest. DSHT allows to obtain *spherical wave-spectra* from the data of an array of sensors (microphones), arranged on a spherical surface. Usually two preconditions are assumed for the calculation of the *spherical wave-spectrum*

- the angular sampling must be suitable to calculate a DSHT
- the data must be angularly band-limited to the maximum order of the DSHT

This chapter provides an overview over a variety of ways to sample the sphere and of actually calculating the DSHT as found in literature. The properties and restrictions for the different DSHT methods are explained. The chapter concludes with a novel comparison of efficiency and angular aliasing properties of different sampling schemes, parts of which have been briefly introduced in [Zot09].

4.1 Matrix/Vector Notation (Spherical Wave Spectrum)

As defined in Chap. 2, the *spherical wave spectrum* can be very useful when describing problems in spherical coordinates. We introduce a vector/matrix notation for the spherical harmonics in order to simplify our computation and the subsequent descriptions of the DSHT. For this purpose, a linear indexing scheme can be introduced, using finite sums:

$$q = \sum_{m'=-n}^{m} 1 + \sum_{n'=0}^{n-1} \sum_{m'=-n'}^{n'} 1 = (n+1) + m + (n)^2 = n^2 + n + m + 1. \qquad (223)$$

Assume a spherical harmonics coefficients b_{nm}. We use the q to index $b_q = b_{nm}$ linearly. It is then simple to define a vector $\boldsymbol{b}_{\mathrm{N}} = \mathrm{vec}\left\{b_q\right\} = \mathrm{vec}_{\mathrm{N}}\left\{b_{nm}\right\}$ containing

all coefficients for $0 \leq n \leq \mathrm{N}$:

$$\boldsymbol{b}_{\mathrm{N}} = \mathrm{vec}\left\{b_q\right\} = \begin{pmatrix} b_1 \\ b_2 \\ \vdots \\ b_{(\mathrm{N}+1)^2} \end{pmatrix} = \mathrm{vec}_{\mathrm{N}}\left\{b_{nm}\right\} := \begin{pmatrix} b_{0,\,0} \\ b_{1,-1} \\ \vdots \\ \left.\begin{matrix} b_{n,-n} \\ \vdots \\ b_{n,n} \end{matrix}\right\} 2n+1 \\ \vdots \\ b_{\mathrm{N,N}} \end{pmatrix}. \tag{224}$$

If the expansion b_n is independent of m, the following can be used:

$$\boldsymbol{b}_{\mathrm{N}} = \mathrm{vec}_{\mathrm{N}}\left\{b_n\right\} = \begin{pmatrix} b_0 \\ b_1 \\ \vdots \\ \left.\begin{matrix} b_n \\ \vdots \\ b_n \end{matrix}\right\} 2n+1 \\ \vdots \\ b_{\mathrm{N}} \end{pmatrix}.$$

Similarly, we define a spherical harmonics diagonal matrix as:

$$\mathrm{diag}_{\mathrm{N}}\left\{b_{nm}\right\} = \mathrm{diag}\left\{\boldsymbol{b}_{\mathrm{N}}\right\} = \begin{pmatrix} b_{0,\,0} & 0, & 0 & 0 & \dots & 0 \\ 0 & b_{1,-1} & 0 & 0 & \dots & 0 \\ 0 & 0 & b_{1,\,0} & 0 & \dots & 0 \\ 0 & 0 & 0 & b_{1,\,1} & \ddots & 0 \\ \vdots & \vdots & \vdots & \ddots & \ddots & \vdots \\ 0 & 0 & 0 & 0 & \dots & b_{\mathrm{N,N}} \end{pmatrix}. \tag{225}$$

For the sound pressure and the sound-particle velocity, the notation of the *spherical wave spectrum* becomes compact:

$$\boldsymbol{\psi}_{\mathrm{N}}\left(kr\right) = \quad \mathrm{diag}_{\mathrm{N}}\left\{j_n\left(kr\right)\right\}\ \boldsymbol{b}_{\mathrm{N}} \ + \quad \mathrm{diag}_{\mathrm{N}}\left\{h_n^{(2)}\left(kr\right)\right\}\ \boldsymbol{c}_{\mathrm{N}} \tag{226}$$

$$\boldsymbol{\nu}_{\mathrm{N}}\left(kr\right) = \mathrm{diag}_{\mathrm{N}}\left\{\frac{\mathrm{i}\ j_n'\left(kr\right)}{\rho_0 c}\right\}\ \boldsymbol{b}_{\mathrm{N}} \ + \mathrm{diag}_{\mathrm{N}}\left\{\frac{\mathrm{i}\ h_n'^{(2)}\left(kr\right)}{\rho_0 c}\right\}\ \boldsymbol{c}_{\mathrm{N}}. \tag{227}$$

Matrices consist of a collection of vectors $\boldsymbol{b}_{\mathrm{N}}^{(l)}$ in the shape

$$\begin{aligned} \boldsymbol{B}_{\mathrm{N}} &= \mathrm{mtx}\left\{\boldsymbol{b}_{\mathrm{N}}^{(l)}\right\} = \mathrm{mtx}_{\mathrm{N}}\left\{b_{nm}^{(l)}\right\}, \\ &= \left(\boldsymbol{b}_{\mathrm{N}}^{(1)},\ \ \dots,\ \ \boldsymbol{b}_{\mathrm{N}}^{(\mathrm{L})}\right). \end{aligned} \tag{228}$$

These kind of matrices are required when dealing with discrete spherical angle geometries.

4.2 Discrete Spherical-Harmonics-Transforms and Sampling the Sphere

In many cases, it is desirable to obtain the spherical harmonics decomposition from a discrete-point representation on the sphere. Specifically, we can obtain a spherical wave-spectrum of a sound field from the discrete distribution measured with a spherical microphone array. The spherical harmonics can also be understood as approximative interpolation between the spatially discrete points.

Closely related to the question how spherical distributions can be transformed into spherical harmonics, a sampling strategy for spherical surfaces has to be found. This question is of importance for both spherical loudspeaker and microphone arrays in acoustics. Its solution offers important answers to down-to-earth questions:

How shall I arrange ...

- ... a surrounding spherical loudspeaker array for higher-order Ambisonics playback?
- ... a compact spherical microphone array for higher-order Ambisonics recordings?
- ... a compact spherical loudspeaker array for directivity pattern synthesis?
- ... a surrounding spherical microphone array for directivity pattern capture?

Transform on the continuous sphere. As we know from Eq. (28), the spherical harmonics transform is computed by an integral. This integral can be written as a projection of a distribution $g(\boldsymbol{\theta})$ on the base of the continuous spherical harmonics $\boldsymbol{y}(\boldsymbol{\theta}) = \mathrm{vec}_{\mathrm{N}}\{Y_n^m(\boldsymbol{\theta})\}$ over the unit sphere $\mathbb{S}^2$, with $\mathrm{N} \to \infty$:

$$\boldsymbol{\gamma} = \int_{\mathbb{S}^2} \boldsymbol{y}(\boldsymbol{\theta})\ g(\boldsymbol{\theta})\ d\boldsymbol{\theta}, \tag{229}$$

$$\boldsymbol{y}(\boldsymbol{\theta}) = \mathrm{vec}_{\mathrm{N}\to\infty}\{Y_n^m(\boldsymbol{\theta})\}. \tag{230}$$

Eq. (224) gives a definition of the above vector notation. Complementary to this integral, the scalar, continuous space function $g(\boldsymbol{\theta})$ is obtained by an infinite sum over all the spherical harmonics weighted by the coefficient vector $\boldsymbol{\gamma}$:

$$g(\boldsymbol{\theta}) \quad = \quad \boldsymbol{y}(\boldsymbol{\theta})^{\mathrm{T}}\ \boldsymbol{\gamma}. \tag{231}$$

4.2.1 Types of Discrete Spherical Harmonics Transforms

The spherical harmonics expansion on a sampled sphere is directly equivalent to Eq. (231). The distribution $g(\boldsymbol{\theta})$ is sampled on a set of L discrete spherical-angles

$\{\boldsymbol{\theta}_l\}$ and written as a vector $\boldsymbol{g}$:

$$\boldsymbol{g} = \begin{pmatrix} g\left(\boldsymbol{\theta}_1\right) \\ g\left(\boldsymbol{\theta}_2\right) \\ \vdots \\ g\left(\boldsymbol{\theta}_\mathrm{L}\right) \end{pmatrix} \tag{232}$$

Usually, the spherical harmonics expansion is assumed to be band-limited by the order $n \leq \mathrm{N}$. Accordingly, the expansion given in Eq. (231) is written as

$$\boldsymbol{g} = \boldsymbol{Y}_\mathrm{N}^\mathrm{T}\, \boldsymbol{\gamma}_\mathrm{N}, \tag{233}$$

$$\boldsymbol{Y}_\mathrm{N}^\mathrm{T} = \mathrm{mtx}_\mathrm{N}\left\{Y_n^m(\boldsymbol{\theta}_l)\right\}^\mathrm{T}, \qquad \boldsymbol{\gamma}_\mathrm{N} = \mathrm{vec}_\mathrm{N}\left\{\gamma_{nm}\right\}. \tag{234}$$

Using L nodes and the $(\mathrm{N}+1)^2$ band-limited spherical harmonics, the maximum order for an (over-)determined transform pair equals $\mathrm{N}_\mathrm{max} = \lfloor\sqrt{\mathrm{L}}-1\rfloor$. For various types of transforms, the truncation has to be smaller than that $\mathrm{N} \leq \mathrm{N}_\mathrm{max}$. The ordered list below shows the most important types of transforms. These transforms impose descendingly strict requirements on the sampling grid $\{\boldsymbol{\theta}_l\}$:

1. *Hyperinterpolation* on the sphere requires exactly $\mathrm{L} = (\mathrm{N}+1)^2$ (critical) sampling nodes on the sphere. The sampling nodes must provide a well-conditioned matrix $\boldsymbol{Y}_\mathrm{N}$, so that an exact inverse exists $\boldsymbol{Y}_\mathrm{N}\boldsymbol{Y}_\mathrm{N}^{-1} = \boldsymbol{Y}_\mathrm{N}^{-1}\boldsymbol{Y}_\mathrm{N} = \boldsymbol{I}$. Given such points, the expansion reconstructs perfectly at every node.

2. For *equal-weights quadrature/t-design*, the rows of the matrix $\boldsymbol{Y}_\mathrm{N}$ must be orthonormal (up to a scale factor) , i.e. $\boldsymbol{Y}_\mathrm{N}\,\boldsymbol{Y}_\mathrm{N}^\mathrm{T} = a\boldsymbol{I}$. The few sampling constellations fulfilling this requirement are usually over-determined, i.e. $(\mathrm{N}+1)^2 < \mathrm{L}$. Therefore only band-limited distributions $\boldsymbol{g} = \boldsymbol{Y}_\mathrm{N}^\mathrm{T}\,\boldsymbol{\gamma}_\mathrm{N}$ can be fully resolved, reconstruction at $\{\boldsymbol{\theta}_l\}$ is only approximate otherwise.

3. For *weighted quadrature* the rows of the matrix $\boldsymbol{Y}_\mathrm{N}$ must become orthonormal, at least after applying specific weights $\sqrt{w_l}$ to the nodes. Usually, weighted quadrature grids are over-determined. With the squared weights in a vector $\boldsymbol{w} = \mathrm{vec}\,\{w_l\}$, this reads $\boldsymbol{Y}_\mathrm{N}\,\mathrm{diag}\,\{\boldsymbol{w}\}\;\boldsymbol{Y}_\mathrm{N}^\mathrm{T} = \boldsymbol{I}$.

4. For a *least-squares* transform, the matrix $\boldsymbol{Y}_\mathrm{N}\boldsymbol{Y}_\mathrm{N}^\mathrm{T}$ needs not equal unity, but must be well-conditioned. Usually, suitable sampling grids will have to be over-determined. Using the least-squares inverse, the transform yields the best approximation, which is the exact inverse only in case of a strictly band-limited distribution $\boldsymbol{g} = \boldsymbol{Y}_\mathrm{N}^\mathrm{T}\,\boldsymbol{\gamma}_\mathrm{N}$. Otherwise, only approximate reconstruction is feasible. Approximation errors tend to be high in weakly sampled regions on the sphere.

5. For a *weighted least-squares* solution, the matrix $\boldsymbol{Y}_\mathrm{N}\,\mathrm{diag}\,\{\boldsymbol{w}\}\,\boldsymbol{Y}_\mathrm{N}^\mathrm{T}$ does not need to equal the unity matrix, but must be well-conditioned. Usually, suitable sampling grids are over-determined. With properly chosen weights $\boldsymbol{w}$, the condition number gets better and the approximation error is more uniformly distributed.

6. *Regularized (weighted) least-squares, discarding linear dependencies* can help if the matrix inversion is ill-conditioned for the required order N. This is mostly due to unevenly distributed sampling nodes or missing parts on the sphere. Exclusion of linearly dependent rows from $\boldsymbol{Y}_\mathrm{N}$ or forming new harmonics can regularize the matrix inversion. Exclusion is done either by iteratively removing the harmonics that are most correlated over the sampling grid $\boldsymbol{Y}_\mathrm{N}\boldsymbol{Y}_\mathrm{N}^\mathrm{T}$ or by exploiting *a priori* knowledge based on spherical harmonic symmetries. Alternatively, a regularized inversion using reduced sets of base functions can be found by eigenvalue decomposition that yields excellent approximations. Some of these transforms, however, may require relaxation of the general assumptions about band- and angular-limitation of the data on the sphere.

7. *Exact sample match, minimum spectral-power transform* can be applied if more spherical harmonics are analyzed than there are sampling points $(\mathrm{N}+1)^2 > L$. Hereby, only a partial band-limitation is assumed, but all angular samples can be represented accurately. The minimization that ensures a solution creates valleys between the sampling nodes, the depth of which increases with N.

8. *Direct transform on a triangulated mesh* is a technique that assumes discrete distributions within spherical triangles. These triangles can be transformed analytically at unbounded spherical bandwidth N without any requirements on the sampling. However, any reduction of N leads to approximations of the distribution on the sphere. This approach could be thought of as being a type of *sample-and-hold* technique for the spherical harmonics transform.

There is recent literature on *Spherical Wavelets* cf. [FW97, MP05, AV99, ADJV02, SS95, Les07]. The key problem is how to determine (bi-)orthonormal wavelets for discrete spheres by *lifting schemes* or sampling of continuous wavelets. Some works use subdivisions of Platonic solids as sampling strategy. It seems a high degree of symmetry has to be provided by the sampling grid. Since in terms of the Helmholtz equation spherical harmonics decompositions are required, spherical wavelets are not the first method of choice herein.

Another interesting source for interpolatory DSHT on the $(N + 1)(2N + 2)$ Gauß-Legendre grid can be found in [Boy00]. On this grid *cardinal functions* are known, which are zero at all sampling nodes except for one. Using the spherical harmonics representations of all *cardinal functions*, a one-to-one correspondence, i.e. *interpolation*, can be established at the sampling nodes.

4.2.2 Hyperinterpolation on the Sphere

Sloan and Womersley [SW99, WS01, SW04] extensively study the properties of several approaches of obtaining optimal sets of sampling nodes. Essentially, they introduce the term *hyperinterpolation* and describe *polynomial interpolation* on the sphere instead of approximations like *quadrature* or *least-squares*. The key difference is that interpolation exactly represents all the values at the given nodes without approximation errors. For this purpose the $L = (N + 1)^2$ nodes sampling the spherical harmonics must lead to a well-conditioned full-rank matrix $\boldsymbol{Y}_N$, so that matrix inversion is feasible

$$\boldsymbol{\gamma}_N \;=\; \left(\boldsymbol{Y}_N^T\right)^{-1} \boldsymbol{g}. \tag{235}$$

The authors present an extensive list of node configuration they computed for the orders $N = 1, \ldots, 191$. The numerical optimization efforts to obtain suitable sampling nodes greatly exceeds the efforts for orthonormal sampling nodes (*quadrature*). This kind of critical sampling is generally not orthonormal $\boldsymbol{Y}_N^T \neq \boldsymbol{Y}_N^{-1}$, but it allows for exact inversion.

4.2.3 Quadrature

The computationally most efficient way to obtain a spherical harmonics transform from discrete points on the sphere is called *quadrature* - for higher dimensionality often referred to as *cubature*. Basically, quadrature assumes a spherical bandwidth of the measured spherical distribution limited by the spherical harmonics order N. In particular, a *quadrature rule* defines an appropriate set of *quadrature nodes* and *weights* on the sphere $\{\boldsymbol{\theta}_l, w_l\}$ for a particular N. What makes quadrature particularly interesting is its simplicity. It does not require matrix inversion, which can be advantageous for large numbers of nodes L.

Quadrature with equal weights (orthogonal sampling). In the simplest case, quadrature is equally weighted $w_l = 1$. Equal-weights quadrature nodes with L points will usually not work above a prescribed truncation number N. In many cases, quadrature only supports orders lower than the highest (over-)determined order $N < N_{max} = \lfloor \sqrt{L} - 1 \rfloor$. Unlike every equidistant distribution of points on a

circle, there are only a few regular samplings on the sphere that are orthogonal. The quadrature with equal weights is defined as

$$\boldsymbol{\gamma}_{\mathrm{N}} \;=\; \boldsymbol{Y}_{\mathrm{N}}\, \boldsymbol{g}. \tag{236}$$

Equal weights quadrature (1): Platonic sampling. For the 5 Platonic solids (tetrahedron, hexahedron, octahedron, dodecahedron, icosahedron) that are known to be the only 5 strictly regular sampling grids on the sphere with $\mathrm{L} = \{4, 8, 6, 20, 12\}$ points, the orthonormality of the spherical harmonics $\boldsymbol{Y}_{\mathrm{N}}\, \boldsymbol{Y}_{\mathrm{N}}^{\mathrm{T}} = a\boldsymbol{I}$ holds for values of N at most $\mathrm{N} \leq \{1, 1, 1, 2, 2\}$. All Platonic samplings except for the tetrahedron, which has $\mathrm{L} = (\mathrm{N}_{\max} + 1)^2$ points, are over-determined. Therefore, they allow for approximate reconstruction of the sample values only. The dodecahedral grid with its $\mathrm{L} = 20$ nodes is neither a quadrature with equal, nor with unequal weights for the highest order $\mathrm{N} = 3$. Although the spherical harmonics up to $\mathrm{N} = 3$are already over-determined for the dodecahedral nodes, they are only a quadrature for $\mathrm{N} = 2$.

Equal weights quadrature (2): spherical t-designs. In another terminology, equal-weights quadrature rules are called spherical t-designs. Most prominently in this field, Fliege and Maier [FM96] have provided interesting proofs on the existence of such cubature/quadrature formulae for different orders.

Moreover, Hardin and Sloane [HS96] show a detailed list of t-designs and their correspondence to known Platonic/Archimedian polyhedra. They also explicitly give several t-designs for large N. These examples are defined by K-points lying within a single geodesic pentagon of a dodecahedron, which can be completed to a set of $\mathrm{L} = 12\mathrm{K}$ by utilizing the icosahedral symmetries. There is also a very deep field of spherical codes[1], lattices and packing problems (Conway, Sloane [CS99], Martinet [Mar03]) associated with this analytical approach, also considering the question: If any, how many equal weights quadrature rules exist for the order N ?

Weighted quadrature. Extending the *quadrature rule* by *quadrature weights* $\boldsymbol{w}$, the projection for the transform becomes:

$$\boldsymbol{\gamma}_{\mathrm{N}} \;=\; \boldsymbol{Y}_{\mathrm{N}}\, \mathrm{diag}\,\{\boldsymbol{w}\}\; \boldsymbol{g}. \tag{237}$$

The weights $\boldsymbol{w}$ are used to enable orthonormality of the sampled spherical harmonics: $\boldsymbol{Y}_{\mathrm{N}}\, \mathrm{diag}\,\{\boldsymbol{w}\}\, \boldsymbol{Y}_{\mathrm{N}}^{\mathrm{T}} = \boldsymbol{I}$. Probably the most famous rules, for which weighted quadrature works are:

[1] As far as understood here, a *spherical code* denominates generator polynomials defined on the spherical surface $\mathbb{S}^2$ having spherical periodicity; these polynomials are used to generate the quadrature nodes.

1. the *equi-angle quadrature* [DH94, Sne94, MNV97], for which the equator is sampled with 2N + 1 longitude-circles and the longitude in 2N or 2N + 1 equally spaced latitude-circles.

2. and the Gauß quadrature with (N + 1)(2N + 2) nodes [Moh99]. For Gauß quadrature, only the azimuth is equidistantly sampled. The grid-lines in elevation lie at the zeros of the Legendre polynomial $P_{\mathrm{N}+1}$.

3. Lebedev [Leb77, Del96] sampling (octahedral symmetry), Fliege [FM96] nodes, Hardin and Sloane [HS96] (icosahedral symmetry).

For the longitude-latitude grids (1 and 2), there exist fast transform implementation, as shown in [DH94, SJ96, SB96, MNV97, HRKM98, PST98, Moh99, IBM01, KR03, SS03, HKR04, KP03].

In the work of Mhaskar [MNW00], the existence of weighted quadrature in general has been shown. For any set of nodes on the sphere and an order N, which is limited by a separation measure of the quadrature nodes, there exists a positively weighted quadrature. Equal weights are only feasible in special cases.

Quadrature weights. The question remains of how to obtain suitable weights. In [MNW00] or [DH94], the property of the weights is defined using quadrature over a constant value $\mathbf{1}$, which results in the zero-order coefficient $\sqrt{4\pi}$ only:

$$\begin{pmatrix} \sqrt{4\pi} \\ 0 \\ \vdots \end{pmatrix} = \boldsymbol{Y}_{\mathrm{N}} \operatorname{diag}\{\boldsymbol{w}\}\ \mathbf{1} = \boldsymbol{Y}_{\mathrm{N}}\, \boldsymbol{w}, \tag{238}$$

$$\Rightarrow \boldsymbol{w}_{\mathrm{mv}} = \boldsymbol{Y}_{\mathrm{N}}^{\mathrm{T}} \left(\boldsymbol{Y}_{\mathrm{N}}\, \boldsymbol{Y}_{\mathrm{N}}^{\mathrm{T}}\right)^{-1} \begin{pmatrix} \sqrt{4\pi} \\ 0 \\ \vdots \end{pmatrix}. \tag{239}$$

The solution of the under-determined system Eq. (238) is given in Eq. (239), which is the minimum variance inversion. Even if the equation is usually regular for suitable N, it is necessary to check whether $\boldsymbol{Y}_{\mathrm{N}} \operatorname{diag}\{\boldsymbol{w}\}\, \boldsymbol{Y}_{\mathrm{N}}^{\mathrm{T}} = \boldsymbol{I}$, i.e. quadrature, is feasible.

A strict definition of the quadrature weights can be obtained from Eq. (238) by left multiplication with $\boldsymbol{Y}_{\mathrm{N}}^{\mathrm{T}}$. This definition is given in the various works of Fliege and Maier, Sloan and Womersley [FM96, SW99, WS01, SW04] wherein $\boldsymbol{G}$ is denoted as *reproducing kernel/Gram matrix*:

$$\boldsymbol{G} = \boldsymbol{Y}_{\mathrm{N}}^{\mathrm{T}}\, \boldsymbol{Y}_{\mathrm{N}} \tag{240}$$

$$\mathbf{1} = \boldsymbol{G}\, \boldsymbol{w}. \tag{241}$$

Since N must be fairly low in many cases, the matrix $\boldsymbol{G}$ will usually be singular. Sloan and Womersley describe that even optimal sets of nodes tend to give a singular matrices $\boldsymbol{G}$ [SW99, WS01, SW04].

According to Sneeuw [Sne94], for longitude-latitude sampling grids only the classes of zenith angles ϑ'_i are required to write down this *first Neumann method* as set of equations:

$$\begin{pmatrix} 1 & \cdots & 1 & 1 \\ \cos(2\vartheta'_1) & \cdots & \cos(2\vartheta'_{\mathrm{M}}) & -1 \\ \cos(4\vartheta'_1) & \cdots & \cos(4\vartheta'_{\mathrm{M}}) & 1 \\ \vdots & & \vdots & \vdots \\ \cos(2\mathrm{M}\vartheta'_1) & \cdots & \cos(2\mathrm{M}\vartheta'_{\mathrm{M}}) & \pm 1 \end{pmatrix} \begin{pmatrix} w'_1 \\ w'_2 \\ \vdots \\ w'_{\mathrm{M}} \\ w'_{\mathrm{M}+1} \end{pmatrix} = \begin{pmatrix} 1 \\ -1/3 \\ -1/15 \\ \vdots \\ \frac{-1}{4\mathrm{M}^2-1} \end{pmatrix}. \tag{242}$$

The weights for the individual points are obtained by division of the corresponding longitude weight w_i with the number of latitude subdivisions K:

$$w_l = w'_i/\mathrm{K}. \tag{243}$$

Note that this approach also yields good weights in many cases for that quadrature is not feasible.

4.2.4 Transforms by Least-Squares

The transform using least-squares (best fit in the least-squares sense) represent a class of transforms different to quadrature or hyperinterpolation. In general, its requirements on the set of sampling nodes are not as strict. Essentially, the transform by inversion only requires a regular least-squares inverse, which means the spherical harmonics sampled at L nodes must have rank $(\mathrm{N}+1)^2$ and can therefore be orthogonalized. Note that in many cases this will only work for N smaller than $\mathrm{N}_{\max} = \lfloor\sqrt{\mathrm{L}} - 1\rfloor$, which may, however, take larger values than for quadrature.

Least-squares. Least-squares fitting of discretized spherical harmonics seems to be suitable for DSHT because it works more flexibly with respect to given sampling nodes than quadrature. Instead of using the discrete vector projection on the sampled spherical harmonics, the vectors of the least-squares inverse are used for transformation [HG06]:

$$\begin{aligned} &J(\boldsymbol{\gamma}_{\mathrm{N}}) = \left\|\boldsymbol{g} - \boldsymbol{Y}_{\mathrm{N}}^{\mathrm{T}}\boldsymbol{\gamma}_{\mathrm{N}}\right\|^2 \to \min \quad \Rightarrow \frac{\partial}{\partial \boldsymbol{\gamma}_{\mathrm{N}}^{\mathrm{T}}} J(\boldsymbol{\gamma}_{\mathrm{N}}) = \boldsymbol{Y}_{\mathrm{N}}\,\boldsymbol{g} - \boldsymbol{Y}_{\mathrm{N}}\,\boldsymbol{Y}_{\mathrm{N}}^{\mathrm{T}}\,\boldsymbol{\gamma}_{\mathrm{N}} \stackrel{!}{=} 0, \\ &\Longrightarrow \boldsymbol{\gamma}_{\mathrm{N}} = \underbrace{\left(\boldsymbol{Y}_{\mathrm{N}}\,\boldsymbol{Y}_{\mathrm{N}}^{\mathrm{T}}\right)^{-1}\boldsymbol{Y}_{\mathrm{N}}}_{:=\left(\boldsymbol{Y}_{\mathrm{N}}^{\mathrm{T}}\right)^{+}}\,\boldsymbol{g}. \end{aligned} \tag{244}$$

The choice of the sampling nodes is very important as it determines whether the matrix $\boldsymbol{Y}_{\mathrm{N}}\boldsymbol{Y}_{\mathrm{N}}^{\mathrm{T}}$ is singular or not. In addition, if given a non-uniform set of sampling nodes, the least-squares error is also non-uniformly distributed; errors emerge in the case of distributions that are not band-limited $\boldsymbol{g} \neq \boldsymbol{Y}_{\mathrm{N}}^{\mathrm{T}}\,\boldsymbol{\gamma}_{\mathrm{N}}$.

Weighted-least-squares. In terms of the *color* of the error, i.e., the uniformity of the error distribution on the sphere, a weighted least-squares approach allows to influence the error per surface, using a vector $\boldsymbol{w}$ of positive weights and minimization of $(\boldsymbol{g}^{\mathrm{H}} - \boldsymbol{\gamma}_{\mathrm{N}}^{\mathrm{H}}\,\boldsymbol{Y}_{\mathrm{N}})\,\mathrm{diag}\,\{\boldsymbol{w}\}\;(\boldsymbol{g} - \boldsymbol{Y}_{\mathrm{N}}^{\mathrm{T}}\,\boldsymbol{\gamma}_{\mathrm{N}}) \rightarrow \min$:

$$\boldsymbol{\gamma}_{\mathrm{N}} \;=\; \underbrace{\left(\boldsymbol{Y}_{\mathrm{N}}\,\mathrm{diag}\,\{\boldsymbol{w}\}\,\boldsymbol{Y}_{\mathrm{N}}^{\mathrm{T}}\right)^{-1}\boldsymbol{Y}_{\mathrm{N}}\,\mathrm{diag}\,\{\boldsymbol{w}\}}_{:=\left(\boldsymbol{Y}_{\mathrm{N}}^{\mathrm{T}}\right)^{+\boldsymbol{w}}}\,\boldsymbol{g}. \tag{245}$$

Inserting a quadrature rule into the above expression is equivalent to quadrature itself. However, weighted least-squares often provides transforms with larger orders N than accessible with quadrature.

The existence of a well-conditioned weighted least-squares transform has been shown in [KKP07]. For this purpose, the order N has to be bounded by separation measures of the given sampling grid. The weights $\boldsymbol{w}$ are based on the areas of Voronoi cells associated with the sampling nodes, as described in the next paragraphs.

Weights for the nodes. Usually, the weights for quadrature defined in the above sections Eqs. (239), (241), (242) show good performance for weighted least-squares. However, the inversion of $\boldsymbol{G}$ in Eq. (241) is usually ill-conditioned for large orders. As a rough work-around, a double minimum-variance inversion of the factors $\boldsymbol{Y}_{\mathrm{N}}^{\mathrm{T}}$ and $\boldsymbol{Y}_{\mathrm{N}}$ in $\boldsymbol{G}$ can be used:

$$\boldsymbol{w} = \boldsymbol{Y}_{\mathrm{N}}\;\left(\boldsymbol{Y}_{\mathrm{N}}\,\boldsymbol{Y}_{\mathrm{N}}^{\mathrm{T}}\right)^{-2}\;\boldsymbol{Y}_{\mathrm{N}}^{\mathrm{T}}\;\boldsymbol{1} \tag{246}$$

Alternatively, $\boldsymbol{G}$ can be inverted using eigendecomposition. Preceding the inversion, a truncation to the relevant eigenvector-eigenvalue pairs provides regularization. Moreover, the areas of the spherical longitude-latitude compartments can be used as weights. These are easily determined geometrically for the zenith angle ϑ_i by

$$w_i' = \frac{1}{2}\left[\cos\left(\frac{\vartheta_{i-1}+\vartheta_i}{2}\right) - \cos\left(\frac{\vartheta_i+\vartheta_{i+1}}{2}\right)\right]. \tag{247}$$

For arbitrary sampling, such area weights can be computed using Voronoi cells on the sphere [AP85, KKP07, DFG99, DGJ03, Bur06]. Voronoi cells are the set of the areas around each node on the sphere bounded by the symmetry lines to the

neighboring nodes. The Delaunay triangulation is the dual to the Voronoi cells as it consists of lines connecting the nodes with their neighbors. The algorithms on the websites of John Burkardt [Bur06] (STRIPACK, Robert Renka) and Jens Keiner [Kei07] (CSTRIPACK) can be used to compute Voronoi cells/Delaunay triangles on the sphere.

4.2.5 Regularized Least-Squares

The continuous spherical harmonics are only orthonormal on the complete and unweighted sphere. Given only finite segments of the sphere, or more generally a mask $a(\boldsymbol{\theta})$ selecting a bounded spherical domain, yields linear dependencies among the spherical harmonic functions

$$\int_{\mathrm{S}^2} a(\boldsymbol{\theta})\, Y_n^m(\boldsymbol{\theta})\, Y_{n'}^{m'}(\boldsymbol{\theta})\, d\boldsymbol{\theta} \neq \delta_{nn'}\delta_{mm'}, \qquad \forall a(\boldsymbol{\theta}) \neq 1. \tag{248}$$

This problem is important as incomplete sampling drastically reduces the feasible order N of least-squares transforms.

Given prior knowledge about a simple finite spherical segment, i.e., a hemisphere, deterministic harmonics selections can be found using symmetry properties of the spherical harmonics, see Fig. 18 and [PZ09]. For a hemisphere, only the harmonics with even or odd index $(n-m)$ could be used, which either describe even or odd symmetry with respect to the z-axis and both being orthogonal. Similarly, symmetries regarding the y-axis and rotational symmetries can be described, cf. Fig. 18.

Alternatively, independent base-functions for arbitrary fractions of the sphere do not suffer from interference artifacts obtained by symmetry assumptions, and they further have the advantage of providing a minimum energy representation on the unused portion of the sphere [PZ09]. This superior formulation can be found in satellite geodesy. The problem occurs with satellites since there is frequently no way of keeping them near the poles of the earth. Solutions can be found in the works of Sneeuw, Baur, and van Gelderen [SvG97, BS06], Albertella, Sansò and Sneeuw [ASS99], Simons, Dahlen and Wieczorek [SD06, SDW06, DS07] under the key-words *Polar-Gap Problem* and *Slepian functions*. In principle, the functions described in these works are a selection of functions that support decompositions of finite domains on the sphere. An important approach has been presented in Pail, Plank, and Schuh [PPS01] and has been considered in [PZ09]. Using an eigendecomposition of the matrix $\boldsymbol{Y}_{\mathrm{N}}\boldsymbol{Y}_{\mathrm{N}}^{\mathrm{T}}$ helps finding useful orthonormal base functions that have full rank, in order to obtain a well-defined transform. It is also advisable to rotate the new space of base-functions to improve their relation to the spherical harmonics. For details on the solution the reader is referred to [PZ09].

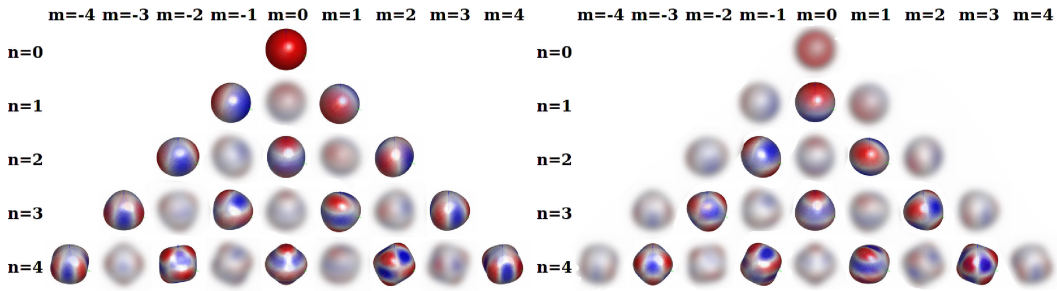

(a) even and odd symmetric wrt. z, e.g. for decompositions on hemispheres.

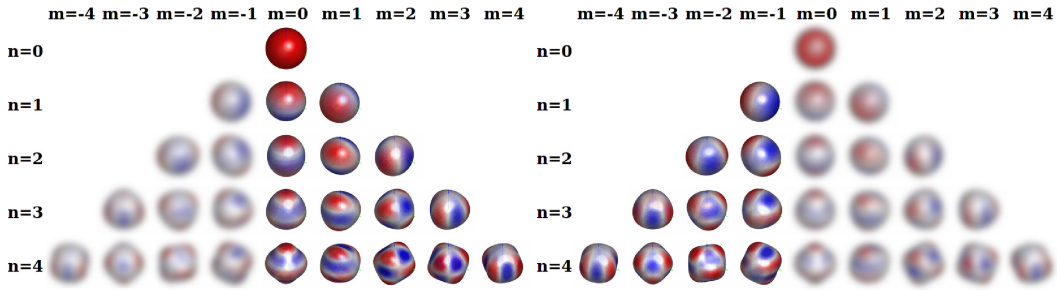

(b) even and odd symmetric wrt. y, e.g. for decompositions on hemispheres.

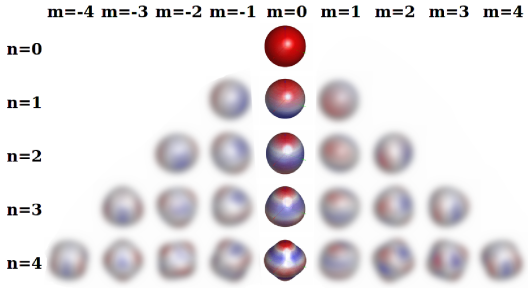

(c) rotationally symmetric wrt. z

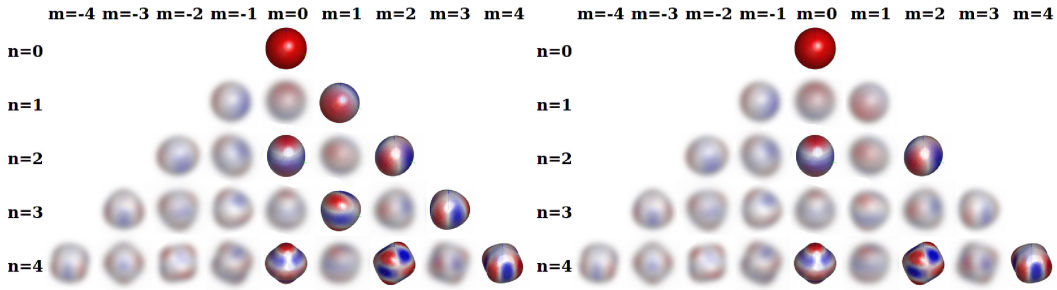

(d) even symmetric functions for quarter and eighth spheres.

Figure 18: Examples of spherical harmonics symmetries.

Similarly, but with a somewhat different idea, Hannemann *et al* use a singular-value decomposition (SVD) to obtain a regularized system inversion [HLDS07, HD08] they name *Multipole-Matching*. Furthermore the work of Zhang *et al* describes solutions [ZKA08].

4.2.6 Exact Sample Match, Minimum Spectral-Power Transform

If all the samples on the sphere shall be represented correctly in the angular domain, but no *hyperinterpolation* is available, another optimization approach is feasible. In this case, the order is chosen to be high enough $\mathrm{N} > \sqrt{\mathrm{L}} - 1$ to make the system under-determined, having infinitely many adequate solutions. Unique coefficients are found by minimization of the wave-spectral power $\|\boldsymbol{\gamma}_\mathrm{N}\|^2$

$$\begin{aligned} \|\boldsymbol{\gamma}_\mathrm{N}\|^2 &\rightarrow \min. \\ \text{subject to: } \boldsymbol{g} &\stackrel{!}{=} \boldsymbol{Y}_\mathrm{N}^\mathrm{T}\,\boldsymbol{\gamma}_\mathrm{N}, \qquad \Rightarrow J(\boldsymbol{\gamma}_\mathrm{N}, \boldsymbol{\lambda}) = \|\boldsymbol{\gamma}_\mathrm{N}\|^2 + (\boldsymbol{g}^\mathrm{T} - \boldsymbol{\gamma}_\mathrm{N}^\mathrm{T}\,\boldsymbol{Y}_\mathrm{N})\,\boldsymbol{\lambda}, \end{aligned} \tag{249}$$

with the optimization error $J(\boldsymbol{\gamma}_\mathrm{N}, \boldsymbol{\lambda})$ and the Lagrange-multipliers $\boldsymbol{\lambda}$. Optimization yields (cf. [HG06]):

$$\begin{aligned} I: \ \frac{\partial}{\partial \boldsymbol{\gamma}_\mathrm{N}^\mathrm{T}} J(\boldsymbol{\gamma}_\mathrm{N}, \boldsymbol{\lambda}) = \boldsymbol{\gamma}_{\mathrm{N,opt}} - \boldsymbol{Y}_\mathrm{N}\,\boldsymbol{\lambda} &\stackrel{!}{=} 0, \qquad \Rightarrow \boldsymbol{\gamma}_{\mathrm{N,opt}} = \boldsymbol{Y}_\mathrm{N}\,\boldsymbol{\lambda}, \\ II: \ \frac{\partial}{\partial \boldsymbol{\lambda}_\mathrm{T}} J(\boldsymbol{\gamma}_\mathrm{N}, \boldsymbol{\lambda}^\mathrm{T}) = \boldsymbol{g} - \boldsymbol{Y}_\mathrm{N}^\mathrm{T}\,\boldsymbol{\gamma}_\mathrm{N} &\stackrel{!}{=} 0, \qquad \stackrel{\text{with I}}{\Rightarrow} \boldsymbol{\lambda}_\mathrm{opt} = (\boldsymbol{Y}_\mathrm{N}^\mathrm{T}\,\boldsymbol{Y}_\mathrm{N})^{-1}\,\boldsymbol{g}, \\ &\Longrightarrow \boldsymbol{\gamma}_{\mathrm{N,opt}} = \boldsymbol{Y}_\mathrm{N}(\boldsymbol{Y}_\mathrm{N}^\mathrm{T}\,\boldsymbol{Y}_\mathrm{N})^{-1}\,\boldsymbol{g}. \end{aligned} \tag{250}$$

Note that the solution is not exact anymore in terms of band-limited input patterns $\boldsymbol{g}_\mathrm{N}$ and its result depends on the orientation of the sampling nodes in space. Because of the minimization wrt. power, cavities appear between the sampling nodes (Parseval theorem, cf. Chap. 2, Eq.(30)).

As a variation, a weighting matrix $\mathrm{diag}\{\boldsymbol{\varpi}_\mathrm{N}\}$ can be introduced, controlling these cavities by differently weighting the spectral powers at each order

$$\begin{aligned} \boldsymbol{\gamma}_\mathrm{N}^\mathrm{T}\,\mathrm{diag}\{\boldsymbol{\varpi}_\mathrm{N}\}\,\boldsymbol{\gamma}_\mathrm{N} &\rightarrow \min \\ \boldsymbol{\gamma}_{\mathrm{N,opt}} &= \mathrm{diag}\{\boldsymbol{\varpi}_\mathrm{N}\}\,\boldsymbol{Y}_\mathrm{N}\,(\boldsymbol{Y}_\mathrm{N}^\mathrm{T}\mathrm{diag}\{\boldsymbol{\varpi}_\mathrm{N}\}\boldsymbol{Y}_\mathrm{N})^{-1}\,\boldsymbol{g}. \end{aligned} \tag{251}$$

4.2.7 Direct Spherical Transforms

Mousa, Chaine, Akkouche, and Galin [MCAG06a, MCAG06b, MCAG07] show a way to utilize Stokes' or the curl theorem to compute a DSHT on the sphere. Thereby they reduce the surface integral over individual triangular patches to the constituent line integrals. This technique can be adopted to compute discrete spherical harmonics transforms of acoustic signals on the sphere, given a suitable Delaunay triangulation between the points of observation.

4.2.8 Sampling Strategies

Rob Womersley provides an illustrative overview of several sampling strategies on the sphere on his website [Wom06]. Another nice overview can be found on Anton Sherwood's website [She07]. Furthermore the website of Hugo Pförtner is interesting [Pfö06]. In fact, there are many strategies based on packing and covering the spherical surface, volume maximization, and area equalization, cf. [SHS00]. The main objective is to distribute sampling points evenly across the sphere by optimization or analytic solutions. Optimization criteria include: minimization of the overlap between circles centered around the nodes, the minimization of the potential energy of repelling particles, equalization of the Voronoi cell sizes, maximization of the volume of a convex polyhedron, and minimization of the condition number of the transform.

Optimization based on minimum energy criterion. Fliege and Maier [FM96] find sets of points converging towards quadrature nodes, using an optimization method. Their basic assumption can be thought of as a conducting spherical surface, onto which a set of L mutually repelling electrons are placed. In a state of *minimum energy*, those electrons will distribute uniformly. Some results based on the *minimum energy approach* can be found on Rob Womersley's website [Wom03].

A more flexible approach uses the Riesz s-Energy to find the *minimum energy points*. The method has been employed by Rakhmanov, Saff, Zhou, Hardin, Brauchart [RSZ94, RSZ95, SK97, HS04, BHS08], also for various types of manifolds (e.g. the *poppy seed bagel problem* [Orl05]). The Riesz s-Energy assumes an adjustable law for the repelling forces, proportional to the distance with $1/d^s$ with the parameter s. For the exception of $s = 0$, the logarithm $-log(d)$ is used as repelling force. They prove that the *minimum energy* as well as the separation distance of the points in equilibrium is bounded for a given s.

Spherical centroidal Voronoi tessellation. Du *et al* [DFG99, DGJ03] show a strategy for sampling (also the sphere) using an iterative algorithm based on Voronoi-partitions. If the mass centers of the Voronoi cells are identical to the sampling nodes, the nodes generate a centroidal Voronoi tesselation (CVT). Several approaches are investigated that find a CVT. CVT is also applicable to anisotropic sampling densities. A source code of STRIPACK (Robert Renka) for spherical Voronoi partitioning can be found at John Burkardt's website [Bur06].

Sampling based on spherical designs/quadrature/hyperinterpolation. The t-designs of Hardin, Sloane, and Smith can be found on their website [SHS00].

From the given K points, 12K can be computed when applying the underlying icosahedral symmetry. Their computations are based on solving analytic equations numerically.

I. V. Lebedev [Leb77] derived quadrature rules for many orders based on the assumption of octahedral symmetry for high-order systems, with an analytical approach, cf. [Del96]. This assumption is utilized to break up the solution of the non-linear equations for quadrature nodes and weights into smaller subsystems with easier solutions. The arithmetic accuracy is defined to be $\eta = (\mathrm{N}+1)^2/(3\mathrm{N})$. From the solutions in the primary octant, a complete set of nodes is obtained by the 8 permutations of the Cartesian coordinates signs. Some other works from De Wit [Wit00], Sangwoo Heo and Yuan Xu [HX01] were found dealing with *fully symmetric* quadrature rules, which is claimed to be more general. A more recent work of Shamsiev [Sha06] gives an excellent overview over other works on cubature/quadrature formulae mostly in Russian language and presents proofs on the existence and derivations of quadrature/cubature formulae on n-dimensional hyper-spheres. For further details, the advanced reader is also referred to Kuperberg's article on numerical cubature [Kup06], Conway and Sloane's book [CS99] as well as [Mar03] on sphere packings, codes and lattices.

The nodes computed by Sloan and Womersley [SW99, WS01, SW04] and the corresponding quality measures can be found on the website [Wom03]. These nodes have been computed for orders 1 up to 191 and are based on maximization of the determinant of $\boldsymbol{Y}_\mathrm{N}$. Since this matrix is very likely to be singular, other optimization approaches, i.e. the *minimum energy* points, were employed by the authors to find stable initialization points for the optimization procedure.

Tessellation of Platonic solids. Within the category of weighted quadrature rules, the Archimedian solids play an important role. For instance, the truncated icosahedron (Bucky/soccer-ball) with 32 nodes, but also other variants of truncated Platonic polyhedra offer reasonable nodes for quadrature with near-uniform sampling the sphere. On a similar basis, tiling approaches can be used to construct grids from Platonic solids. Some examples are Tegmark's icosahedron-based method for discretization of the sphere [Teg96], the Platonic-solid based Discrete Global Grid Systems [SWK03], and the octahedron-based HEALPIX [GHB+05]. All of these approaches offer flexible and uniform sampling. However, there sampling does not exist for all cardinal numbers of sample points. From the implementation perspective and some other practical aspects, the HEALPIX [GHB+05] scheme seems to offer some advantages due to the hierarchical distribution the nodes.

Longitude-latitude grids. To accomplish simpler layouts, several other quadrature rules in a longitude-latitude grid can be defined. The most famous quadrature rule is the Gauß quadrature [Sne94, SB96], which uses equi-angular sampling for azimuth and the zeros of the $P_{\mathrm{N}+1}(\cos\vartheta)$ polynomial as sampling grid for the elevation angle ϑ. This layout is similar to an equi-angle grid, but has non-equidistant nodes in latitude (elevation). Most commonly, the equi-angle [DH94, SB96, MNV97] grid is an equidistant sampling on the sphere with $\varphi_k = \frac{2\pi}{\mathrm{M}_\varphi - 1}\, k$ and $\vartheta_l = \frac{2\pi}{\mathrm{M}_\vartheta - 1}\, l$.

Some effort has been taken to create fast versions of this type of transform by separation of the transforms in the angular variables [DH94, SJ96, SB96, MNV97, HRKM98, PST98, Moh99, IBM01, KR03, SS03, HKR04, KP03]. These approaches are mainly based on fast Fourier-transforms on the latitude circles, followed by a Legendre-transform in the longitude dimension. Intermediately, a fast cosine-transform, i.e. a transform into Chebychev-polynomials $T_n(\cos(\vartheta)) = \cos(m\vartheta)$ is employed. Due to sparse relations between Legendre- and Chebyshev-polynomials $P_n(\mu)$ and $T_n(\mu)$ and the Chebyshev polynomials $T_n(\mu)$ fast transforms are possible. The recurrence relations of the polynomials is used to obtain coefficients for $m \neq 0$.

Igloo/rectangular equal area grids. Rakhmanov and Saff [RSZ94, SK97], Crittenden [CT98b], and Paul Leopardi [Leo06a, Leo06b] use rectangular partitions on the sphere with equal area, aligned in latitude rings. These, so called *igloo-* or *equal area* samplings, follow from the objective of partitioning the sphere in equal area rectangular compartments. A MATLAB toolbox from Paul Leopardi can be found on the website [Leo07]. This toolbox allows for equal area partitioning of the n-dimensional unit-sphere into a freely chosen number of sampling points/areas.

Generalized spiral points. Spirals with subdivisions of the parameter range are also used to distribute points on the sphere. The approach has been shown to support *minimum energy* properties in [RSZ94, SK97]. A recent improvement has been posted online by Knud Thomsen [Tho07], see also Robert Bauer [Bau00, Bau01]. The advantage of the generalized spiral points is their analytic description, which easily leads to sampling nodes by simple recurrence.

4.2.9 Sampling Performance Examples

In the following paragraphs a few measures to compare different sampling methods are discussed. The Figs. 21 and 22 give some examples.

Sampling efficiency comparison. Table 2 shows a comparison of different sampling methods with respect to the number of points required. In order to compare the different methods, the condition number $\kappa = \operatorname{cond}\left\{\boldsymbol{Y}_\mathrm{N}\,\boldsymbol{Y}_\mathrm{N}^\mathrm{T}\right\}$ for least-squares inversion of the sampled spherical harmonics has been taken as a measure of numerical quality. Each sampling method is adjusted so that the smallest possible number of points L lets the condition number fulfill $\kappa \leq 1.2\kappa_{hi}$. κ_{hi} is the condition number when using *hyperinterpolation*, and $\mathrm{L_{hi}} = \mathrm{L_{min}} = (\mathrm{N}+1)^2$ is the lowest possible number of nodes. Using weights $\boldsymbol{w}$ does not cause substantial change of the values in Table 2, except for the condition number of the Gauß-Legendre grid, which turns into $\kappa_{\boldsymbol{w}} = \operatorname{cond}\left\{\boldsymbol{Y}_\mathrm{N}\,\operatorname{diag}\{\boldsymbol{w}\}\,\boldsymbol{Y}_\mathrm{N}^\mathrm{T}\right\} = 1$. The fraction $\mathrm{L_{min}}/\mathrm{L}$ can be used to describe the sampling efficiency. Naturally,

	hi [Wom03]	eq [Leo07]	sp [RSZ94]	gl [Moh99]	hp [GHB+05]
L	$\mathrm{L_{min}}$	$1.23\,\mathrm{L_{min}} - 3.49$ ± 1.34	$1.16\,\mathrm{L_{min}} + 2.6$ ± 3.36	$2\,\mathrm{L_{min}}$	$1.49\,\mathrm{L_{min}} + 12.9$ $\pm 3\mathrm{N}$
κ	$2.4 < \kappa < 16$	$1.9 < \kappa < 4.8$	$2.6 < \kappa < 18$	$1.8 < \kappa < 7$	$1.2 < \kappa < 3.4$

Table 2: Comparison of different sampling methods, with $\mathrm{L_{min}} = (\mathrm{N}+1)^2$ for the orders $\mathrm{N} = 3, \ldots, 15$ and the condition number $\kappa = \operatorname{cond}\left\{\boldsymbol{Y}_\mathrm{N}\,\boldsymbol{Y}_\mathrm{N}^\mathrm{T}\right\}$. The sampling methods were adjusted to achieve a similar κ than the *hyperinterpolation* method, cf. Fig. 20. (hi=*hyperinterpolation*, eq=*equal area partitions*, sp=*generalized spiral points*, gl=*Gauß-Legendre*, hp=*healpix*)

hyperinterpolation is most efficient. Considering the other sampling methods, the equal area partitioning scheme performs best for $\mathrm{N} \leq 8$. Above $\mathrm{N} = 8$, the generalized spiral points slightly outperform the equal area partitioning. Fig. 19 gives an overview.

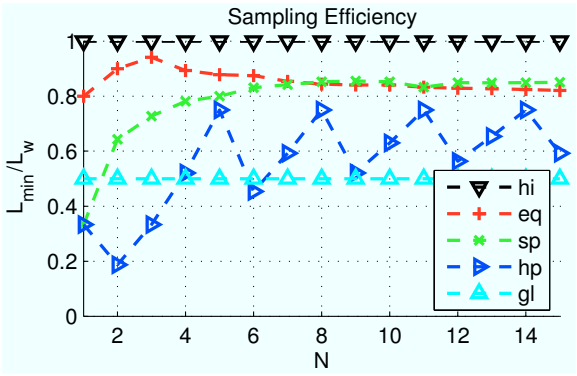

Figure 19: Sampling *efficiency* using different sampling methods. The condition number has been constrained to match closely to *hyperinterpolation*. (hi=*hyperinterpolation*, eq=*equal area partitions*, sp=*generalized spiral points*, hp=*healpix*, gl=*Gauß-Legendre*)

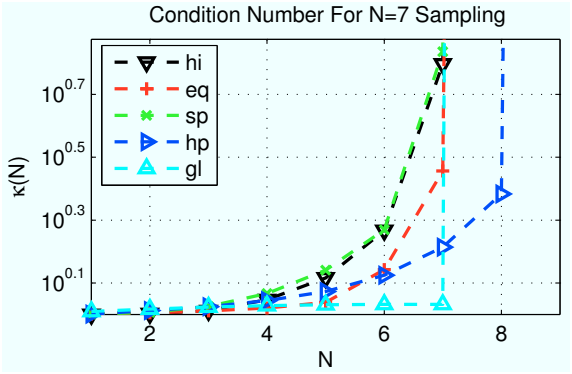

Figure 20: The condition number κ plotted for different $\mathrm{N} = 1, \ldots, 9$ exhibits abrupt transitions from well- to ill-conditioned for all sampling methods designed for $\mathrm{N} = 7$. (hi=*hyperinterpolation*, eq=*equal area partitions*, sp=*generalized spiral points*, hp=*healpix*, gl=*Gauß-Legendre*)

Aliasing error comparison. In order to evaluate aliasing of different sampling methods, we have to define a measure for aliasing errors. A description of aliasing considers the sampled spherical harmonics $\boldsymbol{Y} = \boldsymbol{Y}_\mathrm{P}$ without truncation, i.e. $\mathrm{P} \to \infty$, and compares it with results obtained for $\boldsymbol{Y}_\mathrm{N}$ with finite $\mathrm{N} < \infty$. Given a broad-band spherical harmonics input spectrum $\boldsymbol{\gamma}$, we obtain a discrete distribution by $\boldsymbol{g} = \boldsymbol{Y}^\mathrm{T} \boldsymbol{\gamma}$. Performing a decomposition of $\boldsymbol{g}$ into band-limited harmonics $\boldsymbol{Y}_\mathrm{N}$ as in Eq. (245), full suppression of higher-order harmonics $n > \mathrm{N}$ is desirable. *Ideally*, the desired truncated spectrum $\boldsymbol{\gamma}_\mathrm{N}$ remains:

$$\boldsymbol{\gamma}_\mathrm{N} = \underbrace{\boldsymbol{Y}_\mathrm{N}^{\mathrm{T}+w}\ \boldsymbol{Y}^\mathrm{T}}_{\stackrel{!}{=}(\boldsymbol{I},\boldsymbol{0})}\ \boldsymbol{\gamma}. \tag{252}$$

The total squared-errors $\|e(\boldsymbol{\gamma})\|^2$ depends on the error system $\boldsymbol{E}$ and the broad-band spherical harmonics spectrum $\boldsymbol{\gamma}$, cf. [ZPS08].

$$\|\boldsymbol{e}\,(\boldsymbol{\gamma})\|^2 = \boldsymbol{\gamma}^\mathrm{T} \boldsymbol{E}^\mathrm{T} \boldsymbol{E} \boldsymbol{\gamma}, \tag{253}$$

$$\boldsymbol{E} = \left[\left(\boldsymbol{Y}_\mathrm{N}^\mathrm{T}\right)^{+w}\ \boldsymbol{Y}^\mathrm{T} - (\boldsymbol{I},\boldsymbol{0}) \right]. \tag{254}$$

Note that for $n \leq \mathrm{N}$ the system works perfectly and yields vanishing errors. Consequently, only errors in the columns representing $n > \mathrm{N}$ need to be considered. The total squared-errors of high-order components $\sigma^2_{e_{nm}}$ with $n > \mathrm{N}$ has been presented in [RWB07] to illustrate the aliasing topology:

$$\sigma^2_{e_{nm}} = \left\| \left(\boldsymbol{Y}_\mathrm{N}^\mathrm{T}\right)^{+w}\ \boldsymbol{Y}^\mathrm{T} \begin{pmatrix} 0 \\ \vdots \\ 1 \\ \vdots \end{pmatrix} \leftarrow nm \right\|^2. \tag{255}$$

Figs 21 and 22 show these aliasing-maps in the right column for the selected sampling examples. It is clearly visible that partial aliasing suppression occurs for over-determined (=inefficient) sampling methods, e.g. Fig 22.

Aliasing vs. ideal truncation example: Shifted monopole source. The radiation of a monopole source that is displaced from the origin to $\boldsymbol{r}_0$, cf. Eq. (85), exhibits substantial higher-order energy proportional to $j_n(kr_0)$. However, performing a discrete decomposition with perfect aliasing-suppression, discards high-order components. Consequently, perfect aliasing-suppression attenuates monopoles that are shifted outside the origin. Whether a partial aliasing suppression or the uniform (*friendly*) aliasing of *hyperinterpolation* is more acceptable (Fig. 21) is an important question. It can be discussed regarding the centering problem presented in Chapter. 5.

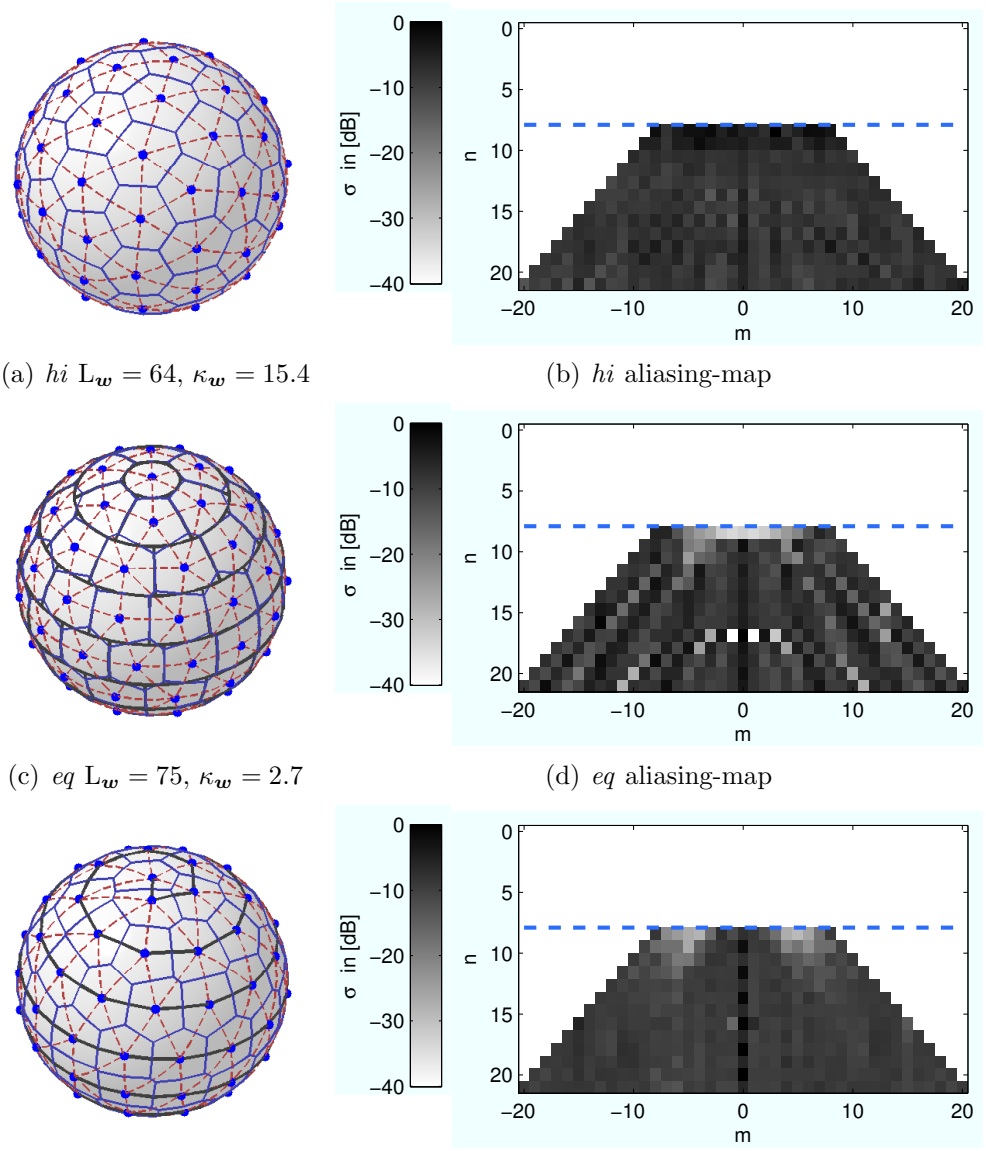

(a) *hi* $L_{\boldsymbol{w}} = 64$, $\kappa_{\boldsymbol{w}} = 15.4$

(b) *hi* aliasing-map

(c) *eq* $L_{\boldsymbol{w}} = 75$, $\kappa_{\boldsymbol{w}} = 2.7$

(d) *eq* aliasing-map

(e) *sp* $L_{\boldsymbol{w}} = 76$, $\kappa_{\boldsymbol{w}} = 16.4$

(f) *sp* aliasing-map

Figure 21: Images of different sampling methods suitable for N = 7 have been plotted using CSTRIPACK [Kei07]. (hi=*hyperinterpolation*, eq=*equal area partitions*, sp=*generalized spiral points*).

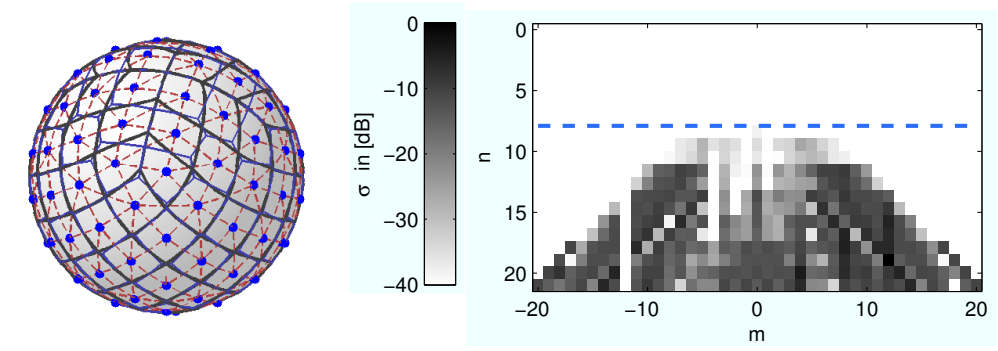

(a) *hp* $L_{\boldsymbol{w}} = 108$, $\kappa_{\boldsymbol{w}} = 1.7$ (b) *hp* aliasing-map

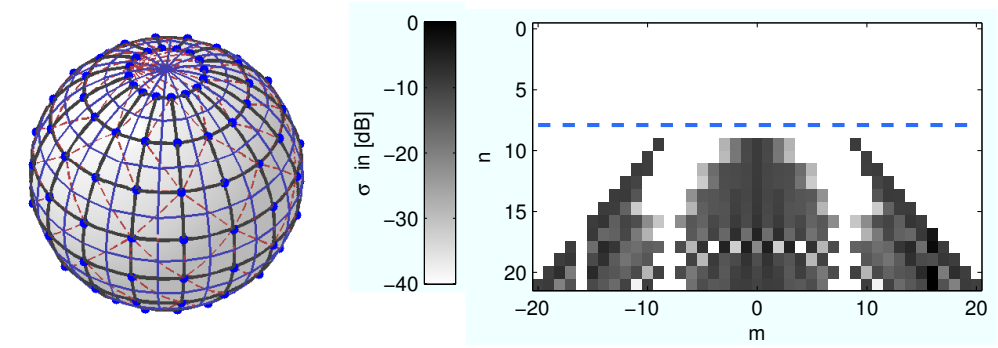

(c) *gl* $L_{\boldsymbol{w}} = 128$, $\kappa_{\boldsymbol{w}} = 1.1$ (d) *gl* aliasing-map

Figure 22: Different sampling methods suitable for N = 7. (hp=*healpix*, gl=*Gauß-Legendre*).

Chapter V

ANALYSIS OF SOUND-RADIATION USING SURROUNDING SPHERICAL MICROPHONE ARRAYS

Introduction of sound-radiation analysis. The most comprehensive and still highly relevant reference works on directivity of musical instruments have been authored by Jürgen Meyer [Mey66, Mey72, Mey08, Mey09]. For these contributions, the body directivities of various instruments have been measured using a turntable, an exciter, and a microphone to capture one horizontal and two vertical slices. The measurement results were analyzed and drawn by hand, using a curve-template. The drawings are valuable for a large group of people: musicians, audio engineers, room acousticians, etc..

Later, Gabriel Weinreich and Eric Arnold [WA80] show a method of how to determine the acoustic radiation of sound sources that is based on spherical acoustic holography. Using a violin with artificially excited strings as a sound source, they measure the sound in every direction of radiation, at two radii, Fig. 23(a). The theory behind these measurements is very elaborate and its contemporary application, though simplified, is found in this thesis.

Another early and notable work about the directivity of sound sources has been contributed by Franck Giron [Gir96]. It introduces a theoretical framework and many case studies on musical instruments. Interestingly, Giron presents two approaches for the decomposition of directivity patterns: the spherical harmonics transform, and the monopole-source synthesis. Using a spatial correlation and a search algorithm, radiation patterns are decomposed into an arrangement of monopole-sources, each of which driven with individual amplitude and phase. A measurement setup is shown in Fig. 23(b)

Further works about capturing directivity responses of musical instrument bodies have been published by Perry Cook, Dan Trueman [CT98a], and Georg Essl, George Tzanetakis [CETT98]. These papers present an interesting way of capturing the radiation by a surrounding icosahedral spherical microphone array that takes simultaneous recordings, which is considered being the most versatile approach here, see Fig. 23(c). Furthermore, they present an LPC-based method to calculate spatial residuals and resonances detected at the individual array microphones.

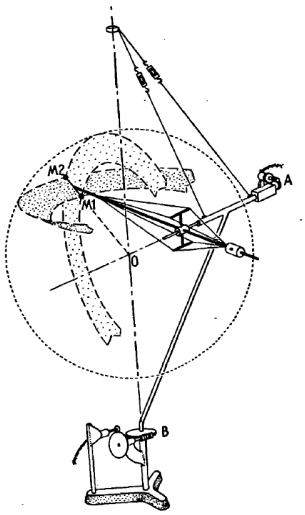

(a) Ann Arbor, Michigan, Weinreich/Arnold [WA80]

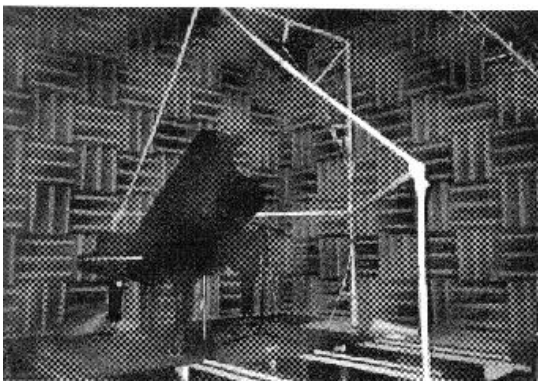

(b) Bochum, Giron [Gir96]

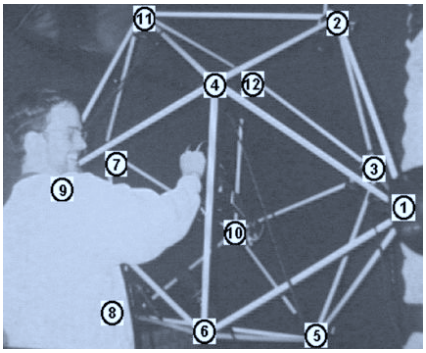

(c) 12 ch., Princeton [CETT98]

Figure 23: Early works on sound-radiation capture of musical instruments in Ann Arbor, Bochum, and Princeton. The first figure shows a virtual dual sphere array.

Felipe Otondo, Jens Holger Rindel, Linda Parati, and Brent Kirkwood [OR02, ORC+02, OR03, PO03, OK03, OR04, OR05, RO05] have authored several publications concerning measurement of directivity as well as involving directivity patterns in room acoustics simulations. They distinguish between averaged and tone-specific directivity patterns. Several multi-channel directivity recordings of musical instruments were captured, which were followed by psychoacoustic evaluation of the auralized results. Interestingly, they could show significant differences in the perceived timbre using either averaged or tone-specific directivity patterns, whereas the differences in estimation of perceived spaciousness was not as clear.

Lily Wang and Courtney Burroughs [WB99, WB01] did insightful near-field acoustic holography studies on a bowed violin, showing the radiation pattern. Wang and Michelle Vigeant [VW04, WV07, VWR07, VW07] published experiments on evaluating the perception of directivity in auralization. Their work

indicates that multi-channel directivity recordings increase the realism of single sources, whereas in the auralization of instrumental ensembles there was no significant improvement of realism due to multi-channel source directivities.

Surrounding spherical microphone arrays. More recently than the first synchronous spherical recordings [CT98a, CETT98], Martin Pollow [Pol07] (ITA Aachen) published a way of decomposing directivity patterns into spherical harmonics with a magnitude only approach. This approach uses standard nonlinear optimization techniques in order to get an improved magnitude fit. In the thesis of Stefan Reuter [Reu08] and the work with Dirk Schröder, Gottfried Behler and Ingo Assenmacher [SRBA08], a way of obtaining high-quality directivity recordings is demonstrated, see Fig. 24(a). Furthermore, the paper [PBM09] considers the question of phase alignment and centering.

Tapio Lokki, J Pätynen, and Ville Pulkki [LPP08, PPL08] (Espoo) took directional multi-channel recordings of individual orchestra instruments playing their part in an anechoic room, synchronized by a conductor, see Fig. 24(b), for the purpose of room acoustics auralizations. From Tapoi Lokki, I received the article [PLar] that shows detailed study on the average directivities of the instruments, which will be published soon.

During the finalizing steps of this thesis, a 64 channel microphone array has been constructed in Graz [Hoh09], see Fig. 24(c). Other microphone arrays that have been used in this thesis, cf. [ZS06, ZSNH07, SZEH07], are depicted in the later sections, Figs. 32(a), 30(a). In addition, I gratefully received saxophone recordings from the researchers at ITA Aachen, which are part of the following analysis; the results were presented in [Zot08].

Side note on compact spherical microphone arrays for incident fields. This short insertion provides a brief overview over recent literature on compact spherical microphone arrays for incident sound field capture. Even if not all the involved functions match exactly the problems to be solved in this work, this field has evolved over a longer period of time and is helpful to understand surrounding spherical microphone arrays. The essential references have been recently gathered thoroughly by Wookeun Song, Wolfgang Ellermeier and Jørgen Hald in [SEH08].

The following short list mentions some of the most important works in this field: Jens Meyer and Gary Elko [ME02, ME07], Boaz Rafaely [RP04, Raf04, Raf05, RWB07], Ilya Balmages [BR04, BR07], Munhum Park [PR05], Ramani Duraiswami [DLZ+05], Zhiyun Li [LDG04, Li05, LD06], Svend-Oscar Petersen [Pet04], Heinz Teutsch [Teu07], Séebastien Moreau [Mor06, MDB06], Jêrôme Daniel [Dan07], Stéphanie Bertet [BDP+07], Anton Schlesinger [SGL+07], Gover and Stinson [Gov04,

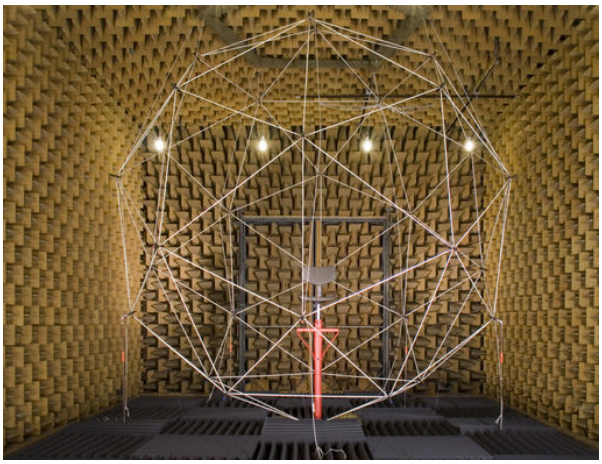

(a) 32 ch., Aachen [Reu08]

(b) 20+2 ch., Espoo [LPP08]

(c) 64 ch., Graz [Hoh09]

Figure 24: Surrounding spherical microphone arrays.

Gov06], Abhaya Parthy, Craig Jin, and André van Schaik [PJvS06].

5.1 Capture and Analysis of Sound-Radiation

Although physical models can be built describing both sound and radiation of sound sources, cf. [FR91, TR03, Smi06], musical acoustics and music may skip the extensive modeling effort by using measurements/recordings with surrounding spherical microphone arrays for radiation capture instead. To label the captured quantity, the term *sound-radiation signal* may be introduced.

5.1.1 Sound-Radiation Signal

Within this work, the term *sound-radiation signal* is used as denominator expressing a sound signal originating from a sound source observed at a given radius in the sound field. To cover all directions of sound-radiation, *sound-radiation*

signals need to provide information about the directional dependency of the radiated sound-signal. Consequently, a *sound-radiation signal* $x(\boldsymbol{\theta}, t)$ depends on the spherical angles $\boldsymbol{\theta}$ and the time t.

Discrete sound-radiation signal. In most practical embodiments, a *sound-radiation signal* $x(\boldsymbol{\theta}, t)$ will be recorded at discretized angles and times, only. Hence it is expressed as a multichannel signal

$$\boldsymbol{x}[\eta] = \begin{bmatrix} x_1[\boldsymbol{\theta}_1, \eta] \\ \vdots \\ x_{\mathrm{L}}[\boldsymbol{\theta}_1, \eta] \end{bmatrix} \tag{256}$$

observable at the discrete angles $\boldsymbol{\theta} = \boldsymbol{\theta}_l$, $l = 1, \ldots, \mathrm{L}$, and times[1] η / f_s, $\eta \in \mathbb{Z}$.

Requirements on representations and models of sound-radiation. Discrete *sound-radiation* should be convertible to representations that allow for discrete re-sampling or continuous reconstruction of *sound-radiation*. Moreover, there is also interest in decompositions into other parametric models of *sound-radiation*. In summary, all these decompositions shall yield the means to perform manipulations. These could be for instance:

1. time-frequency modifications:
   - discrete-time re-sampling, continuous-time reconstruction
   - time / pitch / frequency / dynamics manipulation
   - filtering / vocoding
2. space-frequency-domain modifications:
   - discrete-angle re-sampling, continuous-angle reconstruction
   - translation / rotation / rotational matching / translational tracking
   - angular multiplication and convolution
3. space-time-frequency modifications:
   - cross-directivity-pattern synthesis
   - real-time:
     - directivity-analysis / synthesis / modulation / see also 2.
     - full parametric rendering and auralisation

[1] Usually, the discrete-time index is denoted by n instead of η, [OSB99]. However, n is already in use as a spherical harmonic index within this work.

The third point on this list seems to be both most challenging and exciting. However, it becomes necessary to regard sound-radiation in a time-frequency representation, with all its drawbacks concerning time and frequency resolution. Nevertheless, spatio-temporal-spectral representations should be considered as being perceptually important, actually necessary. Many of the requirements will be solved in the remaining parts of this chapter.

5.1.2 Discrete Transform and Continuous Expansion of Sound-Radiation

Given a finite set of observation times $\eta = 0, \ldots, \mathrm{N}_{\mathrm{DFT}} - 1$ at the angles $\{\boldsymbol{\theta}_l\}$, $\boldsymbol{x}[\eta]$ can be transformed by DSHT into spherical harmonics of the orders $0 \leq n \leq \mathrm{N}$, and by DFT into a discrete frequency-domain using the index $\zeta = 0, \ldots, \mathrm{N}_{\mathrm{DFT}} - 1$ (*discrete Fourier transform* [OSB99]):

$$\boldsymbol{\chi}_{\mathrm{N}}[\zeta] = \mathcal{DFT}_{\mathrm{N}_{\mathrm{DFT}},\eta}\{\mathcal{DSHT}_{\mathrm{N}}\{\boldsymbol{x}[\eta]\}\}. \tag{257}$$

The resulting transform signal $\boldsymbol{\chi}_{\mathrm{N}}[\zeta]$ becomes an $(\mathrm{N}+1)^2$-channel signal.

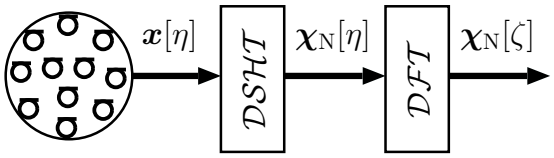

(a) Discrete capture and transform of sound-radiation.

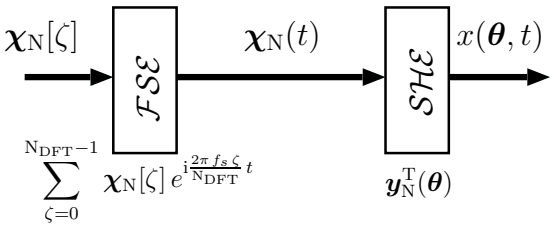

(b) Continuous Fourier-series and spherical harmonics expansion.

Figure 25: Block diagrams describing the discrete-angle and discrete-time sound-radiation capture and transform, and the retrieval of continuous-angle and continuous-time sound-radiation using spherical harmonics and Fourier series expansions.

The main motivation for the discrete transform representations is to enable Fourier series and spherical harmonics expansion (FSE, SHE, see Fig. 25 (b)) over the continuous variables $\boldsymbol{\theta}$ and t:

$$x(\boldsymbol{\theta}, t) = \boldsymbol{y}_{\mathrm{N}}^{\mathrm{T}}(\boldsymbol{\theta}) \sum_{\zeta=0}^{\mathrm{N}_{\mathrm{DFT}}-1} \boldsymbol{\chi}_{\mathrm{N}}[\zeta]\, \mathrm{e}^{\mathrm{i}\frac{2\pi f_s \zeta}{\mathrm{N}_{\mathrm{DFT}}} t}, \tag{258}$$

hence discrete re-sampling or continuous reconstruction in time and space becomes feasible. As a prerequisite for the correctness of the above procedure (discrete transform and continuous expansion), the band-limitedness of the underlying

sound-radiation signal $x(\boldsymbol{\theta}, t)$ in both frequency and spherical harmonics is necessary.

5.1.3 Functional SIMO-Model of Sound-Radiation

Fig. 26 illustrates a functional SIMO model (single-input multiple-output) for the *sound-radiation signal* $\boldsymbol{\chi}_{\mathrm{N}}(\omega)$. The model is described by a simple relation:

$$\boldsymbol{\chi}_{\mathrm{N}}(\omega) = \boldsymbol{\gamma}_{\mathrm{N}}(\omega) \cdot s(\omega), \tag{259}$$

which states that the *sound-radiation signal* $\boldsymbol{\chi}_{\mathrm{N}}(\omega)$ is constituted by a single

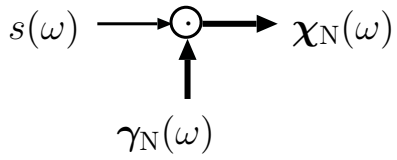

Figure 26: The functional single-input-multiple-output (SIMO) *sound-radiation* model is expressed in both Fourier domains (spherical harmonics and frequency), yielding a sound-radiation signal $\boldsymbol{\chi}_{\mathrm{N}}(\omega)$. It consists of a primal signal $S(\omega)$ multiplied with the spherical harmonics radiation pattern $\boldsymbol{\gamma}_{\mathrm{N}}(\omega)$.

input signal, the primal signal $s(\omega)$, multiplied by a frequency-dependent *radiation pattern* $\boldsymbol{\gamma}_{\mathrm{N}}(\omega)$. This model is suitable for single sources only, and as it is linear, it cannot account for a Doppler frequency shift of sources moving fast.

5.1.4 Spectral Model Total-Power Spectrogram and Multichannel Partial Tracking

To solve the primal signal and SIMO identification problem, a spectral model has been utilized for the analysis in [ZSNH07, Zot08]. It is based on the decomposition of the multi-channel sound-radiation signals into partial-tones, using auditory analysis and a monophonic *total-power spectrogram* representation. Note that this approach is not suitable to retrieve a stochastic noise residual, as described e.g. in [SS92]. However, it is well-suited to extract radiation associated with partial tones of a sound.

It is common practice to use short-time Fourier transforms (STFTs cf. [OSB99], i.e. time-shifted DFT) as an analysis stage for spectral modeling of the partials of a sound, cf. [MQ86, SS92, WBF+00]. We can also apply this approach in the microphone-array multi-channel case. One single-channel STFT of the discrete-time microphone signal $x_l[\eta]$ of the channel l is described as the $\mathrm{N}_{\mathrm{DFT}}$-points DFT along a chain of unit delays with the impulse response $\delta[\eta - 1]$

$$x_l[\tau, \eta] = x_l[\eta] \, (\star\delta[\eta - 1])^{\tau - 1} = x_l[\eta - \tau], \tag{260}$$

$$x_l[\zeta, \eta] = \mathcal{DFT}_{\tau} \left\{ x_l[\tau, \eta] \right\}_{\mathrm{N}_{\mathrm{DFT}}}. \tag{261}$$

Auditory frequency-warping. In order to obtain a suitable frequency scale of the spectrograms, the all-pass warping proposed in Smith and Abel [SA99] can be applied. For that purpose, the signal is running over a chain of all-pass filters with the impulse response $a[\eta]$ instead of unit-delays:

$$x_l[\tau, \eta] = x_l[\eta] \, (\star a[\eta])^{\tau - 1} \tag{262}$$

Assuming a complex exponential of the digital frequency ξ as input signal $x_l[\eta] = \mathrm{e}^{\mathrm{i}(\xi\eta + \phi_0)}$, the change of the signal along the homogeneous chain of elements is described as the all-pass phase $\mathrm{e}^{\mathrm{i}\tau \angle a(\xi)}$ including the position τ on the chain

$$x_l[\tau, \eta] = \mathrm{e}^{\mathrm{i}(\xi\eta + \phi_0 + \tau \angle a(\xi))}. \tag{263}$$

Taking the discrete-time Fourier transform (DTFT) of $x_l[\tau, \eta]$ along an infinite chain of elements $\tau = 0, \ldots, \infty$ yields a DTFT spectrum with a peak at $\xi' = \angle a(\xi)$

$$x_l(\xi', \eta] = \mathcal{DTFT}_\tau\{x_l[\eta, \tau]\} = \mathrm{e}^{\mathrm{i}(\xi\eta + \phi_0)} \, \delta\left(\xi' - \angle a(\xi)\right). \tag{264}$$

It is obvious that the complex exponential at frequency ξ is mapped to the DTFT-location ξ'. Using a finite number of all-pass filters by application of an $\mathrm{N_{DFT}}$ points window function $c[\tau]$, the DFT reads as

$$x_l[\zeta', \eta] = \mathcal{DFT}_\tau\{c[\tau] \, x_l[\tau, \eta]\} = \left(x_l(\xi', \eta] \overset{\mathrm{mod}}{\underset{\mathrm{N_{DFT}}}{\star}} c(\xi') \right) \Big|_{\xi' = \zeta' \frac{2\pi}{\mathrm{N_{DFT}}}}. \tag{265}$$

According to the mapping relation given for continuous frequencies ξ' and ξ, the linear DFT index ζ maps to ζ' by

$$\zeta' = \frac{\mathrm{N_{DFT}}}{2\pi} \angle A\left(\frac{2\pi}{\mathrm{N_{DFT}}} \zeta \right). \tag{266}$$

Using suitable all-pass parameters, this frequency mapping can be adjusted to match an auditory scale, see [SA99].

Auditory masking. For most musical acoustics analyses it should be sufficient to regard the radiation patterns of audible partials only. For this reason, it is useful to calculate the auditory masking threshold $AMT\{|x_l[\zeta, \eta]|^2\}$ in each microphone channel l. We define a simple criterion for the audibility of the spatio-temporal STFT-components $|x_l[\zeta, \eta]|^2$:

$$\prod_{l=1}^{\mathrm{M}} \left(|x_l[\zeta, \eta]|^2 < c \cdot AMT_l\{|x[\zeta, \eta]|^2\} \right) = \begin{cases} 1\text{: inaudible} \\ 0\text{: audible.} \end{cases} \tag{267}$$

In words: the frequency bin ζ is considered to be inaudible (masked) at the time instant η for all the channels only if its magnitude stays below the auditory masking threshold in every channel. c is a constant adjusting the masking threshold; values in the range $-3\mathrm{dB} \cdots -22\mathrm{dB}$ were suitable in the simulations.

The auditory masking threshold is built after applying outer- and middle-ear filters, cf. [Pfl97, Zot04], e.g. according to Zwicker [ZF99], or Terhardt [Ter98]. In the implementation used here, the warped-spectrogram was smoothed by moving average with ERB/Bark width. Using the spectral power of this modified spectrogram (*specific loudness*), the absolute threshold of hearing can be considered, and the up- and downwards masking skirts are easily computed in the warped-spectrum domain, see Fig. 27.

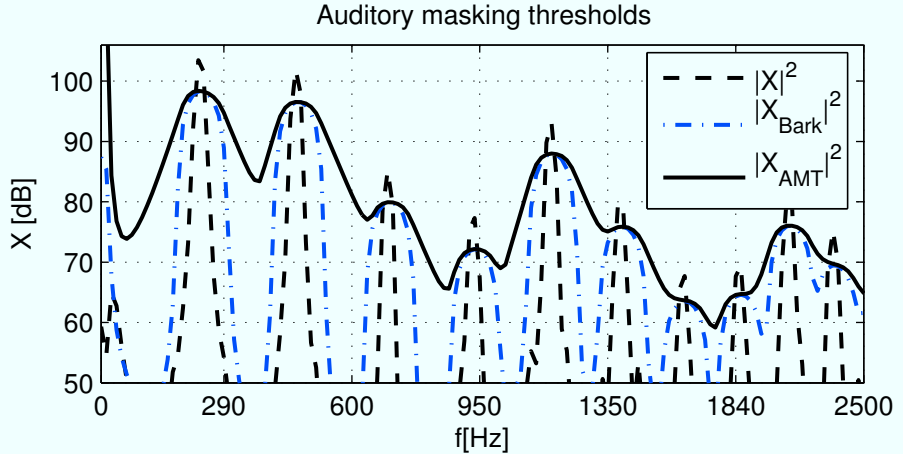

Figure 27: Using outer-middle-ear weighting and auditory warping, a Bark-band smoothed version X_{Bark} of the spectrogram slice X is found, and the simultaneous+absolute masking thresholds X_{AMT}. Unmasked partials are the parts of X exceeding X_{AMT}.

Monophonic total-power spectrogram and primal signal model. For partial-tone decompositions in the multi-channel-case, it is necessary to group and retrieve partials, matching them across the array channels l, in order to obtain a compact description of the sound. As this is a complex task, a simplified approach will be preferred here. For the application with binaural signals in [RE08], a reference channel was selected for each partial according to the channel showing the larger spectral peak. This allows subsequent monophonic partial tracking. However, rather than the maximum amplitude channel, the concept of a total radiated sound is considered here.

Summing up the STFT energy of all microphone signals (weighted sum) yields a single energy distribution in the time-frequency plane. Let's call this the *total-power spectrogram*

$$\left|\mathrm{x}_{\mathrm{total}}[\zeta', \eta]\right|^2 = \sum_{l=1}^{\mathrm{M}} w_l \left|x_l[\zeta', \eta]\right|^2 . \tag{268}$$

w_l denote the weights for each channel according to its energetic contribution.

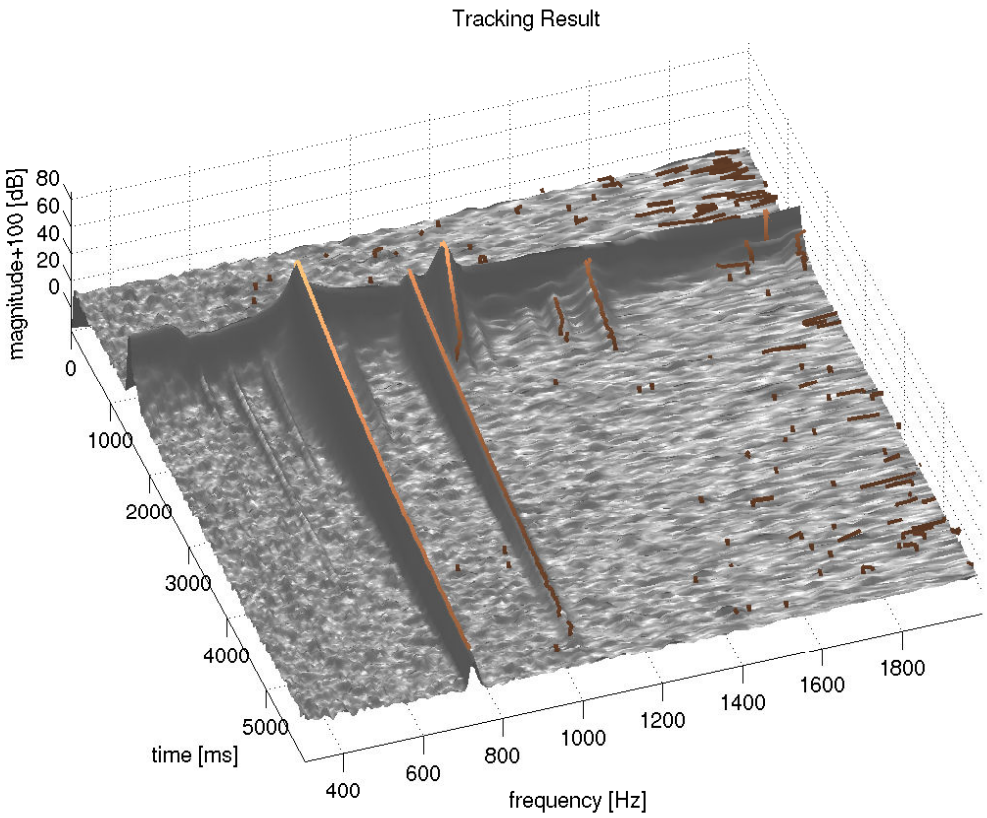

Figure 28: Total-power warped spectrogram with tracking results for a tone of the *bonang barung*.

This weight depends on the sphere surface area covered by the l^{th} microphone. Note that the phase information in $\mathrm{x}_{\text{total}}$ gets lost.

Using the *total-power spectrogram* $|\mathrm{x}_{\text{total}}[\zeta', \eta]|^2$, partial-tracking like in a single-channel application becomes feasible. The basic approach is given in McAulay [MQ86], but only quadratic phase modulation can be considered here since phase-information is unavailable. For sinusoidal components, this yields an estimate of the instantaneous magnitude $\alpha[\eta]$ and frequency $\hat{\zeta}'[\eta]$. Improvements in the frequency localization of clearly resolved partials[2] is achieved by zero-padding and parabolic interpolation, cf. Smith and Serra [SS92]. Finally, Eq. (266) maps the warped instantaneous-frequency estimates $\hat{\zeta}'[\eta]$ back to a linear frequency-scale $\hat{\zeta}[\eta]$.

The *primal signal model* $\hat{s}[\eta]$ for one partial is determined by magnitude $\hat{\alpha}[\eta]$ and instantaneous-frequency candidate $\hat{\zeta}[\eta]$

$$\hat{s}[\eta] = \hat{\alpha}[\eta] \cdot \mathrm{e}^{\mathrm{i}\hat{\phi}[\eta]}, \tag{269}$$

$$\text{with } \hat{\phi}[\eta] = \hat{\phi}[\eta - 1] + \frac{2\pi}{\mathrm{N}_{\text{DFT}}} \frac{\hat{\zeta}[\eta] + \hat{\zeta}[\eta - 1]}{2},$$

[2]The 3 frequency bins involved in parabolic interpolation must only contain a single narrow-band component in order to improve frequency localization.

using a trapezoidal integration rule for $\hat{\zeta}[\eta]$. For sound synthesis, the real part of the complex-exponential, a cosine, is sufficient.

Radiation-pattern retrieval from monophonic model and STFT data. In order to retrieve the spatial magnitude and phase distribution corresponding to the monophonic *primal signal* $\hat{s}[\eta]$ of a single partial, the corresponding complex-valued STFT bins of the multi-channel signals $\hat{\boldsymbol{x}}[\hat{\zeta}', \eta]$ need to be reconsidered. The discrete-space radiation-pattern $\hat{\boldsymbol{g}}[\hat{\zeta}', \eta]$ of this partial is computed by normalization of the STFT signals $\hat{\boldsymbol{x}}[\hat{\zeta}', \eta]$ by its complex-valued *primal signal* $\hat{s}[\eta]$:

$$\hat{\boldsymbol{g}}[\hat{\zeta}', \eta] = \frac{\hat{\boldsymbol{x}}[\hat{\zeta}', \eta]}{\hat{s}[\eta]}. \tag{270}$$

5.1.5 DSHT and the Centering Problem

In order to benefit from the spherical harmonics description of angular distributions, the radiation-pattern $\hat{\boldsymbol{g}}[\zeta', \eta]$ can be decomposed using the DSHT methods presented in chapter 4:

$$\hat{\gamma}_{\mathrm{N}}[\zeta', \eta] = \mathcal{DSHT}_{\mathrm{N}} \left\{ \hat{\boldsymbol{g}}[\zeta', \eta] \right\}. \tag{271}$$

For the analysis, the spherical harmonics representation furthermore allows plotting of smoothly interpolated radiation patterns. As a refinement, DSHT might benefit from suitable weights $\boldsymbol{w}$ according Eqs. (239), (241), (242), (247), or (C)STRIPACK [Bur06, Kei07] in Chap. 4.

Note that the assumption of an angular band-limit N is a prerequisite to DSHT that might become problematic. For instance, the radiation pattern of a central point-source is exactly represented at the order $\mathrm{N} = 0$. However, shifting the source outside the center requires representation with higher orders. Fig. 29 shows that angular band-limitation requires the point-source to stay near the center for accurate (D)SHT re-expansion. In particular at high frequencies that require r_0 to stay small, this poses a *centering problem*:

How can we center a musician with her/his instrument so that every source of sound stays within the given bounds ?

Example: For a surrounding spherical microphone array resolving $\mathrm{N} = 7$, the shift of a point-source must be $r_0/\lambda < 1.53$. At a frequency of 3430Hz ($\lambda = 10$cm), the point-source must lie within $r_0 < 15.3$cm to be fully represented[3]. Consequently, assuming perfect angular band-limitation implies that the representation

[3]This does not mean that any superposition of multiple point-sources inside r_0 can be accurately resolved. In general, combinations of shifted point-sources, i.e. *multipoles*, cf. [Wil99], may yield even higher orders.

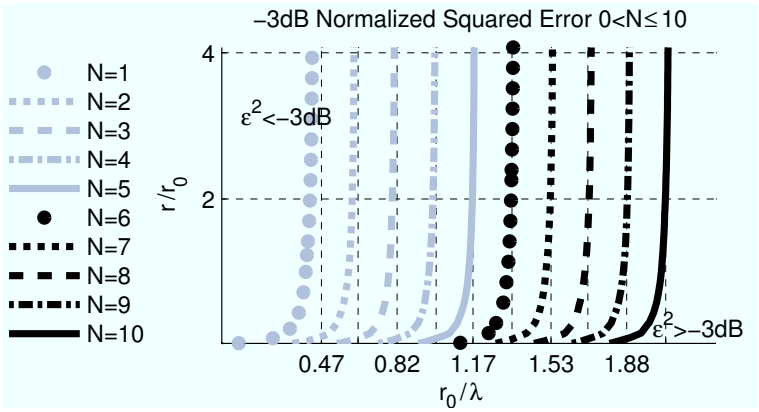

Figure 29: Centering problem: angular band-limitation may cause representation errors. The field of an non-centered point-source at $r_0\,\boldsymbol{\theta}_0$ band-limited to $n \leq \mathrm{N}$ exhibits a representation error that depends on the amount of shift r_0/λ in wave lengths, the relative radius of observation r/r_0, and the angular band-limit N. The contours in the figure indicate the shift r_0/λ, at which the error exceeds a -3dB limit.

of point-sources at $r_0 > 15.3$cm is lacking parts of its actually radiated sound-power. Therefore, nonuniform aliasing might be unacceptable as the direction of the center shift affects the representation. Conversely, uniform aliasing can yield fair approximations under far-field conditions if statistically diffuse radiation is considered.

5.1.6 Examples: Sound-Radiation Analysis Results

gong ageng. [4] The sound-radiation of the *gong ageng* has been captured using the setup depicted in Fig. 30(a) having a radius $r = 1.3$m, and the directivity pattern has been assumed to be rotational symmetric. As given in Chap. 4 on discrete spherical harmonics transforms, the spherical harmonics matrix $\boldsymbol{Y}_\mathrm{N}$ may only contain harmonics with $m = 0$. For a suitable DSHT, a weighted least-squares approach is employed, which uses the weights associated with surface fractions of the sphere, sampled by the microphones, Eq. (247).

The gong can be assumed to produce a dipole-like directivity at its fundamental mode at $f = 43$Hz. From the knowledge about gongs in Varsányi [Var00] and Fleischer [Fle01, Fle02b, Fle02a, Fle03], gongs from Java and Bali have been observed to exhibit beating of two closely spaced frequencies around the octave harmonic. Fig- 30(b) shows the total-power spectrogram and its partials as well as two radiation patterns associated with f_0 and f_1 progressing over time, Figs. 30(c) 30(d). The measurement can be easily extrapolated holographically to larger radii, which is illustrated in Figs. 31(a) 31(b).

[4] The term *gong ageng* denotes the big gong in central Javan Gamelan orchestras.

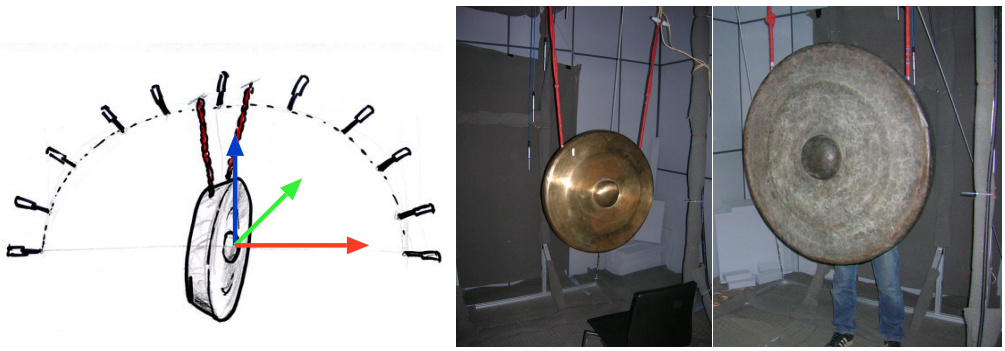

(a) $r = 1.3$m 10 ch. half-circular array, right: *gong ageng*

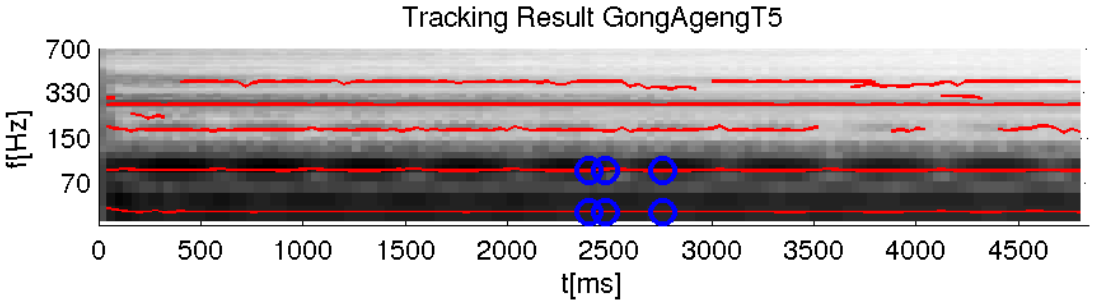

(b) *gong ageng* total-power spectrogram

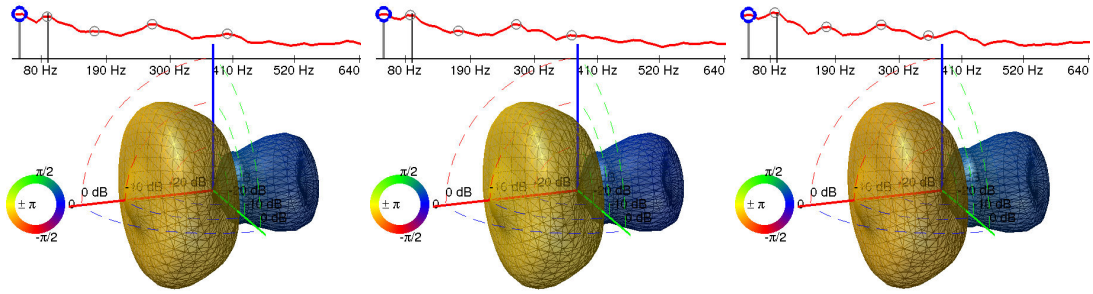

(c) $f_0 = 43$Hz radiation pattern at 2.40s, 2.48s, and 2.76s.

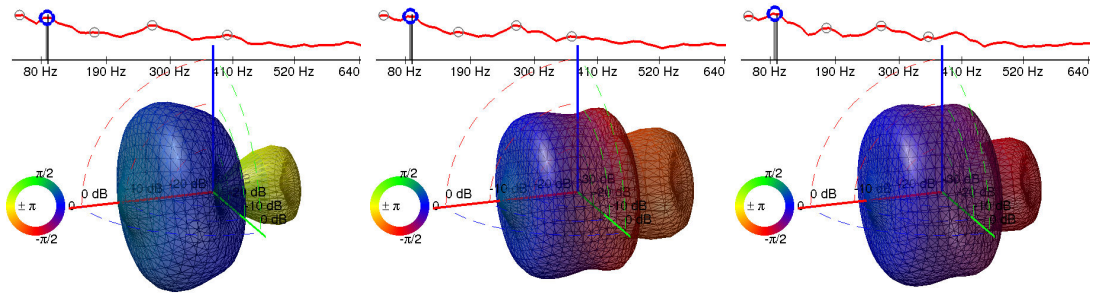

(d) $f_1 = 88$Hz radiation pattern of the beating first harmonic at 2.40s, 2.48s, and 2.76s.

Figure 30: Radiation capture of gongs, and analysis of the *gong ageng*.

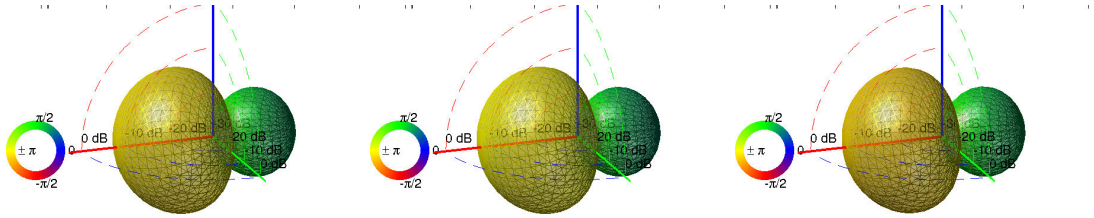

(a) f_0 pattern extrapolated to $r = 10$m

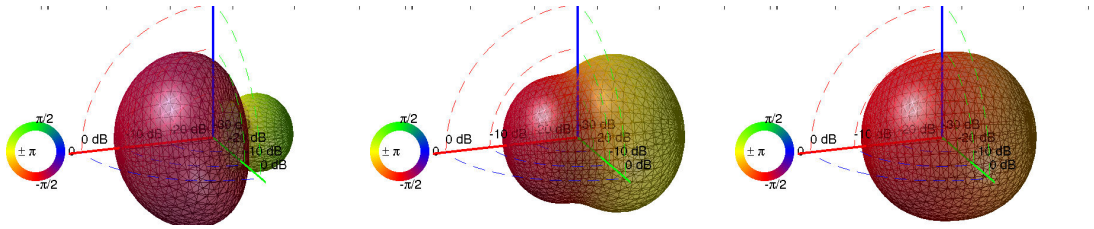

(b) f_1 pattern extrapolated to $r = 10$m

Figure 31: Acoustic holography with the *gong ageng* patterns.

bonang barung. [5] Recalling Chap. 4 on discrete spherical harmonics transforms, we may choose the matrix $\boldsymbol{Y}_{\mathrm{N}}$ to contain only *even* harmonics wrt. $z = 0$ because this instrument is played on a solid, reflecting floor. DSHT is again using weighted least-squares and suitable weights cf. Eq. (247).

Fig. 32(b) shows the total-power spectrogram of a *bonang barung* sound with its partials as well as three radiation patterns Figs. 32(c) associated with these partials at one time-instant. An interesting question, in terms of accuracy in the microphone positions, centering, etc. is: *Would the absolute values detected at the microphones work as radiation pattern as well?* Figs. 32(d) shows the hereby obtained radiation patterns. Note that these patterns cannot exhibit sharp notches as there may be no zero-crossings. Unless captured in the far-field, extrapolation of sound-radiation will become erroneous. This is because the absolute value of a radiation pattern non-linearly generates and mixes spherical harmonics of different orders, which radiate differently beyond the far-field. Usually this must be taken into account at low frequencies.

[5] The term *bonang barung*, see Fig. 3, denotes an instrument consisting of a collection of horizontally mounted small gongs (*bonang*) covering the middle tonal range (*barung*) in the central Javan Gamelan music.

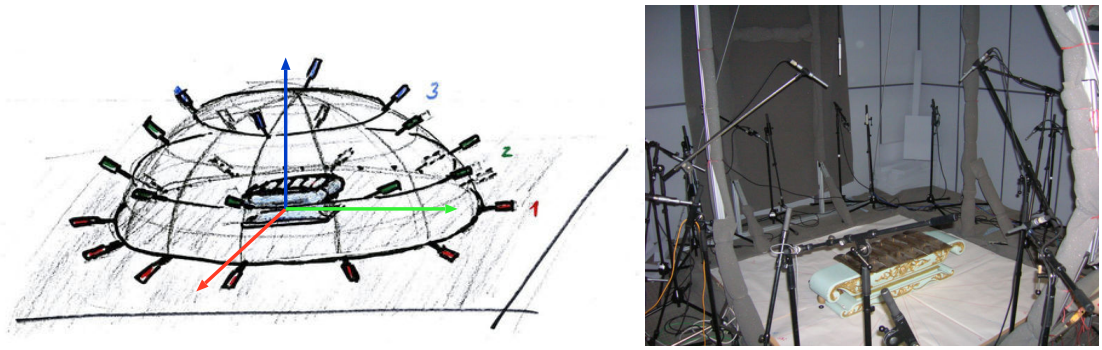

(a) $r = 1.3$m 26 ch. hemispherical array (3 rings); the instrument in the picture differs

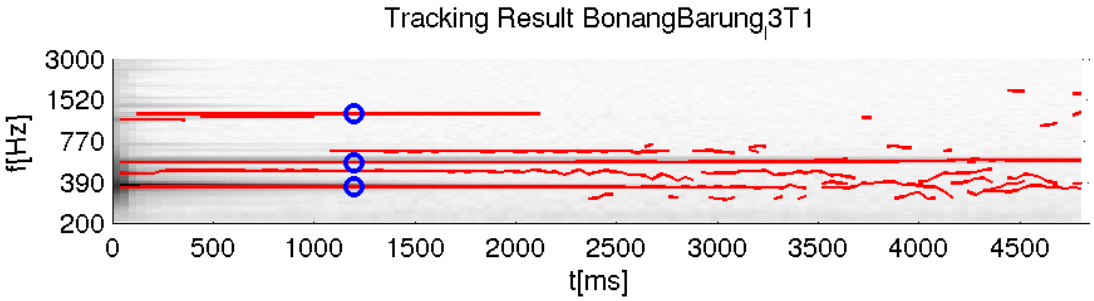

(b) *bonang barung* 3rd tone: total-power spectrogram

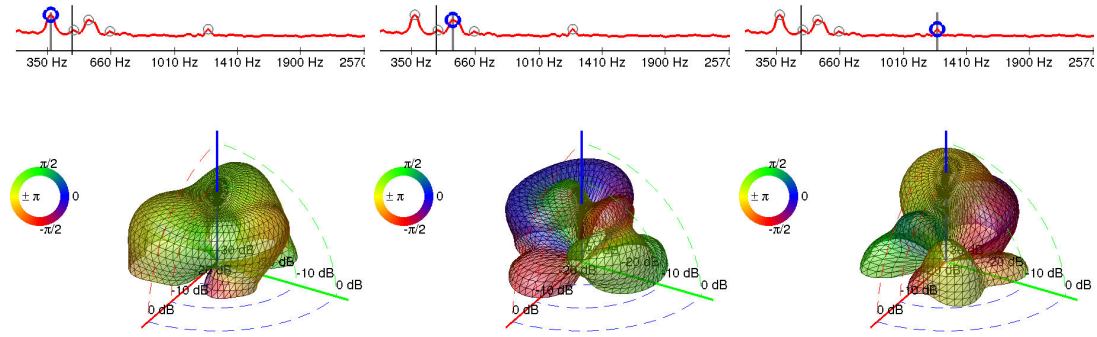

(c) Radiation of $f = \{365,\ 548,\ 1214\}$Hz at 1.2s

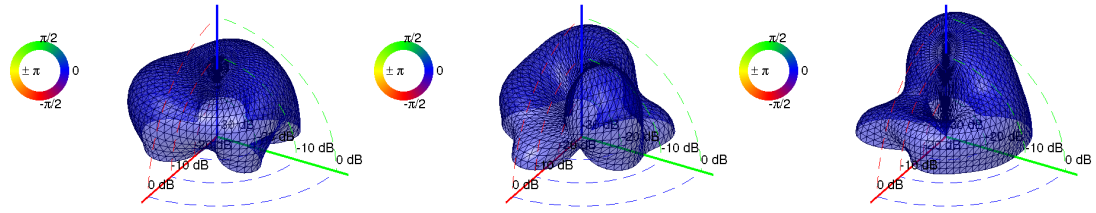

(d) Encoded absolute values of radiation pattern.

Figure 32: Radiation capture of *balungan* instruments, and analysis of the *bonang barung*. The radiation patterns encoded from the absolute values are depicted for comparison.

Saxophone, ITA-Aachen. For this analysis, recordings from the Institute of Technical Acoustics in Aachen (ITA) have been used [Pol07, Reu08, SRBA08]. It has been found insightful to regard radiation patterns at matching frequencies but different notes within a complete melody. The radiation patterns can be reported to be stationary during the tones, but may differ for different notes (instrument configuration Chap. 1).

Fig. 33(a) shows the auditory-scale warped total-power spectrogram of the melody and the markers for the radiation patterns compared in Figs. 33(b) 33(c) 33(d). The radiation patterns of the first harmonic of one note and the fundamental frequency of its octave note seems to match well Fig. 33(b). On the other hand, the matching frequencies associated with matching partials of two other musical intervals do not seem to yield the same directivity patterns for the saxophone Figs. 33(c) 33(d).

Comparisons of this kind become easier using surrounding spherical microphone arrays and provide a new step forward in the understanding the musical acoustics of instruments. For instance, it can be expected that brass instruments exhibit frequency dependent directivity patterns that are invariant for different notes. Whereas the directivity of woodwind and many other instruments will probably depend on the note. The perceptual implications of these differences could be investigated to reduce the effort of computational directivity-models.

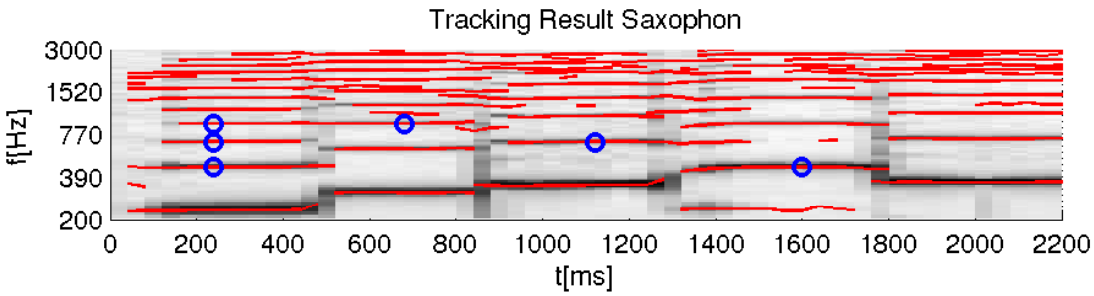

(a) Total-power spectrogram of a saxophone melody recorded with the $r = 2.2$m array Fig. 24(a) at ITA, Aachen [Reu08], played by Sönke Pelzer.

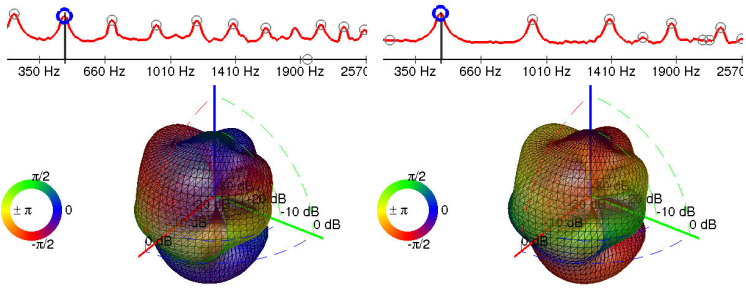

(b) $f = 463$Hz as f_1@0.24s and f_0@1.6s (octave)

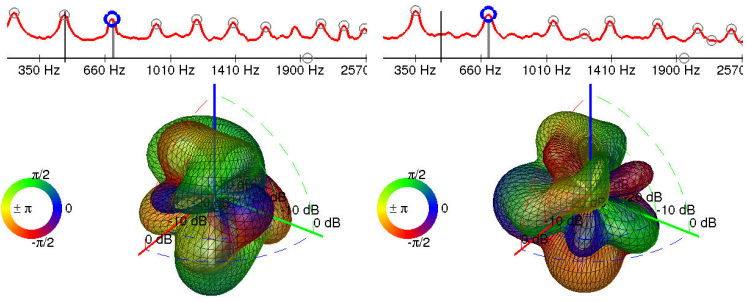

(c) $f = 692$Hz as f_2@0.24s and f_1@1.12s (fifth)

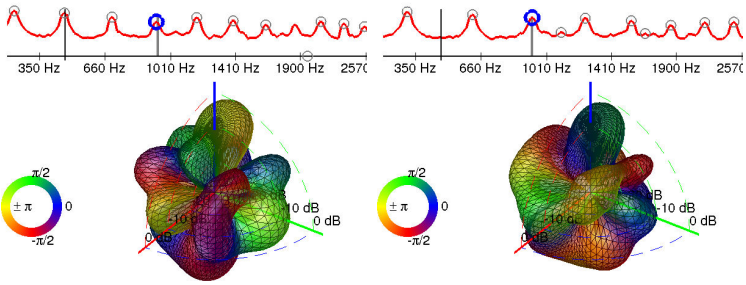

(d) $f = 930$Hz as f_3@0.24s and f_2@0.68s (fourth)

Figure 33: Radiation of the partials of a saxophone (ITA-Aachen).

5.1.7 Outlook on Adaptive Sound-Radiation Identification

The following paragraphs show adaptive identification methods for the SIMO radiation-model as an attractive alternative to the spectral model. Given a multi-channel *sound-radiation signal* $\boldsymbol{\chi}_{\mathrm{N}}(\omega)|_{r=\mathrm{R}}$ the question is: What is the *primal signal* $s(\omega)$, and the *radiation pattern* $\boldsymbol{\gamma}_{\mathrm{N}}(\omega)$?

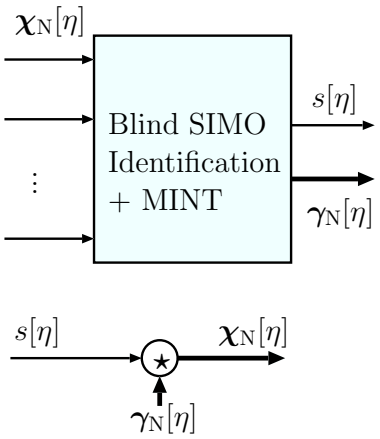

Figure 34: SIMO sound-radiation with source-filter problem. The first stage extracts a primal signal $s[\eta]$ that reconstructs the sound-radiation $\boldsymbol{\chi}_{\mathrm{N}}[\eta]$ best using the radiation impulse response $\boldsymbol{\gamma}_{\mathrm{N}}[\eta]$, i.e. $\boldsymbol{\chi}_{\mathrm{N}}[\eta] \stackrel{!}{=} s[\eta] \star \boldsymbol{\gamma}_{\mathrm{N}}[\eta]$.

Non-blind identification. In order to identify the SIMO impulse responses $\boldsymbol{\gamma}_{\mathrm{N}}[\eta]$, it is desirable to know the primal signal $s[\eta]$. Using $s[\eta]$ as a reference signal, the responses $\boldsymbol{\gamma}_{\mathrm{N}}[\eta]$ could be determined from $\boldsymbol{\chi}_{\mathrm{N}}[\eta]$ by adaptive filters (beamforming, LMS, [Hay02]). However, $s[\eta]$ is usually not accessible. Instead, other reference signals needs to be found.

For incident fields, the zero-order harmonic is likely to contain all the spectral information of sound incident from a single source[6] without co-channel interference (CCI, [HCB06]). Hence Hellerud *et al.* [HSS09, HS09] are able to successfully select the zero-order channel out of their compact spherical microphone array as a suitable reference, from which all irradiation responses are identified. However, this might not be feasible for sound-radiation, and even worse: it could turn out to be an ill-posed choice[7].

Blind channel identification. The spectrum of the primal signal $s[\eta]$ could be identified by averaging power spectra/autocorrelations across the channels of

[6] The advanced reader recognizes this by observing the complex-valued non-zero radial functions in the incident part of translated multipole fields in Eq. (166), Chap. 3

[7] Conversely, the zeroes of the real-valued radial functions in the radiating part of translated multipole fields may cancel components of the measured signal, cf. Eq. (166), Chap. 3.

the radiation signal. However in doing so, all phase information of the primal signal gets lost. Direct summation of all channels is not an option since temporal interference (TI) might destroy parts of the signal.

In order to reconstruct a primal signal with neither temporal interference nor losing phase relations, it could be preferable to perform *blind channel identification* (BCI) of the SIMO response first, cf. [HBC05, HCB06]. According to literature, BCI can be solved by, e.g., the *multi-channel least-mean-square algorithm* (MCLMS), which identifies the radiation impulse responses $\boldsymbol{\gamma}_{\mathrm{N}}[\eta]$ of the given problem. Subsequent to BCI, the application of the *multiple-input/output inverse theorem* (MINT, pseudo-inverse, see [HCB06]) estimates the *primal signal* $s[\eta]$.

This task has neither been implemented nor tested within this thesis and is subject to future work. It has to be remarked, though, that the SIMO identification relies on a fully excited signal spectrum of $s[n]$, which must be reflected in the SIMO channels. This is referred to as *Multichannel Diversity and the Common-Zero Problem* in Sec. 2.7.7 of the book [HCB06]. However, musical instruments will frequently cause violation of these requirements since the spectra of musical sounds tend to be spectrally *sparse*. The SIMO BCI algorithm will yield ambiguous channel responses due to the parts of near-zero spectral energy. Pre-whitening should only be employed with care as spectrally weak parts should not be over-emphasized, potentially causing further degradation of the BCI.

5.1.8 Future Research: Fully Parametric Directivity, Position, and Orientation Tracking of Partials

The most interesting goal that can be imagined as a result of future research, is the decomposition of the sound-radiation of partials into even more parameters:

- time-frequency-amplitude track of the partial
- x-y-z-position track of its origin of radiation
- α-β-γ rotational orientation track of its directivity pattern
- $\boldsymbol{\gamma}_{\mathrm{N}}$ track of its directivity pattern

However, a suitable algorithm for identification of shifted sources, which circumvents the *centering problem* (Sec. 5.1.5), has not been discovered yet. Furthermore, a way of parametrization must be found for stochastic residual signals. Using this parametrization, for example the movements of the directivity patterns, their actual order, position, etc. can be manipulated. These manipulations might offer not only artistic means of expression, but may also reduce the complexity of playback; assuming position and orientation reduces the information stored in the directivity track $\boldsymbol{\gamma}_{\mathrm{N}}$ (order and change rate).

Chapter VI

SYNTHESIS OF SOUND-RADIATION USING COMPACT SPHERICAL LOUDSPEAKER ARRAYS

In the light of the many publications on compact spherical loudspeaker arrays, it is interesting that many important questions remain unanswered in the early works. For example, it is yet unclear whether a common interior air volume is the better choice for a low-frequency array than an individually isolated interior. Furthermore, the high dynamic range of operation needs some research. If we assume that these devices play back spherical patterns at a certain radius r_p, the questions are:

- What range of target sound pressure levels can be covered?
- Which range of radii r_p can be used?
- What is the upper cutoff frequency for spatial aliasing?
- How does the dynamic range of the digital output affect level and radial ranges and the average/peak currents through the loudspeaker coils?
- What is the resulting frequency range?

Before these questions are answered, a comprehensive analysis of compact spherical loudspeaker arrays is required. Therefore, the first half of this chapter studies all representations and computational models presented in [ZSH07, ZH07, ZN07, ZSN08, ZPS08, Pom08] for this type of arrays. This is structured as follows: Introduction of radiation synthesis with compact spherical loudspeaker arrays, system descriptions and angular radiation control based on microphone array measurements, laser vibrometry measurements with cap model, a complete electroacoustic model, synthesis errors and angular aliasing, more efficient control systems, and radial beam steering. Finally, the chapter elaborates on some of the above questions giving an analysis of the influence of the enclosure, yielding the feasible ranges for level, radius, and spherical order.

6.1 Introduction of Synthesis of Sound-Radiation

In 1997, Gabriel Weinreich filed a patent [Wei97] about a *Directional Tone Color* loudspeaker, Fig. 35. This new device attempts to reproduce the radiation pattern of a violin by creating interferences of the sound in space. His loudspeaker creates these interferences by playing the sound through pipes bent about to have different path lengths.

Figure 35: Gabriel Weinreich's Directional Tone Color Loudspeaker that simulates sound-radiation of the violin, Curtin [Cur00].

A few years later, pioneering works on compact spherical loudspeaker arrays for re-synthesis of directivity patterns have been published.

6.1.1 Compact Spherical Loudspeaker Arrays

Compact spherical arrays are particularly suited for acoustic radiation synthesis in real or virtual reality environments. The spherical arrays in the scope of this thesis basically consist of a rigid spherical body or Platonic solid, into which individually driven loudspeakers are mounted.

Omnidirectional compact spherical loudspeaker arrays. Nowadays, this kind of solid compact spherical loudspeaker arrays is mostly used as powerful omnidirectional sound source in room acoustics measurements. An important model analysis using a group theoretical approach has been published by Viggo Tarnow [Tar74], comparing the performance of loudspeaker arrays arranged in the shape of Platonic solids. An interesting lumped-element simulation of the impedances of such loudspeakers is found in the AkAbak Manual, Panzer [PC97].

Another application for omnidirectional Platonic loudspeaker arrays has been found by Yoshihide Hayakawa, Takanori Nishino, and Kazuya Takeda for near-field HTRF measurements [HNT07]. The work of Wieland Weise [Wei04] analyzes the performance of hemispherical loudspeaker arrays with both a spherical harmonics approach (in accordance with [Tar74]) and the boundary element method. A very detailed survey on the omnidirectional characteristics of a huge variety of custom-built Platonic-solid loudspeaker arrays has been carried out by Timothy Leishman, Sarah Rollins, and Heather Smith [LRS06]. Gottfried Behler improved the design of a dodecahedral omni-source by extending the compact spherical loudspeaker array to a 3-way system [Beh00]. Ingo Witew, Behler, and Michael Vorländer pointed out the significant dependency of room acoustics quality measures above 1kHz on the directivity of the measurement source [WBV05].

Compact spherical loudspeaker arrays for radiation synthesis. Recently, there have been several publications by the IRCAM research-group, describing the control of radiation patterns given specific array implementations. After the first studies of René Caussé, J.F. Bresciani, and Olivier Warusfel [CBW92], the first theoretical approach was established by Warusfel, Philippe Derogis, and Caussé [WDC97]. Several practical works from Nicolas Misdariis, Warusfel, Caussé, and François Nicolas followed [MNWC01, WM01, MNWC01, MWC01, MOWN02, WM04].

In the meantime at *Princeton*, Perry Cook, Georg Essl, George Tzanetakis, and Dan Trueman [CETT98] were researching into this new field, targeting an application in their music performances, followed by practical works of Trueman and Cook [TC99, CT99], later also with Curtis Bahn [TBC00], and finally the Princeton Laptop Orchestra (PLOrk) [TCSW06] with also Scott Smallwood and Ge Wang.

Furthermore, the people at CNMAT, Berkeley, launched their research with solid compact spherical loudspeaker arrays with Justin Baird, John and Perrin Meyer, Peter Kassakian, and David Wessel [BMM+01]. Several interesting works on the optimization of directivity pattern filters, and the characterization of compact spherical loudspeaker arrays in terms of their spherical harmonics error range from Kassakian and Wessel followed [KW03, KW04].

The Orbophone, a translucent dodecahedral loudspeaker array, was presented by Damien Lock, Greg Schiemer, and Lulu Ong from the University of Wollongong, as a new device for artistic multimedia performances with audio and light [LSO06, LS06]; note the excellent review on the history of directivity control from a computer music perspective in their papers.

In Brescia, P. G. Beretta, G. Petersini, and E. Piana at the Dipartimento di

Ingegneria Meccanica designed a commercial, well-shaped spherical-surface dodecahedral array [BPP04]; their study also shows the intent towards an extension to a variable directivity loudspeaker.

Presently, Gottfried Behler's research activity in this field has been finding its way into several publications from the ITA in Aachen, [Beh06b, Beh06a, Beh07a, Beh07b] for the application as an auralization tool for concert halls, considering the source directivity of the auralized sound. Furthermore, Martin Pollow's master's thesis [Pol07] at the ITA is an excellent work on the control of a dodecahedral loudspeaker given magnitude directivity data of musical instruments. Some practical work from CNMAT on a solid highly integrated and powerful 120-element tweeter-array was published by Rimas Avizienis, Adrian Freed, Kassakian and Wessel [AFKW06]; which I had the lucky opportunity to work with in the preparation for this thesis. Additionally, low-cost experiments were presented by Michael Zbyszyński on the web [Zby07] and by Peter Lucas Hulen [Hul08]. On the other hand, some research has been published by the IEM research-group in Graz, considering analytical models of the spherical speaker systems, showing their limitations in spatial resolution, a model for crosstalk, and a framework for directivity control [ZS06, ZS07, ZSH07, ZH07, ZN07, Pom08, ZSN08, ZPS08]. Explicit computations of electrical voltages for different (baffled/common) enclosure designs and dealing with an approach for magnitude synthesis have been published by Alexander Mattioli Pasqual, José Roberto Arruda and Philippe Herzog [PAH08b, PAH08a] at Laboratório de Vibroacústica Universidade Estadual de Campinas and LMA-CNRS Marseille. In a newer paper [PAH09], there is an interesting consideration on a modal space with all the degrees of freedom, the *acoustic radiation modes*.

Further questions about the interactive exploration of the perception of directivity patterns have been raised in the papers [FSZ08, Sch09] by Adrian Freed and Andy Schmeder. It turns out that they circumvent the conceptual problems we have with the perception of beams by using interactive interfaces, enabling playful learning of this rather new perceptual quality.

Examples and questions. Fig. 36 gives some examples of compact spherical loudspeaker arrays. Even if this is a narrow selection only, all these loudspeaker systems give rise to several common questions. Given the hardware of a compact spherical loudspeaker array:

- What will be the radiation pattern if I feed one loudspeaker?
- What is the interaction between the speakers?

- How can I determine an over-all characterization by measurement?

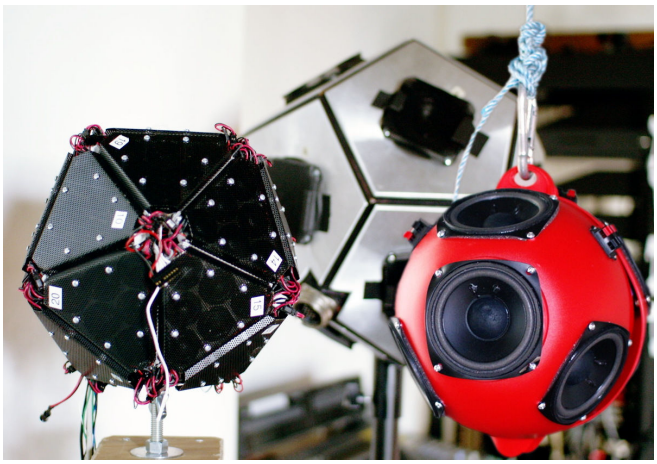

(a) CNMAT spherical loudspeakers, Berkeley

(b) IEM spherical loudspeakers, Graz

(c) ITA spherical loudspeakers, Aachen (photo: ITA, Behler)

Figure 36: Compact spherical loudspeaker arrays.

In its first half, this chapter tries to give answers to these questions.

6.2 System Description Based on Microphone Array Measurements

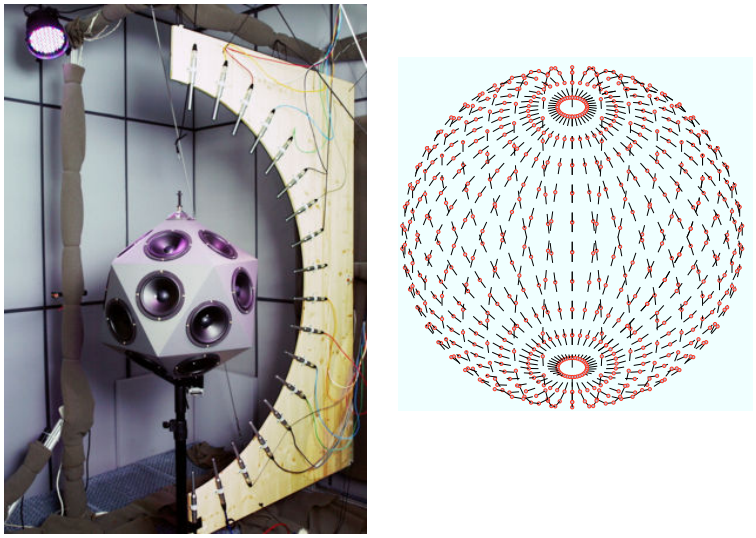

Figure 37: Measurement setup for compact spherical loudspeaker system identification with microphones. An electric turntable facilitates sampling the complete spherical grid depicted on the right [Pom08].

Using an array of microphones located at a certain concentric sphere surrounding the spherical loudspeaker, we are able to determine all transducer directivities, i.e. transfer functions between loudspeakers and microphones, see Fig. 37. How to design a control system based on the measurement data has been presented in [Pom08, ZSN08, ZPS08] as an efficient means of directivity control and will be explained in the following paragraphs.

Output pressure directivity pattern (MIMO). The multiple-input-multiple-output device under test (MIMO, Fig. 38(a)) is described as

$$\boldsymbol{p} = \boldsymbol{G}\,\boldsymbol{u}. \tag{272}$$

The matrix $\boldsymbol{G}$ linearly combines the vector of L loudspeaker input voltages $\boldsymbol{u}$ to form the sound pressure directivity pattern $\boldsymbol{p}$ measured with M microphones, see Fig. 38(a). Note that the dependency on the frequency variable ω has been omitted for better readability, but in this simple form the relation holds for the frequency domain only.

A control system (MIMO-ctl, Fig. 38(b)) optimizing for the desired angular directivity pattern $\boldsymbol{p} \approx \boldsymbol{p}_{\text{ctl}}$ using the least-squares inverse $\boldsymbol{G}^{+}$

$$\boldsymbol{p} = \boldsymbol{G}\,\boldsymbol{G}^{+}\,\boldsymbol{p}_{\text{ctl}}$$

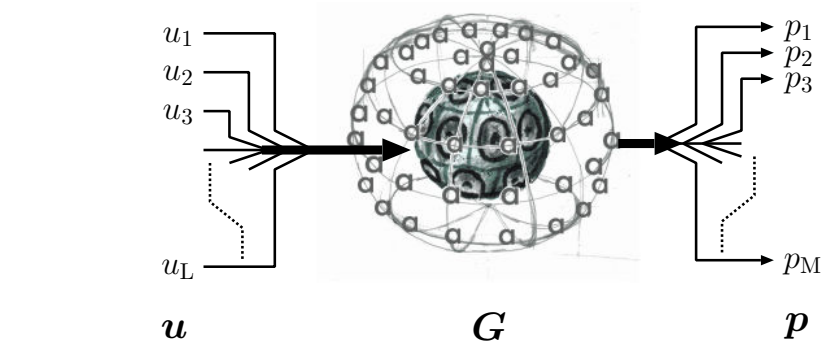

(a) MIMO-system

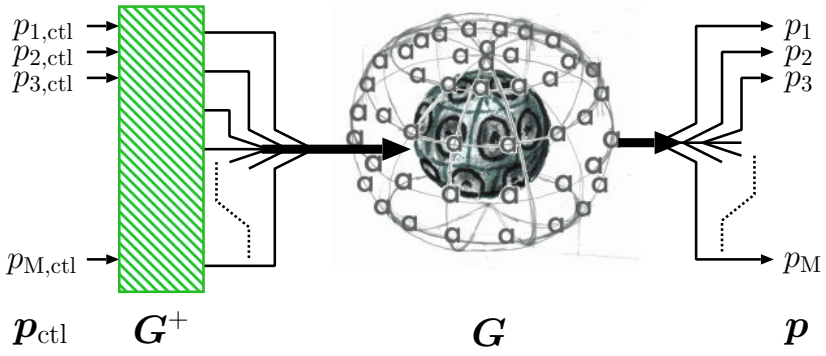

(b) MIMO-ctl

Figure 38: Block-diagrams of MIMO measurement and control of compact spherical loudspeaker arrays. Boxes with -45°-hatching (green) correspond to control blocks.

doesn't seem practical. It yields large approximation errors with unknown spatial error distribution. In the following sections the real-valued spherical harmonics (SH) will be used as base set of angular directivity patterns. They also enable radial beamforming as described in [ZN07] and Sec. 6.7.

The concept of an *angular band limit* seems to be appropriate for directivity control to ensure a rotation invariant bounded resolution within the entire angular space. Spherical harmonics expansions truncated at some order N inherently support this concept, see Sec. 3.3.2.

Spherical harmonics output directivity (MIMO-LSH). [1] A decomposition of the output directivity pattern $\boldsymbol{p}$ into SH can be accomplished using discrete spherical harmonics transform (DSHT). We use a weighted least-squares transform

[1] For abbreviation, the MIMO-system in Eq. (272) transformed into spherical harmonics from different sides are denoted as:
MIMO-LSH ... system transformed to SH from the left, at the system output,
MIMO-RSH ... system transformed to SH from the right, at the system input,
MIMO-SH ... system entirely transformed to SH, from the left and the right. .

according Eq. (245), the microphone angles $\{\boldsymbol{\theta}_l\}$, and $\boldsymbol{Y}_\mathrm{N} = \mathrm{mtx}_\mathrm{N}\,\{Y_n^m(\boldsymbol{\theta}_l)\}$. The DSHT yields the coefficients $\boldsymbol{\psi}_\mathrm{N}$

$$\boldsymbol{\psi}_\mathrm{N} = \left(\boldsymbol{Y}_\mathrm{N}^\mathrm{T}\right)^{+\boldsymbol{w}}\ \boldsymbol{p}, \tag{273}$$

using the weight vector $\boldsymbol{w}$ similar to those given in Sneeuw [Sne94]. With theoretically infinitely many array microphones, the system without truncation $\mathrm{N} \leq \sqrt{M} - 1 \to \infty$ yields the coefficients $\boldsymbol{\psi}_\mathrm{N}$ of the *spherical wave spectrum* of the sound pressure, cf. Sec. 2.3.1. By the above equation, the system Eq. (272) is transformed from the left hand side (MIMO-LSH, Fig. 39(a)) into

$$\begin{aligned}\boldsymbol{\psi}_\mathrm{N} &= \left(\boldsymbol{Y}_\mathrm{N}^\mathrm{T}\right)^{+\boldsymbol{w}}\ \boldsymbol{G}\,\boldsymbol{u} \\ &= \mathring{\boldsymbol{G}}_\mathrm{N}\,\boldsymbol{u}.\end{aligned} \tag{274}$$

Spherical harmonics input directivity (MIMO-RSH). [1] On the other hand, the angularly distributed loudspeaker array voltage signals may also be represented by SH, i.e. described as a SH-coefficient vector $\boldsymbol{\Upsilon}_{\mathrm{N_c}}$. This representation is obtained by an SH-encoder (compare Higher-Order-Ambisonics, HOA, [Dan01, ZPF09]) of the order $\mathrm{N_c}$. We write the encoder as a matrix $\boldsymbol{C}_{\mathrm{N_c}} = \mathrm{mtx}_{\mathrm{N_c}}\,\{Y_n^m(\boldsymbol{\theta}_l)\}$ containing the SHs sampled at the array loudspeaker angles $\{\boldsymbol{\theta}_l\}$, i.e. $\boldsymbol{\Upsilon}_{\mathrm{N_c}} = \boldsymbol{C}_{\mathrm{N_c}}\ \boldsymbol{u}$. For details on the physical meaning of the SH-encoder refer to the matrix $\boldsymbol{A}_{\mathrm{N_c}}$ in Sec. 6.3.2, Eqs. (287)(290). Voltage control by the right inverse $\boldsymbol{u} = \boldsymbol{C}_{\mathrm{N_c}}^+\ \hat{\boldsymbol{\Upsilon}}_{\mathrm{N_c}}$ ensures that $\hat{\boldsymbol{\Upsilon}}_{\mathrm{N_c}} = \boldsymbol{\Upsilon}_{\mathrm{N_c}}$, hence

$$\boldsymbol{u} = \boldsymbol{C}_{\mathrm{N_c}}^+\ \boldsymbol{\Upsilon}_{\mathrm{N_c}}, \tag{275}$$

wherein the so-called HOA- or SH-decoder $\boldsymbol{C}_{\mathrm{N_c}}^+$ is right-inverse to $\boldsymbol{C}_{\mathrm{N_c}}$, i.e. $\boldsymbol{C}_{\mathrm{N_c}}\ \boldsymbol{C}_{\mathrm{N_c}}^+ \stackrel{!}{=} \boldsymbol{I}$. Using this decoder, the original MIMO system Eq. (272) is transformed from the right hand side (MIMO-RSH, Fig. 39(a)) into

$$\begin{aligned}\boldsymbol{p} &= \boldsymbol{G}\,\boldsymbol{C}_{\mathrm{N_c}}^+\ \boldsymbol{\Upsilon}_{\mathrm{N_c}} \\ &= \mathring{\boldsymbol{G}}_{\mathrm{N_c}}\ \boldsymbol{\Upsilon}_{\mathrm{N_c}}.\end{aligned} \tag{276}$$

Spherical harmonics in- and output directivity (MIMO-SH). [1] Employing both, the SH-decoder for input voltages and DSHT for the output sound pressures, the system Eq. (272) becomes (MIMO-SH, Fig. 39(a))

$$\begin{aligned}\boldsymbol{\psi}_\mathrm{N} &= \left(\boldsymbol{Y}_\mathrm{N}^\mathrm{T}\right)^{+\boldsymbol{w}}\ \boldsymbol{G}\,\boldsymbol{C}_{\mathrm{N_c}}^+\ \boldsymbol{\Upsilon}_{\mathrm{N_c}} \\ &= \mathring{\boldsymbol{G}}_{\mathrm{N},\mathrm{N_c}}\ \boldsymbol{\Upsilon}_{\mathrm{N_c}}.\end{aligned} \tag{277}$$

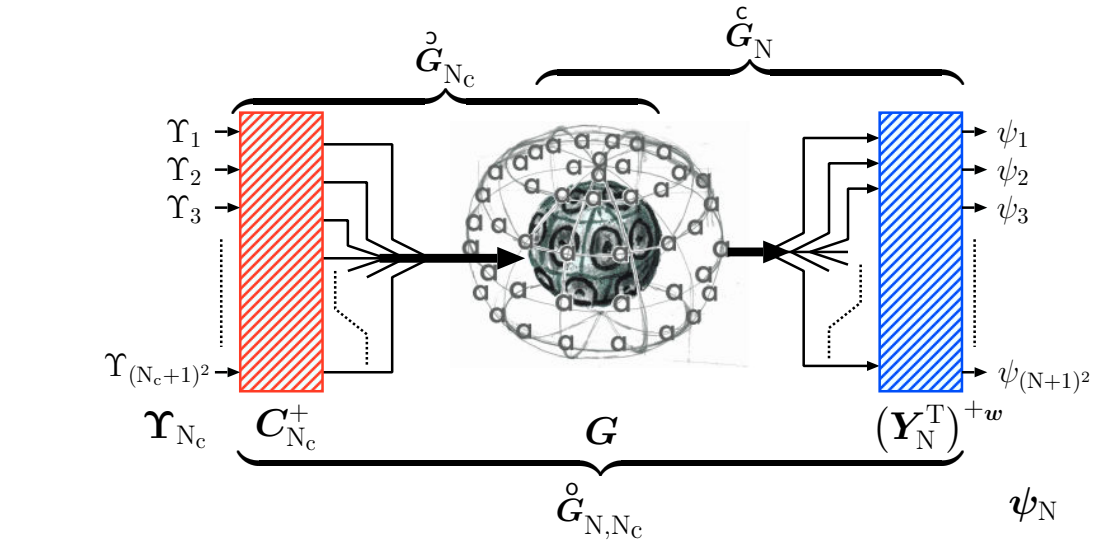

(a) MIMO-LSH/RSH/SH

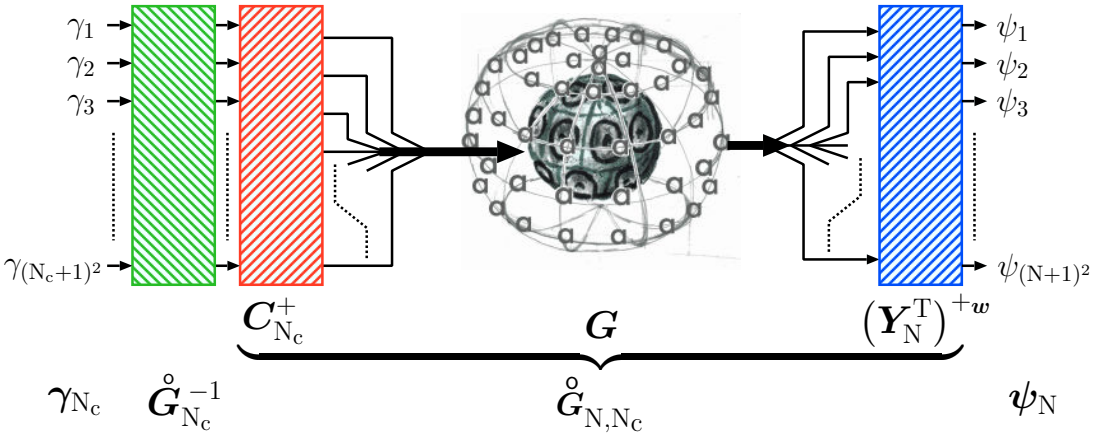

(b) MIMO-SH-ctl

Figure 39: Block diagrams of spherical harmonics representations (MIMO-LSH/RSH/SH) of $\boldsymbol{G}$, and control (MIMO-SH-ctl). +45°-hatching denote transforms (red: from right, blue: from left), -45°-hatching (green) denote control.

6.2.1 Angular Directivity Control

In the paragraphs below, the three main variants of directivity control systems are presented. Each of the systems accomplishes directivity control by voltages $\boldsymbol{u}$ that have been derived from the measured MIMO transfer functions $\boldsymbol{G}$.

- Firstly, direct least-squares inversion of system equation Eq. (272) is used to obtain the L×M control system MIMO-ctl, Figs. 38(a), 38(b). The approach yields an approximation quality that strongly depends on angular sampling.

- Secondly, inversion of the $\mathrm{N_c}$-truncated output spherical wave spectrum can be used to determine an L×$(\mathrm{N_c}+1)^2$ control system MIMO-LSH-ctl, compare Eq. (273) with $\mathrm{N} = \mathrm{N_c}$ and Fig. 39(a). It has the advantage of being exact

within the N_c-angularly band-limited representation.

- As a third alternative, the $(N_c+1)^2 \times (N_c+1)^2$ MIMO-SH-ctl system has been proposed as the favorable variant in [ZSN08, ZPS08], Fig. 39(b). In this representation, some transfer paths may become irrelevant, see Fig. 50.

These variants are expressed as follows, each providing either $\boldsymbol{p} \stackrel{!}{=} \boldsymbol{p}_{\text{ctl}}$ or $\boldsymbol{\psi}_{N_c} \stackrel{!}{=} \boldsymbol{\gamma}_{N_c}$

$$\text{MIMO-ctl:} \quad \boldsymbol{u} = \boldsymbol{G}^{+}\,\boldsymbol{p}_{\text{ctl}} \qquad \Rightarrow \boldsymbol{p} = \boldsymbol{G}\,\boldsymbol{G}^{+}\,\boldsymbol{p}_{\text{ctl}} \approx \boldsymbol{p}_{\text{ctl}}, \tag{278}$$

$$\text{MIMO-LSH-ctl:} \quad \boldsymbol{u} = \overset{c}{\boldsymbol{G}}{}^{+}_{N_c}\,\boldsymbol{\gamma}_{N_c} \qquad \Rightarrow \boldsymbol{\psi}_{N_c} = \overset{c}{\boldsymbol{G}}_{N_c}\,\overset{c}{\boldsymbol{G}}{}^{+}_{N_c}\,\boldsymbol{\gamma}_{N_c} = \boldsymbol{\gamma}_{N_c}, \tag{279}$$

$$\text{MIMO-SH-ctl:} \quad \boldsymbol{u} = \boldsymbol{C}^{+}_{N_c}\,\mathring{\boldsymbol{G}}^{-1}_{N_c}\,\boldsymbol{\gamma}_{N_c} \qquad \Rightarrow \boldsymbol{\psi}_{N_c} = \mathring{\boldsymbol{G}}_{N_c}\,\mathring{\boldsymbol{G}}^{-1}_{N_c}\,\boldsymbol{\gamma}_{N_c} = \boldsymbol{\gamma}_{N_c}. \tag{280}$$

Although the dimensions of the frequency dependent parts of MIMO-SH-ctl are already small $N_{\text{fft}} \times (N_c+1)^2 \times (N_c+1)^2$, it becomes clear later in Sec. 6.6 that regular loudspeaker layouts even yield nearly diagonal SISO, i.e. single-input-single-output, control systems. As the spherical harmonics are eigenfunctions in the continuous angular space, they approximate the eigenvectors of the discrete angular space of the array. This is particularly true if the array layout provides near orthogonal sampling of the SHs. Consequently, the transform nearly diagonalizes the MIMO-SH-ctl at all frequencies. The examples in Fig. 50 for the IEM-icosahedral speaker demonstrate the practical relevance of this relation using theoretical and measured acoustical/mechanical parameters.

6.3 System Description Based on a Surface-Velocity Model and Laser Vibrometry

The loudspeakers within a compact spherical loudspeaker array may interact with each other via acoustic interior and exterior cross-talk paths. Essentially, it is possible to directly determine the acoustically coupled output velocities of the discrete loudspeakers by Laser-Doppler vibrometry measurement [RJ07, JR07]. In principle, this formulation already allows to compute a system that controls the discrete loudspeaker velocities independently. Again, a spherical harmonics representation is desirable in order to get a smooth definition of the angular resolution. Therefore the cap model, an analytic description of the spherical harmonics surface velocity patterns for compact spherical loudspeaker arrays is presented in Sec. 6.3.2. After considering suitable control systems, the corresponding sound-radiation is modeled.

6.3.1 System Identification by Laser-Doppler Vibrometry.

In order to maintain clarity, this section starts with the description of the practical measurements and the underlying MIMO-systems and advances to the analytic model of sound-radiation later on.

Output velocity directivity pattern (MIMO). The MIMO-system identified by laser-vibrometry describes the transfer functions between the L input voltages $\boldsymbol{u}$ and the L loudspeaker output velocities $\boldsymbol{v}$, see Fig. 40

Figure 40: Laser Doppler vibrometry (LDV) measurements on an icosahedral loudspeaker array.

$$\boldsymbol{v} = \boldsymbol{T}\ \boldsymbol{u}. \tag{281}$$

Direct control over the membrane velocities $\boldsymbol{v}$ can be obtained using an L × L control system MIMO-ctl and the steering vector $\boldsymbol{v}_{\text{ctl}} \stackrel{!}{=} \boldsymbol{v}$, which is written as

$$\boldsymbol{v} = \boldsymbol{T}\,\boldsymbol{T}^{-1}\,\boldsymbol{v}_{\text{ctl}}.$$

Given invertibility of $\boldsymbol{T}$, this control system is already usable and mostly well-behaved, but still somewhat expensive to compute. To improve the smoothness and efficiency, the next section presents a cap model that provides spherical harmonics coefficients of the surface velocity distribution due to $\boldsymbol{v}$.

6.3.2 The Spherical Cap Surface Velocity Model

The paper [ZSH07] describes the sphere cap model of a compact spherical loudspeaker array. It models the surface velocity distribution, which can be identified selectively by measurements. Essentially, the compact spherical loudspeaker array is assumed to have spherical geometry and a rigid surface with the radius r_0. The radial surface velocity is assumed to be $v_r|_{r_0} = 0$ everywhere except at the loudspeakers positions. Within the angular region of the l^{th} loudspeaker it is assumed to take a constant value $v_r|_{r_0} = v^{(l)}$.

The abstract setup is depicted in Fig. 41(a) and 43. References for the legitimacy of such a model to describe real loudspeaker arrays can be found in Meyer [MM00] and Pollow [Pol07].

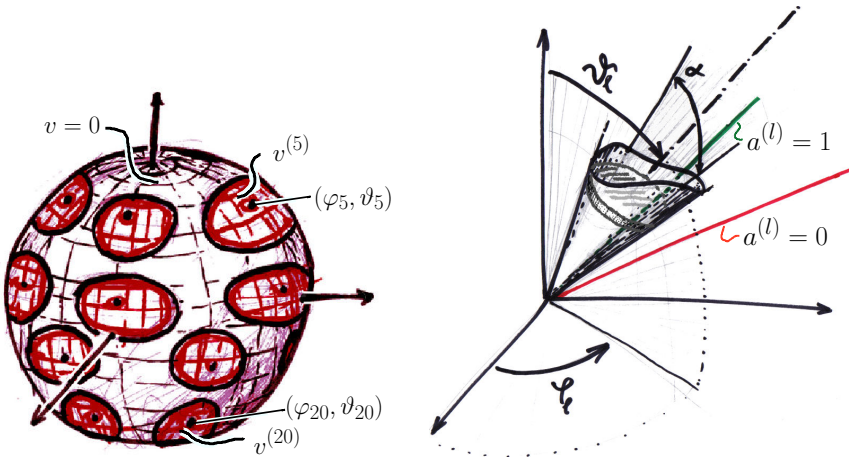

(a) The array model with individually vibrating spherical caps.

(b) The aperture of the l^{th} cap is 1 inside a cone with angle α opening towards (φ_l, ϑ_l), and 0 elsewhere.

Figure 41: Spherical cap model.

Cap model. The aperture function corresponding to the cap model can be described as an angular distribution that equals 1 inside, and 0 outside the region

of a loudspeaker membrane. Specifically, this cap region is enclosed by a cone of angle α with its apex at the origin $r = 0$, and its axis of symmetry extending towards $\boldsymbol{\theta}_l$, see Fig. 41(b)

$$a^{(l)}(\boldsymbol{\theta}) = \begin{cases} 1 & \text{at } l^{\text{th}} \text{ loudspeaker,} \\ 0 & \text{otherwise.} \end{cases} \\ = 1 - u\left[\boldsymbol{\theta}^{\mathrm{T}}\boldsymbol{\theta}_l - \cos\left(\frac{\alpha}{2}\right)\right]. \tag{282}$$

The unit step function $u(x)$ equals 1 for positive x, and 0 otherwise. One part of its argument x, the scalar product $\cos(\beta) = \boldsymbol{\theta}^{\mathrm{T}}\boldsymbol{\theta}_l$, describes the angle β between the unit vectors $\|\boldsymbol{\theta}\| = \|\boldsymbol{\theta}_l\| = 1$ of the variable spherical angle $\boldsymbol{\theta}$ and the loudspeaker angle $\boldsymbol{\theta}_l$. It is a necessary physical requirement that the cap functions do not overlap

$$\int_{\mathbb{S}^2} a^{(i)}(\boldsymbol{\theta})\, a^{(j)}(\boldsymbol{\theta})\; d\boldsymbol{\theta} \stackrel{!}{=} 0, \qquad \forall i \neq j.$$

Considering Eq. (282), the surface velocity distribution for all the moving caps may be defined as

$$v(\boldsymbol{\theta})|_{r_o} = \sum_{l=1}^{\mathrm{L}} a^{(l)}(\boldsymbol{\theta})\; v^{(l)}. \tag{283}$$

Note that this equation also characterizes the motionless parts of the surfaces ($v = 0$).

In general, the distributions $a^{(l)}(\boldsymbol{\theta})$ on the sphere may be expressed just as well in terms of their spherical harmonics expansion coefficients $a_{nm}^{(l)}$, cf. Section 2.2. To facilitate their computation, the properties of the isotropic spherical convolution (see Sec 3.3.2) are exploited. For that purpose, the Dirac delta distribution $\delta\left(1 - \boldsymbol{\theta}_l^{\mathrm{T}}\boldsymbol{\theta}\right)$ pointing at the cap center is convolved with a rotationally symmetric polar cap $\hat{a}(\vartheta)$ to obtain $a_{nm}^{(l)}$

$$\hat{a}(\vartheta) = 1 - u(\vartheta - \alpha/2), \\ a^{(l)}(\boldsymbol{\theta}) = \hat{a}(\vartheta) \overset{\text{sphconv}}{\star} \delta(1 - \boldsymbol{\theta}^{\mathrm{T}}\boldsymbol{\theta}_l), \\ \Longrightarrow a_{nm}^{(l)} = \underbrace{\mathcal{SHT}\left\{\hat{a}(\vartheta)\right\}}_{\hat{a}_n}\; \underbrace{\mathcal{SHT}\left\{\delta\left(1 - \boldsymbol{\theta}_l^{\mathrm{T}}\boldsymbol{\theta}\right)\right\}}_{Y_n^m(\boldsymbol{\theta}_l)} \tag{284}$$

We calculate $\hat{a}_n$ by utilizing the recurrence of the integrated Legendre polynomials $P_n(x)$, cf. Williams [Wil99], Meyer [MM00]

$$\hat{a}_n = \mathcal{SHT}\left\{\hat{a}(\vartheta)\right\} = \sqrt{(2n+1)\,\pi/2}\; \int_{\cos\left(\frac{\alpha}{2}\right)}^{1} P_n\left[\cos(\vartheta)\right]\; d(\cos(\vartheta)) \tag{285}$$

$$\hat{a}_n = \sqrt{(2n+1)\,\pi/2}\; \begin{cases} \cos\left(\frac{\alpha}{2}\right) P_n\left[\cos\left(\frac{\alpha}{2}\right)\right] - P_{n-1}\left[\cos\left(\frac{\alpha}{2}\right)\right], & n > 0 \\ 1 - \cos\left(\frac{\alpha}{2}\right), & n = 0. \end{cases}.$$

Fully expanded, using a truncation number N for the order $n \leq (\mathrm{N}+1)^2$, with $\mathrm{N} \to \infty$, a single cap aperture function reads as

$$a^{(l)}(\boldsymbol{\theta}) = \sum_{n=0}^{\mathrm{N}} \sum_{m=-n}^{n} \overbrace{\hat{a}_n \, Y_n^m(\boldsymbol{\theta}_l)}^{a_{nm}^{(l)}} \, Y_n^m(\boldsymbol{\theta}). \tag{286}$$

Matrix notation. Given the cap expansion coefficients $a_{nm}^{(l)}$ from Eq. (284), an $(\mathrm{N}+1)^2 \times \mathrm{L}$ matrix can be built according Eq. (228), Sec. 4.1. This matrix $\boldsymbol{A}_\mathrm{N}$ contains the set of L spherical harmonics cap coefficients

$$\begin{aligned} \boldsymbol{A}_\mathrm{N} &= \mathrm{mtx}_\mathrm{N}\left\{a_{nm}^{(l)}\right\} = \left[\boldsymbol{a}_\mathrm{N}^{(1)}, \ldots, \boldsymbol{a}_\mathrm{N}^{(\mathrm{L})}\right] \\ &= \mathrm{diag}_\mathrm{N}\left\{\hat{a}_n\right\} \underbrace{\mathrm{mtx}_\mathrm{N}\left\{Y_n^m(\boldsymbol{\theta}_l)\right\}}_{:=\boldsymbol{C}_\mathrm{N}} = \mathrm{diag}_\mathrm{N}\left\{\hat{a}_n\right\} \boldsymbol{C}_\mathrm{N}. \end{aligned} \tag{287}$$

Referring to the surface velocity in Eq. (283), we specify a vector $\boldsymbol{v} = \mathrm{vec}\left\{v^{(l)}\right\}$ containing the L cap velocities, in order to compute the superposition of spherical harmonics cap coefficients as the $(\mathrm{N}+1)^2 \times 1$ surface velocity *spherical wave spectrum* $\boldsymbol{\nu}_\mathrm{N}|_{r_o}$

$$\begin{aligned} \boldsymbol{\nu}_\mathrm{N}|_{r_o} &= \mathrm{vec}_\mathrm{N}\{\mathcal{SHT}_\mathrm{N}\{v(\boldsymbol{\theta})|_{r_o}\}\} \\ &= \sum_{l=1}^{\mathrm{L}} \boldsymbol{a}_\mathrm{N}^{(l)} \, v^{(l)} = \boldsymbol{A}_\mathrm{N} \begin{bmatrix} v^{(1)} \\ v^{(2)} \\ \vdots \\ v^{(\mathrm{L})} \end{bmatrix} = \boldsymbol{A}_\mathrm{N} \, \boldsymbol{v}. \end{aligned} \tag{288}$$

Spherical harmonics output directivity (MIMO-LSH). The surface velocity distribution of a compact spherical loudspeaker array has been modeled in terms of spherical harmonics by using the $(\mathrm{N}+1)^2 \times \mathrm{L}$ cap aperture matrix $\boldsymbol{A}_\mathrm{N}$ from Eq. (287). The linear combination of its columns by the actual membrane velocities $\boldsymbol{v}$ yields the surface velocity *spherical wave spectrum* of the array Eq.(288). Hence, the MIMO-LSH representation is directly obtained from the discrete velocity pattern of the MIMO system Eq. (281) by left multiplication with $\boldsymbol{A}_\mathrm{N}$

$$\begin{aligned} \boldsymbol{\nu}_\mathrm{N}|_{r_o} &= \boldsymbol{A}_\mathrm{N} \boldsymbol{T} \, \boldsymbol{u} \\ &= \overset{\mathrm{c}}{\boldsymbol{T}}_\mathrm{N} \, \boldsymbol{u}. \end{aligned} \tag{289}$$

Spherical harmonics in- and output directivity (MIMO-SH). Equivalently to the microphone array-based MIMO-SH system Eq. (277), a *decoder* $\boldsymbol{A}_{\mathrm{N_c}}^{+}$ can be applied to define the input voltages $\boldsymbol{u}$. Hereby the relation between a

spherical harmonics voltage vector $\boldsymbol{\Upsilon}_{\mathbf{N_c}}$ and the *spherical wave spectrum* of the velocity is established

$$\begin{aligned}\boldsymbol{\nu}_{\mathrm{N}}|_{r_o} &= \boldsymbol{A}_{\mathrm{N}}\, \boldsymbol{T}\, \boldsymbol{A}^{+}_{\mathrm{N_c}}\, \boldsymbol{\Upsilon}_{\mathrm{N_c}} \\ &= \mathring{\boldsymbol{T}}_{\mathrm{N,N_c}}\, \boldsymbol{\Upsilon}_{\mathrm{N_c}}.\end{aligned} \tag{290}$$

Note that the *decoder* carries now a physical meaning. Instead of $\boldsymbol{C}^{+}_{\mathrm{N_c}}$, which was used in the previous section, the inverse cap apertures $\boldsymbol{A}^{+}_{\mathrm{N_c}}$ are employed here. As a consequence, the input quantity $\boldsymbol{\Upsilon}_{\mathrm{N_c}}$ is related to the output surface velocity distribution $\boldsymbol{\nu}_{\mathrm{N}}|_{\mathrm{r_0}}$ by $\mathring{\boldsymbol{T}}_{\mathrm{N,N_c}}$, which will be derived entirely analytically in Sec. 6.4 based on an electroacoustic model.

6.3.3 Angular Directivity Control

In order to control the angular velocity distribution, i.e. the angular directivity $\boldsymbol{v}$, or its angularly band-limited SH representation $\boldsymbol{\nu}_{\mathrm{N_c}}$, by voltages $\boldsymbol{u}$, the following control systems provide either $\boldsymbol{v} \overset{!}{=} \boldsymbol{v}_{\mathrm{ctl}}$, or $\boldsymbol{\nu}_{\mathrm{N_c}} \overset{!}{=} \boldsymbol{\gamma}_{N_c}$

$$\text{MIMO-ctl:} \quad \boldsymbol{u} = \boldsymbol{T}^{+}\, \boldsymbol{v}_{\mathrm{ctl}} \qquad \Rightarrow \boldsymbol{v} = \boldsymbol{T}\, \boldsymbol{T}^{+}\, \boldsymbol{v}_{\mathrm{ctl}} \approx \boldsymbol{v}_{\mathrm{ctl}}, \tag{291}$$

$$\text{MIMO-LSH-ctl:} \quad \boldsymbol{u} = \mathring{\boldsymbol{T}}^{+}_{\mathrm{N_c}}\, \boldsymbol{\gamma}_{\mathrm{N_c}} \qquad \Rightarrow \boldsymbol{\nu}_{\mathrm{N_c}} = \mathring{\boldsymbol{T}}_{\mathrm{N_c}}\, \mathring{\boldsymbol{T}}^{+}_{\mathrm{N_c}}\, \boldsymbol{\gamma}_{\mathrm{N_c}} = \boldsymbol{\gamma}_{\mathrm{N_c}}, \tag{292}$$

$$\text{MIMO-SH-ctl:} \quad \boldsymbol{u} = \boldsymbol{A}^{+}_{\mathrm{N_c}}\, \mathring{\boldsymbol{T}}^{-1}_{\mathrm{N_c}}\, \boldsymbol{\gamma}_{\mathrm{N_c}} \qquad \Rightarrow \boldsymbol{\nu}_{\mathrm{N_c}} = \mathring{\boldsymbol{T}}_{\mathrm{N_c}}\, \mathring{\boldsymbol{T}}^{-1}_{\mathrm{N_c}}\, \boldsymbol{\gamma}_{\mathrm{N_c}} = \boldsymbol{\gamma}_{\mathrm{N_c}}. \tag{293}$$

6.3.4 Sound-Radiation of the Cap Model

According Sec. 2.3 Eqs. (47)-(48), the surface velocity $\boldsymbol{\nu}|_{r_o}$ Eq. (288) can be directly employed into the definition of the spherical exterior Neumann (particle velocity) boundary value problem. With the spherical Hankel function[2] $h^{(2)}_n(kr)$, and $h^{\prime(2)}_n(kr)$, its derivative, the *spherical wave spectrum* of the radiated sound pressure yields

$$\psi^m_n(kr) = \frac{\rho_0 c\, h^{(2)}_n(kr)}{\mathrm{i}\, h^{\prime(2)}_n(kr_o)} \sum_{l=1}^{\mathrm{L}} a^{(l)}_{nm}\, v^{(l)}, \tag{294}$$

$$\begin{aligned}\boldsymbol{\psi}_{\mathrm{N}}(kr) &= \mathrm{diag}_{\mathrm{N}}\left\{\frac{\rho_0 c\, h^{(2)}_n(kr)}{\mathrm{i}\, h^{\prime(2)}_n(kr_o)}\right\} \sum_{l=1}^{\mathrm{L}} \boldsymbol{a}^{(l)}_{\mathrm{N}}\, v^{(l)} \\ &= \mathrm{diag}_{\mathrm{N}}\left\{\frac{\rho_0 c\, h^{(2)}_n(kr)}{\mathrm{i}\, h^{\prime(2)}_n(kr_o)}\right\} \boldsymbol{A}_{\mathrm{N}}\, \boldsymbol{v},\end{aligned} \tag{295}$$

wherein $\mathrm{i} = \sqrt{-1}$, the air density is $\rho_0 = 1.2$, the speed of sound $c = 343\mathrm{m/s}$, the wave number $k = \omega/c$, and $\mathrm{diag}_{\mathrm{N}}\left\{\frac{\rho_0 c\, h^{(2)}_n(kr)}{\mathrm{i}\, h^{\prime(2)}_n(kr_o)}\right\}$ following the definitions in Sec. 4.1.

[2] $h^{(2)}_n(kr)$ is used to provide a causal solution to the Fourier expansion $\mathrm{e}^{\mathrm{i}\omega t}$.

For comparison of the velocity MIMO-system with the sound pressure MIMO-system described in Sec. 6.2, the following conversions hold[3]

$$\text{MIMO-LSH:} \qquad \overset{\circ}{\boldsymbol{G}}_{\mathrm{N}} = \mathrm{diag}_{\mathrm{N}} \left\{ \frac{\rho_{\mathrm{o}} c \, h_n^{(2)}(kr_p)}{\mathrm{i} \, h_n'^{(2)}(kr_o)} \right\} \overset{\circ}{\boldsymbol{T}}_{\mathrm{N}}, \tag{296}$$

$$\text{MIMO-SH:} \qquad \mathring{\boldsymbol{G}}_{\mathrm{N,N_c}} = \mathrm{diag}_{\mathrm{N}} \left\{ \frac{\rho_{\mathrm{o}} c \, h_n^{(2)}(kr_p)}{\mathrm{i} \, h_n'^{(2)}(kr_o)} \right\} \mathring{\boldsymbol{T}}_{\mathrm{N,N_c}}. \tag{297}$$

It is obvious that the diagonal weighting term $\mathrm{diag}_{\mathrm{N}} \left\{ \frac{\rho_{\mathrm{o}} c \, h_n^{(2)}(kr_p)}{\mathrm{i} \, h_n'^{(2)}(kr_o)} \right\}$ that describes the sound-radiation from the surface velocity is missing in the definitions of $\boldsymbol{T}$. Ways of including these transfer functions in a control system are illustrated in Sec. 6.7 on radial beam steering.

[3]To be rigorous, the definition of $\boldsymbol{C}_{\mathrm{N_c}}$ in the MIMO-SH $\mathring{\boldsymbol{G}}_{\mathrm{N_c}}$ Sec. 6.2 Eq. (280) should be changed to $\boldsymbol{A}_{\mathrm{N_c}}$ to match exactly.

6.4 System Description Based on an Electroacoustic Model

For a complete electroacoustic model, the sphere cap model was extended to a spherical shell cap model in [ZH07, ZPS08]. This model incorporates the interaction of the caps over the interior and exterior field as well as the electrical and mechanical transducer characteristics. A block diagram of the spherical shell cap model is shown in Fig. 42.

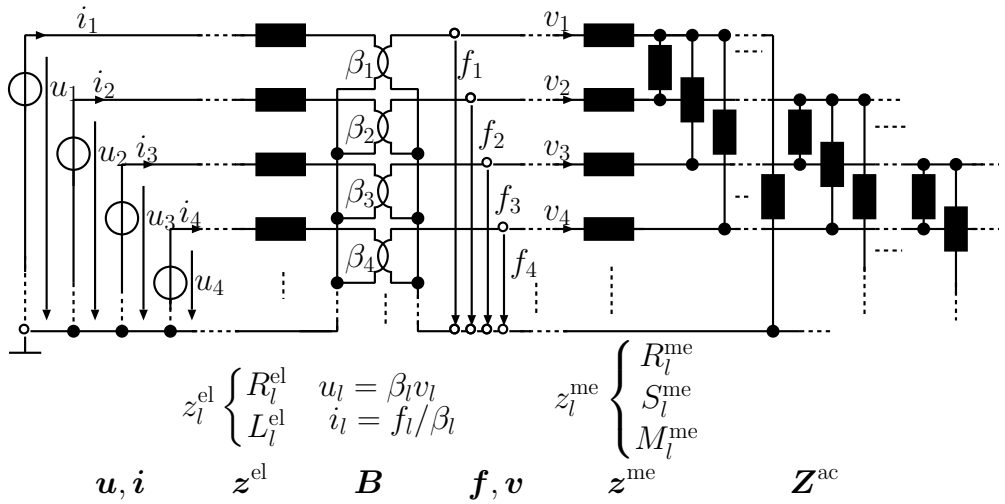

Figure 42: For the l^{th} array loudspeaker, the electroacoustic model consists of an electrical amplifier voltage u_l and current i_l, an electrical resistance and inductance $R_l^{\mathrm{el}}, L_l^{\mathrm{el}}$ of the loudspeaker coil, the electro-dynamical transduction constant β_l that relates electric quantities to mechanical forces and velocities f_l, v_l, as well as the mechanical impedance z_l^{me} at each membrane. The membranes are acoustically loaded by the impedance $\boldsymbol{Z}^{\mathrm{ac}}$ that mutually couples the loudspeakers, in general.

Shell model / modeling the acoustic impedance $\boldsymbol{Z}^{\mathrm{ac}}$. A model considering the acoustic impedance needs to describe the acoustic crosstalk between the array transducers via the interior and exterior sound field. Therefore, the spherical cap model from Fig. 41(a) is re-drawn as a spherical shell having a finite thickness between the interior and exterior surface radii r_i, and r_o, see Fig. 43.

The *spherical wave spectrum* of the sound pressure in both fields, the interior and exterior, is given similarly to Eq. (295) in terms of a mixed Neumann boundary problem (II), see Sec. 2.3

$$\boldsymbol{\psi}_{\mathrm{N}}(kr) = \begin{cases} \mathrm{diag}_{\mathrm{N}} \left\{ \frac{\rho_{\mathrm{o}} c \, h_n^{(2)}(kr)}{\mathrm{i} \, h_n'^{(2)}(kr_o)} \right\} \boldsymbol{A}_{\mathrm{N}} \, \boldsymbol{v}, & \text{for } r \geq r_o \\ \mathrm{diag}_{\mathrm{N}} \left\{ \frac{\rho_{\mathrm{o}} c_i \, j_n(k_i r)}{\mathrm{i} \, j_n'(k_i r_i)} \right\} \boldsymbol{A}_{\mathrm{N}} \, \boldsymbol{v}, & \text{for } r \leq r_i. \end{cases} \tag{298}$$

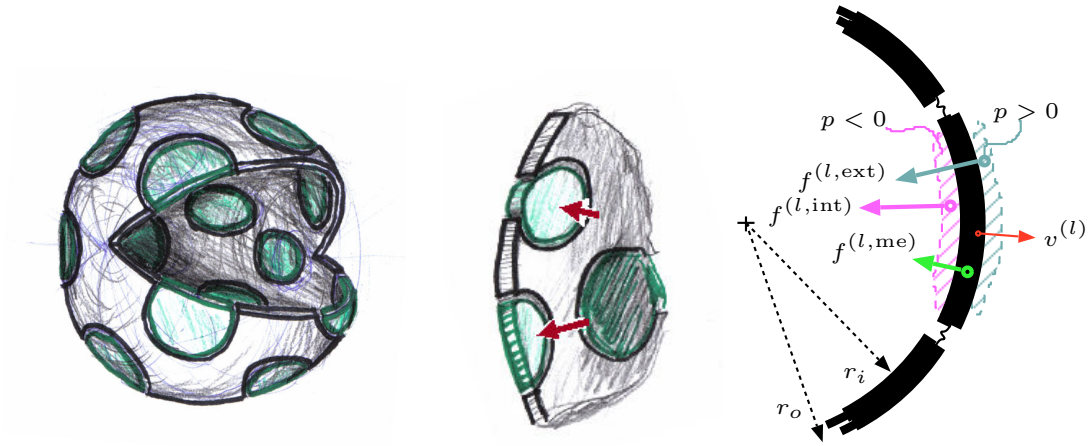

(a) Hollow spherical shell with vibrating caps.

(b) The caps mutually interact over the sound field.

(c) Acoustical and mechanical forces on a spherical cap in radial direction.

Figure 43: Hollow spherical cap model for interaction modeling.

Here, we choose a different notation c_i and k_i to account for the propagation properties of the enclosure medium. For an interior filled with damping wool these are $c_i = 0.93\, c$ and $k_i = k/0.93$.

Assuming a static model, in which every cap is motionless, i.e. $v^{(l)} = 0$, $\forall l = 1, \ldots, \mathrm{L}$, the computation of the impact forces due to both sound fields becomes feasible. First of all, the explicit sound pressure distributions on either side of the spherical shell are required, i.e. $p\left(\boldsymbol{\theta}\right)|_{r_o}$ on the exterior, and $p\left(\boldsymbol{\theta}\right)|_{r_i}$ on the interior side. Integrating both sound pressures over the aperture $a^{(l)}\left(\boldsymbol{\theta}\right)$ of the l^{th} motionless cap yields the induced radial force $f^{(l)}$, cf. Fig. 43(c):

$$f^{(l)} = \int_{\mathbb{S}^2} a^{(l)}\left(\boldsymbol{\theta}\right) \left[p\left(\boldsymbol{\theta}\right)|_{r_o} + p\left(\boldsymbol{\theta}\right)|_{r_i}\right] d\boldsymbol{\theta}. \tag{299}$$

These pressures are equivalent to the *spherical wave spectra* from Eq. (298) in the spherical harmonics domain evaluated at r_o and r_i

$$\psi_n^m|_{r_o} = \mathcal{SHT}\left\{p\left(\boldsymbol{\theta}\right)|_{r_o}\right\}, \text{ and } \quad \psi_n^m|_{r_i} = \mathcal{SHT}\left\{p\left(\boldsymbol{\theta}\right)|_{r_i}\right\}. \tag{300}$$

The integral Eq. (299) reduces to a sum after insertion of both factors, the apertures $a^{(l)}(\boldsymbol{\theta})$ Eq. (284), and the pressures $p(\boldsymbol{\theta})|_{r_o}$, $p(\boldsymbol{\theta})|_{r_i}$, in their spherical harmonics expansions. Due to the orthonormality Eq. (27) of the normalized spherical

harmonics, this yields

$$f^{(l)} = \int_{\mathbb{S}^2} \left[\sum_{n'=0}^{\infty} \sum_{m'=-n'}^{n'} a_{n'm'}^{(l)} Y_{n'}^{m'}(\boldsymbol{\theta}) \right] \left[\sum_{n=0}^{\infty} \sum_{m=-n}^{n} \left(\psi_n^m|_{r_o} + \psi_n^m|_{r_i} \right) Y_n^m(\boldsymbol{\theta}) \right] d\boldsymbol{\theta},$$

$$= \sum_{n'=0}^{\infty} \sum_{m'=-n'}^{n'} \sum_{n=0}^{\infty} \sum_{m=-n}^{n} a_{n'm'}^{(l)} \left(\psi_n^m|_{r_o} + \psi_n^m|_{r_i} \right) \underbrace{\int_{\mathbb{S}^2} Y_n^m(\boldsymbol{\theta}) Y_{n'}^{m'}(\boldsymbol{\theta}) \, d\boldsymbol{\theta}}_{=\delta[n-n']\delta[m-m']}$$

$$f^{(l)} = \sum_{n=0}^{\infty} \sum_{m=-n}^{n} a_{nm}^{(l)} \left(\psi_n^m|_{r_o} + \psi_n^m|_{r_i} \right). \tag{301}$$

In matrix notation of $a_{nm}^{(l)}$ and vector notation of $\psi_n^m|_{r_o}$ and $\psi_n^m|_{r_i}$, the L impact forces remain (ideally $\mathrm{N} \to \infty$)

$$\boldsymbol{f}^{\mathrm{ac}} = \begin{bmatrix} f^{(1)} \\ f^{(2)} \\ \vdots \\ f^{(\mathrm{L})} \end{bmatrix} = \boldsymbol{A}_{\mathrm{N}}^{\mathrm{T}} \left(\boldsymbol{\psi}_{\mathrm{N}}|_{r_o} + \boldsymbol{\psi}_{\mathrm{N}}|_{r_i} \right). \tag{302}$$

For a linear model, we assume that the principle of linear superposition holds. Therefore, the *spherical wave spectra* of the actually vibrating caps Eq. (298) may be plugged into Eq. (302) for motionless caps to obtain the impact forces obtained due to the sound fields. The equation for the acoustical forces $\boldsymbol{f}^{\mathrm{ac}}$ and the resulting acoustic impedance, the acoustic load, are:

$$\begin{aligned} \boldsymbol{f}^{\mathrm{ac}} &= \frac{\rho_0 c}{\mathrm{i}} \boldsymbol{A}_{\mathrm{N}}^{\mathrm{T}} \operatorname{diag}_{\mathrm{N}} \left\{ \left(\frac{c_i}{c} \frac{j_n(k_i r_i)}{j_n'(k_i r_i)} + \frac{h_n^{(2)}(kr_o)}{h_n'^{(2)}(kr_o)} \right) \right\} \boldsymbol{A} \, \boldsymbol{v}, \\ &= \boldsymbol{Z}^{\mathrm{ac}} \, \boldsymbol{v}. \end{aligned} \tag{303}$$

Mechanical impedance $\boldsymbol{Z}^{me}$. In addition to the acoustic load on the caps, specific radial mechanical forces $\boldsymbol{f}^{\mathrm{me}}$ are required to induce the velocities $\boldsymbol{v}$ of the spherical caps. Proportionality is represented by the mechanical impedances $\boldsymbol{Z}^{\mathrm{me}} = \operatorname{diag}\{\boldsymbol{z}^{\mathrm{me}}\}$ of the membranes:

$$\boldsymbol{f}^{\mathrm{me}} = \boldsymbol{Z}^{\mathrm{me}} \, \boldsymbol{v}. \tag{304}$$

Note that these individually independent impedances are determined by the mass M_l^{me}, the stiffness S_l^{me}, and the friction R_l^{me} of the loudspeaker membranes, which are serially connected

$$z^{\mathrm{me}} = \mathrm{i}\omega M_l^{\mathrm{me}} + S_l^{\mathrm{me}}/(\mathrm{i}\omega) + R_l^{\mathrm{me}}. \tag{305}$$

For specific values, data sheets or impedance measurements with the delta mass method (cf. Dickason [Dic01]) can be used.

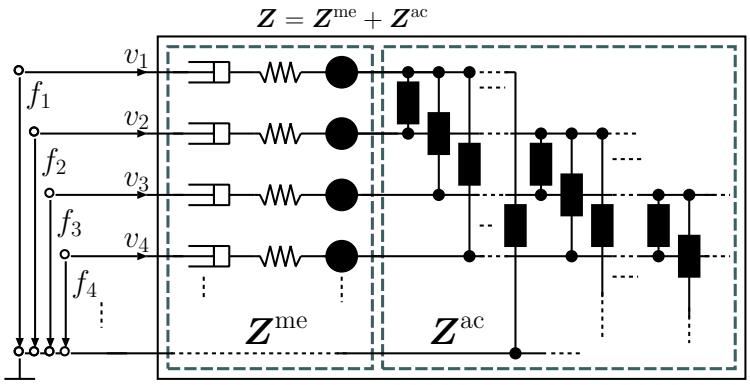

Figure 44: Mechano-acoustic crosstalk system.

The inhomogeneous equation of motion with the excitation force vector $\boldsymbol{f}$ becomes in sum $\boldsymbol{f} = \boldsymbol{f}^{\mathrm{ac}} + \boldsymbol{f}^{\mathrm{me}} = (\boldsymbol{Z}^{\mathrm{me}} + \boldsymbol{Z}^{\mathrm{ac}})\, \boldsymbol{v}$. Inserting the acoustical and mechanical forces (Eq. (303) and Eq. (304)), this yields:

$$\begin{aligned} \boldsymbol{f} &= \underbrace{\left[\mathrm{i}\rho_0 c\, \boldsymbol{A}^{\mathrm{T}}\, \mathrm{diag}_{\mathrm{N}} \left\{ \left(\frac{c_i}{c} \frac{j_n(k_i r_i)}{j_n'(k_i r_i)} + \frac{h_n^{(2)}(kr_o)}{h_n'^{(2)}(kr_o)} \right) \right\} \boldsymbol{A} + \boldsymbol{Z}^{\mathrm{me}} \right]}_{\boldsymbol{Z}} \boldsymbol{v}, \\ \boldsymbol{f} &= \boldsymbol{Z}\, \boldsymbol{v}. \end{aligned} \tag{306}$$

The new expression $\boldsymbol{Z}$ represents the impedance matrix (Fig. 44) for the acoustical and mechanical properties of the array.

Transduction and electrical impedance. Normally, electrical amplifiers and electro-dynamical transducers are used to control the mechanical loudspeaker velocities and forces. This transduction involves a *gyrator* that converts an input voltage u to an output force f and an input current i to an output velocities $\boldsymbol{v}$ by the transduction constant β. The electro-dynamical transducer model is depicted in Fig. 45.

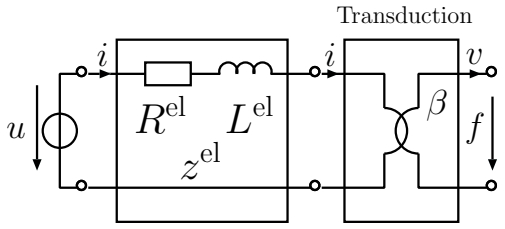

Figure 45: Electrical amplification, transmission, and transduction model of an electro-dynamical loudspeaker.

For each transducer, the equation

$$z^{\mathrm{el}} = R^{\mathrm{el}} + L^{\mathrm{el}}/(i\omega) \tag{307}$$

holds. The equation uses the electrical resistance R^{el} and inductance L^{el}. The electrical quantity R^{el} is modeling the resistance of the amplifier, the cable, as well as the transducer coil in sum. A transducer constant β_l, a coil resistance, and an inductance L_l have to be obtained from measurements or the transducer data sheet. For all loudspeakers, this part of the system is described by the diagonal (uncoupled) matrices $\boldsymbol{R}^{\mathrm{el}} = \mathrm{diag}\left\{R_l^{\mathrm{el}}\right\}$, $\boldsymbol{L}^{\mathrm{el}} = \mathrm{diag}\left\{L_l^{\mathrm{el}}\right\}$, $\boldsymbol{\beta}^{\mathrm{el}} = \mathrm{diag}\left\{\beta_l^{\mathrm{el}}\right\}$, and $\boldsymbol{Z}^{\mathrm{el}} = \boldsymbol{R}^{\mathrm{el}} + \frac{1}{\mathrm{i}\omega}\boldsymbol{L}^{\mathrm{el}}$

$$\boldsymbol{i} = \boldsymbol{B}^{-1}\,\boldsymbol{f}, \tag{308}$$

$$\boldsymbol{u} = \boldsymbol{Z}^{\mathrm{el}}\,\boldsymbol{i} + \boldsymbol{B}\,\boldsymbol{v}, \tag{309}$$

$$\Longrightarrow \boldsymbol{u} = \boldsymbol{Z}^{\mathrm{el}}\,\boldsymbol{B}^{-1}\,\boldsymbol{f} + \boldsymbol{B}\,\boldsymbol{v}. \tag{310}$$

The voltages $\boldsymbol{u}$ in the second line are the sum of the gyrator voltages $\boldsymbol{B}\,\boldsymbol{v}$ and voltages due to the electrical impedances $\boldsymbol{Z}^{\mathrm{el}}\boldsymbol{i}$.

Fully analytic spherical shell cap-model. Completing the description from Eqs. (306),(310) we obtain for the compact spherical loudspeaker model

$$\boldsymbol{v} = \underbrace{\left(\boldsymbol{Z}^{\mathrm{el}}\,\boldsymbol{B}^{-1}\,\boldsymbol{Z} + \boldsymbol{B}\right)^{-1}}_{:=\boldsymbol{T}}\,\boldsymbol{u}, \tag{311}$$

with $\boldsymbol{T}$ defined as in Sec. 6.3.1 (about laser vibrometry), Eq. (281). Considering the equations for output and input spherical harmonics representations Eqs. (289), (290), the shell model for $\boldsymbol{T}$ yields MIMO, MIMO-LSH, and MIMO-SH systems:

$$\text{MIMO:} \qquad \boldsymbol{T} = \left(\boldsymbol{Z}^{\mathrm{el}}\,\boldsymbol{B}^{-1}\,\boldsymbol{Z} + \boldsymbol{B}\right)^{-1}, \tag{312}$$

$$\text{MIMO-LSH:} \qquad \overset{\mathrm{c}}{\boldsymbol{T}}_{\mathrm{N}} = \boldsymbol{A}_{\mathrm{N}}\,\boldsymbol{T}, \tag{313}$$

$$\text{MIMO-SH:} \qquad \overset{\circ}{\boldsymbol{T}}_{\mathrm{N,N_c}} = \boldsymbol{A}_{\mathrm{N}}\,\boldsymbol{T}\,\boldsymbol{A}^{+}_{\mathrm{N_c}}. \tag{314}$$

Comparison, conversion, angular directivity control. The above defined system $\boldsymbol{T}$ directly compares to the laser vibrometry MIMO system. Hence, also the conversions in Eqs. (296), (297) hold if a comparison with the microphone array measurements of the MIMO-LSH and MIMO-SH systems is desirable.

The control systems MIMO-ctl ($\boldsymbol{T}^{-1}$), MIMO-LSH-ctl ($\overset{\mathrm{c}}{\boldsymbol{G}}^{+}_{\mathrm{N_c}}$, $\overset{\mathrm{c}}{\boldsymbol{T}}^{+}_{\mathrm{N_c}}$) and MIMO-SH ($\overset{\circ}{\boldsymbol{G}}^{-1}_{\mathrm{N_c}}$, $\overset{\circ}{\boldsymbol{T}}^{-1}_{\mathrm{N_c}}$) are found by truncation with $\mathrm{N_c}$ and least-squares inversion in every frequency, as in Eqs. (279), (280), (291), (292), (293).

6.5 Synthesis Error Evaluation and Angular Aliasing

To evaluate the synthesis performance, spatial aliasing has to be considered, i.e. all spherical harmonics $\mathrm{N} \rightarrow \infty$ need to be taken into account. An ideal control system equals the identity matrix for $n \leq \mathrm{N_c}$, and zero for $n > \mathrm{N_c}$. The system error $\boldsymbol{e}\left(\boldsymbol{\gamma}_{\mathrm{N_c}}\right) = \boldsymbol{E}\,\boldsymbol{\gamma}_{\mathrm{N_c}}$ depends on the steering vector and is defined as deviation from this idealized behavior

$$\boldsymbol{E} = \begin{bmatrix} \mathring{\boldsymbol{G}}_{\mathrm{N_c}} \\ \mathring{\boldsymbol{G}}_{>\mathrm{N_c},\mathrm{N_c}} \end{bmatrix} \mathring{\boldsymbol{G}}_{\mathrm{N_c}}^{-1} - \begin{bmatrix} \boldsymbol{I}_{\mathrm{N_c}} \\ \boldsymbol{0}_{>\mathrm{N_c},\mathrm{N_c}} \end{bmatrix} = \begin{bmatrix} \boldsymbol{0}_{\mathrm{N_c}} \\ \mathring{\boldsymbol{G}}_{>\mathrm{N_c},\mathrm{N_c}} \mathring{\boldsymbol{G}}_{\mathrm{N_c}}^{-1} \end{bmatrix}. \tag{315}$$

Following a similar approach as in [KW04], the minimum and maximum power of the error result from an eigendecomposition of the squared error, see also [Pom08]

$$\begin{aligned} \left\|\boldsymbol{e}\left(\boldsymbol{\gamma}_{\mathrm{N_c}}\right)\right\|^2 &= \boldsymbol{\gamma}_{\mathrm{N_c}}^{\mathrm{H}} \boldsymbol{E}^{\mathrm{H}} \boldsymbol{E}\, \boldsymbol{\gamma}_{\mathrm{N_c}}, \\ \boldsymbol{E}^{\mathrm{H}}\boldsymbol{E} &= \boldsymbol{Q}\, \mathrm{diag}\left\{\boldsymbol{\sigma}_e\right\}^2\, \boldsymbol{Q}^{\mathrm{H}}, \\ \Rightarrow \mathrm{argmin}\{\boldsymbol{\sigma}_e\}^2 \leq \frac{\left\|\boldsymbol{e}\left(\boldsymbol{\gamma}_{\mathrm{N_c}}\right)\right\|^2}{\left\|\boldsymbol{\gamma}_{\mathrm{N_c}}\right\|^2} &\leq \mathrm{argmax}\{\boldsymbol{\sigma}_e\}^2, \end{aligned} \tag{316}$$

wherein $()^{\mathrm{H}}$ denotes Hermitian transposition. As all eigenvectors in $\boldsymbol{Q}$ are normalized, the magnitude of the squared error is determined by the eigenvalues only. The following sections apply the hereby defined error bounds and an average $\frac{\|\boldsymbol{\sigma}_e\|^2}{(\mathrm{N_c}+1)^2}$ to characterize the system performance.

As $\sigma_{e,q}^2$ are the variances of the individual spectral components of the error system $\boldsymbol{E}^{\mathrm{H}}\boldsymbol{E}$, and $\boldsymbol{Q}$ is an orthonormal system, the minimum and maximum eigenvalues, $\sigma_{e,min}^2$ and $\sigma_{e,max}^2$, describe the normalized error variances associated with the two eigenvectors, $\boldsymbol{\gamma}_{best}$ and $\boldsymbol{\gamma}_{worst}$. These eigenvectors represent the most and least accurate re-synthesis patterns on the given arrangement. Again, a -3dB border is suitable to illustrate the tendencies. An example is given in Fig. 46(a). In [ZSH07], the transition of the total squared-error surface over the -3dB border is depicted for a few examples of spherical array layouts, in dependency of different array diameter $\phi_o = 2r_o$, and the ratio between the target synthesis radius r_p and the array radius r_o. The contours in Fig. 46(a) are less restrictive. A simulation with decreased cap sizes in Fig. 46(b) exhibits that the cap size has only a small influence on the accuracy.

Further interesting insights can be obtained for a spherical array when looking at the spherical harmonics magnitudes of the eigenvectors in $\boldsymbol{Q}$, compared to the corresponding eigenvalue $\sigma_{e,q}^2$, see Fig. 47.

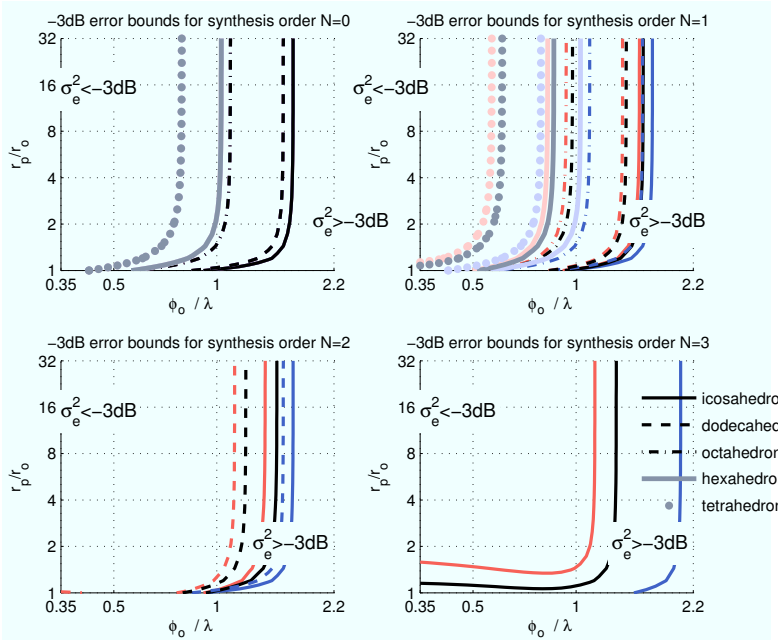

(a) $\alpha = \alpha_{\max}(solid)/2$

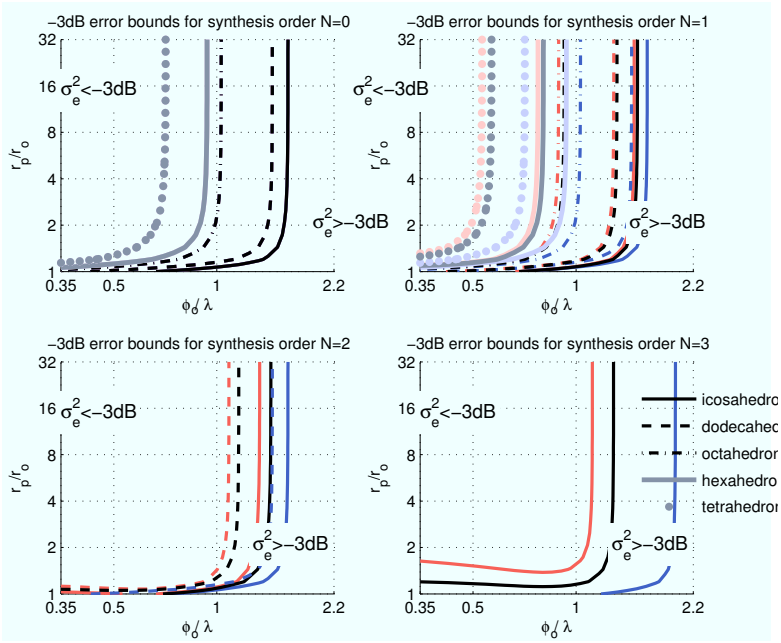

(b) $\alpha = \alpha_{\max}(solid)/8$

Figure 46: Error analysis of Platonically sampled spherical arrays with cap size α, proportional to the maximum non-overlapping size $\alpha_{\max}$; the array diameter $\phi_o = 2r_o$ is normalized to the wavelength λ in the above diagram. The lines are the -3dB contours of the average (black/gray), minimum- (blue), and maximum- (red) square synthesis errors. A rough rule of thumb for array-design can be given according the average errors: $\phi_o < \lambda$, and $r_p > 2r_o$.

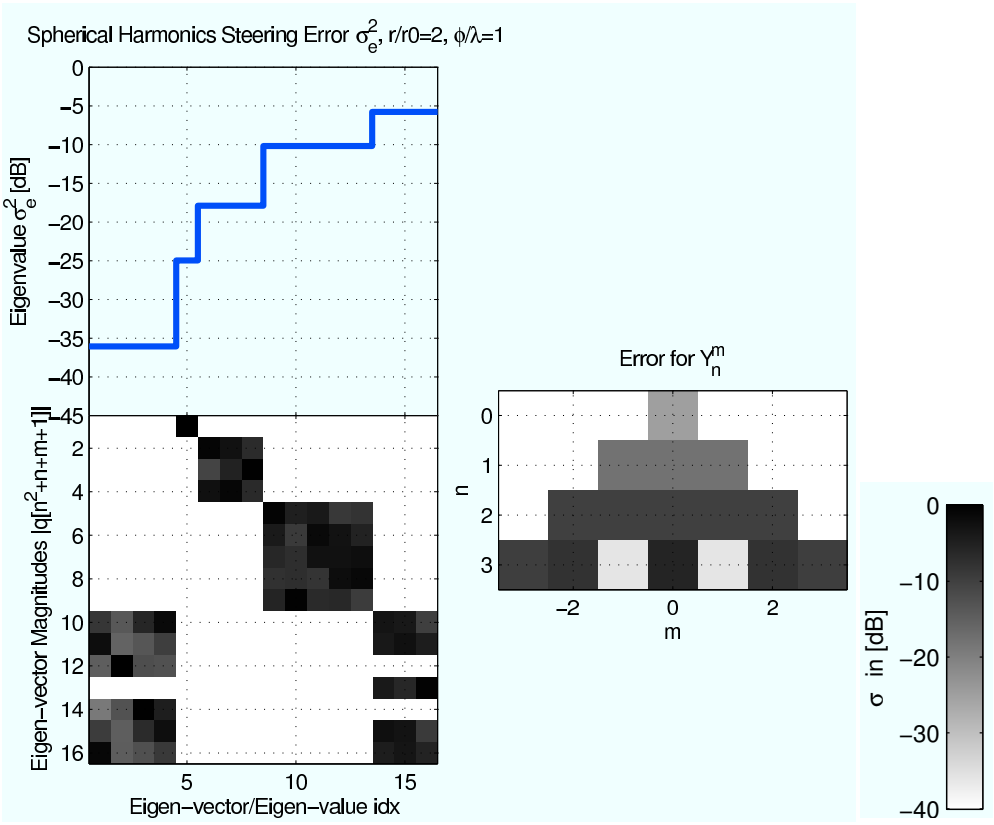

Figure 47: The eigendecomposition of the system error matrix reveals, which eigenvectors $\boldsymbol{\psi}_q$ (left bottom) of the error are associated with which error magnitudes $\sigma^2_{e,q}$ (left top). In the given example (icosahedral array $\alpha = \alpha_{max}(icosahedron)/2$), the $n = 3, m = \{-2, 0, +2\}$ harmonics seem to worst performing, as well as special combinations of 3^{rd} order harmonics (column 14-16). Note that this analysis is dependent on the distance r_p/r_0.

6.6 Comparison of Models and Hardware Implementation, Reduction of Control Filters

The IEM icosahedral array has a radius of $r_o = 0.28$m and its 20 loudspeakers are built into an icosahedron with a common interior, loosely filled with damping wool. This hardware and its parameters shall be used as a reference in the following paragraphs, in order to compare the measured responses with the models introduced in the previous two sections.

Furthermore, this section introduces a way of analyzing the minimum, average, and maximum reproduction errors.

It is also shown, how the MIMO-SH approach makes the control more efficient by discarding low-energy filters in the system matrix.

6.6.1 Microphone Array Measurements.

The measurement setup is depicted in Fig. 37 and uses a 10°-spaced semicircular microphone array with 5° offset from $\vartheta = 0$. The transfer functions in $\boldsymbol{G}$ were measured in 10° azimuthal steps using an electric turntable. With the quadrature or surface fraction weights $\boldsymbol{w}$ (cf. [SB96], [Pom08]) for weighted least-squares inversion, the transfer functions were transformed from the left into $\mathring{\boldsymbol{G}}_{17}$.

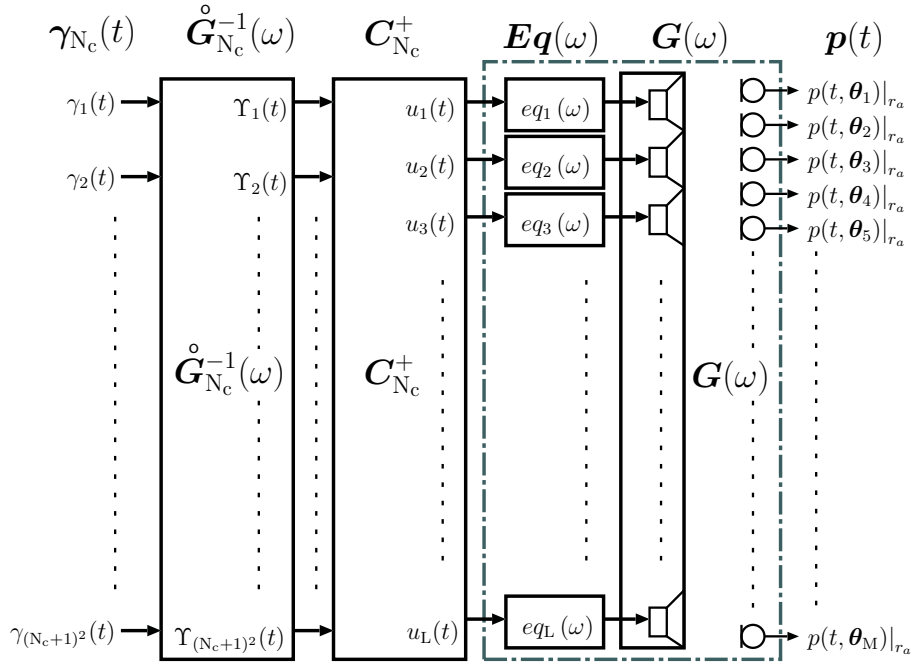

Figure 48: Angular compact spherical loudspeaker beamformer.

From $\mathring{\boldsymbol{G}}_{17}$, the MIMO-LSH-ctl $\mathring{\boldsymbol{G}}^{+}_{3}$ and MIMO-SH-ctl $\mathring{\boldsymbol{G}}^{-1}_{3}$ were computed according the descriptions given above. In addition, analytic versions of the control systems were calculated from the model in the previous sections.

The frequency responses in magnitude of $\mathring{\boldsymbol{G}}_3^{+}$ and $\mathring{\boldsymbol{G}}_3^{-1}$ are depicted in Fig. 49. The dashed colored lines show the results with the electroacoustic model. The model indicates that $\mathring{\boldsymbol{G}}_3^{-1}$ exhibits only equalization filters for each order n, and two additional crosstalk cancellation filters between the orders $10 \leftrightarrow 11$ and $15 \leftrightarrow 16$. Although the frequency responses from the measured data system (thin gray lines) deviate quite obviously from their analytical counterparts, it is nice to see that there are more low-energy transfer paths in $\mathring{\boldsymbol{G}}_3^{-1}$ than in $\mathring{\boldsymbol{G}}_3^{+}$. Note that 20 filters have been applied to equalize all active on-axis loudspeaker responses to one reference channel, which seems to be crucial to keep the nearly diagonal structure. This is easily explained, since the 20 degrees of freedom are reduced to 16 using the spherical harmonics output decoder. Consequently, the variation in the 20 transducer responses can only be equalized in the 20 loudspeaker feeds, see Fig. 48.

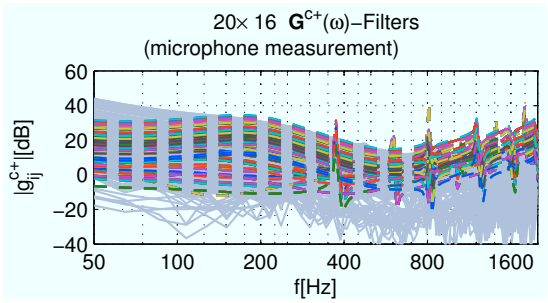

(a) MIMO-LSH-ctl

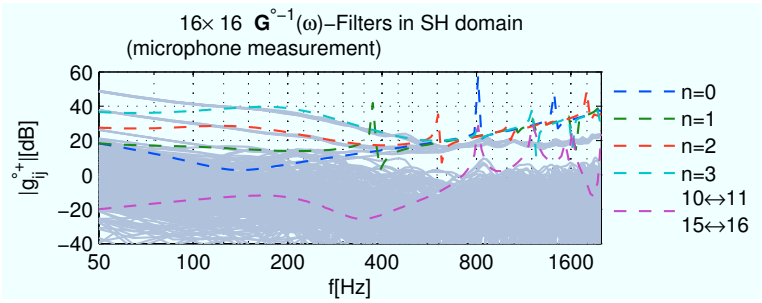

(b) MIMO-SH-ctl

Figure 49: Microphone measured MIMO-LSH-ctl and MIMO-SH-ctl magnitude responses (thin, gray) of the equalized IEM icosahedral array in comparison to the analytic model responses (dashed, colored).

Frequency slice and frequency response. To illustrate the structures of MIMO-SH-ctl and MIMO-LSH-ctl control systems, a cross-section through the frequency-domain filter-matrix is depicted at a frequency of 689Hz. Figs. 50(a) and 50(b) compare the analytic control systems to the corresponding systems based on measurements. It is nice to see that in both, theoretical and practical

results, the MIMO-SH-ctl becomes sparse. However, the reason for the obvious deviation from the theoretical results is not quite clear yet (non-spherical geometry of the icosahedron; inhomogeneous filling and cabling in the interior; losses in the damping wool; slight offsets in the setup).

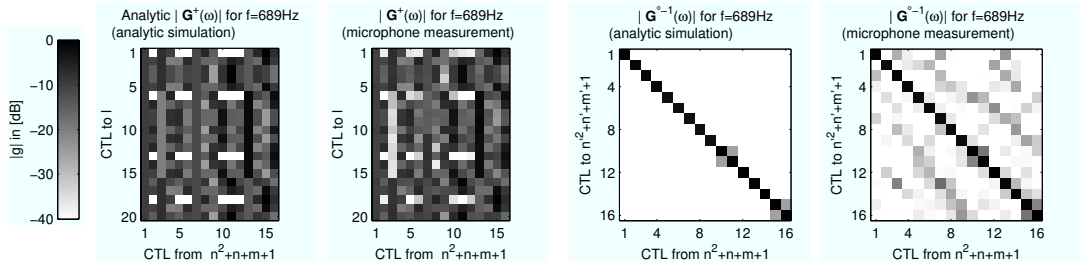

(a) MIMO-LSH-ctl at 689Hz, theoretical vs. measured

(b) MIMO-SH-ctl at 689Hz, theoretical vs. measured

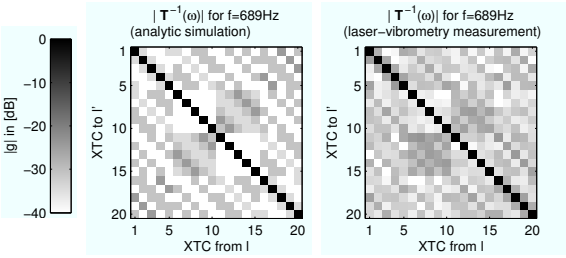

(c) Velocity MIMO-ctl at 689Hz, theoretical vs. measured

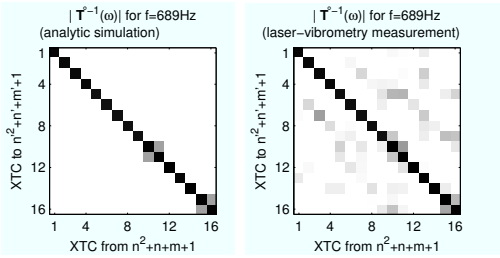

(d) Velocity MIMO-SH-ctl at 689Hz, theor./meas.

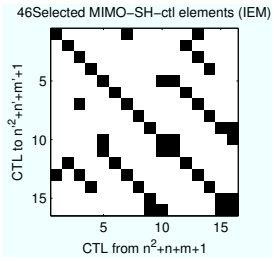

(e) Sparsification mask

Figure 50: Cross-section through the MIMO control systems for the IEM loudspeaker showing magnitudes at one frequency. The simulated systems are compared to measurement based control, using either microphone array measurements (1st row) or laser-vibrometry (2nd row). Measured MIMO-SH-ctl systems do not become entirely sparse. A mask is used to suppress low-energy components (given for mic-array measurement).

Reduction of control filters. In order to re-establish the sparse structure of the reduced control system $\mathring{\boldsymbol{G}}_3^{-1}$ that is shown in Fig. 50 for the analytically modeled MIMO-SH-ctl, a mask needs to be found, omitting irrelevant transfer paths. Fig. 50(e) shows a selection of 46 important transfer functions. The error evaluation according to Eq. (316) in Fig. 51 shows a comparison between the original and "sparsified" MIMO-SH-ctl. Even after a reduction from 256 to 46 transfer functions good results are achievable.

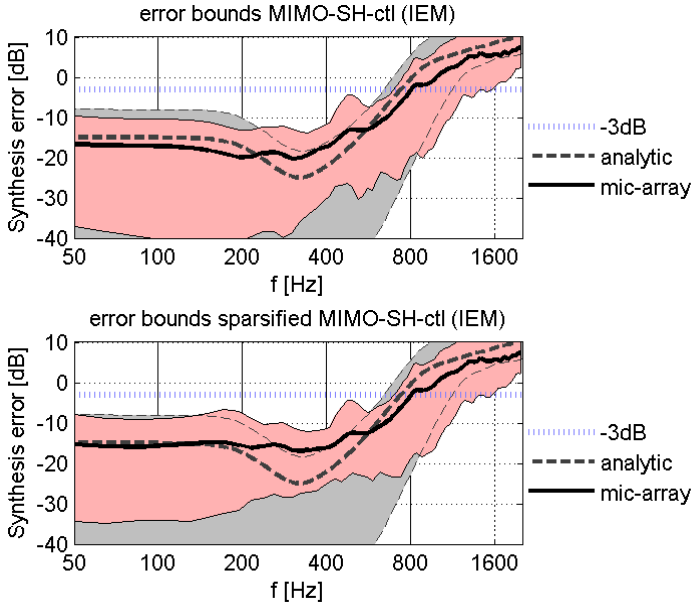

Figure 51: Synthesis errors of the IEM loudspeaker for N=3 comparing the full (top) and the sparsified (bottom) MIMO-SH-ctl. The pink area and its border mark the range from minimal to maximal errors at a given frequency, the solid line draws the mean square error. Results of the analytic model are drawn in dashed lines and gray behind that as a reference.

6.6.2 Laser-Doppler Vibrometry.

Selective laser vibrometry measurements of the surface velocity on a compact spherical loudspeaker array were obtained by a much smaller measurement setup than microphone array measurements, see Fig. 40. This setup is more robust to acoustic reflections, but the measurements only selectively describe the surface velocity and not the acoustic dispersion. The spherical cap model from the previous sections is required to model the radiated sound pressure.

Fig. 52 shows the magnitude frequency responses of the 20×20 MIMO-ctl $\boldsymbol{T}^{-1}$ and the 16×16 MIMO-SH-ctl $\mathring{\boldsymbol{T}}_3^{-1}$ control systems, obtained by laser Doppler vibrometry measurements (see [RJ07, JR07]), in comparison to the electroacoustic model. An interesting side aspect: in terms of the 20×20 MIMO-ctl system, a

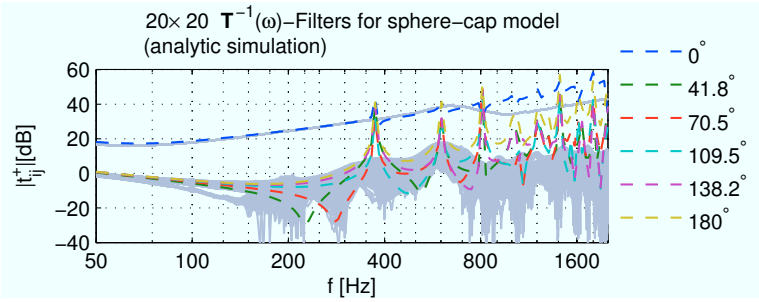

(a) MIMO-ctl

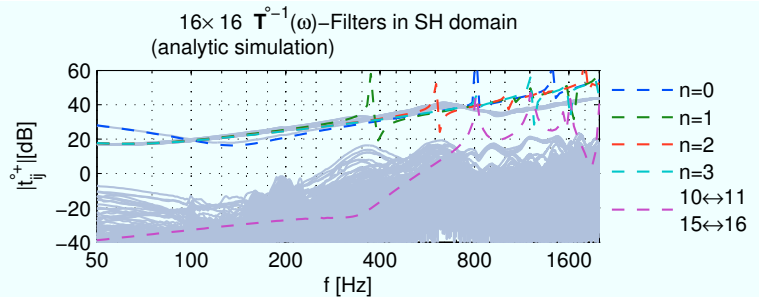

(b) MIMO-SH-ctl

Figure 52: Laser-vibrometry measured velocity MIMO-ctl and MIMO-SH-ctl magnitude responses (thin, gray) from the IEM-loudspeaker in comparison to analytic responses (dashed, colored).

grouping of the responses into the 6 angular distance classes on the icosahedron is obvious. The curves in Fig. 52 can be regarded as to verify the cap model at low frequencies. Model resonances at higher frequencies appear to be damped in the LDV measurements. Deviations of the geometry (Platonic solid, speaker cones and magnets, interior cable harness), as well as losses in the damping wool might be the reason for this behavior.

Fig. 50 compares a cross-section of the analytic control system according to the sphere cap model with the laser vibromentry based system. The measured frequency responses seem to match their analytic counterparts much better than in the case of microphone array measurements.

6.7 Radial Steering of Beam-patterns

The above sections have presented control systems in order to control spherical harmonics beam patterns at a given radius, either as sound particle velocity, or as sound pressure pattern. These systems that only work for fixed radii r_a can be called *angular beamforming*.

However, in some situations it is necessary to displace these angular beam patterns to different radii r_p (Fig. 53). This section shows signal processing methods accomplishing this kind of *radial beam-steering* or *focusing*, or briefly *radial beamforming*.

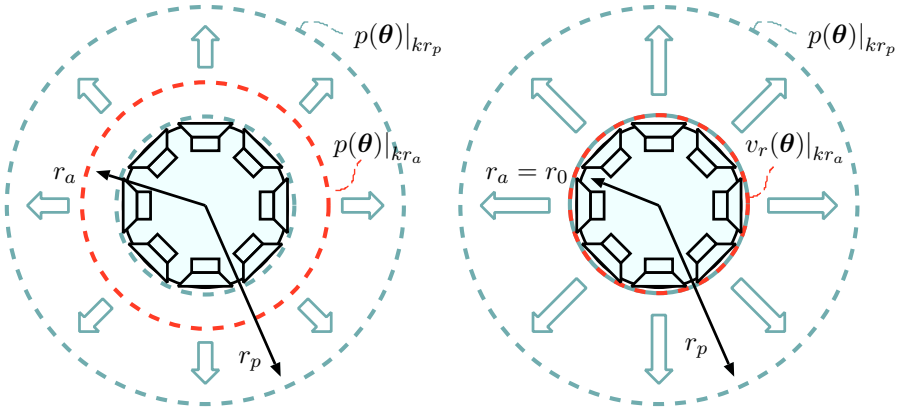

(a) Microphone Array based (b) Cap model based

Figure 53: There are two basic arrangements for directivity pattern synthesis: In (a) the sound pressure distribution $p(\boldsymbol{\theta})|_{r_a}$ at the microphone array sphere (red), and (b) the sound particle velocity distribution $v_r(\boldsymbol{\theta})|_{r_a}$ on the cap model speaker array (red) are synthesized. Despite their different shapes, the *radial beamforming* filters focus the beam pattern sharply at a larger sphere specified by the radius r_p in both cases.

In particular, this section derives fractions of spherical Hankel filters for accurate radial near- and far-field beamforming with a dependency on the (primary) synthesis radius r_a and the target radius r_p, order n, as well as frequency ω. These filters allow for efficient IIR discrete-time implementations that have been presented in [Pom08]. Implementations of quite similar filters accomplishing *distance coding filters* for Ambisonics have been shown in [Dan03], and in [Mor06] for compensation of scattered sound fields in rigid sphere microphone array recordings.

The spherical wave-spectra of the angularly controlled beam patterns are defined as the spherical harmonics transforms

$$\nu_n^m|_{r_a} = \int_{\mathbb{S}^2} v_r\left(\boldsymbol{\theta}\right)|_{r_a} \; Y_n^m\left(\boldsymbol{\theta}\right) \; d\boldsymbol{\theta}, \tag{317}$$

$$\text{or} \quad \psi_n^m|_{r_a} = \int_{\mathbb{S}^2} p\left(\boldsymbol{\theta}\right)|_{r_a} \; Y_n^m\left(\boldsymbol{\theta}\right) \; d\boldsymbol{\theta}. \tag{318}$$

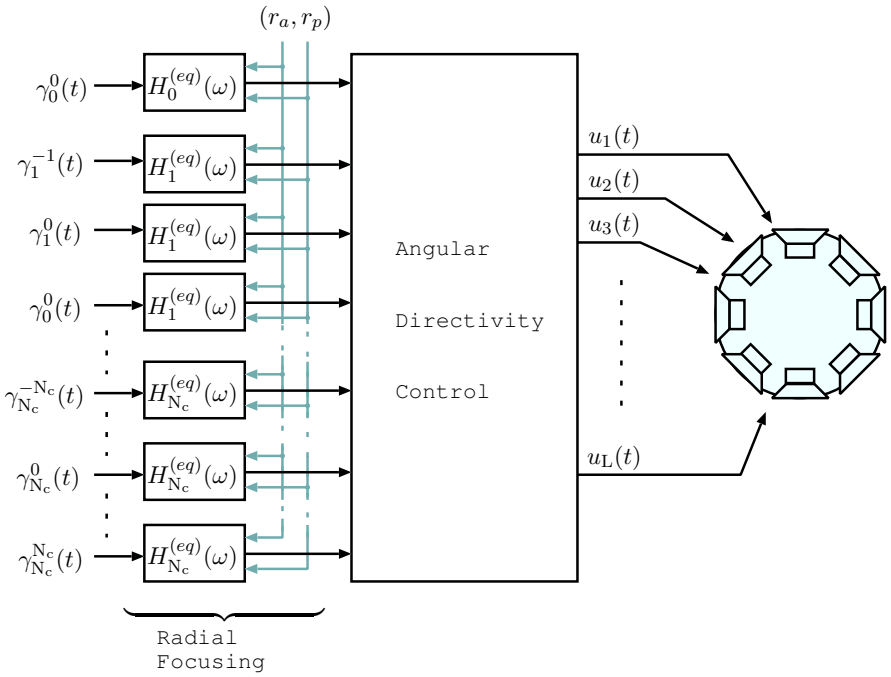

Figure 54: Block diagram of spherical beamforming employing radial beamforming/steering. Given angular directivity control according to the beforehand presented principles (e.g. Fig. 48), a block of specific IIR filters applied to the SH input signals $\gamma_n^m(t)$ achieves radial focusing of the beam pattern to a certain radius r_p.

Corresponding on whether a Neumann $\nu_n^m|_{r_a}$ or a Dirichlet $\psi_n^m|_{r_a}$ boundary value problem is given, the resulting sound pressure waves propagate accordingly

$$\psi_n^m(r) = \frac{\rho_0 c}{\mathrm{i}} \frac{h_n^{(2)}(kr)}{h_n'^{(2)}(kr_a)} \; \nu_n^m|_{r_a}\,, \tag{319}$$

$$\text{or } \psi_n^m(r) = \frac{h_n^{(2)}(kr)}{h_n^{(2)}(kr_a)} \; \psi_n^m|_{r_a}\,, \tag{320}$$

where $k = \omega/c$ is the wave number, $\mathrm{i} = \sqrt{-1}$, ρ_0 is the density of air, and c the speed of sound. $h_n^{(2)}(kr)$ is the spherical Hankel function of the second kind, and $h_n'^{(2)}(kr)$ its derivative.

It is worth mentioning, that all parts of the loudspeaker array – the *inhomogeneous parts of the sound-field* – have to be situated within the sphere $\mathcal{S}_a$ with radius r_a, i.e. $r_a \geq r_0$.

The general signal processing framework of a compact spherical loudspeaker beamformer is depicted in Fig. 54. It is easy to see that the radial and angular components of the beamforming algorithm are separated as will be described in the following sections.

6.7.1 Angular Beamformer Coefficients

Assuming perfect angular pattern re-synthesis on the sphere $\mathcal{S}_a$, either the sound particle velocity $\nu_n^m|_{r_a}$ or the sound pressure $\psi_n^m|_{r_a}$ are given for a finite set of spherical harmonics (n, m) with $n \leq \mathrm{N_c}$ at radius r_a, cf. [ZSH07, ZH07]. This may be labeled as *angular beamforming*. The coefficients $\psi_n^m(r_p)$ of a desired angular directivity pattern $p\left(r_p\, \boldsymbol{\theta}\right)$ at the new radius r_p are calculated by spherical harmonics analysis as

$$\psi_n^m\left(r_p\right) \;=\; \int_{\mathcal{S}^2} p\left(r_p\, \boldsymbol{\theta}\right)\; Y_n^m\left(\boldsymbol{\theta}\right)\; d\boldsymbol{\theta}. \tag{321}$$

Therefore, the spherical harmonic coefficients to form a sharp directional lobe $p(r_p\, \boldsymbol{\theta}) \stackrel{!}{=} \delta\left(1 - \boldsymbol{\theta}^{\mathrm{T}}\, \boldsymbol{\theta}_q\right) = \delta\left(\varphi - \varphi_p, \vartheta - \vartheta_p\right)$ at direction (φ_p, ϑ_p) may be derived as

$$\psi_n^m(r_p) = Y_n^m\left(\varphi_p, \vartheta_p\right), \tag{322}$$

where $\delta\left(1 - \boldsymbol{\theta}^{\mathrm{T}}\, \boldsymbol{\theta}_q\right)$ represents an angular Dirac delta distribution.

6.7.2 Radial Beamformer

In order to achieve a desired angular sound pressure distribution at a target sphere with radius $r = r_p$, a *radial beamformer* is applied. Basically, this radial beamformer inverts the wave propagation Eqs. (319) or (320) by a set of filters $H_n^{(eq)}\left(\omega\right)$. It directly follows from the equations that filters for all orders m of the same order n are equal; the constant multipliers $1/\rho_0 c$ are omitted to improve readability

$$H_n^{(eq,v)}\left(\omega\right) \;=\; \mathrm{i}\frac{h_n'^{(2)}\left(\omega\ \Delta t_a\right)}{h_n^{(2)}\left(\omega\ \Delta t_p\right)}, \tag{323}$$

$$\text{or } H_n^{(eq,p)}\left(\omega\right) \;=\; \frac{h_n^{(2)}\left(\omega\ \Delta t_a\right)}{h_n^{(2)}\left(\omega\ \Delta t_p\right)}. \tag{324}$$

In the equations above, the variables kr_a and kr_p are interpreted as acoustic delays $\Delta t_p = r_p/c$ and $\Delta t_a = r_a/c$ times the angular frequency $\omega = 2\pi f$. This re-interpretation proves to be very practical for the definition of the radial beamforming filters later on.

6.8 Dynamic Range Limits of the Radial Beamformer

This section discusses the applicable dynamic range of the radial beamforming filter shapes. Due to a strong low-frequency boost, most practical implementations require the definition of lower cutoff frequencies. These are defined by bounding the maximum filter gain to a desired dynamic range, i.e. *white noise gain* (WNG), and obtained by observing the filter shapes.

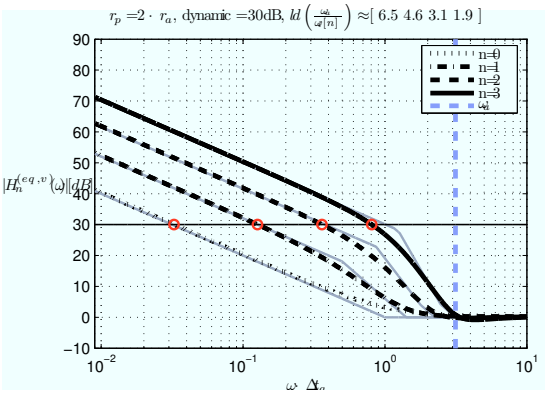

(a) $|H_n^{(eq,v)}(\omega)|$ in dB for $r_p = 2\, r_a$

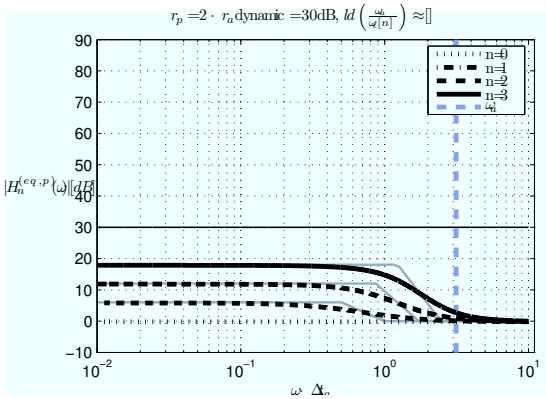

(b) $|H_n^{(eq,p)}(\omega)|$ in dB for $r_p = 2\, r_a$

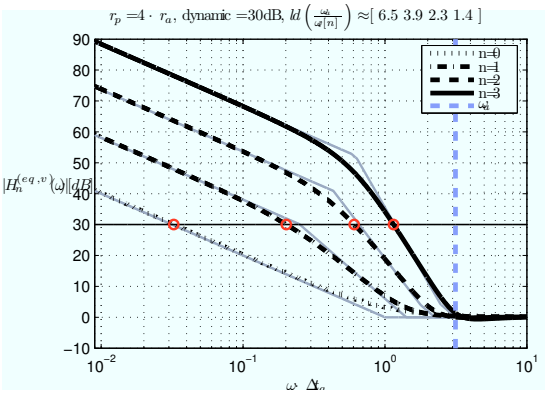

(c) $|H_n^{(eq,v)}(\omega)|$ in dB for $r_p = 4\, r_a$

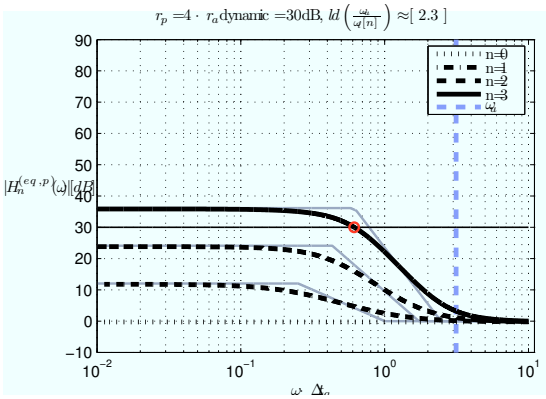

(d) $|H_n^{(eq,p)}(\omega)|$ in dB for $r_p = 4\, r_a$

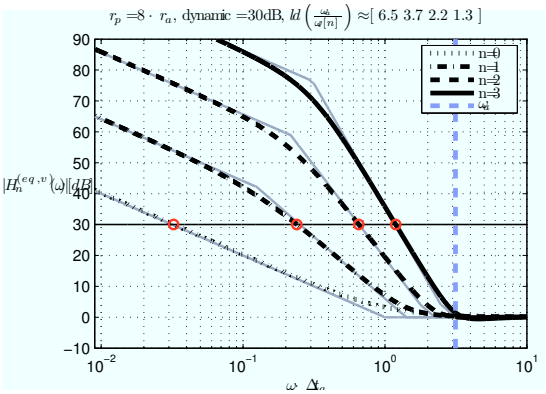

(e) $|H_n^{(eq,v)}(\omega)|$ in dB for $r_p = 8\, r_a$

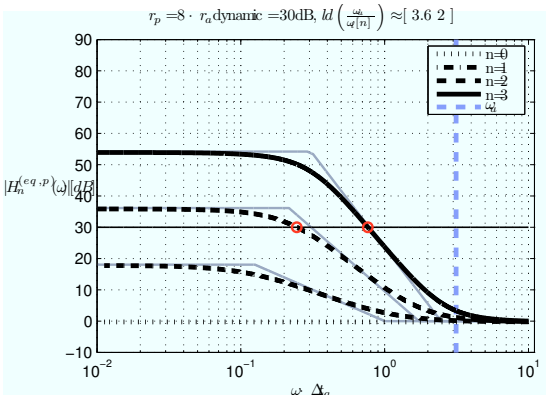

(f) $|H_n^{(eq,p)}(\omega)|$ in dB for $r_p = 8\, r_a$

Figure 55: Frequency responses of radial beamforming filters with different target radii r_p, (a,b) $r_p = 2\, r_a$, (c,d) $r_p = 4\, r_a$, and (e,f) $r_p = 8\, r_a$, derived for angular control at r_a. The left and right column correspond to sound particle velocity Eq. (323) and sound pressure control Eq. (324), respectively. The feasible bandwidth $ld\,(\omega_u/\omega_l[n])$ is indicated for a maximum gain of 30dB. The dashed vertical line indicates the upper aliasing cutoff frequency abd the thin grey lines the asymptotic approximation of the frequency responses; the points mark the lower cutoff frequencies, cf. [Pom08].

Velocity control. The left column of Fig. 55 shows frequency responses of the radial beamforming filters designed for angular velocity control at the radius r_a (cp. Eq. (323)). These frequency responses depend on the target radius r_p and on the order of the spherical harmonics used for synthesis. Assuming a dynamic range of 30dB WNG for the simulations, a feasible synthesis bandwidth $ld\,(\omega_u/\omega_l[n])$ is indicated for different spherical harmonic orders n; where ω_u refers to the upper and $\omega_l[n]$ to the lower cutoff frequencies, respectively.

Example: The IEM compact spherical loudspeaker array [ZH07] features an aperture radius of $r_0 = 30cm$, resulting in an upper cutoff frequency of $f_u \approx 600Hz$. The simulation results for a target distance of $r_p = 4\ r_0$ show that the spherical harmonics of third order may be reproduced properly with a lower cutoff frequency of $f_l = 150Hz$, whereas the harmonics of second order are well synthesized above a minimal frequency $f_l = 75Hz$, respectively.

Pressure control. In contrast, the frequency responses of the radial beamforming filters in the right column of Fig. 55 are designed for angular pressure control at r_a. These responses are comparable to those for angular velocity control, but the curves remain constant over a broad frequency range $\omega\Delta t_a$. In this particular example, not all the filters require a lower cutoff frequency for their filter gains to stay within a 30dB WNG dynamic range bound.

6.9 Radial Beamformer Implementation

In the following section, discrete-time implementations of radial beamformers for accurate synthesis of directivity patterns are derived. As shown in the analytical model presented above, these spherical equalization filters are defined by ratios of the spherical Hankel functions and their derivatives. Once a discrete-time model of the filters is obtained, it is simply applied to compact spherical loudspeaker arrays, cf. Fig. 54.

6.9.1 Spherical Hankel Functions

The spherical Hankel functions of the second kind $h_n^{(2)}(\tilde{\omega})$ and their derivatives $h_n'^{(2)}(\tilde{\omega})$ are defined as follows (cf. [GD04]):

$$h_n^{(2)}(\tilde{\omega}) = \mathrm{i}^{n+1}\frac{\mathrm{e}^{-\mathrm{i}\tilde{\omega}}}{\rho}\sum_{l=0}^{n}\frac{(n+l)!}{l!\,(n-l)!}\left(\frac{1}{2\mathrm{i}\tilde{\omega}}\right)^l \tag{325}$$

$$h_n'^{(2)}(\tilde{\omega}) = -\frac{n-1}{\tilde{\omega}}h_n(\tilde{\omega}) + h_{n-1}(\tilde{\omega}), \tag{326}$$

Note that $\tilde{\omega}$ denotes the normalized frequency $\tilde{\omega} = k\,r|_{r=c}$, which simplifies the following derivations.

Laplace representation of spherical Hankel functions: Jérôme Daniel [DNM03] and [ZH07] give an interpretation of the radial solutions providing a filter design description, starting from the power series expansion of the spherical Hankel function[4], with normalized argument $\tilde{\omega} = kr|_{r=c}$:

$$h_n^{(2)}(\tilde{\omega}) = \mathrm{i}^{n+1}\frac{\mathrm{e}^{-\mathrm{i}\tilde{\omega}}}{\tilde{\omega}}\sum_{l=0}^{n}\frac{(n+l)!}{l!\,(n-l)!}\left(\frac{1}{2\mathrm{i}\tilde{\omega}}\right)^l \tag{327}$$

$$h_n'^{(2)}(\tilde{\omega}) = -\frac{n+1}{\tilde{\omega}}h_n(\tilde{\omega}) + h_{n-1}(\tilde{\omega}). \tag{328}$$

The re-interpretation in the Laplace-domain also uses a normalized argument $\tilde{s} = \mathrm{i}\tilde{\omega}$ and yields a rational function in $\tilde{s}$, and a delay $\mathrm{e}^{-\tilde{s}}$:

$$h_n^{(2)}(\tilde{s}) = -\mathrm{i}^n\frac{\sum_{k=0}^{n} b_n(k)\;\tilde{s}^k}{\tilde{s}^{n+1}}\;\mathrm{e}^{-\tilde{s}} \tag{329}$$

$$h_n'^{(2)}(\tilde{s}) = \mathrm{i}^{n+1}\frac{\sum_{k=0}^{n+1} c_n(k)\;\tilde{s}^k}{\tilde{s}^{n+2}}\;\mathrm{e}^{-\tilde{s}}. \tag{330}$$

For the coefficients $b_n(k)$, we get:

$$b_n(k) = \frac{(2n-k)!}{(n-k)!\;k!\;2^{n-k}}. \tag{331}$$

The coefficients of the numerator polynomials are integer numbers and may be derived using the following difference schemes

$$b_n(n) = 1, \qquad \text{for n}\geq 0 \tag{332}$$

$$b_n(k) = \frac{(2n-k-1)(2n-k)}{2\;(n-k)}\;b_{n-1}(k), \qquad \text{for } k < n \tag{333}$$

$$b_n(k) = 0, \qquad \text{else,} \tag{334}$$

whereas the integer coefficients of the derivative of the spherical Hankel functions are given by

$$c_0(k) = -b_1(k), \qquad \text{for } 0 \leq k \leq 1 \tag{335}$$

$$c_n(k) = (n+1)\;b_n(k) + b_{n-1}(k-2), \qquad \text{for } n \geq 1 \text{ and for } 0 \leq k \leq n+1. \tag{336}$$

[4]Note that the spherical Hankel functions of the second kind match the practical assumptions in system theory and signal processing better than the functions of the first kind, which are anti-causal. As a consequence, the Euler equation, the Sommerfeld radiation condition, the Green's function, and the plane-wave is defined differently, i.e. complex conjugate, in this work than in textbooks in acoustics.

Using a linear factorization of the Laplace-Domain description, it becomes easy to estimate the resulting filter gain for every frequency by asymptotic approximation (see Fig. 7).

If required, spherical Bessel and Neumann functions could be found by taking the real- and imaginary parts

$$j_n(\tilde{s}) = \frac{h_n^{(2)}(\tilde{s}) + h_n^{(2)}(\tilde{s}^*)}{2}, \qquad j_n'(\tilde{s}) = \frac{h_n'^{(2)}(\tilde{s}) + h_n'^{(2)}(\tilde{s}^*)}{2}, \tag{337}$$

$$y_n(\tilde{s}) = \frac{h_n^{(2)}(\tilde{s}) - h_n^{(2)}(\tilde{s}^*)}{2}, \qquad y_n'(\tilde{s}) = \frac{h_n'^{(2)}(\tilde{s}) - h_n'^{(2)}(\tilde{s}^*)}{2}. \tag{338}$$

It is worth mentioning that for a radial beamformer the different re-normalizations with respect to Δt_a and Δt_p have to be taken into account when building the ratio of the spherical Hankel functions:

$$h_n(s\Delta t_i) = \frac{1}{s\Delta t_i}\left(\frac{s-\frac{b_r}{\Delta t_i}}{s}\right)^{mod(n,2)} \times \left(\prod_{l=1}^{div(n,2)} \frac{(s-\frac{b_l}{\Delta t_i})^2 + \frac{\omega_l^2}{\Delta t_i^2}}{s^2}\right), \tag{339}$$

$$h_n'^{(2)}(s\Delta t_i) = \frac{1}{s\Delta t_i}\left(\frac{s-\frac{b_r'}{\Delta t_i}}{s}\right)^{mod(n+1,2)} \times \left(\prod_{l=1}^{div(n+1,2)} \frac{(s-\frac{b_l'}{\Delta t_i})^2 + \frac{\omega_l'^2}{\Delta t_i}}{s^2}\right), \tag{340}$$

with $\Delta t_i = \{\Delta t_p, \Delta t_a\}$ depending on the respective radii. In particular, the scaling $\tilde{\omega}\Delta t_a$ and $\tilde{\omega}\Delta t_p$ yields a displacement of the zeros with $b \to b/\Delta t_i$ and $\omega \to \omega/\Delta t_i$ by a linear scale factor $1/\Delta t_i$.

6.9.2 Discrete-Time Implementation of the Radial Beamforming Filters, Impulse Invariance

The conversion of the fractional filter functions defined in the Laplace-domain can be performed using the bilinear transform [DNM03], or the corrected impulse invariance technique [Pom08]. The corrected impulse invariance technique might seem attractive because it does not distort the linear freqeuncy scale. However, in many applications, it does not make much of a difference, as soon as the spectral knee is at frequencies lower than a sixth of the sampling frequency.

Applying the (ordinary) impulse invariance technique to the first- and second-order sections in Eq. (339) and Eq. (340), the discrete-time transfer function in z

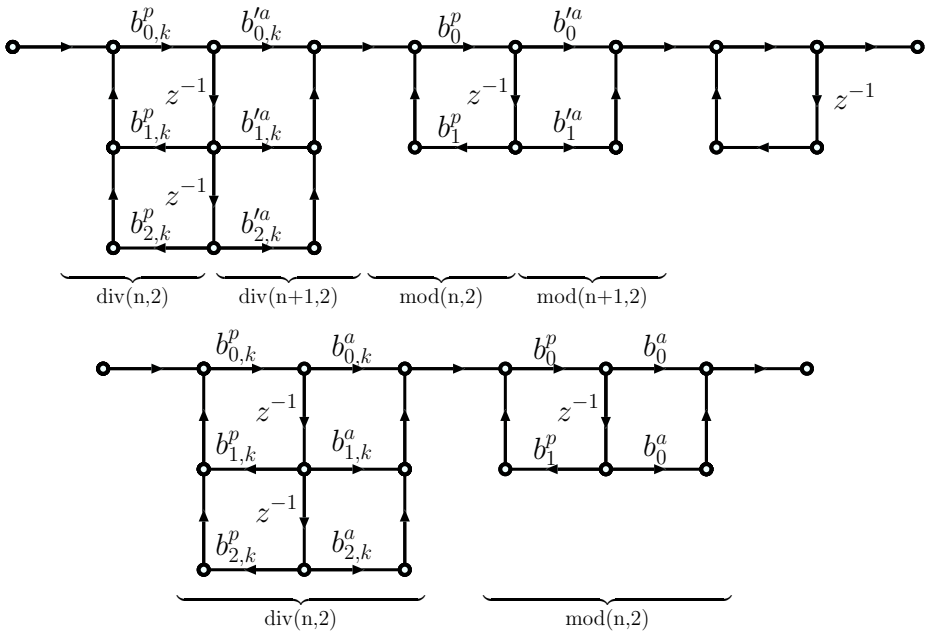

Figure 56: Two examples of digital filter structures for spherical spherical radial beamforming.

may be derived. The following transform pairs are very useful for calculation:

$$H(s) = \frac{s - b_r}{s} \tag{341}$$

$$\overset{iiv.}{\rightarrow} H(z) = \frac{(1 - \tilde{b}_r) - z^{-1}}{1 - z^{-1}}, \tag{342}$$

$$H(s) = \frac{(s - b_l)^2 + \omega_l^2}{s^2} \tag{343}$$

$$\overset{iiv.}{\rightarrow} H(z) = \frac{1 - 2\tilde{b}_l + (\tilde{b}_l^2 + \tilde{\omega}_l^2 + 2\tilde{b}_l - 2)\, z^{-1} + z^{-2}}{\left(1 - z^{-1}\right)^2}. \tag{344}$$

The coefficients $\tilde{b}_l$, $\tilde{b}_r$, and $\tilde{\omega}_l$ denote the respective Laplace-domain coefficients scaled by the factor $1/f_s$, where f_s is the sampling frequency. In Fig. 56 two examples of the resulting filter structures for radial beamforming are given; Fig. 57 shows the match of the transfer functions to the analytic specifications, assuming parameters suitable for the IEM icosahedral loudspeaker [ZH07].

Note that the filters derived in Hannes Pomberger's diploma thesis [Pom08] achieve a better fit, and a detailed comparison between different filter conversion methods can be found there.

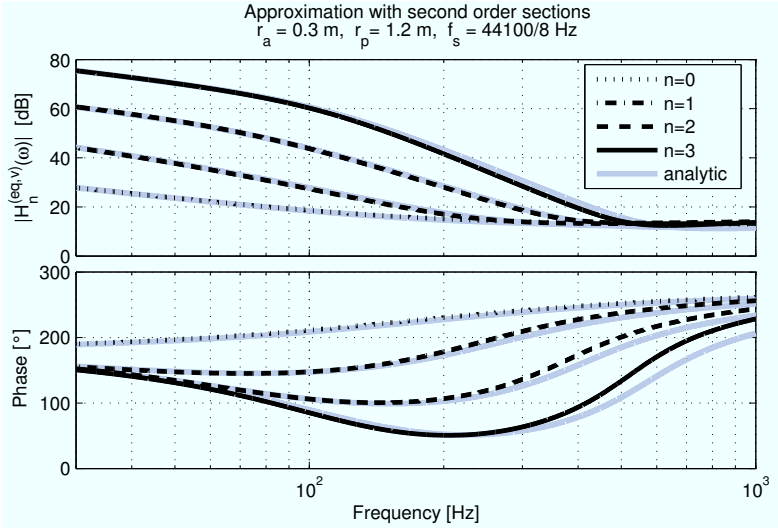

Figure 57: Comparison of frequency responses in magnitude and phase showing the proposed discrete-time radial beamforming filters (black) and their analytic counterparts (gray). A design example using $r_a = 0.3$m, $r_p = 1.2$m, and $f_s = 5512.5$Hz was considered.

6.10 Modeling Dynamic Limitations Due to Shared vs. Isolated Array Speaker Enclosures

For a brief theoretical introduction to spherical acoustical radiators, let's consider a spherical shell with homogeneous sound field on either side, interior and exterior. Further, assume the shell surface to have no own properties, except its being a common sound particle velocity boundary condition for both sound fields. We may also assume its interior radius r_i being related to the fixed exterior radius r_0:

- equals the surface radius $kr_i = kr_0$, (infinitesimal thickness)
- smaller than the surface radius $kr_i < kr_0$, (finite thickness)
- virtually larger than the surface radius $kr_i > kr_0$, (negative thickness)

The third setup appears to be rather strange at first sight. Nevertheless, it tends to be quite useful to account for changes in the medium. For instance increased interior temperature T_i, on one hand, could lead to increased interior sonic speed c_i. On the other hand an enclosure filled with damping wool reduces the adiabatic exponent κ_i and therefore scales the sonic speed c_i. A re-interpretation as either virtually smaller or bigger interior radius r_i helps keeping the description simple while using a single value $k = \frac{\omega}{c}$ only. In doing so, the three variables k, r_o, r_i are sufficient to describe at least 5 different physical quantities[5] ω, $c \propto (\kappa, T)$, $c_i \propto (\kappa_i, T_i)$, r_i, r_o.

[5]The careful reader might notice: she finds herself in the field of acoustics :-).

Radiation to the exterior by the spherical velocity boundary. Using the solutions of the wave equation in the spherical coordinate system, we are able to describe the radiation of a given radial velocity distribution by using its spherical harmonics transform $\nu_n^m|_{r_o} = \int_{\mathbb{S}^2} v(\boldsymbol{\theta})|_{r_o}\ Y_n^m(\boldsymbol{\theta})\ d\boldsymbol{\theta}$, and the *spherical wave spectrum* $\psi_n^m(kr)$ valid for $r \leq r_o$:

$$\psi_n^m|_{r_o} \quad = \quad \mathrm{i}\rho_0 c\, \frac{h_n^{(2)}(kr)}{h_n'^{(2)}(kr_o)}\ \nu_n^m|_{r_o}\,. \tag{345}$$

So given the above model, we obviously need a non-zero radial-velocity pattern along this surface to produce radiation towards $r \leq r_o$.

Impedance of a common enclosure volume. The concept of the above boundary condition provides a basis for the analysis of the impedances of the boundary, associated with the spherical harmonics patterns of vibration. Here, solely defined by the acoustics, the impedance is given as:

$$\begin{aligned} \mathrm{Z}_{ad,nm} \quad &= \quad \frac{\psi_n^m|_{r_o}}{\nu_n^m|_{r_o}} \\ &= \quad \mathrm{i}\rho_0 c \left[\frac{j_n(kr_i)}{j_n'(kr_i)} + \frac{h_n^{(2)}(kr_o)}{h_n'^{(2)}(kr_o)}\right]. \end{aligned} \tag{346}$$

This description tells us, which amount of pressure $\psi_n^m|_{r_o}$ has to be applied to get a surface velocity pattern $\nu_n^m|_{r_o} = 1$. Fig. 58 shows the shape of the impedance curves over the diameter in wavelengths, i.e. $\frac{\phi_o}{\lambda} = kr_o/\pi$. Basically due to the interior resonances of the higher-order modes, peaks appear in the curves, i.e. the sound pressure due to resonances works against the unity velocity excitation. Within the near-field of the Bessel functions though, the enclosure seems to support the higher-order vibration patterns.

Impedance of isolated enclosure volumes. In order to analyse the behavior of isolated interior sound fields that prevent acoustic coupling via the interior, we assume a simple model without angular velocities. Basically, we can divide the surface into infinitesimal fractions, each of which can only be subject to the Y_0^0 mode of the enclosure. Mathematically, this is (numerically) simulated by the impedance of a rectified interior boundary:

$$\mathrm{Z}_{ad,nm} \quad = \quad \mathrm{i}\rho_0 c \left[\frac{j_0(kr_i)}{j_0'(kr_i)} \int_{\mathbb{S}^2} |Y_n^m(\boldsymbol{\theta})|\ Y_0^0(\boldsymbol{\theta})\, d\boldsymbol{\theta} + \frac{h_n^{(2)}(kr_o)}{h_n'^{(2)}(kr_o)}\right].$$

The result is depicted in Fig. 59. Basically, the influence of the notches can be removed, but the support of the higher-order patterns gets lost.

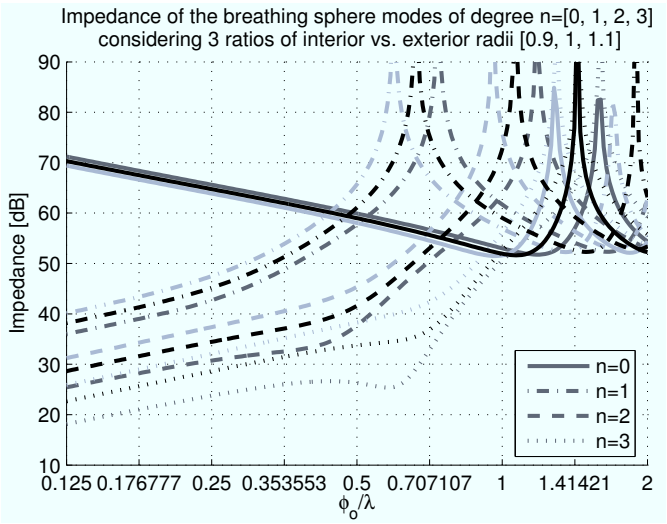

Figure 58: Impedance curves of the spherical boundary condition with varying ratio between the radii $r_i/r_o = [0.9,\ 1,\ 1.1]$ (gray, black, light gray) and for the orders $n = [0,\ 1,\ 2,\ 3]$.

Adding surface impedance. It is very convenient to add a uniformly distributed surface impedance z to the impedance from above, in order to account for friction, stiffness, and mass of the surface. An RLC characteristics can be assumed, like in the electroacoustic cap model

$$\begin{aligned} \mathrm{Z}_{ad,nm,1} &= \mathrm{i}\rho_0 c \left[\frac{j_n\left(kr_i\right)}{j_n'\left(kr_i\right)} + \frac{h_n^{(2)}\left(kr_o\right)}{h_n'^{(2)}\left(kr_o\right)} \right] + z, \\ \mathrm{Z}_{ad,nm,2} &= \mathrm{i}\rho_0 c \left[\frac{j_0\left(kr_i\right)}{j_0'\left(kr_i\right)} \int_{\mathbb{S}^2} \left|Y_n^m\left(\boldsymbol{\theta}\right)\right|\ Y_0^0(\boldsymbol{\theta})\ d\boldsymbol{\theta} + \frac{h_n^{(2)}\left(kr_o\right)}{h_n'^{(2)}\left(kr_o\right)} \right] + z. \end{aligned}$$

Velocity control for radial beam-steering. In order to obtain a unity-gain beam-pattern synthesis at the radius r_p from a boundary of the radius r_o, the velocity must equal $\nu_n^m = \frac{1}{\mathrm{i}\rho_0 c} \frac{h_n'^{(2)}(kr_o)}{h_n^{(2)}(kr_p)}$. In analogy to the discrete-space loudspeaker array model, the sound pressure distribution at the surface shall be controlled with voltage distributions.

$$\begin{aligned} \psi_{ad,nm,1} &= \frac{h_n'^{(2)}\left(kr_o\right)}{h_n^{(2)}\left(kr_p\right)} \left[\frac{j_n\left(kr_i\right)}{j_n'\left(kr_i\right)} + \frac{h_n^{(2)}\left(kr_o\right)}{h_n'^{(2)}\left(kr_o\right)} + \frac{z}{\mathrm{i}\rho_0 c} \right]. \\ \psi_{ad,nm,2} &= \frac{h_n'^{(2)}\left(kr_o\right)}{h_n^{(2)}\left(kr_p\right)} \left[\frac{j_0\left(kr_i\right)}{j_0'\left(kr_i\right)} \int_{\mathbb{S}^2} \left|Y_n^m\left(\boldsymbol{\theta}\right)\right|\ Y_0^0(\boldsymbol{\theta})\ d\boldsymbol{\theta} + \frac{h_n^{(2)}\left(kr_o\right)}{h_n'^{(2)}\left(kr_o\right)} + \frac{z}{\mathrm{i}\rho_0 c} \right]. \end{aligned}$$

Using the parameters of the big IEM icosahedral loudspeaker array, we can try to use this rough method of analysis. As stated before, the magnitude of the pressure depicted here should be proportional to a voltage distribution for the excitation of the sphere. Consequently, performing a velocity control for radial

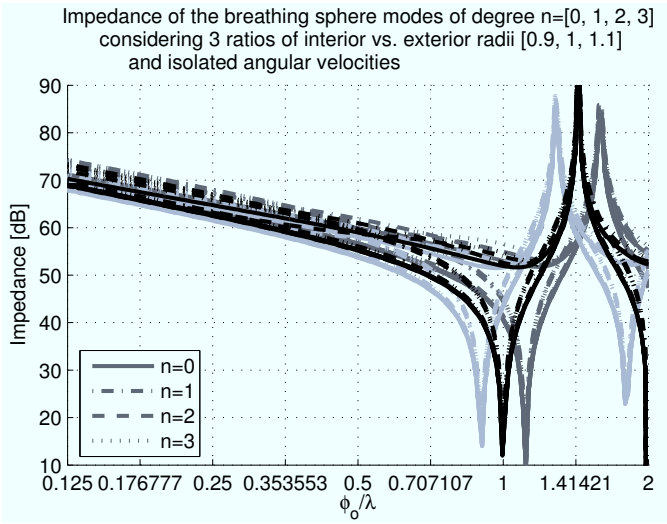

Figure 59: Impedance curves of the spherical boundary condition with varying ratio between the radii $r_i/r_o = [0.9,\ 1,\ 1.1]$ and for the orders $n = [0,\ 1,\ 2,\ 3]$, here the interior angular sound particle velocities have been eliminated.

beam-steering at different focal distances r_p from the origin reveals the required dynamic range of the control voltages. The average surface impedance was assumed to be 20 z^{me}, the total impedance of all membranes. The influence of spatial sampling and angular aliasing is not considered in this impedance model. Fig. 60 compares these dynamic ranges for common versus separated enclosure designs at different spherical harmonic orders n, using the rough, but fair, approximation $\int_{\mathbb{S}^2} |Y_n^m(\boldsymbol{\theta})|\ Y_0^0(\boldsymbol{\theta})\ d\boldsymbol{\theta} \approx 1$.

In comparison, common enclosure designs support the higher-order harmonics more than the separated enclosures design. Therefore control requires less dynamic range for the common interior at large synthesis radii r_p, low frequencies, and $n > 0$. As a drawback, common interior designs exhibit interior resonances depending on n and at lower frequencies than the separated enclosure design.

Using the above model, it becomes possible to include the limits of excursion, current, voltage, or power, in order to calculate the bounds of a playback system. However, these electrical and mechanical quantities become frequency dependent without being scaled with the radius, therefore these examinations require analysis in a more-dimensional space.

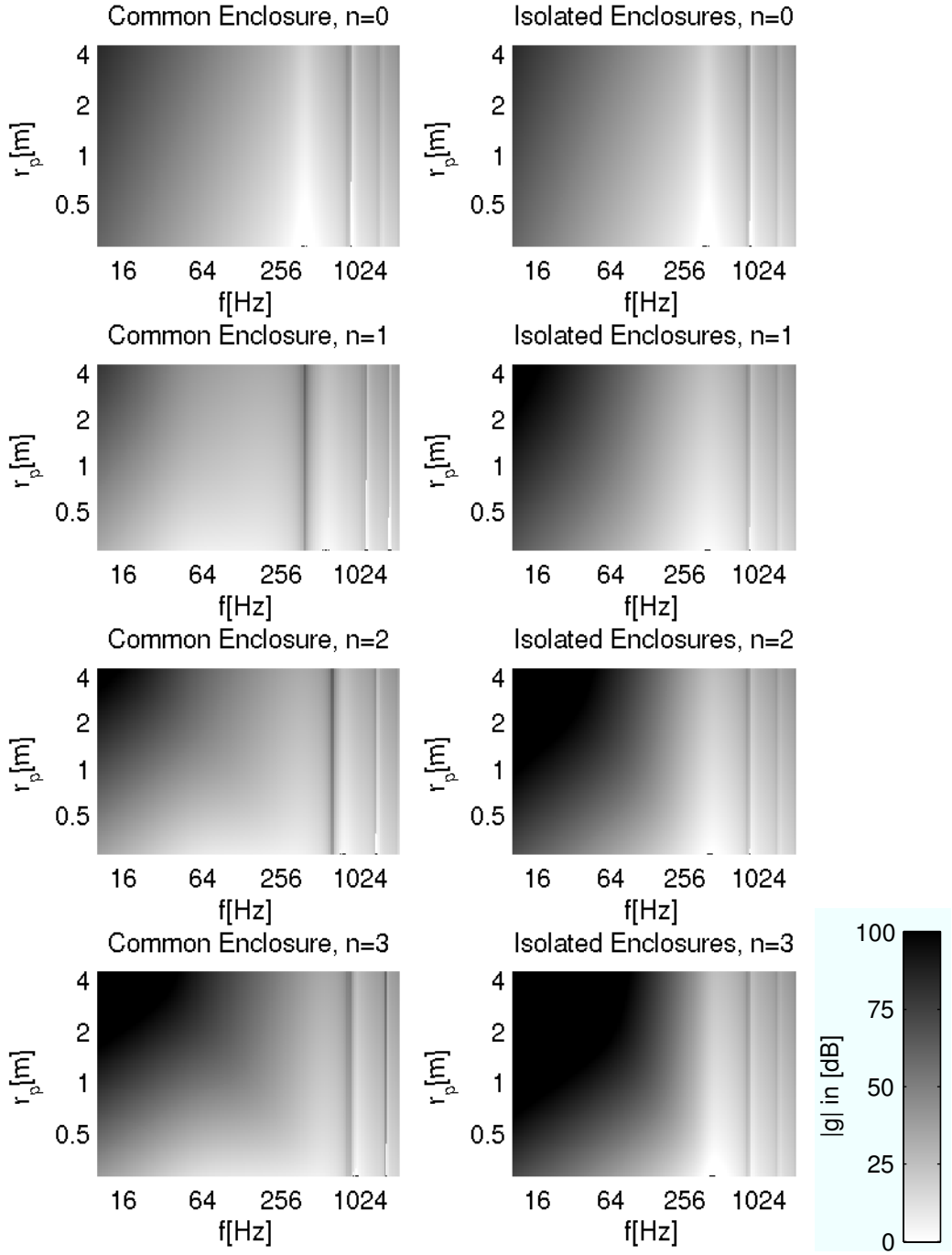

Figure 60: Required magnitude boost for pressure synthesis with a continuous spherical membrane, comparing common enclosure (left column) with isolated enclosures (right column).

Chapter VII

CONCLUSIONS AND OUTLOOK

This chapter summarizes the findings and contributions of the previous chapters. It further provides outlooking considerations associated with the chapters and some overall research questions concerning sound-radiation.

To begin with, a model has been given describing the complexity of the interaction between musician and instrument and its observable product, the sound-radiation, see Figs. 2 and 4, which has been the matter of the presented practical studies. Preliminarily to all practical experiments, prototypes and models thereof, the required theoretical, algorithmic, and discrete implementation aspects are illuminated in Chapters 2–4. Chap. 2 has newly compiled a comprehensive theory of the acoustics in spherical coordinates, giving mathematical equations and describing their properties. Some fundamental relations (e.g. spherical wave-spectrum, boundary value problems, spherical source distributions) provide the means for spherical holography and holophony. This powerful theory is capable of solving analysis and synthesis problems for entire fields of sound-radiation or incident sound.

Methods and algorithms for manipulation of sound-radiation or irradiation signals have been gathered in Chap. 3. These incorporate translation, rotation, multiplication, and rotational matching of sound-radiation or irradiation (Ambisonics). The algorithms for rotation and translation have been newly reformulated for real-valued angular solutions, but the algorithm for translation is represented in the frequency domain only. The algorithm should be extended to time-domain implementations, using the filters from Sec. 6.9. This step will enable real-time holophonic rendering of translated sources or fields, or time-domain fast-multipole-methods. Beyond the presented methods, the palette of manipulation methods should be extended towards artistic applications in the future: Angular warping, sharpening, etc. could offer useful control in large-scale sound installations but currently lack a mathematical formulation.

As required for all kinds of spherical arrays, a thorough research on various sampling schemes on the sphere has been presented in Chap. 4. Discrete spherical harmonics transform methods have been illustrated, which are applicable to different sampling schemes. The measures *sampling efficiency* and *numerical condition* have been introduced and applied together with known measures to characterize important sampling schemes. Most of these rely on uniformly sampled spheres,

so the question is raised of how to deal with incomplete spherical domains, for which some hints have been given. A question of future research remains, how anisotropically resolved spherical distributions can be represented.

After illumination of the background knowledge in the first four chapters, two practical problems have been solved in Chap. 5 and 6. In Chap. 5 the capture of sound-radiation by *surrounding spherical microphone arrays* has been investigated. As main results the definition of a *sound-radiation signal*, its SIMO model Fig. 26, and an analysis approach has been shown. In the various examples, the interesting insights accessible through surrounding spherical microphone arrays have been illustrated. The data offer good material for spatial audio rendering, musical acoustics, computer music, and room acoustics. So future research should consider collecting databases of sound-radiation from various instruments or sound sources. However several questions remain, mainly in determining the resolution required for the capture of sound-radiation. Alternatively to the presented analysis algorithm, it could be fruitful to test adaptive algorithms that potentially enhance the estimation of a primal signal and radiation filters. Furthermore, the feasibility of an algorithm for translation and rotation detection of the acoustic origin should be investigated. Precise knowledge about this "true" origin could reduce aliasing and truncation errors due to the centering problem.

In the last practical Chap. 6 a thorough study of means to model, measure, and control *compact spherical loudspeaker arrays* has been presented. The findings enable efficient control of the angular sound-radiation at a variable radius but also exhibit limitations. On the one hand, discrete arrays create angular aliasing at high frequencies. On the other hand, high-resolution synthesis is difficult at low frequencies, due to dynamic range restrictions of both the electroacoustic system, and signal processing. While angular aliasing can be minimized with small array dimensions, the dynamic range problem worsens. A common enclosure is supporting the low-frequency end but insufficiently. Hence, the questions of how to stabilize low frequency synthesis satisfactorily and how to construct optimal multi-band spherical arrays remain open fields of research.

7.1 Future Work

7.1.1 Room acoustics.

As a novel topic in future research, *new room acoustic measurement problems* can be solved by combining compact spherical loudspeaker and microphone arrays.

7.1.2 Sound-Radiation, its Effects and Perception

Looking further ahead, it is not fully understood, which aspects of sound-radiation are *perceivable* in what way.

Direct sound. For instance, directivity in the free-field will mainly yield coloration of the perceived direct sound, and in special cases it can be used to evoke diffraction on the listener's body (e.g. at shoulders, HRTFs, time-variant cues due to small head movements...) [Sch09]. It is not clear yet, which perceptual effects are generated by the source directivity in this situation.

Sound-radiation in rooms. Probably more commonly, directivity will have several different observable effects in *interaction with a room*. As symbolically shown in Fig. 61, directional sound-radiation effects

- the direct sound and early reflections:
  - in magnitude,
  - sound-coloration,
  - local variation[1] of angles of incidence, time- and magnitude-pattern,
- the magnitude and sound-coloration of the diffuse reverberation,
- the direct to reverberant ratio and its local variation.

Note that the acoustic properties of the floor, walls, and the ceiling have similar effects on all components of the room impulse response observable at the listener's position. It can be supposed that rooms remain static, whereas sources may frequently move, and that directional sources can create an increased local variation of the sound field. Generally, an important research question is in how far and under which circumstances the above-mentioned aspects allow for a perceptual inference on

- properties of the sound source itself,
- its orientation,
- its position,
- the room.

[1] The expression *local variation* refers to the variations in a small area of the sound field, observable by movements of the listener's head.

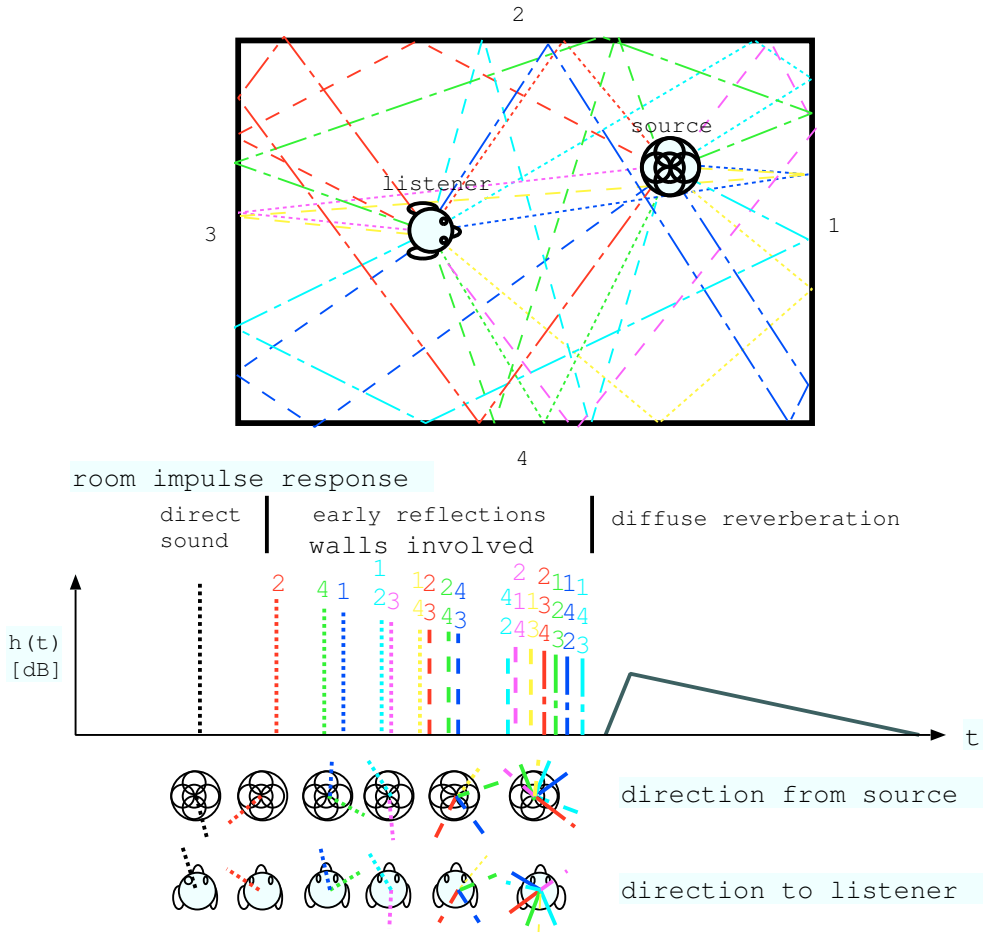

Figure 61: The directional room impulse response at the listener depends on the properties of the room (geometry, surfaces), as well as the directional sound-radiation of the sound source.

Conversely, it should be clarified, in which cases this inference collapses so that the above changes are perceived directly as attributes of the room or sound-color instead of spatial source attributes. And if so, does it yield an annoying or acceptable auditory or audio-visual perception? Informal listening indicates that rapid changes of the directivity pattern orientation during the ringing sound catches a lot of perceptual attention. Therefore, dynamic variation of the orientation should be taken into account as well. Synthetic stimuli as known in other psychoacoustic experiments could be used to start with in order to keep the effort small. Nevertheless, the question which rooms, which listening and playback positions are representative, and which situations allow useful spatial perception has to be answered.

In combination of both, sound-radiation analysis and synthesis, many other interesting issues should be explored in psychoacoustic experiments. It is neither clear yet, which angular resolution is required to represent the sound-radiation of

certain instruments, nor which resolution for its playback in different rooms. For definite results, this will require very high-order spherical arrays to make sure.

7.1.3 Sound-Radiation Loop Machine

Finally, the combination of a surrounding spherical microphone and a compact spherical loudspeaker array could be applied within an artistic context. In particular, a loop-machine, mimicking the sound-radiation in live-performances could be an exciting tool to dream of...

Appendix A

THE SOMMERFELD RADIATION CONDITION

states that the impedance of a radiating source must be positive and real-valued in the far-field, in order to allow for real power dissipation. To find the correct radial solution for radiation, the far-field impedance for radiation is assumed to be one of the following expressions

$$\lim_{r\to\infty} z_r\left(kr\right) = \lim_{r\to\infty} \frac{\rho_0 c}{\mathrm{i}} \cancel{\frac{c_{nm}}{c_{nm}}} \left\{ \frac{j_n\left(kr\right)}{j_n'\left(kr\right)} \;\middle|\; \frac{y_n\left(kr\right)}{y_n'\left(kr\right)} \;\middle|\; \frac{h_n^{(1)}\left(kr\right)}{h_n'^{(1)}\left(kr\right)} \;\middle|\; \frac{h_n^{(2)}\left(kr\right)}{h_n'^{(2)}\left(kr\right)} \right\}. \quad (347)$$

The first two solutions, namely the real-valued $j_n\left(kr\right)$ and $y_n\left(kr\right)$, are not feasible due to the complex multiplier $\frac{\rho_0 c}{\mathrm{i}}$. According to (42), different orders $n \neq l$ of the spherical Hankel functions of the first or second kind share the same order of magnitude in the far-field:

$$\lim_{r\to\infty} \left|h_n^{(1|2)}\left(kr\right)\right| = \frac{1}{kr}. \quad (348)$$

Therefore in the limit the derivative, using the recurrence Eq. (41), simplifies to

$$\lim_{r\to\infty} h_n'^{(1|2)}\left(kr\right) = \lim_{r\to\infty} \left\{ h_{n-1}^{(1|2)}\left(kr\right) - \cancel{\frac{n+1}{kr} h_n^{(1|2)}\left(kr\right)} \right\} = \lim_{r\to\infty} h_{n-1}^{(1|2)}\left(kr\right). \quad (349)$$

The far-field approximation for the functions $h_n^{(1|2)}(kr)$ yields

$$\lim_{r\to\infty} h_n^{(1|2)}\left(kr\right) = \frac{\mathrm{e}^{\pm \mathrm{i}kr}}{\left(\pm\mathrm{i}\right)^{n+1} kr}, \quad (350)$$

and putting together Eq. (349) and (350) the impedance yields

$$\frac{\rho_0 c}{\mathrm{i}} \lim_{r\to\infty} \frac{h_n^{(1|2)}\left(kr\right)}{h_n'^{(1|2)}\left(kr\right)} = \mp \rho_0 c. \quad (351)$$

Therefore only the spherical Hankel function of the second kind fulfills the radiation condition:

$$\lim_{r\to\infty} z_r\left(kr\right) = \begin{cases} \frac{\rho_0 c}{\mathrm{i}} \frac{j_n(kr)}{j_n'(kr)} \notin \mathbb{R}^+, & \text{for } j_n(kr), \\ \frac{\rho_0 c}{\mathrm{i}} \frac{y_n(kr)}{y_n'(kr)} \notin \mathbb{R}^+, & \text{for } y_n(kr), \\ -\rho_0 c \notin \mathbb{R}^+, & \text{for } h_n^{(1)}(kr), \\ \rho_0 c \in \mathbb{R}^+, & \text{for } h_n^{(2)}(kr). \end{cases} \quad (352)$$

Appendix B

EFFICIENT RECCURENT EVALUATION

Efficient computation of N_n^m. We can define these coefficients by recurrence relations, using:

$$N_n^0 = \sqrt{\frac{2n+1}{4\pi}}, \text{ for } n \geq 0 \tag{353}$$

$$\begin{aligned} \frac{N_n^m}{N_n^{m-1}} &= -\sqrt{\frac{(1+\delta[m-1])(n-m)!(n+m-1)!}{(n-m+1)!(n+m)!}} \\ &= -\sqrt{\frac{1}{(n-m+1)(n+m)}}, \text{ for } 1 \leq m \leq n, \end{aligned} \tag{354}$$

$$\begin{aligned} \frac{N_n^{-m}}{N_n^{-m+1}} &= -\sqrt{\frac{(1+\delta[m+1])(n+m)!(n-m+1)!}{(n+m-1)!(n-m)!}} \\ &= -\sqrt{(n+m)(n-m+1)}, \text{ for } -n \leq m \leq 1. \end{aligned} \tag{355}$$

For the coefficients up to an order N, we use the following operation to compute the number of coefficients:

$$\sum_{n=0}^{\mathrm{N}} \sum_{m=-n}^{n} 1 = \sum_{n=0}^{\mathrm{N}} (2n+1) = \sum_{n=0}^{\mathrm{N}} 2n + \sum_{n=0}^{\mathrm{N}} 1 \tag{356}$$

$$= 2\frac{\mathrm{N}(\mathrm{N}+1)}{2} + \mathrm{N} + 1 = (\mathrm{N}+1)^2. \tag{357}$$

Efficient polynomial computation of $P_n^m(\mu)$. Note that the associated Legendre-functions are polynomials multiplied by $\sqrt{1-\mu^2}$ for odd m. Consequently, the polynomial part is conveniently described by its coefficients. In practical implementations, it is most efficient to build a tree of polynomial coefficients for all n, m required and store the coefficients for later use. We use the following notion to compute the number of coefficients: Given that the polynomials $P_n^m(\mu)$ are of

the order $n - mod(|m|, 2)$, see Fig. 62, we write

$$\begin{aligned}
\sum_{n=0}^{\mathrm{N}} \sum_{m=-n}^{n} n + 1 - mod(|m|, 2) &= \sum_{n=0}^{\mathrm{N}} \left[(2n+1)(n+1) - 2 \sum_{m'=0}^{n} mod(m', 2) \right] \\
&= \sum_{n=0}^{\mathrm{N}} \left[2n^2 + 3n + 1 - n - mod(n, 2) \right] \\
&= \sum_{n=0}^{\mathrm{N}} \left(2n^2 + 2n + 1 \right) - \sum_{n=0}^{\mathrm{N}} mod(n, 2) \\
&= \frac{2n^3 + 3n^2 + n}{3} + 2\frac{n(n+1)}{2} + n + 1 - div(n+1, 2) \\
&= \frac{2n^3 + 3n^2 + n + 3n^2 + 3n + 3n + 3}{3} - div(n+1, 2) \\
&= \frac{2n^3 + 6n^2 + 7n + 3}{3} - div(n+1, 2) \qquad (358)
\end{aligned}$$

(For further reference on arithmetic series see Bronstein *et al* [BSMM01]).

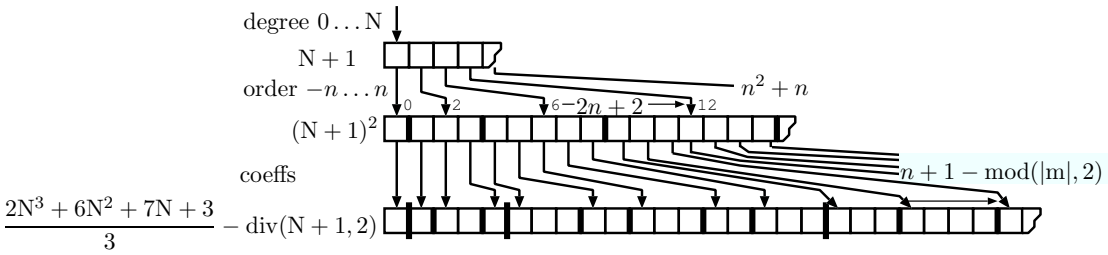

Figure 62: Data structure applicable for Legendre-polynomial coefficients and with smaller depth for normalization constants, and spherical harmonics coefficients.

The associated Legendre functions for negative indices can be determined by a linear scale factor:

$$P_n^{-m}(\mu) = g_n^m \, P_n^m(\mu), \text{ for } n > 0 \text{ and } 0 < m \leq n \qquad (359)$$

$$g_n^0 = 1, \text{ for } n \geq 0 \qquad (360)$$

$$g_n^m = -\frac{g_n^{m-1}}{(n+m)(n-m+1)}, \text{ for } n \geq 0, \text{ and } 0 < m \leq n \qquad (361)$$

Appendix C

UNSTABLE SPHERICAL BESSEL RECURRENCE

Note that the derivatives of $\sin(kr)/(kr)$ become numerically unstable for small values of kr, see Fig. 63. Therefore the recurrence scheme is not exact for small kr. We propose to make use of its power series expansion (Wolfram [Wei08]):

$$j_n(kr) = \frac{(kr)^n}{(2n+1)!!}\left[1 - \frac{\frac{1}{2}(kr)^2}{1!\,(2n+3)} + \frac{\left(\frac{1}{2}(kr)^2\right)^2}{2!\,(2n+3)\,(2n+5)} + \dots\right]. \qquad (362)$$

The expression $(2n+1)!! = 1\ 3\ 5\ \dots\ (2n+1)$ is the double factorial. Already the first term in the power series approximation will help to get around the numerical errors, whenever kr lies in the ranges $kr < 0.25\sqrt{(2n+3)}$ or $kr < \sqrt[n]{1.8e-8\,(2n+1)!!}$. These ranges were empirically found when using double precision (64 bit) floating point numbers. In that range we use the recurrence:

$$\tilde{j}_0(kr) = 1 \qquad (363)$$

$$\tilde{j}_n(kr) = \frac{kr}{(2n+1)}\,\tilde{j}_{n-1}(kr). \qquad (364)$$

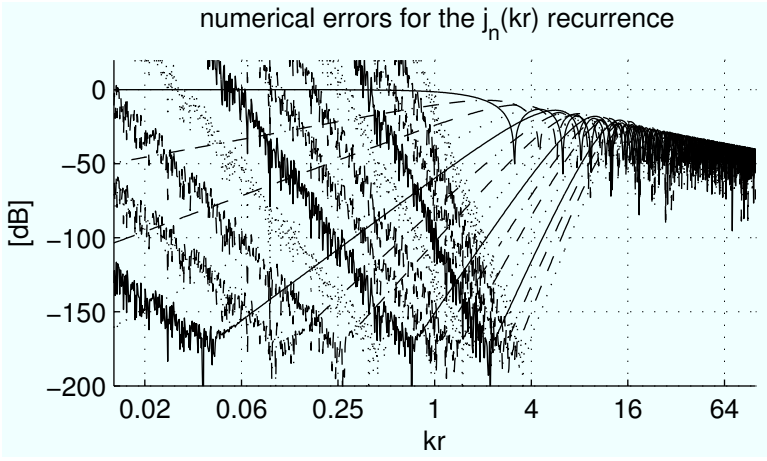

Figure 63: Numerical errors appear in the recurrence for the spherical Bessel functions evaluating small numbers.

REFERENCES

[ADJV02] J.-P. Antoine, L. Demanet, L. Jacques, and P. Vandergheynst, "Wavelets on the sphere: implementation and approximations," *Applied and Computational Harmonic Analysis*, pp. 177–200, 2002.

[AFKW06] R. Avizienis, A. Freed, P. Kassakian, and D. Wessel, "A compact 120 independent element spherical loudspeaker array with programmable radiation patterns," in *Papers of the 120th AES Convention*, Paris, 2006. [Online]. Available: http://cnmat.berkeley.edu/publications/compact_120_independent_element_spherical_loudspeaker_array_programmable_radiation_patterns

[AP85] J. M. Augenbaum and C. S. Peskin, "On the construction of the voronoi mesh on a sphere," *Journal of Computational Physics*, vol. 59, pp. 177–192, 1985.

[ASS99] A. Albertella, F. Sansò, and N. Sneeuw, "Band-limited functions on a bounded spherical domain: the Slepian problem on the sphere," *Journal of Geodesy*, vol. 74, pp. 1432–1394, 1999.

[AV99] J.-P. Antoine and P. Vandergheynst, "Wavelets on the 2-sphere: A group-theoretical approach," *Applied and Computational Harmonic Analysis*, pp. 262–291, 1999.

[AW04] G. B. Arfken and H. J. Weber, *Mathematical Methods for Physicists*. Boston: Academic Press, 2004.

[Bau00] R. Bauer, "Distribution of points on a sphere with application to star catalogs," *Journal of Guidance, Control, and Dynamics*, vol. 23, no. 1, 2000.

[Bau01] ——, "Uniform sampling of SO3," in *Flight Mechanics Symposium, Maryland*, 2001.

[BDP+07] S. Bertet, J. Daniel, E. Parizet, L. Gros, and O. Warusfel, "Investigation of the perceived spatial resolution of higher order ambisonics sound fields: A subjective evaluation involving virtual and real 3d microphones," in *Proceedings of the AES 30th International Conference*, Saariselkä, 15th March 2007.

[Beh00] G. Behler, "Technique for the derivative of wide band room impulse response," in *Proceedings of Tecni Acustica*, Madrid, 2000.

[Beh06a] ——, "How to compare concert halls by listening to music," in *Proceedings of the 4th ASA/ASJ Joint Meeting*, Honolulu, Hawaii, Dec 2006. [Online]. Available: http://www.acoustics.org/press/152nd/behler.html

[Beh06b] ——, "Sound source with adjustable directivity," in *Proceedings of the 19th International Congress on Acoustics*, Honolulu, Hawaii, 2006. [Online]. Available: http://www.akustik.rwth-aachen.de/Veroeff/gkb-asa2006

[Beh07a] ——, "Dodekaeder-Lautsprecher mit variabler Richtcharakteristik," in *Fortschritte der Akustik, 33. DAGA*, Stuttgart, 19th March 2007. [Online]. Available: http://www.akustik.rwth-aachen.de/Veroeff/gkb-daga07-1

[Beh07b] ——, "Sound source for the measurement of room impulse responses for auralisation," in *Proceedings of the 19th International Congress on Acoustics*, Madrid, 2nd Sep 2007.

[BHS08] J. S. Brauchart, D. P. Hardin, and E. B. Saff, "The riesz energy of the N-th roots of unity," 2008.

[BMM+01] J. Baird, J. Meyer, P. Meyer, P. Kassakian, and D. Wessel, "Controlling loudspeaker array radiation in three dimensions," in *Papers of the 111th AES Convention*. New York: Audio Engineering Society, 2001. [Online]. Available: http://cnmat.berkeley.edu/publications/controlling_loudspeaker_array_radiation_three_dimensions

[Boy00] J. P. Boyd, *Chebyshev and Fourier Spectral Methods*. DOVER Publications, 2000.

[BPP04] G. P. Beretta, G. Pedersini, and E. Piana, "Study, construction and analysis of a variable directivity omnidirectional sound source," Outline Professional Audioa, Brescia, Tech. Rep., 2004.

[BR04] I. Balmages and B. Rafaely, "Room acoustics measurements by microphone arrays," in *Proceedings of the Convention of the Electrical and Electronics Engineers in Israel*, 2004.

[BR07] ——, "Open-sphere designs for spherical microphone arrays," *IEEE Transactions on Audio, Speech, and Language Processing*, vol. 15, no. 2, 2007.

[BS06] O. Baur and N. Sneeuw, "The Slepian approach revisited," in *Proceedings of the 3rd GOCE user workshop*, 2006.

[BSMM01] I. Bronstein, K. Semendjajew, G. Musiol, and H. Mühlig, *Taschenbuch der Mathematik*, 5th ed. Thun und Frankfurt am Main: Verlag Harri Deutsch, 2001.

[Bur06] J. Burkardt, "SCVT: Spherical centroidal voronoi tesselation, fortran90 code," 2006. [Online]. Available: http://people.scs.fsu.edu/~burkardt/f_src/scvt/scvt.html

[CBW92] R. Caussé, J. Bresciani, and O. Warusfel, "Radiation of musical instruments and control of reproduction with loudspeakers," in *Proceedings of the International Symposium on Musical Acoustics, ISMA*, Tokyo, 1992. [Online]. Available: http://mediatheque.ircam.fr/articles/textes/Causse92a/

[CETT98] P. Cook, G. Essl, G. Tzanetakis, and D. Trueman, "N>>2: Multi-speaker display systems for virtual reality and spatial audio projection," in *Proceedings of the International Conference on Auditory Display, ICAD*, Glasgow, 1998.

[Che92] W. C. Chew, "Recurrence relations for three-dimensional scalar addition theorem," *Journal of Electromagnetic Waves and Applications*, vol. 6, no. 2, 1992.

[CS99] J. Conway and N. Sloane, *Sphere Packings, Lattices and Groups*, 3rd ed., ser. Sphere Packings, Lattices and Groups. Springer, 1999.

[CT98a] P. Cook and D. Trueman, "A database of measured musical instrument body radiation impulse responses, and computer applications for exploring and utilizing the measured filter functions," in *Proceedings of the International Symposium on Musical Acoustics, ISMA*, Leavenworth, 1998.

[CT98b] R. G. Crittenden and N. G. Turok, "Exactly azimuthal pixelizations of the sky," *The Astrophysical Journal*, 1998.

[CT99] P. Cook and D. Trueman, "Spherical radiation from stringed instruments: Measured, modeled, and reproduced," *Journal of the Catgut Acoustical Society*, 1999.

[Cur00] J. Curtin, "The violin finally speaks / weinreich and directional tone colour," Apr 2000. [Online]. Available: http://www.josephcurtinstudios.com/news/strad/apr00/Gabi_strad.htm

[Dan01] J. Daniel, "Représentation de champs acoustiques, application à la transmission et à la reproduction de scénes sonores complexes dans un contexte multimédia," PhD Thesis, Université Paris 6, 2001.

[Dan03] ——, "Spatial sound encoding including near field effect: Introducing distance coding filters and a viable, new ambisonic format," in *Proceedings of the AES 23rd International Conference*, Copenhagen, 23rd May 2003.

[Dan07] ——, "Spherical arrays for capturing 3d sound fields: Prototype measurements versus analytical models," in *Proceedings of the 19th International Congress on Acoustics*, Madrid, Sept 2007.

[Del96] B. Delley, "High order integration schemes on the unit sphere," *Journal of Computational Chemistry*, vol. 17, no. 9, 1996.

[DFG99] Q. Du, V. Faber, and M. Gunzburger, "Central voronoi tesselations: Applications and algorithms," *SIAM Review*, no. 4, 1999.

[DGJ03] Q. Du, M. D. Gunzburger, and L. Ju, "Constrained central voronoi tesselations for surfaces," *SIAM Journal of Scientific Computation*, vol. 24, no. 5, 2003.

[DH94] J. R. Driscoll and D. M. J. Healy, "Computing fourier transforms and convolutions on the 2-sphere," *Advances in Applied Mathematics*, vol. 15, 1994.

[Dic01] V. Dickason, *Lautsprecherbau*. Elektor Verlag, 2001.

[DLZ+05] R. Duraiswami, Z. Li, D. N. Zotkin, E. Grassi, and N. A. Gumerov, "Plane-wave decomposition analysis for spherical microphone arrays," in *Proceedings of the IEEE Workshop on Applications of Signal Processing to Audio and Acoustics, WASPAA*, 2005.

[DNM03] J. Daniel, R. Nicol, and S. Moreau, "Further investigations of high order ambisonics and wavefield synthesis for holophonic sound imaging," in *Papers of the 114th AES Convention*, Amsterdam, 22nd March 2003.

[DS07] F. A. Dahlen and F. Simons, "Spectral estimation on a sphere in geophysics and cosmology," *arXiv preprint: 0705.308v1*, 2007.

[Fit02] R. Fitzpatrick, *Web site: Advanced Classical Electromagnetism*, Fall 1996/2002. [Online]. Available: http://farside.ph.utexas.edu/teaching/jk1/lectures/lectures.html

[Fle01] H. Fleischer, *Schwingungsuntersuchung an Gongs*. Helmut Fleischer and Hugo Fastl, 2001, no. 1/01, Beiträge zur Vibro- und Psychoakustik.

[Fle02a] ——, *Gehörbezogene Analyse von Gongklängen*. Helmut Fleischer and Hugo Fastl, 2002, no. 2/02, Beiträge zur Vibro- und Psychoakustik.

[Fle02b] ——, *Nichtlinearität bei Gongs: Analyse des Schallsignals*. Helmut Fleischer and Hugo Fastl, 2002, no. 1/02, Beiträge zur Vibro- und Psychoakustik.

[Fle03] ——, "Verzerrungsprodukte in Gongklängen," in *Fortschritte der Akustik, 29. DAGA*, Aachen, 18th March 2003.

[FM96] J. Fliege and U. Maier, "A two-stage approach for computing cubature formulae for the sphere," Dortmund, Tech. Rep., 1996.

[FR91] N. H. Fletcher and T. D. Rossing, *The Physics of Musical Instruments*. Springer, 1991.

[FSZ08] A. Freed, A. Schmeder, and F. Zotter, "Applications of environmental sensing for spherical loudspeaker arrays," in *Proceedings of the IASTED Signal and Image Processing*, Hawaii, 2008.

[FW97] W. Freeden and U. Windheuser, "Combined spherical harmonics and wavelet expansion – a future concept in earth's gravitational determination," *Applied and Computational Harmonic Analysis*, pp. 1–37, 1997.

[GD01] N. A. Gumerov and R. Duraiswami, "Fast, exact, and stable computation of multipole translation and rotation coefficients for the 3-d helmholtz equation," College Park, Tech. Rep., 2001.

[GD03] ——, "Recursions for the computation of multipole translation and rotation coefficients for the 3-d helmholtz equation," *SIAM*, vol. 25, pp. 1344–1381, 2003.

[GD04] ——, *Fast Multipole Methods for the Helmholtz Equation in Three Dimensions*, 1st ed. Elsevier, 2004.

[GHB+05] K. M. Górski, E. Hivon, A. J. Banday, B. D. Wandelt, F. K. Hansen, M. Reinecke, and M. Bartelmann, "Healpix: A framework for high-resolution discretization and fast analysis of data distributed on the sphere," *The Astrophysical Journal*, vol. 622, pp. 759–771, 2005. [Online]. Available: http://healpix.jpl.nasa.gov

[Gir96] F. Giron, "Investigations about the directivity of sound sources," PhD Thesis, Ruhr-Universität Bochum, 1996.

[Gov04] *Directional measurement of airborne sound transmission paths using a spherical microphone array*, San Francisco, 28th Nov 2004.

[Gov06] B. N. Gover, "Spherical microphone arrays for analysis of sound fields in buildings," in *Proceedings of the Canadian Acoustical Association Annual Conference*, 2006.

[Hay02] S. Haykin, *Adaptive Filter Theory*, 4th ed. Prentice Hall, Upper Saddle River, New York, 2002.

[HBC05] Y. A. Huang, J. Benesty, and J. Chen, "Adaptive blind SIMO identication: Derivations of an optimal step size for the unconstrained multichannel lms algorithm," in *IEEE International Conference on Acoustics, Speech, and Signal Processing, ICASSP*, Philadelphia, March 2005.

[HCB06] Y. Huang, J. Chen, and J. Benesty, *Acoustic MIMO Signal Processing*. Springer Berlin Heidelberg New York, 2006.

[HD08] J. Hannemann and K. D. Donohue, "Virtual sound source rendering using a multipole-expansion and method-of-moments approach," *AES Journal*, vol. 56, no. 6, 2008.

[HG06] A. Hjørunges and D. Gesbert, "Complex-valued matrix differentiation: Techniques and key results," *IEEE Transaction on Signal Processing*, 2006.

[HKR04] J. D. M. Healy, P. J. Kostelec, and D. Rockmore, "Towards safe and effective high-order Legendre transforms with applications to FFTs for the 2-sphere," *Advances in Computational Mathematics*, vol. 21, pp. 59–105, 2004.

[HLDS07] J. Hannemann, C. Leedy, K. D. Donohue, and S. Spors, "A comparative study of the perceptual quality of wave field synthesis versus multipole-matching for audio rendering," in *IEEE International Conference on Acoustics, Speech, and Signal Processing, ICASSP*, Honolulu, 2007.

[HNT07] Y. Hayakawa, T. Nishino, and K. Takeda, "Development of small sound equipment with micro-dynamic-type loudspeakers for hrtf measuerment," in *Proceedings of the 19th International Congress on Acoustics, ICA*, Madrid, 2nd Sep 2007.

[Hoh09] F. Hohl, "Aufbau eines 64-kanaligen Kugelmikrofonarrays zur Abstrahlungsanalyse," Master's Thesis, Institut für Elektronische Musik und Akustik, Kunstuni Graz, Technical University Graz, Graz, A, 2009.

[HRKM98] J. D. M. Healy, D. Rockmore, P. J. Kostelec, and S. S. B. Moore, "FFTs for the 2-sphere - improvements and variations," Hanover, NH, Tech. Rep., Jun 1998.

[HS96] R. H. Hardin and N. J. A. Sloane, "Mclaren's improved snub cube and other new spherical designs in three dimensions," *Discrete Computational Geometry*, vol. 15, pp. 429–441, 1996.

[HS04] D. P. Hardin and E. B. Saff, "Discretizing manifolds via minimum energy points," *Notices of the Americal Mathematical Society*, vol. 51, no. 1, 2004.

[HS09] E. Hellerud and U. P. Svensson, "Lossless compression of spherical microphone array recordings," in *Papers of the 126th AES Convention*, Munich, 2009.

[HSS09] E. Hellerud, A. Solvang, and U. P. Svensson, "Spatial redundancy in higher order ambisonics and its use for low delay lossless compression," in *Proceedings of the IEEE International Conference on Acoustics, Speech, and Signal Processing, ICASSP*, 2009.

[Hul08] P. L. Hulen, "A low-cost spherical loudspeaker array for electroacoustic music," in *Proceedings of the International Computer Music Conference, ICMC*, 2008.

[HX01] S. Heo and Y. Xu, "Constructing fully symmetric cubature formulae for the sphere," *Mathematics of Computation*, vol. 70, no. 233, 2001.

[IBM01] M. A. Inda, R. H. Bisseling, and D. K. Maslen, "On the efficient parallel computation of Legendre transforms," *SIAM Journal of Scientific Computation*, vol. 23, no. 1, 2001.

[JR07] C. Jochum and P. Reiner, "Driving filters for the icosahedral louspeaker array / Ansteuerungsfilter für den Ikosaederlautsprecher," Institut für Elektronische Musik und Akustik, Graz, Tech. Rep., May 2007. [Online]. Available: http://iem.at/projekte/dsp/ansteuerung/index_html_en/view

[Kei07] J. Keiner, *CSTRIPACK, URL*, 2007. [Online]. Available: http://www.math.uni-luebeck.de/keiner/sonstiges.shtml

[KKP07] J. Keiner, S. Kunis, and D. Potts, "Efficient reconstruction of functions on the sphere from scattered data," *Journal of Fourier Analysis and Applications*, vol. 13, 2007.

[KP03] S. Kunis and D. Potts, "Fast spherical fourier algorithms," *Journal of Computational and Applied Mathematics*, vol. 161, pp. 75–78, 2003.

[KR03] P. J. Kostelec and D. N. Rockmore, "FFTs on the rotation group," Darthmouth College, Hanover, NH, Tech. Rep., Dec 2003.

[KR08] ——, "FFTs on the rotation group," *Applied Fourier Analysis*, no. 14, 2008.

[Kre99] E. Kreyszig, *Advanced Engineering Mathematics*, 8th ed., 1999.

[Kup06] G. Kuperberg, "Numerical cubature from archimedes' hat-box theorem," *Journal on Numerical Analysis*, vol. 44, pp. 908–935, 2006.

[KW03] P. Kassakian and D. Wessel, "Design of low-order filters for radiation synthesis," in *Papers of the 115th AES Convention*, New York, Oct 2003. [Online]. Available: http://cnmat.berkeley.edu/publications/design_low_order_filters_radiation_synthesis

[KW04] ——, "Characterization of spherical loudspeaker arrays," in *Papers of the 117th AES Convention*, San Francisco, Oct 2004. [Online]. Available: http://cnmat.berkeley.edu/publications/characterization_spherical_loudspeaker_arrays

[LD06] Z. Li and R. Duraiswami, "Flexible and optimal design of spherical microphone arrays for beamforming," in *Proceedings of the IEEE Conference on Speech and Audio Processing*, 2006.

[LDG04] Z. Li, R. Duraiswami, and N. A. Gumerov, "Capture and recreation of higher order 3d sound fields via reciprocity," in *Proceedings of the International Conference on Auditory Display, ICAD*, Sydney, 2004.

[Leb77] V. I. Lebedev, "Spherical quadrature formulas exact to orders 25-29," *Translation from Sibirskii Mathematicheskii Zhurnal*, vol. 18, no. 1, 1977.

[Leo06a] P. Leopardi, "Distributing points on the sphere," PhD Thesis, University of New South Wales, Sydney, 2006.

[Leo06b] ——, "A partition of the unit sphere into regions of equal area and small diameter," *Electronic Transactions on Numerical Analysis*, vol. 25, 2006.

[Leo07] ——, *Web site: Recursive Zonal Equal Area Sphere Partitioning Toolbox*, 2007. [Online]. Available: http://eqsp.sourceforge.net/

[Les07] C. Lessig, "Orthogonal and symmetric haar wavelets on the sphere," Master's Thesis, University of Toronto, Grad. Dep. Comp. Sc., 2007.

[Li05] Z. Li, "The capture and recreation of 3d auditory scenes," PhD Thesis, University of Maryland, College Park, 2005.

[LPP08] T. Lokki, J. Pätynen, and V. Pulkki, "Recording of anechoic symphony music," in *Proceedings of the 2nd ASA-EAA joint conference, ACOUSTICS08*, Paris, Jul 2008.

[LRS06] T. W. Leishman, S. Rollins, , and H. M. Smith, "An experimental evaluation of regular polyhedron loudspeakers as omnidirectional sources of sound," *Journal of the Acoustical Society of America*, vol. 120, pp. 1411–1422, Sept 2006.

[LS06] D. Lock and G. Schiemer, "Orbophone: a new interface for radiating sound and image," in *Proceedings of the International Conference on New Interfaces for Musical Expression, NIME*, Paris, 2006.

[LSO06] D. Lock, G. Schiemer, and L. Ong, "Orbophone: A new interface for radiating sound and image," in *Proceedings of the 12th International Conference on Auditory Display, ICAD*, London, 20th June 2006.

[Mar03] J. Martinet, *Perfect Lattices in Euclidean Spaces*. Springer, 2003.

[MCAG06a] M. Mousa, R. Chaine, S. Akkouche, and E. Galin, "Direct spherical harmonics transform of a triangulated mesh," *Journal of Graphics Tools*, vol. 11, no. 2, 2006.

[MCAG06b] ——, "Frequency-based representation of 3D point-based surfaces using the spherical harmonics," in *Proceedings of the International Conference on Computer Vision and Graphics, ICCVG'06*, 2006.

[MCAG07] ——, "Efficient spherical harmonics represenation of 3D objects," in *Proceedings of the Pacific Graphics conference, PG'07*, Maui, 2007.

[MDB06] S. Moreau, J. Daniel, and S. Bertet, "3d sound field recording with higher order Ambisonics - objective measurements and validation of a 4th order spherical microphone," in *Papers of the 120th AES Convention*, Paris, 2006.

[ME02] J. Meyer and G. Elko, "A highly scalable spherical microphone array based on an orthonormal decomposition of the soundfield," in *Proceedings of the IEEE International Conference on Acoustics, Speech, and Signal Processing, ICASSP*, vol. 2, Orlando, 13th May 2002, pp. 1781–1784. [Online]. Available: http://ieeexplore.ieee.org/xpl/freeabs_all.jsp?arnumber=1006109

[ME07] ——, "Realization of a spherical microphone array," in *Proceedings of the 19th International Congress on Acoustics, ICA*, Sept 2007.

[Mey66] J. Meyer, *Akustik der Holzblasinstrumente in Einzeldarstellungen*, 1st ed. Verlag Das Musikinstrument, Frankfurt/Main, 1966.

[Mey72] ——, *Akustik und musikalische Aufführungspraxis*, 1st ed. Verlag Das Musikinstrument, Frankfurt/Main, 1972.

[Mey08] ——, "Die Schallabstrahlung der Streichergruppen im Orchester / The Sound Radiation of the String Sections in Orchestras," in *25. Tonmeistertagung, Leipzig*, 2008.

[Mey09] ——, *Acoustics and the Performance of Music*, 5th ed. Springer, New York, 2009.

[MF53] P. M. Morse and H. Feshbach, *Methods of Theoretical Physics, Part I.* McGraw-Hill, 1953.

[MM00] P. S. Meyer and J. D. Meyer, "Multi acoustic prediction program (MAPP): Recent results. presented at the institute of acoustics (UK)," Tech. Rep., 2000.

[MNV97] P. F. Muciaccia, P. Natoli, and N. Vittorio, "Fast spherical harmonic analysis: a quick algorithm for generating and/or inverting full sky, high resolution cmb anisotropy maps," *The Astrophysical Journal*, 1997.

[MNW00] H. N. Mhaskar, F. J. Narcowich, and J. D. Ward, "Spherical marcinkiewicz-zygmund inequalities and positive quadrature," *Math. Comp*, vol. 70, pp. 1113–1130, 2000.

[MNWC01] N. Misdariis, F. Nicolas, O. Warusfel, and R. Caussé, "Radiation control on multi-loudspeaker device : La timée," in *Proceedings of the International Conference on Computer Music, ICMC*, La Havana, 21th Sept 2001.

[Moh99] M. J. Mohlenkamp, "A fast transform for spherical harmonics," *Journal of Fourier Analysis and Applications*, vol. 5, 1999.

[Mor06] S. Moreau, "Étude et réalisation d'outils avancés d'encodage spatial pour la technique de spatialisation sonore Higher Order Ambisonics: microphone 3d et contrôle de distance," PhD Thesis, Université du Maine, 2006.

[MOWN02] N. Misdariis, R. C. O. Warusfel, and F. Nicolas, "Le contrôle de la directivité par un système multi haut-parleurs," in *Journ ées d'Informatique Musicale*, 29th Apr 2002.

[MP05] H. N. Mhaskar and J. Prestin, "Polynomial frames: A fast tour," in *Approximation Theory XI: Gatlinburg 2004, Mod. Methods Math*, 2005.

[MQ86] R. J. McAulay and T. F. Quatieri, "Speech analysis/synthesis based on a sinusoidal representation," *IEEE Transactions on Acoustics, Speech, and Signal Processing*, vol. 34, no. 4, pp. 744–754, 1986.

[MWC01] N. Misdariis, O. Warusfel, and R. Caussé, "Radiation control on a multi-loudspeaker device," in *Proceedings of the International Symposium on Musical Acoustics, ISMA*, Perugia, 2001.

[OK03] F. Otondo and B. Kirkwood, "Perceived changes in the musical instrument directivity representation," in *Proceedings of the Stockholm Music Acoustics Conference, SMAC*, Stockholm, 6th Aug 2003.

[OR02] F. Otondo and J. H. Rindel, "New method for the directional representation of musical instruments in auralizations," in *Proceedings of the International Computer Music Conference, ICMC*, 2002.

[OR03] ——, "Directional representation of a clarinet in a room," *ULTRA-GARSAS*, vol. 48, 2003.

[OR04] ——, "The influence of the directivity of musical instruments in a room," *Acta Acustica*, vol. 90, 2004.

[OR05] F. Otondo and J. Rindel, "A new method for the radiation representation of musical instruments in auralizations," *Acta Acustica*, vol. 91, 2005.

[ORC+02] F. Otondo, J. H. Rindel, R. Caussé, N. Misdariis, and P. de la Cuadra, "Directivity of musical instruments in a real performannce situation," in *Proceedings of the International Symposium on Musical Acoustics, ISMA*, Mexico, 2002.

[Orl05] L. Orluc, "Pointilisme, les mathématiques sont enfin au point," *Science & Vie*, 2005.

[OSB99] A. V. Oppenheim, R. W. Schafer, and J. R. Buck, *Discrete-Time Signal Processing.* Prentice Hall, 1999.

[PAH08a] A. M. Pasqual, J. R. Arruda, and P. Herzog, "Effects of enclosure design on the directivity synthesis by spherical loudspeaker arrays." in *Proceedings of the 2nd ASA-EAA joint conference, ACOUSTICS08*, Paris, Jul 2008.

[PAH08b] ——, "Optimal array pattern synthesis with desired magnitude response." in *Proceedings of the 2nd ASA-EAA joint conference, ACOUSTICS08*, Paris, Jul 2008.

[PAH09] ——, "Digital equalization filters for a spherical loudspeaker array," in *Proceedings of the 1st Ambisonics Symposium Graz*, 2009.

[PBM09] M. Pollow, G. Behler, and B. Masiero, "Measuring directivities of natural sound sources with a spherical microphone array," in *Proceedings of the 1st Ambisonics Symposium Graz*, 2009.

[PC97] J. W. Panzer and R. H. Campbell, "Multiple driver modeling with a modern lumped element simulation program," in *Papers of the 102nd AES Convention*, Munich, March 1997.

[Pet04] S.-O. Petersen, "Localization of sound sources using 3d microphone array," Master's Thesis, University of South Denmark, Odense, Sept 2004. [Online]. Available: oscarpetersen.dk

[Pfl97] M. Pflüger, "Modelle des pheriphären Gehörs am Beispiel der menschlichen Lautheitsempfindung," PhD Thesis, Institut für Elektronische Musik und Akustik, Kunstuniversität Graz, Technische Universität Graz, 1997.

[Pfö06] H. Pförtner, *Web site: Optimal illumination of a sphere*, 2006. [Online]. Available: http://www.enginemonitoring.org/illum/illum.html

[PH07a] D. Pinchon and P. E. Hoggan, "New index functions for storing gaunt coefficients," *International Journal of Quantum Chemistry*, vol. 107, 2007.

[PH07b] ——, "Rotation matrices for real spherical harmonics: general rotations of atomic orbitals in space-fixed axes," *Journal of Physics, A*, vol. 40, pp. 1751–8113, 2007.

[PJvS06] A. Parthy, C. Jin, and A. van Schaik, "Optimisation of co-centred rigid and open spherical microphone arrays," in *Papers of the 120th AES Convention*, Paris, 2006.

[PLar] J. Pätynen and T. Lokki, "Directivities of symphony orchester instruments," to appear.

[PO03] L. Parati and F. Otondo, "Comparison of directional sources in simulating a soprano voice," in *Proceedings of the Stockholm Music Acoustics Conference, SMAC*, Stockholm, 6th Aug 2003.

[Pol05] M. A. Poletti, "Three-dimensional surround sound systems based on spherical harmonics," *AES Journal*, vol. 53, no. 11, 2005.

[Pol07] M. Pollow, "Variable directivity of dodecahedron louspeakers," Master's Thesis, Institut für Technische Akustik, RWTH-Aachen, Aachen, D, 2007.

[Pom08] H. Pomberger, "Angular and radial directivity control for spherical loudspeaker arrays," Master's Thesis, Institut für Elektronische Musik und Akustik, Kunstuni Graz, Technical University Graz, Graz, A, 2008.

[PPL08] J. Pätynen, V. Pulkki, and T. Lokki, "Anechoic recording system for symphony orchestra," *Acta Acustica united with Acustica*, vol. 94, no. 6, 2008.

[PPS01] R. Pail, G. Plank, and W.-D. Schuh, "Spatially restricted data distributions on the sphere: the method of ortnonormalized functions and applications," *Journal of Geodesy*, vol. 75, pp. 44–56, 2001.

[PR05] M. Park and B. Rafaely, "Sound-field analysis by plane-wave decomposition using spherical microphone array," *Journal of the Acoustical Society of America*, vol. 118, pp. 3094–3103, Aug 2005.

[PST98] D. Potts, G. Steidl, and M. Tasche, "Fast algorithms for discrete polynomial transforms," *Mathematics of Computation*, vol. 67, pp. 1577–1590, 1998.

[PZ09] H. Pomberger and F. Zotter, "An ambisonics format for flexible layouts," in *Proceedings of the 1st Ambisonics Symposium Graz*, 2009.

[Raf04] B. Rafaely, "Plane-wave decomposition of the sound field on a sphere by spherical convolution," *Journal of the Acoustical Society of America*, vol. 116, pp. 2149–2157, Jul 2004.

[Raf05] ——, "Analysis and design of spherical microphone arrays," *IEEE Transactions on Speech and Audio Processing*, 2005.

[Raf08] ——, "The spherical-shell microphone array," *IEEE Transactions on Audio, Speech, and Language Processing*, vol. 16, no. 4, May 2008.

[RE08] M. Raspaud and G. Evangelista, "Binaural partial tracking," in *Proceedings of the DAFX08*, Espoo, Finland, 2008.

[Reu08] S. Reuter, "Simulation of natural sound sources in immersive virtual environments," Master's Thesis, Institute of Technical Acoustics, RTWH-Aachen, 2008.

[RJ07] P. Reiner and C. Jochum, "Measurement and evaluation of crosstalk within an icosehedral loudspeaker array / Erfassung und Evaluierung der Übersprecheigenschaften des Ikosaederlautsprechers," Graz, Tech. Rep., Feb 2007. [Online]. Available: http://iem.at/projekte/acoustics/awt/erfassung/index_html_en

[RO05] J. H. Rindel and F. Otondo, "The interaction between room and musical instruments studied by multi-channel auralization," *Forum Acusticum*, 2005.

[RP04] B. Rafaely and M. Park, "Super-resolution spherical microphone arrays," in *Convention of the Electrical and Electronics Engineers in Israel*, 2004.

[RSZ94] E. A. Rakhmanov, E. B. Saff, and Y. M. Zhou, "Minimal discrete energy on the sphere," *Mathematical Research Letters*, 1994.

[RSZ95] ——, "Electrons on the sphere," *Computational Methods and Function Theory*, 1995.

[RWB07] B. Rafaely, B. Weiss, and E. Bachmat, "Spatial aliasing in spherical microphone arrays," *IEEE Transactions on Signal Processing*, vol. 55, March 2007.

[SA99] J. O. Smith and J. S. Abel, "Bark and erb bilinear transforms," *IEEE Transactions on Speech and Audio Processing*, 1999.

[SB96] N. Sneeuw and R. Bun, "Global spherical harmonic computation by two-dimensional fourier methods," *Journal of Geodesy*, vol. 70, pp. 224–232, 1996.

[Sch09] A. Schmeder, "An exploration of design parameters for human-interactive systems with compact spherical loudspeaker arrays," in *Proceedings of the 1st Ambisonics Symposium Graz*, 2009.

[SD06] F. J. Simons and F. A. Dahlen, "Spherical Slepian functions and the polar gap in geodesy," *Geophysical Journal International*, vol. 166, pp. 1039–1061, 2006.

[SDW06] F. J. Simons, F. A. Dahlen, and M. A. Wieczorek, "Spatiospectral concentration on a sphere," *SIAM Review*, vol. 48, pp. 504–536, 2006.

[Séb98] D. Sébilleau, "On the computation of the integrated products of three spherical harmonics," *Journal of Physics A*, vol. 31, 1998.

[SEH08] W. Song, W. Ellermeier, and J. Hald, "Using beamforming and binaural synthesis for the psychoacoustical evaluation of target sources in noise," *Journal of Acoustical Society of America*, vol. 123, pp. 910–924, 2008.

[SGL+07] A. Schlesinger, G. D. Galdo, J. Lotze, S. Husung, and B. Albrecht, "Holographic sound field analysis with a scalable spherical microphone array," in *Papers of the 122nd AES Convention*, Vienna, 2007.

[Sha06] E. A. Shamsiev, "On calculation of integrals over spherical domains," *Ukrainian Mathematical Journal*, vol. 58, no. 6, 2006.

[She07] A. Sherwood, "Web site: How can i arrange n points evenly on a sphere?" 2007. [Online]. Available: http://www.ogre.nu/sphere.htm

[SHS00] N. J. A. Sloane, R. H. Hardin, and W. D. Smith, *Web site: Tables of Spherical Codes with Icosahedral Symmetry*, 2000. [Online]. Available: http://www.research.att.com/~njas/icosahedral.codes/index.html

[SJ96] N. Shalaby and S. L. Johnson, "Hierarchical load balancing for fast Legendre transforms," Cambridge, Massachusetts, Tech. Rep., 1996.

[SK97] E. Saff and A. B. J. Kuijlaars, "Distributing many points on a sphere," *The Mathematical Intelligencer*, vol. 19, pp. 523–538, 1997.

[Smi06] J. O. Smith, *Physical audio signal processing for virtual musical instruments and audio effects*. Stanford, CCRMA, 2006.

[Sne94] N. Sneeuw, "Global spherical harmonic analysis by least-squares and numerical quadrature methods in historical perspective," *Geophysical Journal International*, vol. 118, pp. 707–716, 1994.

[SRBA08] D. Schröder, S. Reuter, G. K. Behler, and I. Assenmacher, "Multimodale Darstellung natürlicher Schallquellen in virtuellen Umgebungen," in *Fortschritte der Akustik, 34. DAGA*, Dresden, 10th March 2008.

[SS92] J. O. Smith and X. Serra, "Parshl: An analysis/synthesis program for non-harmonic sounds based on a sinusoidal representation," in *Proceedings of the International Computer Music Conference, ICMC*, 1992.

[SS95] P. Schröder and W. Sweldens, "Spherical wavelets: Efficiently representing functions on the sphere," *Computer Graphics Proceedings (SIGGRAPH 95)*, pp. 161–172, 1995.

[SS03] P. N. Schwartztrauber and W. F. Spotz, "Spherical harmonic projectors," *Mathematics of Computation*, 2003.

[SvG97] N. Sneeuw and M. van Gelderen, *The Polar Gap*. Springer, 1997.

[SW99] I. H. Sloan and R. S. Womersley, *The Uniform Error of Hyperinterpolation on the Sphere*. Wiley, 1999.

[SW04] ——, "Extremal systems of points and numerical integration on the sphere," *Advances in Computational Mathematics*, vol. 21, pp. 107–125, 2004.

[SWK03] K. Sahr, D. White, and A. J. Kimerling, "Geodesic discrete global grid systems," *Cartography and Geographic Information Science*, vol. 30, pp. 121–134, 2003. [Online]. Available: http://www.sou.edu/cs/sahr/dgg/

[SZEH07] A. Sontacchi, F. Zotter, G. Eckel, and R. Höldrich, "IEM Report 40/07: "Klangmodellierung - ein Beitrag zur musikalischen Akustik Endbericht VGG"," Graz, Tech. Rep., Dec 2007. [Online]. Available: http://iem.at/projekte/publications/iem_report/report42_07/index_html/view

[Tar74] V. Tarnow, "Sound radiation from loudspeaker systems with the symmetry of the Platonic solids," Bruel&Kjær, Tech. Rep., 1974.

[TBC00] D. Trueman, C. Bahn, and P. Cook, "Alternative voices for electronic sound," in *Proceedings of the International Computer Music Conference, ICMC*, 2000.

[TC99] D. Trueman and P. Cook, "BoSSA: The deconstructed violin reconstructed," in *Proceedings of the International Computer Music Conference, ICMC*, Beijing, 1999.

[TCSW06] D. Trueman, P. Cook, S. Smallwood, and G. Wang, "Plork: The princeton laptop orchestra, year 1," in *Proceedings of the International Computer Music Conference, ICMC*, New Orleans, 2006.

[Teg96] M. Tegmark, "An icosahedron-based method for pixelizing the celestial sphere," *The Astrophysical Journal*, vol. 470, pp. L81–L84, 1996.

[Ter98] E. Terhardt, *Akustische Kommunikation*. Springer, Berlin Heidelberg, 1998.

[Teu07] H. Teutsch, *Modal Array Signal Processing: Principles and Applications of Acoustic Wavefield Decomposition*, 1st ed., ser. Modal Array Signal Processing: Principles and Applications of Acoustic Wavefield Decomposition, M. Thoma and M. Morari, Eds. Berlin: Springer, 2007.

[Tho07] K. Thomsen, 2007, online posting. [Online]. Available: http://groups.google.com/group/sci.math/browse_thread/thread/327a68f46940226e

[TR03] L. Trautmann and R. Rabenstein, *Digital sound synthesis by physical modeling using the functional transformation method*. Kluwer Academic/Plenum Publishers, New York, 2003.

[Var00] A. Varsányi, *Zur Akustik des javanischen Gong Ageng*. Helmut Fleischer and Hugo Fastl, 2000, no. 2/00, Beiträge zur Vibro- und Psychoakustik.

[VW04] M. C. Vigeant and L. M. Wang, "Objective and subjective evaluation of the use of directional sound sources in auralizations," in *Proceedings of the 18th International Congress on Acoustics, ICA*, Kyoto, 2004.

[VW07] ——, "Investigations of multi-channel auralization technique for various orchestra configurations, with phase-shifted string sections." in *Proceedings of the 2007 International Symposium on Room Acoustics, Seville*, Sept 2007.

[VWR07] M. C. Vigeant, L. M. Wang, and J. H. Rindel, "Investigations of multi-channel auralization technique for solo instruments and orchestra," in *Proceedings of the 19th International Congress on Acoustics, ICA*, Madrid, Sept 2007.

[WA80] G. Weinreich and E. B. Arnold, "Method for measuring acoustic radiation fields," *Journal of the Acoustical Society of America*, vol. 68, pp. 401–411, Aug 1980.

[WA01] D. Ward and T. Abhayapala, "Reproduction of a plane-wave sound field using an array of loudspeakers," *IEEE Transactions on Speech and Audio Processing*, vol. 9, pp. 697–707, 2001. [Online]. Available: http://ieeexplore.ieee.org/xpls/abs_all.jsp?arnumber=943347

[WB99] L. M. Wang and C. Burroughs, "Directivity patterns of acoustic radiation from bowed violins," *Journal of the Catgut Acoustical Society*, vol. 7, pp. 7–15, 1999.

[WB01] ——, "Acoustic radiation from bowed violins," *Journal of Acoustical Society of America*, vol. 110, pp. 543–555, 2001.

[WBF+00] M. Wright, J. Beauchamp, K. Fitz, X. Rodet, A. Röbel, X. Serra, and G. Wakefield, "Analysis/synthesis comparison," *Organised Sound*, vol. 5, pp. 173–189, 1st Dec 2000. [Online]. Available: http://cnmat.berkeley.edu/publications/analysis_synthesis_comparison

[WBV05] I. Witew, G. K. Behler, and M. Vorländer, "About just noticeable differences for aspects of spatial impressions in concert halls," *Acoustical Science and Technology, Acoustical Society of Japan*, vol. 26, pp. 185–192, 2005. [Online]. Available: http://www.jstage.jst.go.jp/article/ast/26/2/26_185/_article

[WDC97] O. Warusfel, P. Derogis, and R. Caussé, "Radiation synthesis with digitally controlled loudspeakers," in *Papers of the 103rd AES Convention*, New York, 1997. [Online]. Available: http://www.aes.org/e-lib/browse.cfm?elib=7202

[Wei97] G. Weinreich, "The DTC loudspeaker," in *Proceedings of the 133rd ASA meeting*, 1997. [Online]. Available: http://www.acoustics.org/press/133rd/2pea4.html

[Wei04] W. Weise, "Investigation of the anisotropy of hemi-dodecahedron noise source radiation," *Journal of Sound and Vibration*, vol. 270, pp. 137–147, Feb 2004.

[Wei08] E. W. Weisstein, *Web site: Wolfram MathWorld*, 2008. [Online]. Available: http://mathworld.wolfram.com

[Wik08a] *Web site: Oblate Spheroidal Coordinates*, August 2008. [Online]. Available: http://en.wikipedia.org/wiki/Oblate_spheroidal_coordinatesOblateSpheroidalCoordinates

[Wik08b] *Web site: Sommerfeld Radiation Condition*, August 2008. [Online]. Available: http://en.wikipedia.org/wiki/Sommerfeld_radiation_condition

[Wil99] E. G. Williams, *Fourier Acoustics*. London/San Diego: Academic Press, 1999.

[Wit00] D. D. Wit, "Gauß cubature for the surface of the unit sphere," *arXiv.org Mathematics, Numerical Analysis*, 2000.

[WM01] O. Warusfel and N. Misdariis, "Directivity synthesis with a 3d array of loudspeakers, application for stage performance," in *Proceedings of the DAFX01*, Limerick, 2001.

[WM04] ——, "Sound source radiation syntheses: From performance to domestic rendering," in *Papers of the 116th AES Convention*, Berlin, 2004. [Online]. Available: http://www.aes.org/e-lib/browse.cfm?elib=12793

[Wom03] R. Womersley, *Web site: Interpolation and Cubature on the Sphere*, 2003. [Online]. Available: http://web.maths.unsw.edu.au/~rsw/Sphere/

[Wom06] ——, *Web site: Distributing points on the sphere*, 2006. [Online]. Available: http://www.maths.unsw.edu.au/school/articles/me100.html

[WS01] R. S. Womersley and I. H. Sloan, "How good can polynomial interpolation on the sphere be?" Sydney, Tech. Rep., Apr 2001.

[WV07] L. M. Wang and M. C. Vigeant, "Evaluations of output from room acoustic computer modeling and auralization due to different sound source directionalities," *Applied Acoustics*, Sep 2007.

[Xu96] Y.-L. Xu, "Fast evaluation of the gaunt coefficients," *Mathematics of Computation*, vol. 65, no. 216, 1996.

[Zby07] M. Zbyszyński, *Web site: Low-cost Spherical Speaker Array*, Apr 2007. [Online]. Available: http://www.instructables.com/id/Low-cost-Spherical-Speaker-Array/

[ZF99] E. Zwicker and H. Fastl, *Psychoacoustics, facts and models*. Springer, Berlin Heidelberg, 1999.

[ZH07] F. Zotter and R. Höldrich, "Modeling radiation synthesis with spherical loudspeaker arrays," in *Proc 19th International Congress on Acoustics, ICA*, Madrid, 2nd Sep 2007. [Online]. Available: http://iem.at/projekte/publications/paper/modeling_radiation

[Zio95] L. J. Ziomek, *Fundamentals of Acoustic Field Theory and Space-Time Signal Processing*, 1995.

[ZKA08] W. Zhang, R. A. Kennedy, and T. D. Abhayapala, "Signal estimation from incomplete data on the sphere," in *IEEE AusCTW*, 2008.

[ZN07] F. Zotter and M. Noisternig, "Near- and far-field beamforming using spherical loudspeaker arrays," in *Proceedings of the 3rd Congress of the Alps Adria Acoustics Association*, Graz, 27th Sep 2007. [Online]. Available: http://iem.at/projekte/publications/paper/near/

[Zot04] F. Zotter, "Unterdrückung hörbarer Störgeräusche in Echtzeitsystemen," Master's Thesis, Institut für Elektronische Musik und Akustik, Kunstuniversität Graz, Technische Universität Graz, 2004.

[Zot08] ——, "Directional recording and analysis of sounds from musical instruments," in *Proceedings of the 2nd ASA-EAA joint conference, ACOUSTICS08*, Paris, Jul 2008. [Online]. Available: http://iem.at/Members/zotter/radiation_capture/TalkRadiationParis08/

[Zot09] ——, "Sampling strategies for acoustic holography/holophony on the sphere," in *Fortschritte der Akustik, NAG/35. DAGA International Conference*, Rotterdam, 23rd March 2009.

[ZPF09] F. Zotter, H. Pomberger, and M. Frank, "An alternative ambisonics formulation: Modal source strength matching and spatial aliasing," in *Papers of the 126th AES Convention*, Munich, May 2009.

[ZPS08] F. Zotter, H. Pomberger, and A. Schmeder, "Efficient directivity pattern control for spherical loudspeaker arrays," in *Proceedings of the 2nd ASA-EAA joint conference, ACOUSTICS08*, Paris, Jul 2008.

[ZS06] F. Zotter and A. Sontacchi, "IEM Report 35/27: Zwischenreport zum Projekt "Virtual Gamelan Graz (VGG)"," Graz, Tech. Rep., Oct 2006. [Online]. Available: http://iem.at/projekte/publications/iem_report/report35_06/project_view

[ZS07] ——, "IEM Report 39/27: Icosahedral loudspeaker array," Graz, Tech. Rep., Jan 2007. [Online]. Available: http://iem.at/projekte/publications/iem_report/report39_07/report39_07/file_view

[ZSH07] F. Zotter, A. Sontacchi, and R. Höldrich, "Modeling a spherical loudspeaker system as multipole source," in *Fortschritte der Akustik, 33. DAGA*, Stuttgart, 19th March 2007. [Online]. Available: http://iem.at/projekte/publications/paper/modeling/

[ZSN08] F. Zotter, A. Schmeder, and M. Noisternig, "Crosstalk cancellation for spherical loudspeaker arrays," in *Fortschritte der Akustik, 34. DAGA*, Dresden, 10th March 2008.

[ZSNH07] F. Zotter, A. Sontacchi, M. Noisternig, and R. Höldrich, "Capturing the radiation characteristics of the bonang barung," in *Proceedings of the 3rd Congress of the Alps Adria Acoustics Association*, Graz, 27th Sep 2007. [Online]. Available: http://iem.at/projekte/publications/paper/capturing/